Detection and characterization of quasi singularities in turbulence

Florian Nguyen

Université de Lille

Université de Lille

Doctoral School **EDSPI Université Lille Nord-de-France**

University Department **Laboratoire de Mécanique des Fluides de Lille-Kampé de Fériet**

Thesis defended by **Florian Nguyen**

Defended on **3rd September, 2020**

In order to become Doctor from Université de Lille

Academic Field **Mécanique**

Detection and characterization of quasi singularities in turbulence

Thesis supervised by Jean-Philippe Laval
Bérengère Dubrulle

Committee members

Referees	Sebastien Galtier	Professor at Univ. Paris–Saclay	
	Patrice Abry	Senior Researcher at ENS Lyon	
Examiners	Pierre Chainais	Professor at École Centrale Lille	Committee President
	Marc Etienne Brachet	Senior Researcher at ENS	
Supervisors	Jean-Philippe Laval	Senior Researcher at CNRS	
	Bérengère Dubrulle	Senior Researcher at CNRS	

Université de Lille

Université de Lille

École doctorale **EDSPI Université Lille Nord-de-France**

Unité de recherche **Laboratoire de Mécanique des Fluides de Lille-Kampé de Fériet**

Thèse présentée par **Florian Nguyen**

Soutenue le **3 septembre 2020**

En vue de l'obtention du grade de docteur de l'Université de Lille

Discipline **Mécanique**

Détection et caractérisation des singularités en turbulence

Thèse dirigée par Jean-Philippe Laval
Bérengère Dubrulle

Composition du jury

Rapporteurs	Sebastien Galtier	professeur à l'Univ. Paris–Saclay	
	Patrice Abry	directeur de recherche à l'ENS Lyon	
Examinateurs	Pierre Chainais	professeur à l'École Centrale Lille	président du jury
	Marc Etienne Brachet	directeur de recherche à l'ENS	
Directeurs de thèse	Jean-Philippe Laval	directeur de recherche au CNRS	
	Bérengère Dubrulle	directrice de recherche au CNRS	

Detection and characterization of quasi singularities in turbulence

Abstract

It is still not known whether the equations of Navier–Stokes are well posed, i.e. whether their solutions can develop singularities from regular initial conditions. This unsolved problem might be the key to explain anomalous dissipation. As such, a method based on local energy transfers has been developed as a mean to identify potentially singular events in turbulence data. In this thesis, a local statistical method derived from multifractal analysis is developed in order to measure local Hölder coefficients. This method provides an estimate of the local regularity of turbulent velocity fields. Combined with local energy transfers, this allows us to locate and characterize quasi singular events. The method is applied in simulation to extract rare irregular structures at the dissipative scale. From the data aggregated, we derive a "typical singular event" bearing similarities with a Burgers vortex. Extending the analysis to time resolved data shows that irregular events are connected with vortex interactions. In parallel, we developed a new simulation scheme for Navier–Stokes based on a particles-in-cell model and using the Clebsch decomposition. Its purpose is to track potential singularities in scale for a comparatively low computational cost.

Keywords: Navier–Stokes, Singularities, Turbulence, Multifractal, Simulations, PIC method

Détection et caractérisation des singularités en turbulence

Résumé

Il n'est pas encore démontré que les équations de Navier–Stokes sont bien posées, c'est à dire que leur solutions ne développent pas de singularités à partir de condition initiales régulières. Résoudre ce problème pourrait conduire à expliquer l'anomalie dissipative. Ainsi, une méthode fondée sur les transferts d'énergie locaux a été développée comme un critère de détection de singularités potentielles. Dans cette thèse, nous développons une méthode à la fois locale et statistique, dérivée de l'analyse multifractale, afin de mesurer des coefficients de Hölder locaux. Cette méthode nous permet d'estimer la régularité locale de champs de vitesse turbulents. Combiné au critère fondé sur les transferts d'énergie, ceci nous permet de localiser et quantifier des événements quasi singuliers. La méthode a été appliquée sur des données de simulation afin d'extraire des structures irrégulières à l'échelle dissipative. A partir des données ainsi obtenues, nous reconstituons un "événement singulier typique" qui présente des similarités avec le vortex de Burgers. L'analyse sur des données résolues en temps montre une connexion avec les interactions entre tourbillons. En parallèle, nous avons construit un nouveau schéma de simulation pour Navier–Stokes fondé sur un modèle particulaire et la décomposition de Clebsch. L'objectif affiché est de suivre à moindre coût les singularités potentielles en échelle.

Mots clés : Navier–Stokes, Singularités, Turbulence, Multifractal, Simulations, Méthode PIC

Laboratoire de Mécanique des Fluides de Lille-Kampé de Fériet
Boulevard Paul Langevin, 59655 Villeneuve d'Ascq

Remerciements

Je voudrais en premier lieu remercier mes directeurs de thèse Bérengère Dubrulle et Jean-Philippe Laval, sans lesquels je n'aurai probablement pas connu le large sujet d'étude qu'est la turbulence et qui ont partagé avec moi leur savoir et leur expérience.

Je remercie également Sébastien Galtier et Patrice Abry pour avoir accepté d'être rapporteurs pour ma thèse. Je remercie en outre Pierre Chainais et Marc Etienne Brachet pour avoir accepté de faire partie de mon jury.

Je remercie mes collègues, à la fois à Lille et au CEA Saclay, pour les discussions éclairante sur des domaines très variés. Je remercie en particulier les résidents du bâtiment M6 pour leur contribution à la vie de laboratoire.

Je remercie les mathématiciens Alexey Cheskidov et Roman Shvydkoy pour le soutien théorique apporté dans le travail de cette thèse.

Finalement, je remercie ma famille pour le soutien morale et logistique apporté tout au long de mon séjour à Lille.

Ce travail a été financé par le biais d'une Allocation Spécifique Normalienne, sous la gestion de l'École Normale Supérieur de Paris et de l'Université de Lille. Il a également bénéficié de financement par l'ANR EXPLOIT, no. ANR-16-CE06-0006-01, et des ressources informatiques du Grand Équipement National de Calcul Intensif par le biais de l'allocation A0062A01741.

Contents

Preambule

Turbulence is a phenomenon manifesting itself in a very wide range of scale, from human size to the atmosphere and up to galaxies. At the human scale, its effects are observed in a multitude of fields including meteorology and aeronautics, but also in food industries. In some cases those effects are beneficial, as it increases the mixing efficiency of slowly diffusive scalar. In other situations, turbulence is problematic, as it increases the energy consumption due to its high level of dissipation. All these factors makes it a subject of major interest for research, as any development can be beneficial for a large range of applications.

The governing equations for fluids mechanic in general and turbulence in particular are the Navier–Stokes equations. Despite having been derived in the 18th century, they are still a subject of active research. A major yet unsolved issue is the regularity of its solutions. This issue has physical implications. Indeed, it was proven that if singularities exist in turbulent velocity fields, they would be able to dissipate energy in a non viscous way. This contribution to the global energy budget might be an explication to the phenomenon of anomalous dissipation, or the fact that the energy dissipation rate no longer depends on viscosity for high enough Reynolds numbers.

The objective of this thesis is to build a new tool to detect potential singularities in both numerical and experimental turbulent velocity fields. This tool is based on a measure of local regularity inherited from the concept of multifractal analysis. It is meant to complement a previously designed criterion based on local energy transfer. Indeed, this other tool is designed to analyze the "anomalous dissipation" part of the problem and does not provide a way to quantify the regularity of a given velocity field. The conjunction of these two tools allows for an in-depth analysis of the extreme events found in turbulent fields. This analysis brings some hints about the distribution, physical mechanism and evolution of the events assimilated to quasi singularities.

In parallel with the elaboration of tools to characterize the flow regularity, we develop a new numerical simulation method based on the Clebsch decomposition.

Its purpose is to simulate the small scales of the flow using the inviscid Euler equations in order to potentially track singularities where they would otherwise be dissipated by viscosity. In order to keep the simulation cost affordable, a Particle in Cell method is used to model those small scales.

This thesis is structured as follow: The Chapter 1 is dedicated to a general introduction about turbulence and singularities. The Chapter 2 is dedicated to local energy transfers and their usefulness as a criterion for the detection of singularities. The Chapter 3 explains the new method to quantify singularities that was developed during this thesis. The results of this method for numerical and experimental datasets are presented in the Chapter 4. Before the conclusion, the Chapter 5 develops the basis for the new simulation method, of which the implementation is unfinished at the time of the redaction of this manuscript.

Chapter 1

Turbulence and singularities

In this chapter, we introduce the properties of turbulence and the Navier–Stokes equation and show why there are interrogations about the existence or non existence of singularities.

1.1 Generalities about turbulence

Turbulence manifests itself in a flow when the viscosity of the fluid is low enough that viscous effects are dominated by inertia. In this section, we recall the governing equations and present some of their properties. We particularly focus on properties leading to the suspicion of singularities.

1.1.1 Navier–Stokes: A governing equation

The governing equations for viscous flow are the Navier-Stokes equations. Derived in the 19th century, they include two partial differential equations, one coming from the conservation of mass and the other from the conservation of momentum. In the incompressible case, they are expressed as follow:

$$\partial_t u_i + u_j \partial_j u_i = -\frac{1}{\rho}\partial_i p + \nu \partial_j \partial_j u_i + f_i, \tag{1.1}$$

$$\partial_j u_j = 0. \tag{1.2}$$

where the Einstein convention for repeated indices is used.

In these equations, hereafter referred to as INSE for *Incompressible Navier–Stokes Equations*,

- $u_i(\boldsymbol{x}, t)$ for $i = 1, 2, 3$ are the three components of the velocity field;

- $p(\boldsymbol{x}, t)$ is the pressure field;
- ν is the molecular viscosity;
- $f_i(\boldsymbol{x}, t)$ corresponds to the volumic forces acting on the fluid.

The first equation is derived from the conservation of momentum (i.e. Newton's second law) applied to an elementary volume of fluid. In this equation, the left hand side, corresponding to a material derivative of the velocity ($\frac{\mathrm{d}u_i}{\mathrm{d}t}$), is the elementary volume acceleration. The right hand side corresponds to the forces applied to the volume. This includes a pressure term, the contribution of viscosity, as well as exterior volumic forces. The second equation expresses mass conservation, or in this incompressible case, the conservation of volume.

Several conditions must be fulfilled for the INSE to be applicable to a flow. The first of those is the **incompressibility** condition. Most fluids can be considered incompressible, i.e. keeping an uniform density ρ, under certain conditions. For this to be valid, the time required to regularise variations of density must be very small compared to the other characteristics time of the flow. This property is captured by the Mach number:

$$M = \frac{u}{c} \tag{1.3}$$

where u is a characteristic velocity of the flow and c is the sound velocity in the medium. The incompressibility condition is then valid provided $M \ll 1$.

Another condition is the **scale separation**, related to the validity of using an elementary volume of fluid when computing the conservation of mass and the conservation of momentum. This is made more apparent when the Navier–Stokes equations are derived using the kinetic theory of gas (see e.g. [42]). The general idea is that for the momentum equation (1.1) to be valid without including molecular effects, the elementary volume must be very large compared to the range of these interactions. This property is captured by the Knudsen number:

$$Kn = \frac{\ell_{mol}}{\ell_{min,flow}} \tag{1.4}$$

where ℓ_{mol} is the scale of the molecular interactions and $\ell_{min,flow}$ is the minimum scale of the flow. This last scale represents the size of the elementary volume of fluid that needs to be considered in order to describe the flow with equation (1.1). Typically, $\ell_{min,flow}$ is the Kolmogorov scale. The scale ℓ_{mol} is typically the mean free path for a gas or the distance between molecules for a liquid. In this thesis, we only use fluids with a molecular scale of the order of 0.1 nm, while the Kolmogorov

scale is always greater than 10 μm. As a result, the scale separation should always be respected.

1.1.2 Inertia versus viscosity

The momentum part of the INSE can be made dimensionless using a characteristic velocity U and a characteristic scale L as follows:

$$\partial_t^* u_i^* + u_j^* \partial_j^* u_i^* = -\partial_i^* p^* + \frac{1}{Re} \partial_j^* \partial_j^* u_i^* + f_i^* \tag{1.5}$$

where the asterisk denotes a dimensionless quantity or derivative and the Reynolds number is defined as:

$$Re = \frac{UL}{\nu}. \tag{1.6}$$

The Reynolds number is thus the main parameter for the INSE. It can be interpreted as a ratio of inertial effect over viscous effects. Indeed, if the Reynolds number is low, the viscous term $\partial_j^* \partial_j^* u_i^*$ dominates the inertial terms in the INSE. This leads to a laminar flow, with a number of properties including symmetry by time reversal. Such flows can be observed for very viscous fluid (e.g. honey) or at very small scale and velocity (e.g. flow around a bacteria swimming).

Conversely, if the Reynolds number is very high, the nonlinear terms $u_j^* \partial_j^* u_i^*$ and $\partial_i^* p^*$ dominate the viscous term. This type of flow is much more chaotic than laminar flows, leading to the name *turbulence*, originating from the Latin *turba* meaning "disorder" or "tumult". Such flow is commonly seen in the wakes of boats or planes for example.

In practice, the exact threshold of Reynolds number separating laminar and turbulent flow depends on the geometry of the system.

1.1.3 A multiscale phenomenon

One characteristic of turbulent flows is the corresponding wide range of scales. This property is observed visually in the velocity fields as one can observe vortices of very different size in a same flow. Examples of such velocity field are given in Chapter 4.

Meanwhile, the multiplicity of scales is also something that can be anticipated from the INSE. This is particularly the contribution of the non linear terms, fundamental to turbulence. Indeed, let us suppose an initial condition of velocity with

only one mode of wave number k. By the trigonometric formula

$$cos(kx)^2 = \frac{cos(2kx) + 1}{2}, \tag{1.7}$$

this initial mode will cause the apparition of a mode with wave number $2k$. This process is repeated, leading to cover a large range of scales. In the limit of zero viscosity, corresponding to the Euler equations, this cascade continues indefinitely. However, in the case of a finite viscosity, this process is interrupted as the viscous term becomes comparable to the non linear term. Using the dissipation rate ϵ as a basis for dimensional analysis, one can estimate the characteristic velocity at scale ℓ as $u_\ell = (\epsilon\ell)^{1/3}$. This means that the corresponding viscous term (resp. nonlinear term) has an order of magnitude of $\nu\epsilon^{1/3}\ell^{-5/3}$ (resp. $\epsilon^{2/3}\ell^{-1/3}$). Those terms are balanced at the scale $\ell = \eta$, known as the Kolmogorov scale:

$$\eta = \left(\frac{\nu^3}{\epsilon}\right)^{1/4}. \tag{1.8}$$

This "cascade" can be observed in the energy spectra corresponding to turbulent velocity fields. Such spectra are shown in Chapter 3, and a schematic illustration is presented in figure 1.1. The main feature observed is a large range of modes, named the inertial range, over which the energy follows a power law in $k^{-5/3}$. This is the Kolmogorov law, named after Andrey Kolmogorov who derived it in his famous 1941 paper [39]. It can be recovered less rigorously using an argument based on dimensional analysis. Indeed, as the inertial range observed experimentally occurs above the Kolmogorov scale, the viscous effect are still dominated by inertial effects. Removing viscosity, the only pertinent physical parameter for the analysis is the energy dissipation rate ϵ (in a stationary regime, this is also the energy injection rate). As such, the energy of the mode of wave number k must scale as $E(k) \propto \epsilon^{2/3}k^{-5/3}$.

The inertial range is followed at small scale by the dissipative range (also referred to as the viscous range). For scales close to the Kolmogorov scale, viscosity becomes effective and energy is dissipated. On the other side of the inertial range, at large scale, is the injection range. This corresponds to the scales at which energy is injected in the flow. The exact behavior at this range is highly dependent on the method of forcing and the geometry of the flow.

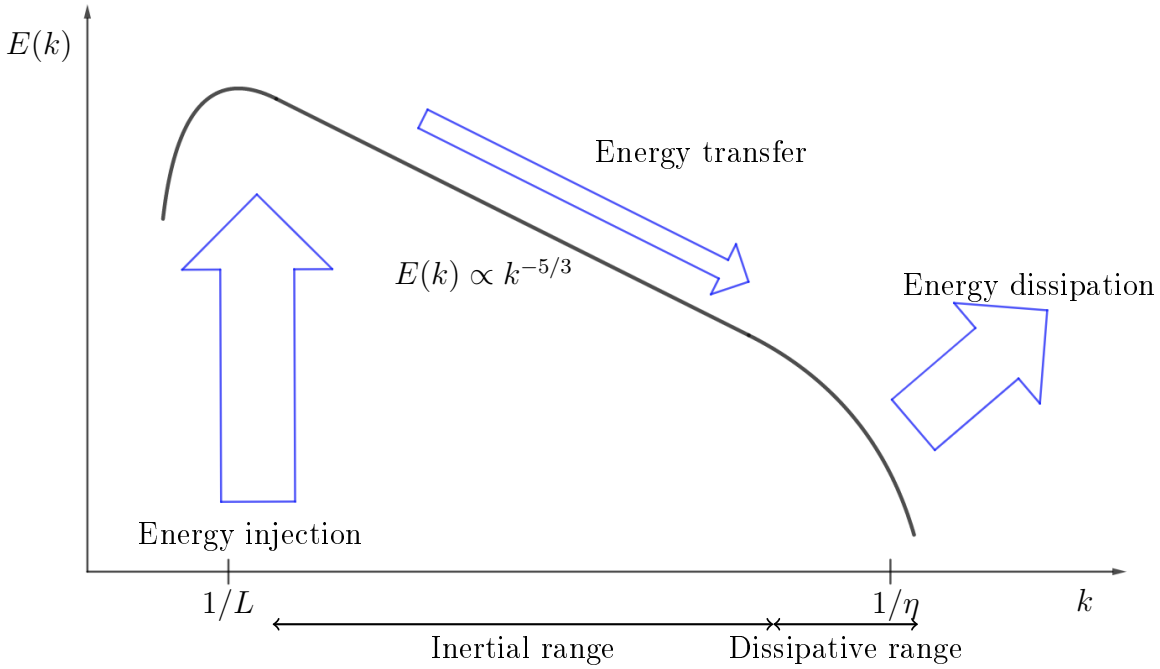

Figure 1.1: Schematic illustration of the energy spectra in a turbulent flow in log-log.

1.1.4 The zeroth law of turbulence

The viscous term in the INSE leads to energy dissipation. The energy balance assuming smooth solutions reads:

$$\partial_t \left(\frac{1}{2}|\boldsymbol{u}|^2\right) + \nabla \cdot \left[\left(\frac{1}{2}|\boldsymbol{u}|^2 + p\right)\boldsymbol{u} - \nu\nabla\left(\frac{1}{2}|\boldsymbol{u}|^2\right)\right] = -\nu|\nabla \boldsymbol{u}|^2 \qquad (1.9)$$

where the dissipative term is on the right hand side. Thus, the average dissipative term $\epsilon = \langle \nu|\nabla \boldsymbol{u}|^2\rangle$, the average being taken in space and time, appears to scale with the viscosity ν. In other world, it would be expected that the lower the viscosity of the fluid (i.e. the higher the Reynolds number), the less forcing is required to keep it in motion. This intuition is however disproved by both experiment and simulations. In what is referred to as the **zeroth law of turbulence** or **anomalous dissipation**. This behavior is schematically illustrated in the figure 1.2. What is observed is that for low values of Reynolds number, the dissipation rate indeed scales proportionally to the inverse of Re, i.e. to the viscosity. However, past a certain critical Reynolds number, this scaling changes and the dissipation rate no longer depends on the Reynolds number [63].

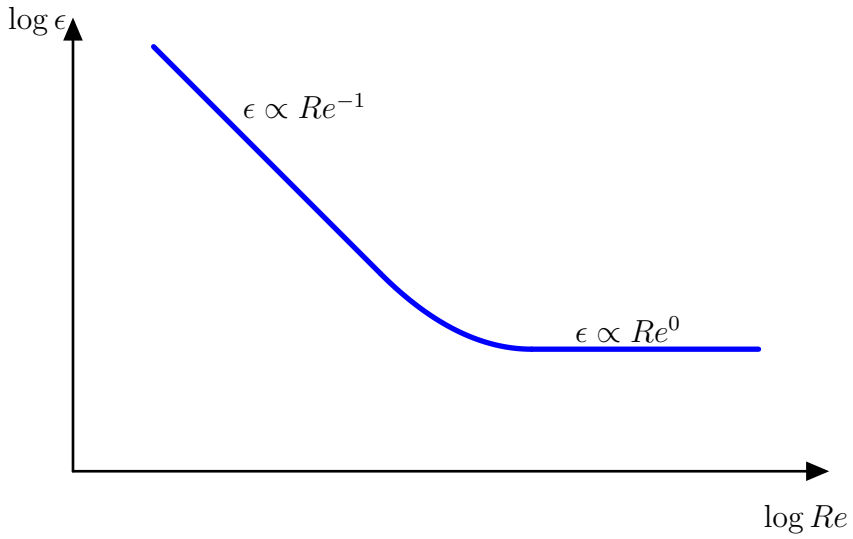

Figure 1.2: Schematic of anomalous dissipation scaling.

1.2 Singularities of Navier–Stokes

1.2.1 Onsager's conjecture

This observation about dissipation becoming independent of viscosity at high Reynolds number leads to a first argument for the singular behavior of the flow. Indeed, if the term ϵ becomes independent of ν for high Reynolds number, this means that the gradients of velocity $\nabla \boldsymbol{u}$ become larger and larger as the viscosity increases. As the corresponding scaling would be $\nabla \boldsymbol{u} \propto Re^{-1/2}$, the limit $Re \to \infty$ leads to a divergence of the velocity gradient.

From another point of view, at $\nu = 0$ the Navier–Stokes equations 1.1 become the Euler equation. This equation is such that, assuming smooth solutions, the energy is conserved. As such, it appears paradoxical that the limit $\nu \to 0$ is observed to have a constant, non zero dissipation. Lars Onsager [61] proposed a solution to this contradiction: a non smooth velocity field solution of the Euler equations would allow for a non zero dissipation.

> ". . . in three dimensions a mechanism for complete dissipation of all kinetic energy, even without the aid of viscosity, is available."
>
> (Onsager)

1.2.2 Mathematical results

In this thesis, we are interested in looking for such loss of smoothness. In particular, a major problem which has yet to be resolved since the 19th century is whether the

3D incompressible Euler and Navier–Stokes equations are well posed. The later in particular is the object of one of the "Millenium Problems" set by the Clay Mathematics Institute of Cambridge. This problems are a collection of difficult mathematical questions, the resolution of which would be rewarded by a prize of one million dollars.

The well posedness of an equation has three requirements in the meaning of Hadamard [29]. Those are the existence of a solution, its unicity and its regularity. For this last criterion, it appears indeed that if a solution to Navier–Stokes is not at least twice differentiable, the Laplacian in the viscous term of equation (1.1) is not properly defined.

In the 2D case, the well posedness of the Euler equations [77] and the Navier–Stokes equations [43] have already been proven. The proof in the 3D case is much more difficult. For the 3D incompressible Euler equations, it was proven that there is no unicity of the solution, if it exists [66]. Moreover, it was proven that if a non regular solution exists, then the vorticity is unbounded [7]. There are however no result proving the existence of solutions, nor their regularity or non regularity.

For the case of the Navier Stokes equations, Leray [46] actually proved the existence of solutions in the weak sense, without any assumption about regularity. This leaves uniqueness and regularity as open questions. Some results have been obtained for this second point. First, Constantin [14] proved that if singularity exists in Navier–Stokes, then they take the form of an unbounded velocity $|\boldsymbol{u}| \to \infty$. This is an even stronger condition than for the Euler case. Moreover, it was also proven that singularity must be very rare events. More precisely, singularities cannot form continuous curves in space-time, i.e. they must be punctual, instantaneous events [11]. Finally, singular stationary solutions of Navier–Stokes have been found [47]. This however does not provide a proof for the regularity of solutions starting from a regular initial condition, which would be more pertinent from a physical point of view.

1.2.3 Physical approach to singularities

The impact of those mathematical results on our understanding of the physical flow described by the Navier–Stokes equations is not obvious. In particular, the physical reality of a point like singularity or a diverging velocity is questionable. Under these circumstances, it is important to make the distinction between the mathematical equations and the phenomena observable in real flows, as well as simulated flows.

The objective of this thesis is to approach the question of the regularity of

the solutions to the Navier–Stokes equations from a physical point of view. The working hypothesis is that mathematical singularities do exist, i.e. that there exist solutions becoming singular in a finite time from a regular initial condition. This hypothesis does not lead to the existence of singularities in a real flow. Indeed, for the INSE to work as a model of the flow, the conditions exposed in section 1.1.1 must be fulfilled. However, the very concept of punctual singularity, in other words a structure at scale $\ell = 0$, is contradictory with the condition of **scale separation**. Furthermore, the mathematical result by Constantin [14] means that a singularity of Navier-Stokes would lead to an unbounded velocity. From the strict perspective of the Navier–Stokes equations, this would mean breaking the **incompressibility condition**, as the Mach number would locally blow up: $Ma \gg 1$.

In summary, the existence of singularities in Navier–Stokes would lead to locations of the flow where the INSE are no longer the valid model. The detection of such events, hereafter called potential singularities or quasi singularities, is the target of this thesis. In accordance to the mathematical results already presented [11], such events are expected to be rare. This means that there is no reason to question the validity of the Navier–Stokes equations in general to describe a turbulent flow. However, in accordance with Onsager's conjecture, the mathematical singularities could lead to a non viscous energy dissipation, enough to explain anomalous dissipation. This would mean that quasi singularities might be relevant to the global energy budget despite their rarity. The questions of energy transfers are further discussed in the next chapter.

In this thesis, we will primarily work using numerical simulations, even though all tools described are similarly applicable to experimental results. By their nature, simulations fundamentally differ from the real flow in the relationship with Navier–Stokes singularities. Indeed, as the simulations are based on the equations, the conditions of validity of the INSE do not matter. The difference with the complete Navier–Stokes equations manifests itself in the numerical scheme used to discretize them. For example, a spatial derivative can be approximated using a **finite difference** method using the following method (in 1D):

$$\frac{\mathrm{d}f}{\mathrm{d}x}(x) \approx \frac{f(x+\Delta x) - f(x-\Delta x)}{2\Delta x}. \tag{1.10}$$

These approximations fundamentally relies on the Taylor expansion of the function f. In other words, a certain regularity is required for the derivatives to be accurate. On the other hand, the **spectral method** uses exact derivatives of functions decomposed over Fourier modes. The approximation in the spectral method

comes from the limited number of modes that can be computed, effectively cutting off fluctuations at a lower scale. In other words, the accuracy of the simulation of the INSE requires a grid step smaller than the smallest scales of the flow, such that $\Delta x < \ell_{min,flow}$. Typically, the discretization scale Δx is chosen of the order of the Kolmogorov length η. This means that if the solution to the Navier–Stokes equations contains real mathematical singularities, those cannot be observed in the equivalent simulations. Note that more complex methods, for example using an adaptive mesh, may not have a definite smallest scale. Even for these methods, the scale $\ell = 0$ of a punctual singularity is still inaccessible.

We expect that wherever a real singularity would happen in the INSE, we would detect a quasi singularity in the simulated velocity field, resolved down to Δx. This justifies our use of simulations for the detection of singular features. In this aspect, our approach is similar to several previous studies which exhibited emergent irregular structures in simulations. These studies are preferentially conducted using the Euler equations, like the works by Luo and Hou [48] or Pumir [64], who observed events with a diverging vorticity. Similarly, numerous numerical studies have been performed by Kerr (e.g. [33, 34, 35, 32]) in order to study the relationship between potential singularities and vortex dynamics using criteria based on enstrophy and vorticity. Other such simulations include works by Grauer et al. [27], Uhlig et al. [69] and Grafke et al. [26]. Some studies have been performed using the full Navier–Stokes equations. This is the case in particular of a work by Vassilicos et al. [70], which uses a criterion based on the geometry of the streamlines of velocity to search for singularities. This thesis uses Navier–Stokes simulations and a new detection tool in order to locate and quantify quasi singularities.

We discussed that the real flow and the simulated one would no longer verify the INSE in case of a mathematical Navier–Stokes singularity for different reasons. As such, one might worry that the quasi singularities observed in these two cases would be different. However, we will suppose that the INSE represent a valid model down to the Kolmogorov scale even in presence of quasi singularities. Likewise, we expect the INSE to be simulated accurately down to the same scale. In consequence, the events qualified as potential singularities should be the same in experimental and simulation data. In this thesis, only simulations will be studied but some element of comparison with the experimental results by Paul Debue [15] are provided. Additionally, the tools developed are designed to be later used on experimental data.

Chapter 2

Tracking singularities using local energy transfer and the turbulent force

As the anomalous dissipation is suspected to be related with singularities, it is natural to try to use an approach based on energy transfer when searching for them. As a result, local energy budgets have already been used as the main criterion to detect and quantify singularities, in particular in the thesis by Dennis Kuzzay [40] and Paul Debue [15]. More precisely, the criterion is based on a scale by scale energy budget. The underlying idea is that if singularities exist and are related to the anomalous energy dissipation, then they would transfer energy to lower and lower scales without ever being dissipated by viscosity. This would go on until some hypothesis required for the formalism is broken and the energy is dissipated in a non viscous way. In contrast, in absence of singularity, the cascade of energy to lower scales would be interrupted by viscous dissipation. As such, locating regions of extreme energy transfer at a dissipative scale is an intuitive way to probe for singularities. This method is also used in this thesis. As a result, we detail the derivation of the local energy budget and some previous results in this chapter. We also describe a similar method based on the turbulent force.

2.1 Derivation using the weak formulation

2.1.1 Smoothed velocity field

The formalism used was introduced by Duchon and Robert in their paper [19]. The derivation of this formalism is based on an energy budget on the weak INSE. This is akin to smooth the velocity fields using a regularizing function, such that supposing their regularity is no longer required. Said another way, for all terms

involving a derivative in the equation, the derivative operator is applied to the regularizing function instead of the velocity field. The smoothed velocity field $\boldsymbol{u}^\ell$ in 3D for a scale ℓ is expressed as a convolution of the velocity field and the smoothing function ϕ^ℓ:

$$\boldsymbol{u}^\ell(\boldsymbol{x}) = \phi^\ell * \boldsymbol{u}(\boldsymbol{x}) = \int \phi^\ell(\boldsymbol{y})\boldsymbol{u}(\boldsymbol{x}-\boldsymbol{y})\mathrm{d}\boldsymbol{x}. \tag{2.1}$$

The regularizing function ϕ^ℓ is defined by:

$$\phi^\ell(\boldsymbol{x}) = \frac{\phi(\boldsymbol{x}/\ell)}{\int \phi(\boldsymbol{y}/\ell)\mathrm{d}^3\boldsymbol{y}} \tag{2.2}$$

where ϕ is an even function, positive of norm unity. As a consequence ϕ^ℓ is also even, positive with norm unity. As a result of the filtering, increasing the scale ℓ reduces the amount of small scales in $\boldsymbol{u}^\ell$. On the other hand, we can verify that in the sense of distributions, $\lim_{\ell\to 0}\boldsymbol{u}^\ell = \boldsymbol{u}$.

In this thesis, for all computation related to the Duchon Robert formalism, we will use a simple Gaussian:

$$\phi(\boldsymbol{x}) = \frac{1}{(2\pi)^{3/2}}\exp\left(-\frac{\boldsymbol{x}^2}{2}\right). \tag{2.3}$$

Spatial derivatives of the filtered velocity field $\boldsymbol{u}^\ell$ can thus be interpreted as wavelet transforms of the velocity using a Gaussian wavelet.

2.1.2 Energy budget on the filtered velocity by Duchon and Robert

Applying the convolution with ϕ^ℓ to the INSE (without forcing) yields:

$$\partial_j u_j^\ell = 0, \tag{2.4}$$

$$\partial_t u_i^\ell + (u_j\partial_j u_i)^\ell = -\partial_i p^\ell + \nu\partial_j\partial_j u_i^\ell. \tag{2.5}$$

By computing an energy budget on these equations, Duchon and Robert [19] obtained the following relation:

$$\frac{1}{2}\partial_t u_i u_i^\ell + \partial_i T_i^\ell = \frac{1}{2}\nu\partial_j\partial_j(u_i u_i^\ell) - \nu\partial_j u_i\partial_j u_i^\ell - D_I^\ell \tag{2.6}$$

where:

$$T_i^\ell = \frac{1}{2}\left[u_j u_j^\ell u_i + p^\ell u_i + p u_i^\ell\right] + \frac{1}{4}\left[(u_i u_j u_j)^\ell - (u_j u_j)^\ell u_i\right] \tag{2.7}$$

and

$$D_I^\ell(\boldsymbol{x}) = \frac{1}{4}\int \nabla\phi^\ell(\boldsymbol{\xi})\cdot\delta_{\boldsymbol{\xi}}\boldsymbol{u}(\boldsymbol{x})(\delta_{\boldsymbol{\xi}}\boldsymbol{u}(\boldsymbol{x}))^2\mathrm{d}\boldsymbol{\xi}. \tag{2.8}$$

where $\delta_{\boldsymbol{\xi}}\boldsymbol{u}(\boldsymbol{x}) = \boldsymbol{u}(\boldsymbol{x}+\boldsymbol{\xi}) - \boldsymbol{u}(\boldsymbol{x})$ is the velocity increment.

They then demonstrated that in the limit $\ell \to 0$, the equation (2.6) converges in the sense of distributions to:

$$\partial_t \frac{u_i^2}{2} + \partial_j\left[u_j\left(\frac{u_i^2}{2}+p\right)\right] = \nu\Delta\frac{u_i^2}{2} - \nu\partial_j u_i\partial_j u_i + D(\boldsymbol{u}) \tag{2.9}$$

where $D(\boldsymbol{u}) = lim_{\ell\to 0}D_I^\ell$. This limits holds for all smoothing function ϕ verifying the properties stated in the previous section.

This result adds the term $D(\boldsymbol{u})$ to the classical energy budget. If the velocity field is regular, a Taylor expansion leads to $\delta_{\boldsymbol{\xi}}\boldsymbol{u} \approx \boldsymbol{\xi}\cdot\boldsymbol{\nabla}u$ for small increments. In consequence, the scaling of the local energy transfer is $D_I^\ell \propto \ell^2$ and hence we have $D(\boldsymbol{u}) = 0$. This is however not true in the presence of strong enough singularities, which would lead to an additional energy dissipation independent of viscosity. This property is also true in the case of the Euler equations. This term is proven positive for the weak solutions of the INSE proposed by Leray.

2.1.3 Physical interpretation

For our objective of evaluating energy transfers in situations where the velocity field might not be regular, the equation (2.6) is still problematic as computing the right hand side requires to apply derivative on the unsmoothed velocity field $\boldsymbol{u}$. We can rearrange the terms to obtain this equation [17]:

$$\frac{1}{2}\partial_t u_i u_i^\ell + \partial_i J_i^\ell = -D_\nu^\ell - D_I^\ell \tag{2.10}$$

where

$$J_i^\ell = T_i^\ell - \frac{1}{2}\nu\partial_i[(u_j u_j)^\ell + u_j u_j^\ell] + \nu u_j\partial_i u_j^\ell \tag{2.11}$$

and

$$D_\nu^\ell(\boldsymbol{x}) = \nu\int \nabla^2\phi^\ell(\boldsymbol{\xi})\frac{\delta_{\boldsymbol{\xi}}\boldsymbol{u}(\boldsymbol{x})^2}{2}\mathrm{d}\boldsymbol{\xi}. \tag{2.12}$$

We can interpret the different terms of the equation as follows:

- the spatial transport, pressure term and viscous diffusion are contained in the term $\partial_i J_i^\ell$.
- the viscous dissipation at scale ℓ: D_ν^ℓ.

- the energy transfer to the lower scales: D_I^ℓ.

Using this interpretation, we can define a strategy on how to detect potential singularities. Indeed, if it exists, a true singularity would carry energy to the scale $\ell \to 0$. Similarly, a quasi singularity can be expected to transport energy to a scale smaller than the Kolmogorov scale η. As a result, the general idea of using local energy transfers to detect rare irregular structures consists in finding locations where the term D_I^ℓ stays high at low scale. The natural quantity to which compare D_I^ℓ is the viscous term D_ν^ℓ. As such, the method to detect quasi singularities is to identify the locations where the energy transfer D_I^ℓ is greater than the energy dissipation D_ν^ℓ at a scale $\ell \sim \eta$.

In order to further refine this intuition, let us suppose the velocity field is such that velocity increments over a distance ℓ verify a scaling $\|\delta_\ell(\boldsymbol{u})\| \sim \ell^h$, with $0 < h < 1$. This concept is formalized in the next chapter. By injecting this scaling in equations (2.8) and (2.12), we get the scalings:

$$D_I^\ell(\boldsymbol{x}) \propto \ell^{3h-1}, \tag{2.13}$$

$$D_\nu^\ell(\boldsymbol{x}) \propto \nu\ell^{2h-2}. \tag{2.14}$$

As a result, we can obtain an estimate for the scale at which the energy transfer term D_I^ℓ and the energy dissipation term D_ν^ℓ are balanced:

$$\eta_h \propto \nu^{1/(h+1)}. \tag{2.15}$$

Those two terms being balanced means that the velocity field starts to get regularized at scale η_h. In other words, the velocity increments no longer follow the initial power law $\|\delta_\ell(\boldsymbol{u})\| \sim \ell^h$ for $\ell < \eta_h$.

For a Hölder exponent of $h = 1/3$, which would correspond to the K41 scaling [39] in the inertial range, this regularizing scale matches the classical Kolmogorov scale $\eta_{h=1/3} = \eta$. However, if the velocity field is more singular, i.e. $h < 1/3$, this means that the regularizing scale η_h gets lower than η. In the case of a true singularity, we would have $\eta_h = 0$ as the velocity field is never regularized, leading to a Hölder coefficient of $h = -1$. The case $h < 0$ has not been discussed in section 3.1 and would correspond to a local blowup of velocity, which is coherent with the result by Constantin [14].

Using those scalings, our intuition of the energy budget around a potential singularities can be refined: For a singularity of "regularity" $h < 1/3$, the dissipation term D_ν^ℓ only catches up to the energy transfer term D_I^ℓ below the Kolmogorov

scale. However, this interpretation is only based on scalings and might not be perfectly robust. In order to confirm the strength of a singularity located using this criterion, it might be necessary to actually extract the power law behavior of these terms with respect to ℓ. The computational cost of this operation makes it impractical. A more easily implemented choice is to consider any event with an extreme value of energy transfer $D_I^\ell \gg \epsilon$ as a candidate for singularity [41]. This situation is one of the reason why the aim of this thesis is to develop a method to compute local Hölder exponent that could be used as a direct criterion for the detection of quasi singularities.

2.1.4 Turbulent force

We can also study the filtered INSE (2.5) for the velocity. Following a process much similar to the previous one, the following equation was derived by Eyink [20]:

$$\partial_t u_i^\ell + u_j^\ell \partial_j u_i^\ell = -\partial_i p^\ell + \nu \partial_j \partial_j u_i^\ell + F_i^\ell \tag{2.16}$$

where $\boldsymbol{F}^\ell$ can be identified as a force perceived at scale ℓ caused by the fluctuations of the flow at smaller scales. This force will hereafter be referred to as the turbulent force and is computed as follow:

$$F_i^\ell(\boldsymbol{x}) = \frac{1}{\ell}\left\{\int \partial_j \phi^\ell(\boldsymbol{\xi}) \delta_{\boldsymbol{\xi}} u_i(\boldsymbol{x}) \delta_{\boldsymbol{\xi}} u_j(\boldsymbol{x}) \mathrm{d}\boldsymbol{\xi} - \int \partial_j \phi^\ell(\boldsymbol{\xi}) \delta_{\boldsymbol{\xi}} u_i(\boldsymbol{x}) \mathrm{d}\boldsymbol{\xi} \int \phi^\ell(\boldsymbol{\xi'}) \delta_{\boldsymbol{\xi'}} u_j(\boldsymbol{x}) \mathrm{d}\boldsymbol{\xi'}\right\}. \tag{2.17}$$

One might interpret this turbulent force from the point of view of the Large Eddy Simulations (LES). In the context of LES, the turbulent force would correspond to the gradient of the Reynolds tensor. This term is then modeled, in order to avoid resolving the small scales required for its computation.

Following the same method as for the local energy transfer, one can evaluate the scaling of the turbulent force defined in equation (2.17) as:

$$\|\boldsymbol{F}^\ell\| \propto \ell^{2h-1}. \tag{2.18}$$

This means that the norm of the turbulent force diverges when $\ell \to 0$ whenever the local h exponent verifies $h < 1/2$. In other words, a criterion based on the anomalous turbulent force would be more sensitive than one based on the local energy transfer.

2.2 Implementation

The explicit computation of the integrals in the energy transfer from equations (2.8), the viscous dissipation from equation (2.12), and the turbulent force from equation (2.17) would be too computationally intensive. It is however possible to rearrange the terms in a more favorable way.

Using the Einstein summation convention, the equation (2.8) can be rewritten as:

$$D_I^\ell(\boldsymbol{x}) = \frac{1}{4}\int (\partial_i \phi^\ell)(\boldsymbol{\xi}) \cdot \delta_{\boldsymbol{\xi}} u_i(\boldsymbol{x}) \delta_{\boldsymbol{\xi}} u_j(\boldsymbol{x}) \delta_{\boldsymbol{\xi}} u_j(\boldsymbol{x}) \mathrm{d}\boldsymbol{\xi}. \tag{2.19}$$

By reinserting the definition of the increments $\delta_{\boldsymbol{\xi}} u_j(\boldsymbol{x}) = \boldsymbol{u}(\boldsymbol{x}+\boldsymbol{\xi}) - \boldsymbol{u}(\boldsymbol{x})$ and expanding the products, we obtain:

$$\begin{aligned} D_I^\ell(\boldsymbol{x}) = \frac{1}{4}\Big\{ & \int \partial_i \phi^\ell(\boldsymbol{\xi}) u_i(\boldsymbol{x}+\boldsymbol{\xi}) u_j(\boldsymbol{x}+\boldsymbol{\xi}) u_j(\boldsymbol{x}+\boldsymbol{\xi}) \mathrm{d}\boldsymbol{\xi} \\ & - u_i(\boldsymbol{x}) \int \partial_i \phi^\ell(\boldsymbol{\xi}) u_j(\boldsymbol{x}+\boldsymbol{\xi}) u_j(\boldsymbol{x}+\boldsymbol{\xi}) \mathrm{d}\boldsymbol{\xi} \\ & + u_j(\boldsymbol{x}) u_j(\boldsymbol{x}) \int \partial_i \phi^\ell(\boldsymbol{\xi}) u_i(\boldsymbol{x}+\boldsymbol{\xi}) \mathrm{d}\boldsymbol{\xi} \\ & - 2u_j(\boldsymbol{x}) \int \partial_i \phi^\ell(\boldsymbol{\xi}) u_i(\boldsymbol{x}+\boldsymbol{\xi}) u_j(\boldsymbol{x}+\boldsymbol{\xi}) \mathrm{d}\boldsymbol{\xi} \\ & + 2u_i(\boldsymbol{x}) u_j(\boldsymbol{x}) \int \partial_i \phi^\ell(\boldsymbol{\xi}) u_j(\boldsymbol{x}+\boldsymbol{\xi}) \mathrm{d}\boldsymbol{\xi} \Big\}. \end{aligned} \tag{2.20}$$

The integrals in this last expression can be interpreted as convolutions up to a minus sign, knowing that ϕ is even so its derivative is odd. The resulting convolutions can then be computed efficiently using Fast Fourier Transforms (FFTs). This makes it particularly convenient in the processing of data from simulations with periodic boundary conditions. The same method can be applied to compute D_ν^ℓ or $\boldsymbol{F}^\ell$ using FFTs. The code has been developed in C with OpenMP parallelization and uses the FFTW3 library [22]. It has been validated against two other independently developed codes for the computation of the energy transfer term D_I^ℓ.

2.3 Localization of potential singular events using the local energy transfer and turbulent force

These tools have been used in the past to track rare and potentially singular events in turbulent fields. The results discussed in this section are extracted from the thesis of Dennis Kuzzay and Paul Debue. They focus particularly on the

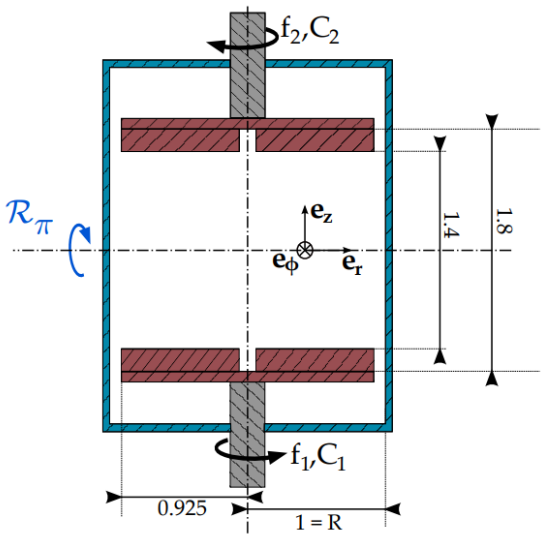

Figure 2.1: Schematic representation of a Von–Kármán setup. Figure reproduced from [40].

local energy transfers. The earlier work performed by Dennis Kuzzay gives us an element of comparison for the potential of the turbulent force as a criterion for the detection of potential singularities. The thesis by Paul Debue is focused on the study of events in experimental data, which serves as a good reference for our numerical study in Chapter 4.

2.3.1 Detection of singularities in experimental measurements

Both of these thesis applied these tools to experimental measurements in a Von–Kármán setup. The set-up consists of a vertical cylindrical tank of radius $R = 100\ mm$ and height $H = 240\ mm$. The flow is generated by two counter-rotating impellers. These are flat disks of diameter 185 mm fitted with 8 curved, radial blades of height $h_b = 20\ mm$ and curvature $|\alpha| = 72$. The distance between the impellers is $h = 180\ mm$. The impellers are driven by two independent motors set to rotate at the same speed in order to get exact counter-rotating regime. These motors maximum frequency is around $f \approx 10\ Hz$. A schematic representation of the setup is given in figure 2.1.

In the thesis of Dennis Kuzzay, the measurement were performed using Stereo Particle Image Velocimetry (or SPIV). Using this method allowed him to extract velocity fields with the three components of velocity on a 2D vertical plane passing through the center of the setup. The most interesting results for us were obtained

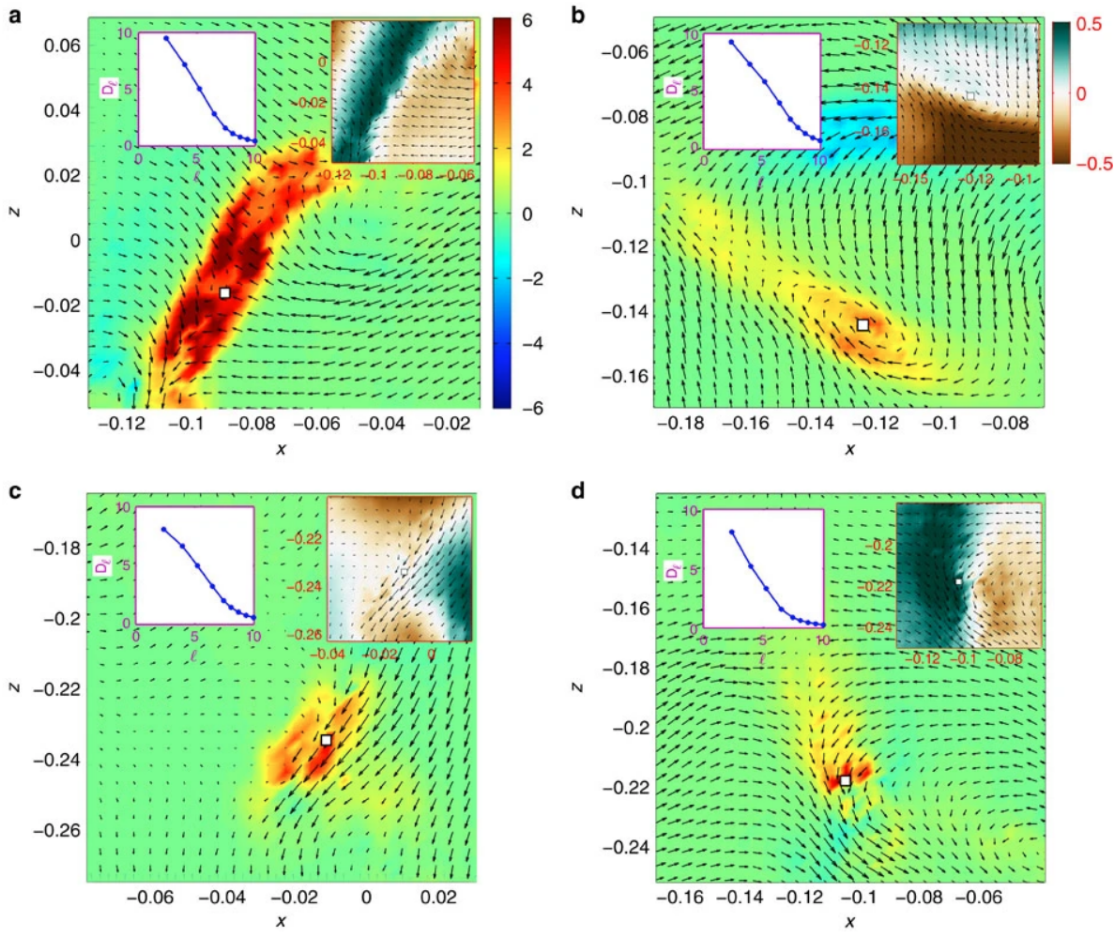

Figure 2.2: Four types of singularities found among the extreme events extracted from the data at the dissipative scale, where the Kolmogorov scale is resolved. **Main figures**: colormap of the dimensionless $D_I^\ell(\boldsymbol{u})$ field. The arrows correspond to in plane velocity. The white square materializes the location with the largest turbulent force in norm. **Vector field insets**: Velocity field near the singularity. The arrows stand for the radial (x) and axial (z) components while the colour scale stand for the azimuthal (y) component. **Plot insets**: $D_I^\ell(\boldsymbol{u})$ in dimensionless unit near the singularity as a function of ℓ/η. Figure reproduced from [41].

from an experiment using a mixture of water and glycerol. This mixture allows to reduce the Reynolds number down to $Re = 2\pi R^2 f/\nu \approx 6000$, which allows measurements down to the Kolmogorov scale. Using these measurements, 33 potentially singular events have been found using a criterion based on local energy transfers. Among those, four different categories were observed. Visualizations are provided in figure 2.2. Those categories, based on an interpretation using only a 2D slice, are "front","vortex", "jet" and "cusp". The "front" singularities, which include events where two volumes of fluid with very distinct velocity appear to interact, are the most common. The evolution of the local energy transfer as a function of scale provided in inset illustrates the behavior discussed previously: the local energy transfer is still increasing at a scale close to Kolmogorov.

The same events can also be detected using a method based on the turbulent force instead. Among the events detected with extreme value of the turbulent force in norm, we recognize the same 4 categories found by Dennis Kuzzay, as illustrated in figure 2.3. The evolution of the turbulent force as a function of scale is represented in the insets in the same figure. In all the cases illustrated, we observe a rise of the turbulent force as the scale decreases, which is then dampened for a scale of order $\ell = 5\eta$ (with the notable exception of the event in figure 2.3a). This short rise is similar to the blow up at small scale expected for real singularities. In this case, the divergence is interrupted, although it is not clear if it is by viscosity or if the limited resolution introduces errors in the computation of the turbulent force. This is what is typically expected for quasi singularities, i.e. a singular behavior observed close to the Kolmogorov scale but interrupted either by viscosity or by the resolution of the dataset.

The comparison of the events found using the turbulent force and the local energy transfers shows that we encounter the same types of event. Moreover, the computational cost associated to turbulent forces is higher than for local energy transfer. For these reasons, we prefer using only the local energy transfer in the following.

This study and classification has been expanded to events found in 3D measurements in Paul Debue's thesis. Those results will be discussed in more details in Chapter 4.

2.4 The Velocity Gradient Tensor Invariants

Another tool used by Paul Debue in order to characterize the singular events is the Velocity Gradient Tensor (VGT) invariant method. This method is first described

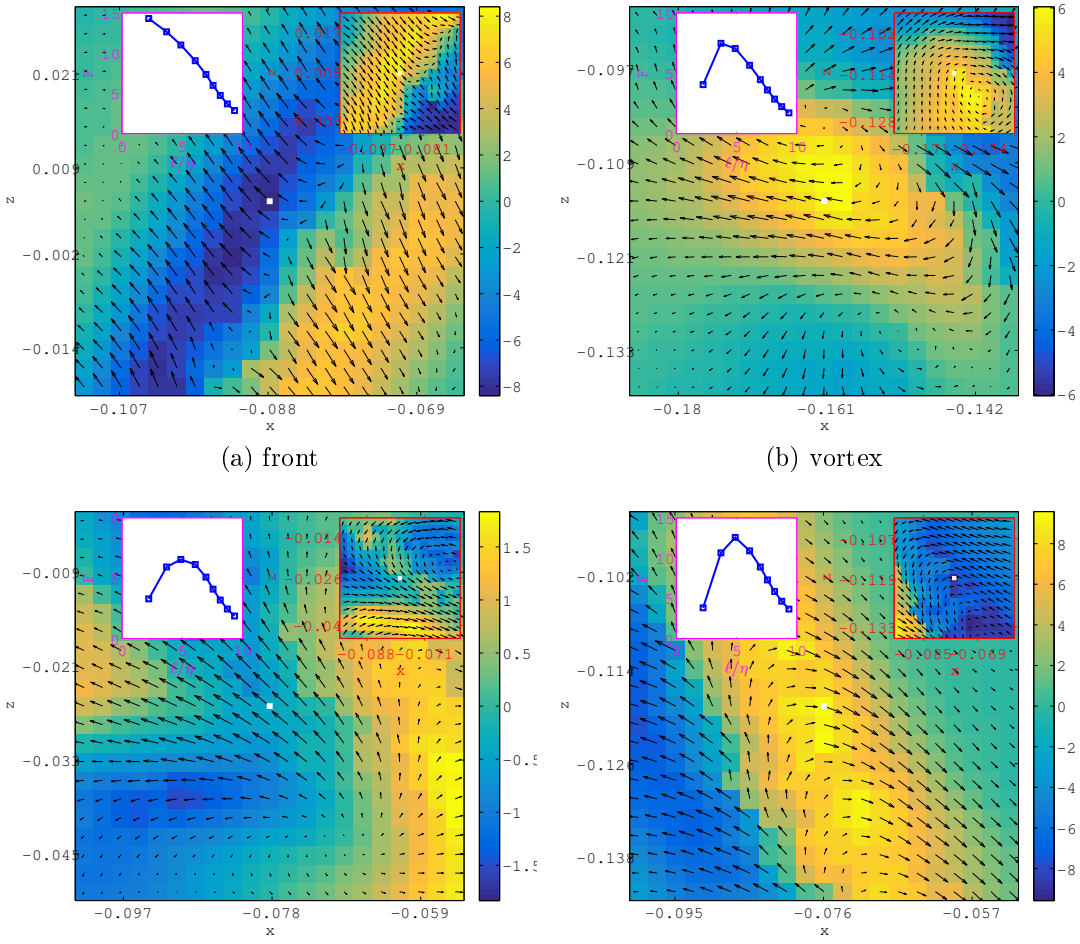

(a) front (b) vortex

(c) jet (d) cusp

Figure 2.3: Four types of singularities found among the extreme events extracted from the data at the dissipative scale, where the Kolmogorov scale is resolved. **Main figures**: dimensionless F_ℓ vector field for $\ell \approx 5\eta$. The arrows stand for the radial (x) and axial (z) components while the colour scale stand for the azimuthal (y) component. The white square materialize the location with the largest turbulent force in norm. **Vector field insets**: Velocity field near the singularity with the same conventions. **Plot insets**: Maximum of F_ℓ in dimensionless unit near the singularity as a function of ℓ/η.

in a paper by Chong [13] and is used to classify the different possible topology for the streamlines of velocity. This classification relies on the eigenvalues of the VGT: $(\boldsymbol{\nabla u})_{ij} = \partial_j u_i$. Depending on the degeneracy of these eigenvalues, whether they are complex or real, positive or negative, there are only a finite amount of possible configurations. Assuming those eigenvalues are λ_1,λ_2 and λ_3 in no particular order, the VGT invariants P, Q and R are computed as follow:

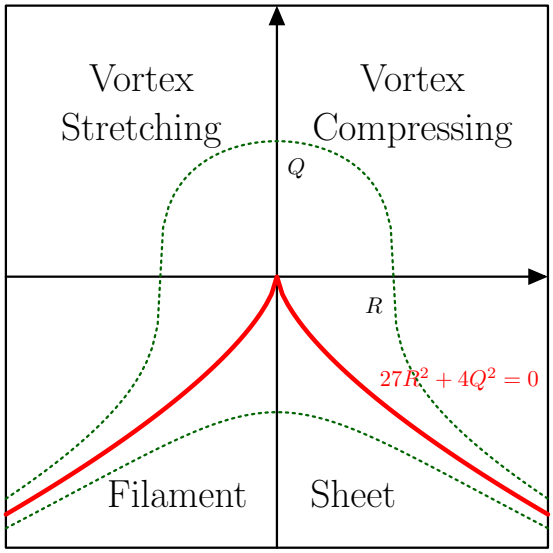

Figure 2.4: QR plane with the different topologies and three Vieillefosse lines [71] drawn.

$$P = \lambda_1 + \lambda_2 + \lambda_3, \tag{2.21}$$

$$Q = \lambda_1\lambda_2 + \lambda_1\lambda_3 + \lambda_2\lambda_3, \tag{2.22}$$

$$R = -\lambda_1\lambda_2\lambda_3 \tag{2.23}$$

such that the characteristic polynomial is $\lambda^3 + P\lambda^2 + Q\lambda + R$.

Furthermore, the incompressibility condition translates to $P = 0$. As a result, the computation of the invariants Q and R simplifies to:

$$Q = -\frac{1}{2}\,\mathrm{Tr}(\boldsymbol{\nabla u})^2, \tag{2.24}$$

$$R = -\det(\boldsymbol{\nabla u}). \tag{2.25}$$

With these constraints, only 4 main topologies remain possible. Those are placed on the QR plane in figure 2.4. In detail, they are the following:

- The **filament**: As $27R^2+4Q^2 < 0$, all three eigenvalues are real. With $R < 0$, only one of them is positive. The fluid is compressed in two directions and stretched in a third one, without rotation.

- The **sheet**: Like for the filaments, all eigenvalues are real, but as $R > 0$, two of them are positive. The fluid is compressed in one direction and stretched in another, still without rotation.

- The **vortex stretching**: As $27R^2 + 4Q^2 > 0$, there are two complex conjugate eigenvalues. As $R < 0$, the remaining eigenvalue is positive. As the name suggest, the corresponding structure is a vortex spiraling inward stretched in the third direction.

- The **vortex compressing**: Like for the vortex stretching, two eigenvalues are complex conjugate. As $R > 0$, the third eigenvalue is negative. This corresponds to a vortex spiraling outward and compressed in the third direction.

In the same figure 2.4 are drawn three Vieillefosse lines, defined by:

$$27R^2 + 4Q^3 = cst. \tag{2.26}$$

According to a paper by Vieillefosse [71], these lines described the possible trajectories of an elementary fluid particle in an inviscid liquid not subject to anisotropic pressure effects. The corresponding equations would be:

$$\dot{Q} = -3R/2, \tag{2.27}$$

$$\dot{R} = Q^2/3. \tag{2.28}$$

In consequence, should the elementary particle of fluid follow these trajectory, this would lead to $Q \to -\infty$ and $R \to +\infty$ in finite time. In other words, this would lead to a singularity. As such, it is pertinent to verify the behavior of the criteria for the detection of singularity on the QR plane. This work has been done in Paul Debue's thesis, by taking conditional average of D_I^ℓ for given Q and R. The results feature a higher average local energy transfer below the right branch of the Vieillefosse line drawn in red in figure 2.4, in the "sheet" region. Those results are reproduced in this thesis in Chapter 4.

Chapter 3

Measure of local regularity

The quasi singularities can be identified using the local energy transfers as a criterion, as described in the previous chapter. However, such method only provides an incomplete picture of the intensity of the singularities. In particular, while the criterion based on local energy transfers allows to detect intense events, it does not provide a quantitative measurement of how singular those events are. The ideal tool for this task would be a local scalar that gives a measure of the strength of singularities.

This chapter presents the method developed during this thesis to compute such a scalar. In order to reach this method, we first describe the multifractal framework which provides statistical tools to quantify the global regularity of a function. We then present a more recent concept of active volumes, which is a mathematical tool developed to locate regions of interest in a turbulent velocity field. These two preexisting concepts are then combined in order to obtain local information about the regularity of velocity fields.

3.1 Overview of the multifractal framework

3.1.1 The Hölder exponents or a measure of regularity

In order to quantify the regularity of the velocity field when searching for quasi singularities, we need a mathematical tool that quantifies the regularity of a function. The concept of *Hölder exponents* (or *Hölder coefficients*) is such a tool. This scalar is a local measure of the regularity of a function. The Hölder coefficient of the velocity field $\boldsymbol{u}$ at point $\boldsymbol{x}_0$ is defined [50, 49, 4] as the larger value of $h(\boldsymbol{x}_0)$ such that there exists a polynomial P_n of degree $n < h(\boldsymbol{x}_0)$ and a constant $C > 0$

such that for $\boldsymbol{x}$ in the vicinity of $\boldsymbol{x}_0$:

$$|\boldsymbol{u}(\boldsymbol{x}) - \boldsymbol{u}(\boldsymbol{x}_0) - P_n(\boldsymbol{x} - \boldsymbol{x}_0)| \leqslant C\,|\boldsymbol{x} - \boldsymbol{x}_0|^{h(\boldsymbol{x}_0)}\,. \tag{3.1}$$

If the velocity field is n times differentiable in $\boldsymbol{x}_0$, its Taylor expansion around $\boldsymbol{x}_0$ can be used for P_n which leads to $h(\boldsymbol{x}_0) > n$. Likewise, for $0 < h < 1$, the equation 3.1 becomes:

$$|\boldsymbol{u}(\boldsymbol{x}) - \boldsymbol{u}(\boldsymbol{x}_0)| \leqslant C\,|\boldsymbol{x} - \boldsymbol{x}_0|^{h(\boldsymbol{x}_0)}\,. \tag{3.2}$$

When interpreting the equation (3.2), one can observe that it is equivalent to the simple continuity in the limit $h \to 0^+$. Likewise, the limit $h \to 1$ gives the property of Lipschitzianity, which is close to differentiability. As a result, the Hölder exponent for $0 < h < 1$ is a scalar that makes the bridge between these two concepts and gives a measure of the regularity of the velocity field over a continuous spectrum. This observation can be generalized for $h > 1$ using the equation (3.1). Hence, the general interpretation is that the higher the Hölder exponent is, the more regular is the velocity field. Computing a local Hölder exponent is required to both locate quasi singularities and estimate their strength.

One pitfall however is that this measure of regularity is only able to detect algebraic singularities (a.k.a. *cusps*) but not oscillating singularities (a.k.a. *chirps*). Those two types of singularities are illustrated in figure 3.1. For oscillating singularities, the Hölder exponent only evaluates the regularity of the envelop. As a result, the measure of the regularity of a chirp event using the Hölder exponent gives an inaccurate estimation of its strength, in particular with regard to the strong associated gradients. A generalized measure including oscillating singularities exists (see e.g. [30, 1]) but will not be considered during this study. This will effectively limit the reach of all our tools based on Hölder regularity to cusps. Ideally, we hope that if the INSE generate chirp singularities, their corresponding quasi singularities observable in numerical and experimental datasets would still be detectable using the tool for cusps.

3.1.2 The multifractal framework

Hölder exponents were first used in turbulence in the context of the multifractal framework. This model has been introduced by Parisi and Frisch [62] and is based

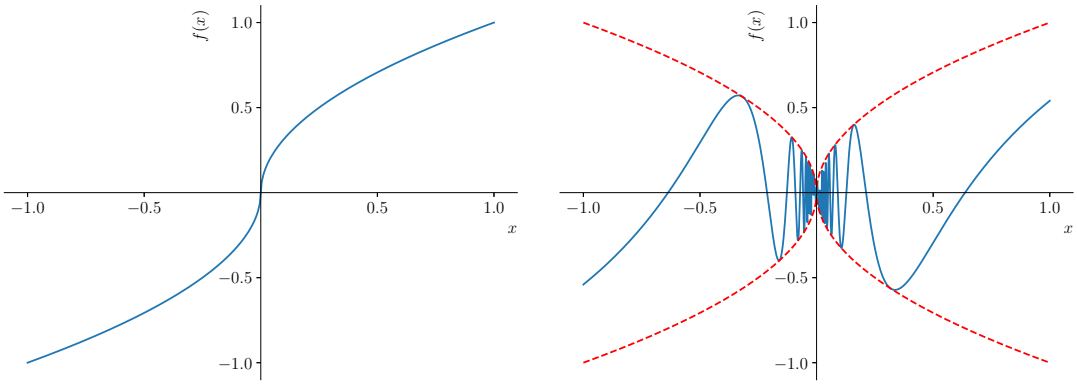

(a) Cusp (b) Chirp

Figure 3.1: Two functions with $h = 0.5$ at $x = 0$.

on the power law behaviour of the structure functions [23, 55]:

$$\langle \|\delta \boldsymbol{u}_\ell\|^p \rangle \propto \ell^{\zeta_p}. \tag{3.3}$$

The Hölder exponent from equation (3.2) is interpreted as a measure of the local scale invariance of the velocity increment $\|\delta \boldsymbol{u}_\ell(\boldsymbol{x})\| \propto \ell^{h(\boldsymbol{x})}$. The relative distribution of the Hölder exponents in space is represented by the *multifractal spectrum* or *singularity spectrum*. Given the subset of Hölder exponent $\Delta(h)$ defined by

$$\Delta(h) = \{x | \|\delta \boldsymbol{u}_\ell(\boldsymbol{x})\| \propto \ell^h\}, \tag{3.4}$$

the multifractal spectrum $D(h)$ is the Hausdorff dimension of $\Delta(h)$:

$$D(h) = \mathrm{Dim}_H(\Delta(h)). \tag{3.5}$$

The Hausdorff dimension is one flavor of fractal dimension. Where a line has a dimension of 1 and a surface a dimension of 2, fractal dimensions are a generalization of this concept for more complex structures that do not fall in any simple category. A more easily interpreted concept, used further in this chapter, is the box counting dimension.

Another interpretation can be made in terms of "frequency". In the case of the subsets defines in equation (3.4), the closer the value $D(h)$ is to the dimension of the space, the more ubiquitous are the points with Hölder exponent h.

From here, the rate function of the Hölder exponent is derived as:

$$\text{Prob}\left[\ln(\|\delta \boldsymbol{u}_\ell\|) = h\ln(\ell/L)\right] \sim e^{\ln(\ell/L)(D-D(h))} = \left(\frac{\ell}{L}\right)^{D-D(h)}. \tag{3.6}$$

where D is the dimension of the full space. By injecting equation (3.6) in the computation of the average in equation (3.3), we can demonstrate that the multifractal spectrum and the scaling exponents of the velocity structure function are connected through a Legendre transform [23]:

$$\zeta_p = \min_h(ph + D - D(h)) \tag{3.7}$$

As pointed out by Muzy et al. [56], multiple difficulties arise in derivating the multifractal spectrum directly from the structure function exponents. In particular, the potential existence of regular regions with $h > 1$ would mean using the definition from equation (3.1) instead of equation (3.2). This would impact the computation of the coefficients ζ_p and thus the derivation of the multifractal spectrum through a Legendre transform [6, 57, 3].

3.1.3 Wavelet transforms

The velocity increments used until now can also be interpreted as a particular type of *wavelet transforms* [28, 53, 54]. More explicitly, in 1D, the increment of a signal $\delta_\ell f(x_0) = f(x_0 + \ell) - f(x_0)$ can be written as:

$$\delta_\ell f(x_0) = \frac{1}{\ell}\int \Delta^{(1)}\left(\frac{x - x_0}{\ell}\right) f(x)\mathrm{d}x \tag{3.8}$$

where $\Delta^{(1)}(x) = \delta(x+1) - \delta(x)$.

Wavelet transforms were introduced by Morlet and Grossman in the context of seismology as a powerful tool in signal processing. The transformation consists in decomposing a signal using a set of functions characterized by a position x_0 and a scale ℓ. This property makes it suitable to study local scale invariance, which is the fundamental property of multifractals.

Hence, Arneodo et al. [3] proposed a new method to apply the multifractal analysis that does no share the problems of the structure function based method and can thus be applied on functions with $h > 1$. This methods relies on continuous wavelet transforms while the classical method used box increments.

In this thesis, we will only consider two different types of wavelets: the Gaussian

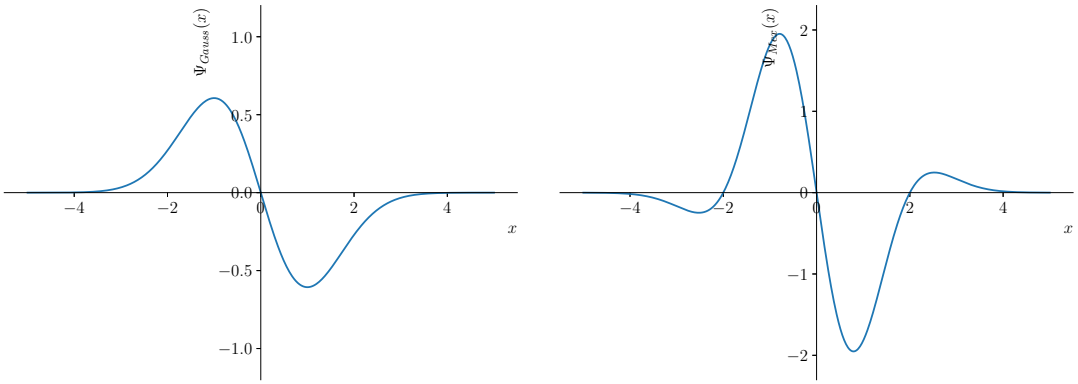

(a) Gaussian (b) Mexican

Figure 3.2: Representation of the two wavelets in 1D.

wavelet and the Mexican wavelet. They are respectively defined using the Gaussian and the mexican hat as smoothing functions:

$$\phi_{Gauss}(x) = \mathrm{e}^{-x^2/2}, \tag{3.9}$$

$$\phi_{Mex}(x) = (2 - x^2)\mathrm{e}^{-x^2/2}. \tag{3.10}$$

In one dimension, this leads to:

$$\Psi_{Gauss}(x) = \frac{\mathrm{d}\phi_{Gauss}}{\mathrm{d}x}(x) = -x\mathrm{e}^{-x^2/2}, \tag{3.11}$$

$$\Psi_{Mex}(x) = \frac{\mathrm{d}\phi_{Mex}}{\mathrm{d}x}(x) = x(x^2 - 4)\mathrm{e}^{-x^2/2}. \tag{3.12}$$

Those two wavelets are represented in figure 3.2.

The wavelet transform is then computed by:

$$T_\Psi\{f\}(x, \ell) = \int \frac{1}{\ell}\Psi(\frac{x - y}{\ell})f(y)\mathrm{d}y. \tag{3.13}$$

Extending this concept in several dimensions imposes to compute elementary wavelets that are partial derivatives of the smoothing function with respect to each direction:

$$\Psi_i = \frac{\partial\phi}{\partial x_i}. \tag{3.14}$$

The total wavelet transform is then expressed as a vector. In 3D, this results

in:

$$\boldsymbol{T_\Psi}\{f\}(\boldsymbol{x},\ell) = \begin{pmatrix} T_{\Psi_1}\{f\}(\boldsymbol{x},\ell) = \int \ell^{-3}\Psi_1(\ell^{-1}(\boldsymbol{x}-\boldsymbol{y}))f(\boldsymbol{y})\mathrm{d}\boldsymbol{y} \\ T_{\Psi_2}\{f\}(\boldsymbol{x},\ell) = \int \ell^{-3}\Psi_2(\ell^{-1}(\boldsymbol{x}-\boldsymbol{y}))f(\boldsymbol{y})\mathrm{d}\boldsymbol{y} \\ T_{\Psi_3}\{f\}(\boldsymbol{x},\ell) = \int \ell^{-3}\Psi_3(\ell^{-1}(\boldsymbol{x}-\boldsymbol{y}))f(\boldsymbol{y})\mathrm{d}\boldsymbol{y} \end{pmatrix}. \tag{3.15}$$

As such, multidimensional wavelet transforms capture the variation of a function along all directions. This makes the norm of the wavelet transform an equivalent to the increments.

One particular advantage of the wavelet transforms is the ability to deal with the $h > 1$ case which was problematic for the structure function method. Indeed, a judicious choice of wavelet can cancel out the polynomial P_n from the signal. Formally, let's take a function f with a local Hölder exponent $h(x_0) \in]n, n+1[$. Taking the same interpretation as before, this means that around x_0:

$$f(x) - f(x_0) - P_n(x - x_0) \sim |x - x_0|^{h(x_0)}. \tag{3.16}$$

Now let us take a wavelet Ψ with n_Ψ cancellation, i.e. such that:

$$\forall k \in [\![0, n_\Psi]\!], \int x^k \Psi(x)\mathrm{d}x = 0. \tag{3.17}$$

Taking the wavelet transform of f around x_0 then gives [16, 4]:

$$\begin{cases} \text{if } n_\Psi > h(x_0) : T_\Psi\{f\}(x) \sim |x - x_0|^{h(x_0)}, & (3.18) \\ \text{if } n_\Psi < h(x_0) : T_\Psi\{f\}(x) \sim |x - x_0|^{n_\Psi}. & (3.19) \end{cases}$$

Using Gaussian wavelets allows us to get good results for $h < 1$ and using Mexican wavelets extends this range to $h < 3$.

3.1.4 The WTMM method

What follows is a brief overview of the *Wavelet Transform Modulus Maxima* method or *WTMM*. The reader is invited to peruse the original references for the details and original implementation (see [16] for 1D and 2D WTMM and [36] for the 3D generalization).

The general idea of the 1D method consists in extracting the local Maxima of the Modulus of the Wavelet Transform (hence the name) of the signal f at any given scale ℓ. These maxima are linked across scales to form *lines of maxima* Λ_k that converge when $\ell \to 0$ to the position of singularities. The position of the local

maximum of the line Λ_k at scale ℓ is noted $\Lambda_k(\ell)$.

The line of maxima corresponding to a singularity of Hölder exponent $h < n_\Psi$ verifies for small scales:

$$\mathcal{M}_\Psi\{f\}(\Lambda_k(\ell), \ell) \sim \ell^h \tag{3.20}$$

where $\mathcal{M}_\Psi\{f\}$ is the modulus of the wavelet transform $\boldsymbol{T}_\Psi\{f\}$ defined in equation (3.15). The *wavelet transform skeleton* is then defined as the set of lines of maxima $\{\Lambda_k\}$.

The WTMM method is a statistical tool using this skeleton to determine the multifractal spectrum $D(h)$. Calling $\Lambda(\ell)$ the set of lines, subset of $\{\Lambda_k\}$, that exists at scale ℓ, we define the partition functions:

$$\mathbb{Z}(q, \ell) = \sum_{\Lambda_k \in \Lambda(\ell)} \Big(\mathcal{M}_\Psi\{f\}(\Lambda_k(\ell), \ell)\Big)^q \tag{3.21}$$

where $q \in \mathbb{R}$.

Those partitions functions behave as a power law for small scales, leading to the definition of the exponents $\tau(q)$:

$$\mathbb{Z}(q, \ell) \propto \ell^{\tau(q)}. \tag{3.22}$$

The singularity spectrum is then obtained by Legendre transform:

$$D_T(h) = \min_q (qh - \tau(q)). \tag{3.23}$$

In practice, we bypass the Legendre transform by computing:

$$h(q, \ell) = \sum_{\Lambda_k \in \Lambda(\ell)} \ln |\mathcal{M}_\Psi\{f\}(\Lambda_k(\ell), \ell)| \mathcal{W}(q, \Lambda_k, \ell), \tag{3.24}$$

$$D(q, \ell) = \sum_{\Lambda_k \in \Lambda(\ell)} \mathcal{W}(q, \Lambda_k, \ell) \ln \Big(\mathcal{W}(q, \Lambda_k, \ell)\Big) \tag{3.25}$$

where $\mathcal{W}(q, \Lambda_k, \ell) = \frac{1}{\mathbb{Z}(q,\ell)} \Big(\mathcal{M}_\Psi\{f\}(\Lambda_k(\ell), \ell)\Big)^q$ is a Boltzmann weight computed from the wavelet transform skeleton. These quantities behave with respect to the scale ℓ as follows:

$$h(q, \ell) \sim h(q) \ln(\ell), \tag{3.26}$$

$$D(q, \ell) \sim D(q) \ln(\ell). \tag{3.27}$$

By combining the exponents $h(q)$ and $D(q)$ obtained as functions of the parameter q, we can recover the singularity spectrum $D(h)$. Note that the multiscale nature of turbulence means that this spectrum is not independent of the scale at which the power laws are measured. We do not expect to observe the same multifractal spectrum in the inertial range and in the dissipative range. By simplicity, we omit the dependency in scale unless required.

The generalization of this method for scalar and vector fields in several dimensions follows the same general construction, the main difference coming from the determination of the skeleton $\{\Lambda_k\}$. In particular, applying the method to a 3D velocity field $\boldsymbol{u}$ requires the use of a tensorial wavelet transform, defined by:

$$\boldsymbol{T_\Psi}\{\boldsymbol{u}\}(\boldsymbol{x},\ell) = \begin{pmatrix} T_{\Psi_1}\{u_1\}(\boldsymbol{x},\ell) & T_{\Psi_1}\{u_2\}(\boldsymbol{x},\ell) & T_{\Psi_1}\{u_3\}(\boldsymbol{x},\ell) \\ T_{\Psi_2}\{u_1\}(\boldsymbol{x},\ell) & T_{\Psi_2}\{u_2\}(\boldsymbol{x},\ell) & T_{\Psi_2}\{u_3\}(\boldsymbol{x},\ell) \\ T_{\Psi_3}\{u_1\}(\boldsymbol{x},\ell) & T_{\Psi_3}\{u_2\}(\boldsymbol{x},\ell) & T_{\Psi_3}\{u_3\}(\boldsymbol{x},\ell) \end{pmatrix}. \tag{3.28}$$

The process of determining the skeleton of maxima and the multifractal spectrum requires the Singular Value Decomposition of $T_{\boldsymbol{\Psi}}\{\boldsymbol{u}\}$, leading to:

$$\mathcal{M}_\Psi\{\boldsymbol{u}\} = \max_j \sigma_j \tag{3.29}$$

where σ_j are the singular values of $T_{\boldsymbol{\Psi}}\{\boldsymbol{u}\}$. The computation of the multifractal spetrum $D(h)$ can then be performed using this new definition of $\mathcal{M}_\Psi\{\boldsymbol{u}\}$ in equations (3.24) and (3.25).

All these methods have been implemented in the program xsmurf [37], which we use in the sequel for all computations related to the WTMM method, with only minor modifications to the software.

3.2 A local estimate of Hölder exponents

The WTMM method is based on statistical properties, which makes it very robust with respect to noise and limited statistics. However, using this method only yields *global* information about the regularity of the velocity field, through the multifractal spectrum. Meanwhile, in order to study the extreme irregular structures of the velocity field, we need *local* information about the Hölder exponents.

Some methods have been designed to provide such information based on the chains of maxima from the WTMM method (see e.g. [68]). The general idea behind those methods is to extract the power law behaviour from a single chain of maxima in order to determine the local Hölder exponent of the corresponding

singularity. However, this involves at least partially giving up on the advantage of the statistical method. Furthermore, the method relies on a fractal behavior robust in scale. With its multiscale nature, turbulence does not fulfill the conditions for this method. One objective of this thesis being the study of experimental data, we need to preserve the robustness with respect to experimental noise of the statistical method. Moreover, our method must take into account the multiscale nature of turbulence.

Our objective in the following is to devise a *local statistical* analysis, which would allow us to evaluate the local Hölder continuity while keeping the robustness of the WTMM method [59]. The idea of the method is to combine the results from the WTMM, which gives information about the distribution of the Hölder exponent in the space, with a local method delimiting regions of interest in space closely related to Hölder exponents. In this process, we eventually come back to an intuitive approach of the local regularity: the larger the local gradients, the least regular the field. The objective of the method is to transform this intuition into a rigorous, reproducible method, which would associate a value of Hölder exponent in accordance to the intensity of the local gradients or the amplitude of the local velocity increments.

3.2.1 Wavelet velocity increments

In order to devise this new method, on need to modify the type of wavelet based increments used. Indeed, the method originally developed by Kestener and Arneodo [38] defines velocity increments using the singular values of the matrix $|G_{ij}^{\ell}|$.

The method that we propose will require to use the local velocity increments. As a result, the use of the singular values might introduce undesired noise. This motivates us to define the wavelet velocity increments $\delta W(\mathbf{u})$ through the smoothed velocity gradient G_{ij}^{ℓ} and its symmetric and antisymmetric parts:

$$G_{ij}^{\ell} = \ell \int \frac{\mathrm{d}\mathbf{y}}{\ell^3} \nabla_j \Psi\left(\frac{\mathbf{y}}{\ell}\right) u_i(\mathbf{y}), \tag{3.30}$$

$$S_{ij}^{\ell} = \frac{1}{2}\left(G_{ij}^{\ell} + G_{ji}^{\ell}\right), \tag{3.31}$$

$$A_{ij}^{\ell} = \frac{1}{2}\left(G_{ij}^{\ell} - G_{ji}^{\ell}\right), \tag{3.32}$$

where the base wavelet $\Psi(\mathbf{x})$ will be chosen later.

The normal, longitudinal and perpendicular (also referred to as "transverse")

wavelet velocity increments are defined as:

$$\delta_L W_\ell(\mathbf{u}) = \max_{ij} |S_{ij}^\ell|, \tag{3.33}$$

$$\delta_P W_\ell(\mathbf{u}) = \max_{ij} |A_{ij}^\ell|, \tag{3.34}$$

$$\delta_G W_\ell(\mathbf{u}) = \left(\delta_L W_\ell(\mathbf{u})^2 + \delta_P W_\ell(\mathbf{u}^2)\right)^{1/2}. \tag{3.35}$$

By construction, the longitudinal component $\delta_L W_\ell(\mathbf{u})$ contain the information about the potential part of the velocity field while the perpendicular component $\delta_P W_\ell(\mathbf{u})$ provides information about the vortical component. Their combination $\delta_G W_\ell(\mathbf{u})$ is thus a good choice to provide general scaling properties of the velocity field. In the following, the subscript G will be droped when referencing to the global velocity increment $\delta_G W_\ell(\mathbf{u})$.

This definition uses neither derivatives over the velocity field nor singular values. This makes our wavelet based velocity increment the smoothest choice possible to quantify the scaling properties of both the potential and the rotational part of a velocity field.

In the WTMM method described in section 3.1.4, the three type of velocity increments defined in equations (3.33)-(3.35) can be used as a substitute of the velocity increment based on singular values. One might wonder whether the wavelet transform skeleton $\{\Lambda_k\}$ needs to be recomputed using these new increments. By simplicity, we made the choice of keeping the same skeletons as the original method. The results presented in the following of the thesis will show that this choice preserves the multifractal spectra obtained through the standard WTMM method.

3.2.2 Active volumes and multifractal

The modified WTMM only yields global information about the regularity of the velocity field. In order to reach local information, we need to combine these results with a more local concept. This new source of information comes from the definition of *actives volumes* for a turbulent velocity field [59]. The original motivation for the development of active volumes is reported in annex B of [59].The method delimits the so called active regions by clever thresholding on the velocity increments. In this aspect, it appears closely related to our objective of estimating the local regularity based on the intuition of strong velocity increments corresponding to more singular regions.

We first define a family of thresholds $\mathcal{T}_{p,dp}$ as:

$$\mathcal{T}_{p,dp}(\ell) = \left(\frac{\langle (\delta W_\ell(\mathbf{u}))^{p+dp} \rangle}{\langle (\delta W_\ell(\mathbf{u}))^{p} \rangle} \right)^{1/dp}. \tag{3.36}$$

The limit as $dp \to 0$ can be computed as:

$$\mathcal{T}_p(\ell) \equiv \mathcal{T}_{p,0}(\ell) = \exp \left(\frac{\langle \ln \left(\delta W_\ell(\mathbf{u})\right) \left(\delta W_\ell(\mathbf{u})\right)^p \rangle}{\langle \left(\delta W_\ell(\mathbf{u})\right)^p \rangle} \right). \tag{3.37}$$

On the other hand, assuming the velocity field $\mathbf{u}$ is multifractal, i.e. $\delta W_\ell(\mathbf{u})^p \propto \ell^{\zeta(p)}$, then we have the scaling:

$$\mathcal{T}_{p,dp}(\ell) \propto \ell^{(\zeta(p+dp)-\zeta(p))/dp}. \tag{3.38}$$

Hence, the limit $dp \to 0$ gives the scaling:

$$\mathcal{T}_p(\ell) \propto \ell^{h(p)}, \tag{3.39}$$

where $h(p) = \frac{\mathrm{d}\zeta(p)}{\mathrm{d}p}$ is obtained in a way alternative to the WTMM method. Note that the expression of $\mathcal{T}_p$ in equation (3.37) is analogous to the expression of equation (3.24) used in the WTMM method, so we do not expect this method to yields different results.

The active volume A_p is then defined as:

$$\mathbf{x} \in A_p \quad iff \quad \delta W_\ell(\mathbf{u})(\mathbf{x}) \geqslant c_p \mathcal{T}_p(\ell), \tag{3.40}$$

where c_p is a scale independent constant, to be determined later.

Given the scaling law of the thresholds $\mathcal{T}_p$ from equation (3.39), the property of the points in the active volume A_p can be rewritten as $\delta W_\ell(\mathbf{u})(\mathbf{x}) \geqslant C_p \ell^{h(p)}$ with C_p a scale independent constant. This property is analogous to the definition of Hölder exponents from the equation (3.2), with a reversed inequality. This similarity can thus be used as a connection point between the information about the regularity of the field provided by the WTMM method and the local property of active volumes. As a result, we define the scalar field $\tilde{h}$, coined *local singularity exponent* and by abuse of language *local Hölder exponent*, such that all elements $\mathbf{x}$ in A_p verify $\tilde{h}(\mathbf{x}) \leqslant h(p)$. This means that the frontier set of A_p, which is also the isosurface corresponding to the velocity increment $\delta W_\ell(\mathbf{u}) = c_p \mathcal{T}_{p,0}(\ell)$, is the set of points $\boldsymbol{x}$ of local singularity exponent $\tilde{h}(\boldsymbol{x})$.

The wavelet based velocity increment $\delta W_\ell(\mathbf{u})$ is continuous in space. This property is thus transferred to the singularity exponent $\tilde{h}$. This property differs from the multifractal framework, and instead would be more accurate to a multifractional framework [5]. This difference means that the quantity $\tilde{h}$ is not a real measure of the local Hölder exponent. We will however show that it shares some properties of the real Hölder exponent, making it relevant for measuring the local regularity of the velocity field.

3.2.3 Box counting method

The definition of the scalar field $\tilde{h}(\mathbf{x})$ is dependent of the choice of the constants c_p. In order to properly mesh the local method with the WTMM, we must ensure that the properties of the field $\tilde{h}$ match the ones of the Hölder exponent as closely as possible. In particular, the "multifractal spectrum" associated with $\tilde{h}$ which dictates its distribution in space must match the results of the WTMM. Expressed using the fractal dimension of the isosurfaces of $\tilde{h}$, this means:

$$\mathrm{Dim}\left(\left\{\mathbf{x}|\tilde{h}(\mathbf{x}) = h\right\}\right) = D(h). \tag{3.41}$$

As discussed previously, the isosurface of $\tilde{h} = h(p)$ is defined as the frontier of the volume A_p. This frontier is an isosurface of the velocity increment $\delta W_\ell(\mathbf{u})$, such that:

$$\mathrm{Dim}\left(\{\mathbf{x}|\delta W_\ell(\mathbf{u})(\mathbf{x}) = c_p \mathcal{T}_p(\ell)\}\right) = D(h(p)). \tag{3.42}$$

In practice, the fractal dimension can be estimated using a box counting method. The principle of this methods is to count the number of boxes of size a required to recover a set $\mathcal{S}$. For boxes small enough, this number follows the scaling $N(a) \propto a^{-d}$ where $d = D_{bc}(\mathcal{S})$ is the box counting dimension of the set $\mathcal{S}$.

The intuitive interpretation of this method relies on the following. Let us consider a line segment of length b. This is a structure of dimension 1, and it takes b/a boxes of size a in order to cover it, which gives a scaling $N(a) \propto a^{-1}$. Likewise, a square of size b takes b^2/a^2 boxes of size a to cover. This gives a scaling $N(a) \propto a^{-2}$ for a structure of dimension 2.

The same process can be applied to cases of non integer dimension, which are frequent for fractal structures. As such, the box counting algorithm consists in counting the boxes needed to recover a set and express this number as a function of the box size in order to determine the corresponding power law. The figure 3.3 illustrates the process applied to a well known fractal, the Sierpinski triangle [21].

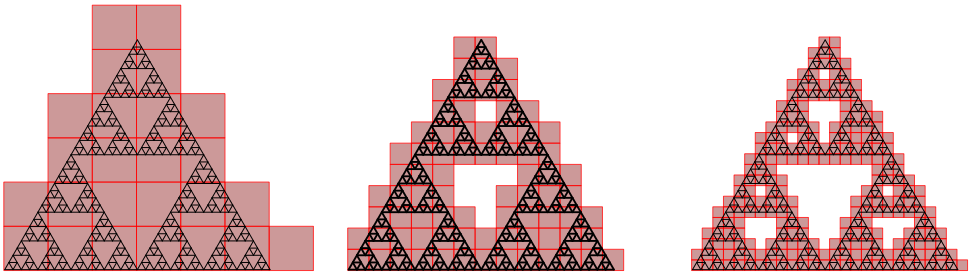

Figure 3.3: Three steps of box counting applied to the Sierpinski triangle (drawn here with 5 iterations). If the main triangle is of size 30, the box sizes are from left to right 5, 2.4 and 1.2. The respecting box counts are 24, 76 and 240.

Based on just the three steps represented, the measured fractal dimension would be $d \approx 1.6$. As the Hausdorff dimension of this fractal is actually $\ln(2)/\ln(3) \approx 1.58$, this is a good example of the accuracy of the method.

In this work, the concrete implementation of the box counting algorithm consist of a fixed grid scan: using a grid of step a starting at the origin, the number $N(a)$ is computed by counting the number of boxes covering the measured set [52]. The mathematical definition of the box counting dimension would normally require us to determine an optimal covering, i.e. covering the structure using the minimal number of boxes, including rotations and offsets. Using a fixed grid might impact the precision of the measured dimension. However, this choice has the advantage of a very fast implementation, so we rely on the large amount of statistics in order to compensate for the inaccurate count of the optimal number of boxes.

Hence, applying the box counting to compute the dimension of the left hand side of equation 3.42 leads to:

$$D_{bc}^{\ell}(c_p \mathcal{T}_p(\ell)) = D(h(p)). \tag{3.43}$$

where $D_{bc}^{\ell}(\mathcal{T})$ is the box-counting dimension of the isosurface of the velocity increment at scale ℓ of value $\delta W_\ell(\mathbf{u}) = \mathcal{T}$.

3.2.4 Statistical fitting of the constants

Most of the terms in the equation 3.43 can be computed. Indeed, the term $\mathcal{T}_p(\ell)$ can be computed from the velocity field using equation (3.37), the multifractal spectrum $D(h)$ is accessible through the WTMM method and the function $D_{bc}^{\ell}(\mathcal{T})$ can be evaluated by using box counting. The term $h(p)$ is accessible both from the WTMM and the power laws on the $\mathcal{T}_p(\ell)$ as described in equation (3.39). We can

choose to use the scaling on the $\mathcal{T}_p(\ell)$ for simplicity, as the two methods should be equivalent.

As a result, we can use equation (3.43) to solve for c_p. As the functions involved are not monotonous, there can be several solutions. Noting $\mathcal{T}_{max}$ the isovalue of velocity increments corresponding to the largest box counting dimension, we lift the ambiguity by imposing $c_p\mathcal{T}_p(\ell) < \mathcal{T}_{max}$ for $p > 0$ and $\mathcal{T}_{max}$ and $c_p\mathcal{T}_p(\ell) > \mathcal{T}_{max}$ for $p < 0$. This choice originates from the fact that a larger velocity increment should correspond to a less regular point of the velocity field. Matching the dimensions from equation (3.43) gives a relationship in the form of:

$$h_\ell(p) = f_\ell(c_p\mathcal{T}_p(\ell)). \tag{3.44}$$

The dependency with respect to ℓ of the Hölder exponent $h(p)$ and of the function resulting of the matching of the fractal dimensions are made explicit using a subscript. This provides an unique definition of c_p.

It is worth noting that the computation of the coefficients c_p is not technically required to recover the scalar field $\tilde{h}(\mathbf{x})$. Indeed, it is possible to derive a relationship between the isovalue $\mathcal{T}$ and the local singularity exponent $\tilde{h}$ using the following equation:

$$D^\ell_{bc}(\mathcal{T}) = D(\tilde{h}), \tag{3.45}$$

which is derived from equation (3.41). As before, we lift the ambiguity by imposing $\tilde{h}(\mathcal{T}) < h(p = 0)$ for $\mathcal{T} > \mathcal{T}_{max}$ and reciprocally. This leads to the equation:

$$\tilde{h}_\ell(\boldsymbol{x}) = f_\ell(\delta W_\ell(\mathbf{u})). \tag{3.46}$$

using the same matching function f_ℓ.

In summary, the algorithm to evaluate maps of local singularity exponent $\tilde{h}$ at a given scale ℓ is performed as follow:

1. First the WTMM method is applied using the velocity increments defined in equation (3.35). This provides the multifractal spectrum of the velocity field $D(h)$. Given that the fitting of the power law is performed around the scale ℓ, the results are specific to this scale.

2. In parallel, we compute the thresholds $\mathcal{T}_p$ from equation (3.36) and fit their power law behaviour around the same scale ℓ using equation (3.39).

3. Finally, we compute the box counting dimensions $D_{bc}(\mathcal{T})$ for isosurfaces of velocity increment $\delta W_\ell(\mathbf{u}) = \mathcal{T}$.

4. The last step is to aggregate the results of those three steps using equation (3.46) to get a function matching a value of $\tilde{h}$ to velocity increments. This directly allows us to compute maps of local singularity exponent from a snapshot of velocity field.

Note that step 2 is only required in order to compute the coefficient c_p. While the knowledge of the coefficients c_p is not required to compute the maps of singularity exponents at a given scale, it is still pertinent. Indeed, these coefficients are independent of the scale ℓ. This property can be intuited from equation (3.40) as both the velocity increments and the thresholds follow the same power law as a function of the scale. This allows to compute the function f_ℓ from equation (3.44) at a different scale ℓ without needing to recompute the multifractal spectrum at this new scale, thus skipping steps 1 and 3. This will be proven to be useful as step 1 is both expensive in computations and sensitive to the fitting range used. The invariance of the coefficients c_p with respect to scale will be further discussed in the following. Note however that the method exposed here does not provide any guarantee for the behavior of the coefficient c_p as a function of the Reynolds number.

3.2.5 Scalings in the dissipative range

One of the objective of this thesis is to measure the regularity of the field in the dissipative range. For this purpose, we would need to apply the tools described in this chapter in a range without the inertial scaling laws. In absence of a robust scaling law, one might doubt about the applicability of the WTMM method described in section 3.1.4. Likewise, the scaling of equation (3.39) is necessary for the local method to work.

However, we believe that the method described here can work even outside of the inertial range. The reason for this comes from an universal scaling law exhibited in a paper by Geneste et al. [25]. In terms of structure functions, this universal law for turbulence is expressed as:

$$\beta(Re)\log\frac{S_p(\ell)}{S_3^{p/3}(\ell)} = H(\beta(Re)\log(\ell/\eta), p) \tag{3.47}$$

where the S_p are the structure functions, H is some function, and β bears the dependency in Reynolds. This last function is empirically found to be $\beta = 4/(3\log(R_\lambda))$ where R_λ is the Taylor based Reynolds number [25].

The interesting point about this universal law for our purpose is that it includes

a large range over which the extended self similarity holds, i.e. such that:

$$\frac{S_p(\ell)}{S_3^{p/3}(\ell)} \propto \ell^{h(p)-\zeta(3)p/3}. \tag{3.48}$$

where the exponent $h(p) - \zeta(3)p/3$ is invariant with respect to scale. Such scaling law would be enough for the methods described in this chapter to be functional.

We can rewrite this universal law for our thresholds $\mathcal{T}_p$. The universality would be expressed as:

$$\beta(Re) \log \frac{\mathcal{T}_p(\ell)}{\mathcal{T}_0(\ell)} = G(\beta(Re) \log(\ell/\eta), p) \tag{3.49}$$

where we choose the threshold at $p = 0$ as a reference and G is some function. This choice is motivated by the fact $p = 0$ would correspond to the most probable Hölder exponent. With this choice, we would have the same extended fitting range as for the structure functions:

$$\frac{\mathcal{T}_p(\ell)}{\mathcal{T}_0(\ell)} \propto \ell^{h(p)-h(0)}. \tag{3.50}$$

The extended range over which the scaling is verified allows us a better estimation of the power laws, although the final accuracy of the Hölder exponents is limited by the estimation of $h(0)$. Indeed, when using the method in the dissipative range, this last term has to be computed using a narrow range of scales.

This universal law can also provide some insight about the behavior of the coefficients c_p with respect to the Reynolds number. Indeed, taking the definition of active volumes in equation (3.40) and dividing by $\mathcal{T}_0$, we get:

$$\mathbf{x} \in A_p \quad iff \quad \frac{\delta W_\ell(\mathbf{u})(\mathbf{x})}{\mathcal{T}_0(\ell)} \geqslant c_p \frac{\mathcal{T}_p(\ell)}{\mathcal{T}_0(\ell)}. \tag{3.51}$$

The universal law from equation (3.49) tells us that the right hand side of this inequality behaves as follows:

$$c_p \mathcal{T}_p(\ell)/\mathcal{T}_0 = c_p \exp\left(\frac{1}{\beta(Re)} G(\beta(Re) \log(\ell/\eta), p)\right). \tag{3.52}$$

At the same time, the left hand side can be interpreted as the ratio between the velocity increment $\delta W_\ell(\mathbf{u})$ and the most probable increment $\mathcal{T}_0$. Using the same thermodynamic analogy as in [25], we would expect this ratio to follow a scaling of the type $\exp(-\Delta F/\beta(Re))$ where ΔF is a difference in free energy.

Hence, for the expression of equation (3.52) to have the correct behavior, we

would expect the coefficients c_p to verify the following for all Reynolds numbers:

$$c_p^{\beta(Re)} = cst(p). \tag{3.53}$$

Taking into account that $\beta(Re) \sim 1/\log(Re)$ [25], this would lead to:

$$c_p = Re^{\alpha(p)} \tag{3.54}$$

with a function $\alpha(p)$ to be determined.

In this thesis, the datasets analyzed are produced at only two different Reynolds numbers. This will be insufficient to verify this property with a sufficient accuracy, leaving it as a work for the future.

3.3 Validation of the method on fractional Brownian motion (fBm)

The method explained above is designed to yield a measure of the local regularity of a velocity field through the scalar $\tilde{h}$, assimilated to a local Hölder exponent. However, while this scalar satisfies some properties of the true Hölder exponent by construction, we are not able to provide a mathematical proof that it is the Hölder exponent. As a result, a validation is required in order to use the local singularity exponent as a criterion for the detection of singularities in a real velocity field. In addition to provide a validation of the method, this section is meant as a step by step illustration of the algorithm.

3.3.1 Definition and implementation of fBm

A first test of our method is to apply it to synthetic fields with well known fractal behaviour. In this case, a simple choice is the case of the fractional Brownian motion (or fBm), which has also been used in [38]. Such a field is designed to have an uniform regularity. As such, its fractal behaviour can be described by a uniform Hölder exponent H, called in this case the Hurst exponent [51].

This means that its multifractal spectrum in dimension d degenerates to a single point:

$$D(h) = \begin{cases} d & \text{if } h = H, \\ -\infty & \text{otherwise.} \end{cases} \tag{3.55}$$

By Legendre transform, this leads to the following formula for the exponent

$\tau(q)$:

$$\tau(q) = qH - d. \tag{3.56}$$

The objective of the following test is to recover the value of H from a generated database of fBm. A similar test was performed to validate the original WTMM method in [36], which justifies that we use the same test to validate our variation of it, using the different components of the wavelet based velocity increments. The fBm are generated in 2 dimensions with 3 components of velocity (2D3C) with a value of $H = 1/3$. The generation is performed by filtering the Fourier transform of a white noise, which gives a good approximation of the expected scale invariance properties.

3.3.2 Test of the global MFR analysis

A total of one hundred 2D3C fBm are generated in squares of size unity with a resolution of 4096×4096. The output of our method using the velocity increments defined in equations (3.33) to (3.30), as well as the original WTMM method using Singular Value Decomposition are shown in figure 3.4.

The results from our method match the theoretical prediction, although with less accuracy than the original method. Indeed, the value of Hölder exponent found using the new method is $H \approx 0.31$, while the classic WTMM gives a result of $H \approx 0.33$. While it is expected that the multifractal spectrum computed from a finite number of snapshot does not fully degenerate as in equation (3.56), we also observe that the spectrum computed using our method spreads over a larger range of Hölder exponents. The loss of accuracy might be partially explained by the lack of the third dimension hindering the computation of the perpendicular component from equation (3.34).

3.3.3 Test of the local estimate

The next step consists in extracting the local singularity exponent $\tilde{h}$ from the fBm snapshots. For these computations, we set a scale $\ell = 2.8 \times 10^{-3}$ corresponding to 11.4 grid points for the resolution of the field. This guarantees that the wavelets are well resolved and allows to probe small structures. The different quantities to compute in order to apply the method are the box counting dimensions associated with the isosurfaces of velocity increments $D^{\ell}_{bc}(\mathcal{T})$ (equation (3.45)) shown in figure 3.5 and the thresholds $\mathcal{T}_p(\ell)$ (equation (3.37)) shown in figure 3.6. Both are computed using the full statistics. We check that the power law behavior of

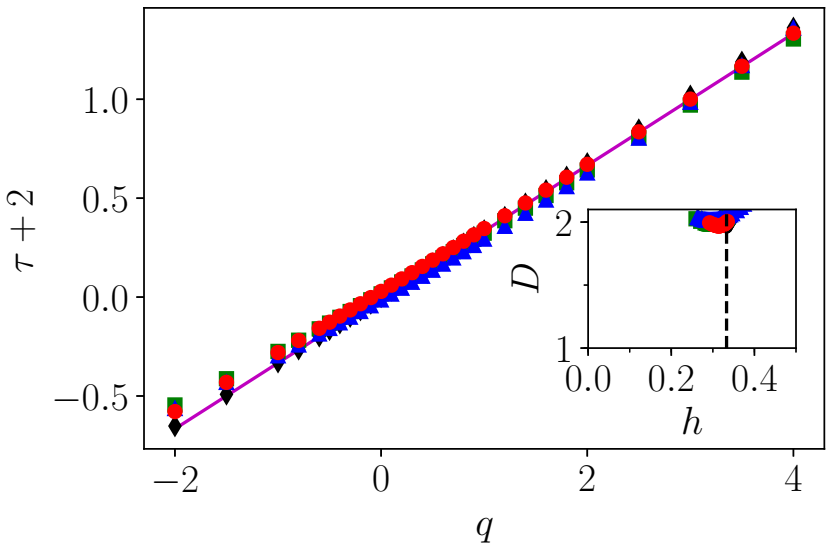

Figure 3.4: **Main figure:** Exponent τ as a function of the parameter q for the global (red), longitudinal (green), perpendicular (blue) components as well as for the original WTMM method (black) applied to 100 fields of fBm in 2 dimensions with 3 components of velocity at $H = 1/3$. The 3 components are generated independently before enforcing the divergence free condition. The theoretical curve from equation (3.56) is materialized in magenta. **Inset figure:** Corresponding parametric plot of $D(q)$ with respect to $h(q)$. The dashed line materializes the theoretical value of $H = 1/3$.

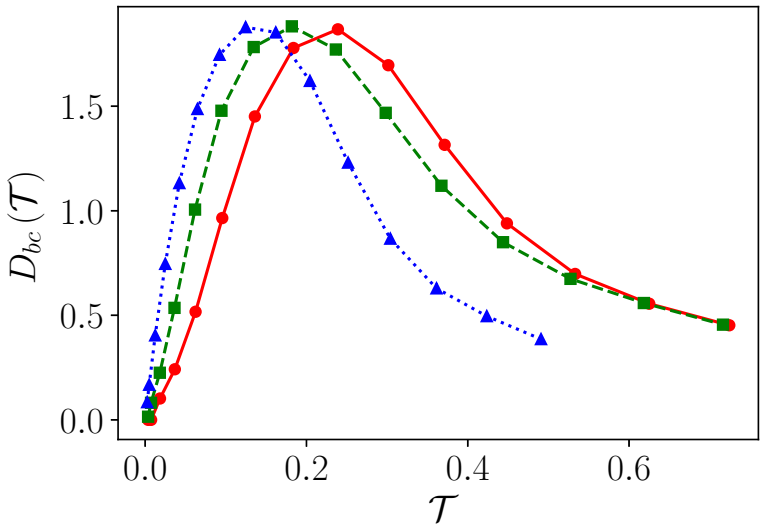

Figure 3.5: Box counting dimension of the isocontours of the different components of the wavelet based velocity increments for $\ell = 2.8 \times 10^{-3}$ for the fBm. The color code for the different components is the same as for figure 3.6.

the threshold from equation (3.39) is consistent over a large range of scales. Furthermore, we observe little dependency of $\tilde{h}$ with respect to p as expected for a monofractal, with a measured value of $h \approx 0.34$. This is close to the expected value of $H = 1/3$.

At this point, the method described in section 3.2.3 would involve matching the multifractal spectrum from figure 3.4 with the box counting dimension from figure 3.5. However, as the spectrum is degenerated in this case, this step is impractical. A substitute for this monofractal case would be to choose the c_p such that for all p, $c_p \mathcal{T}_p(\ell) = \mathcal{T}_{max}$, effectively guaranteeing the degeneracy of the spectrum. Furthermore, we take the freedom to renormalize the box counting dimension $D^{\ell}_{bc}(\mathcal{T})$ such that $D^{\ell}_{bc}(\mathcal{T}_{max}) = 2$. This is justified by the fact that getting measurements of box counting dimension that exactly reach 2, the dimension of the space, is very difficult given the accuracy of the power laws fitted. If the fractal dimensions from the WTMM and the box counting method are not properly renormalized, this would lead to an unnatural jump in the matching function f_ℓ obtained through equation (3.46).

The monofractal nature of fBm makes maps of $\tilde{h}$ of little interest. A more instructive test is to verify the scale invariance of the coefficients c_p in order to compute fields of local exponent $\tilde{h}$ at a different scale. For this purpose, we compute the box counting dimension at the lower scale $\ell = 8.2 \times 10^{-4}$ corresponding to approximately 3.4 grid points. The objective is to verify that the equation (3.43)

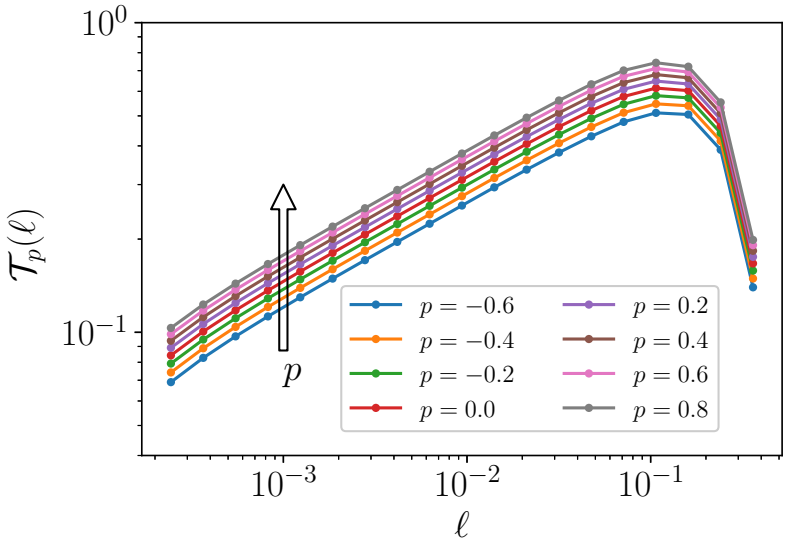

Figure 3.6: Values of the threshold $\mathcal{T}_p(\ell)$ for the global increments as a function of scale for several p for the fBm.

is satisfied at this new scale.

The box counting dimensions of the isosurfaces of "velocity" increments are shown in figure 3.7. By combining it with the c_p computed at the scale ℓ and the scaling exponents from the $\mathcal{T}_p(\ell)$, we can recover the multifractal spectrum using equation (3.43). The results are displayed in figure 3.8. They match the theoretical spectrum, with a slightly higher value of Hölder exponent than the value found by the WTMM method. This is coherent with the previous results and provides a first validation of the scale invariance of the coefficients c_p.

Summary of this chapter

In this chapter, we introduced the multifractal framework and the WTMM method used to compute multifractal spectra [36]. These can provide **global** statistical information about the regularity of a velocity field. We combined these concepts with the notion of active volumes, providing **local** information about the turbulent velocity fields. The resulting method allows us to estimate the local Hölder exponents of a velocity field, provided statistical information about the dataset. The validity of this method has then been tested using a synthetic case.

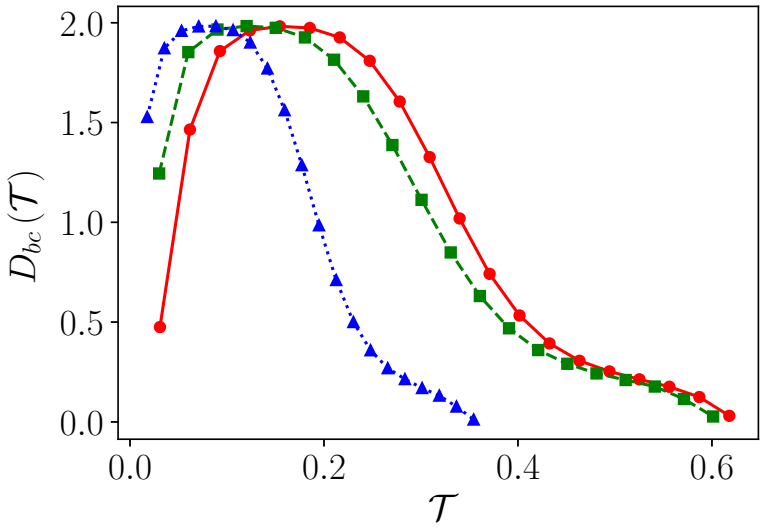

Figure 3.7: Box counting dimension of the isocontours of the different components of the wavelet based velocity increments for $\ell = 8.2 \times 10^{-4}$ for the fBm. The color code for the different components is the same as for figure 3.6.

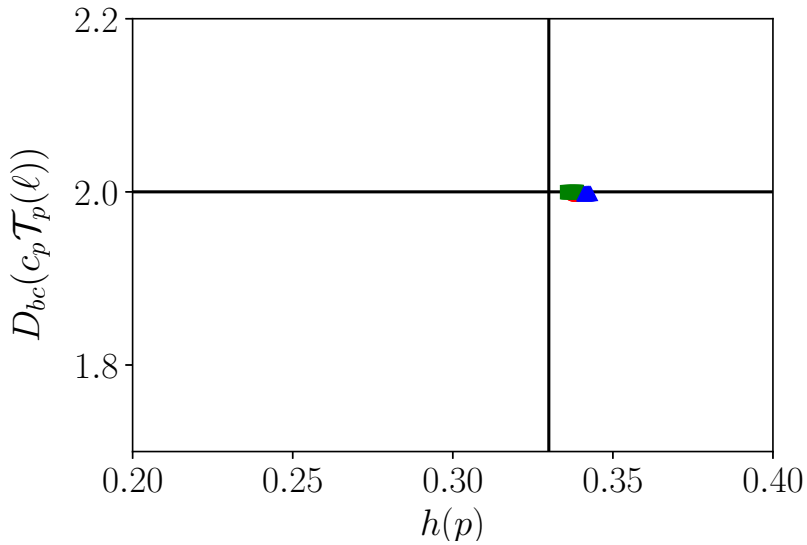

Figure 3.8: Pseudo "multifractal spectrum" reconstructed from the boxcounting dimensions of isovalues of velocity increments at scale $\ell = 8.2 \times 10^{-4}$ and the scaling laws over the $\mathcal{T}_p(\ell)$. The solid vertical line materializes the theoretical $h = 1/3$.

Chapter 4

Applications to turbulent fields

In this part, we apply the methods described previously on turbulent velocity fields originating from Direct Numerical Simulations (DNS).

The first objective is to further validate the method based on local Hölder exponent. For this aim, it is ideal to use fields for which we can precisely control the parameters, hence the numerical simulation. The main advantages to DNS fields in this case are the absence of noise and the well controlled and periodic boundary conditions. For the sake of the validation of the method, we can use the turbulent field in the inertial range, as this provides a range of scale over which we know that the Hölder regularity is of the order of $h = 1/3$ (see [39]).

Once the validation is done, the second objective is to detect and characterize potential singularities using both the local Hölder regularity and the local energy transfers. For this purpose, we need to probe velocity fields in the dissipative range, down to the Kolmogorov scale. This study will likewise be performed on numerical velocity fields, but can be extended to experimental results.

4.1 Simulation in the inertial range

4.1.1 Description of the datasets

The turbulent velocity fields are generated using two DNS in a periodic box of size $(2\pi)^3$. The parameters for the simulations are presented in Table 4.1. The code used is a pseudo spectral code adapted [9] with a Taylor-Green forcing. The code is parallelized using OpenMP and the Fourier Transform are computing using the FFTW library [22]. Such forcing is chosen in order to make the parallel between the simulations and the experimental fields that have been extracted from a Von–Kármán experiment. The experimental results which have been mentioned in

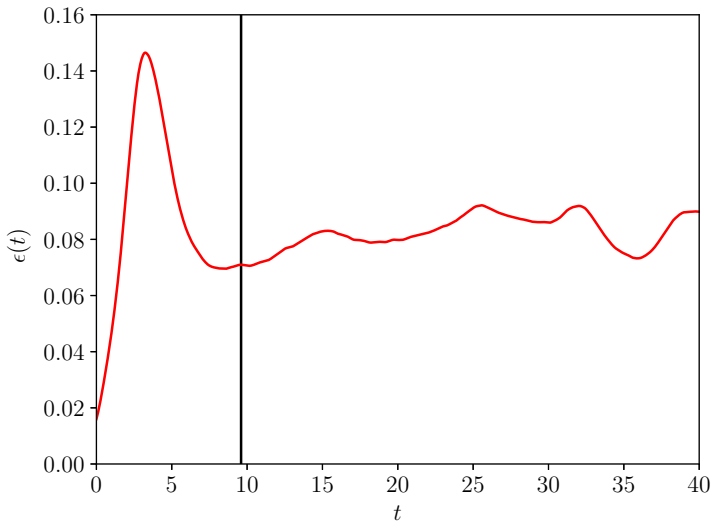

Figure 4.1: Time evolution of the energy dissipation rate as a function of time for the Run I. The vertical line materializes the time at which the first snapshot of velocity was extracted.

Chapter 2 will be the object of further comparisons in this chapter.

The averaged energy spectra corresponding to those two simulations are presented in figure 4.2. This illustrates that the first simulation (Run I) features a large range of scale in the inertial regime while the second simulation (Run II) is resolved beyond the Kolmogorov scale. As such, we can use the first simulation in order to validate the method using a well known power law behavior. Meanwhile, the extensive dissipative range allows us to probe the actual singular behavior of the flow.

The simulations have been run on the Jean-Zay supercomputer, equipped with Intel Cascade Lake 6248 processors. Using 20 cores for each simulation, the total integration time is of the order of 20,000 CPUh.

In this section, we focus on the results from the Run I. The simulation has been integrated over a total time of 40s, or more than 400 eddy turnover times $t_\eta = (\nu/\epsilon)^{1/2}$. As can be observed from the plot of the time evolution of energy dissipation represented figure 4.1, this integration time includes a transitory period of about 10s. The statistics used for the inertial case are computed from 10 snapshots of velocity fields extracted evenly from the end of the transitory period. As such, two successive fields are separated by a period of about 3s, or more than 30 eddy turnover times. As a result, the fields are uncorrelated, which ensures better statistical convergence.

Run	ν	L	λ	η	$\langle u^2 \rangle^{1/2}$	ϵ	ηk_{max}	Re_L	Re_λ
I	7.5×10^{-4}	0.79	0.19	0.0083	0.54	0.089	2.1	570	140
II	5×10^{-3}	0.94	0.48	0.034	0.55	0.097	8.5	104	53

Table 4.1: Parameters used in the simulations with grid resolution 768^3. ν is the kinematic viscosity, L is the integral scale, λ is the Taylor scale, η is the Kolmogorov scale, $\langle u^2 \rangle^{1/2}$ is the rms velocity, ϵ is the energy dissipation rate, ηk_{max} characterizes the resolution ($\eta k_{max} > \pi$ is well resolved), Re_L is the Reynolds number based on the integral scale, and Re_λ is the Reynolds number based on Taylor scale λ.

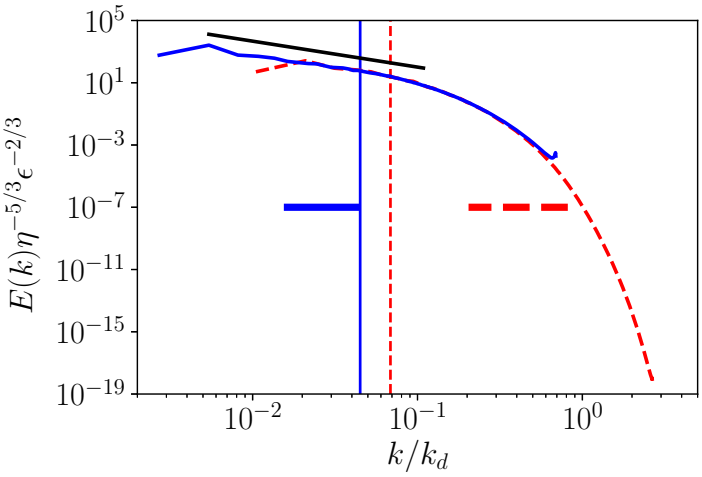

Figure 4.2: Energy spectra for the two simulations. The blue continuous (resp. red dashed) curve stands for the simulation in the inertial (resp. dissipative) range. The black line materializes the $k^{-5/3}$ slope for the inertial range. The horizontal lines of the same color as the curves materialize the corresponding fitting range used when computing power laws. The vertical lines materialize the Taylor scale wave number k_λ for each simulation.

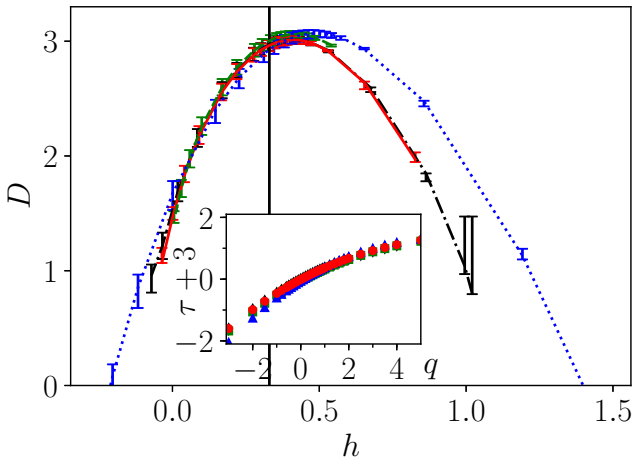

Figure 4.3: **Main figure:** Multifractal spectra for the velocity fields from simulation in the inertial region. The red (resp. green, blue) curve corresponds to the global (resp. longitudinal, perpendicular) increments. The black curve corresponds to the increments based on singular value decomposition used in the original WTMM method. The vertical line materializes the expected exponent of $h = 1/3$ according to K41. The error bars correspond to a shift of the fitting range by 5% for the power laws. **Inset:** Exponents τ as a function of q.

4.1.2 Validation of the WTMM method in the inertial range

The first step for the validation of the method in the inertial range consists in applying the modified WTMM method to the velocity fields from Run I. This is both a verification that the modification we made to the method does not compromise its accuracy in the multifractal case, and a step towards the application of the local method. Furthermore, we can take the opportunity to test the multifractal behavior of the different components of the velocity increments (i.e the longitudinal and perpendicular components) independently.

The method is applied on 10 snapshots of velocity field decorrelated in time. Given the resolution of 768^3, this represent more than 4 billions data points, enough to guarantee the convergence of results presented in figure 4.3. The power law fitting required from equations (3.26) and (3.27) (as well as equation (3.22)) are performed over the range of scale specified in figure 4.2, well within the inertial range. While a Gaussian wavelet might work in this case as we expect $h < 1$, we use a Mexican wavelet for the sake of comparison with the dissipative range.

The multifractal spectrum computed is centered around a value of $h = 0.40$ for all components but the perpendicular one. This is higher than the value of $h = 1/3$ expected from the Kolmogorov 41 theory [39]. We however observe a

very close agreement between our modified method using the global increment $\delta_G W_\ell(\boldsymbol{u})$ and the unmodified version of the WTMM, which is enough to validate our modification. The discrepancy of the results compared to the expected singularity exponent can be attributed to the anisotropy of the flow chosen. Indeed, using the same method, Arneodo [2] has found a most probable Hölder exponent of around $h = 0.34$ for isotropic turbulent velocity fields. The different behavior of the multifractal spectrum for the perpendicular component at this scale may also be attributed to the anisotropy caused by the Taylor–Green forcing.

4.1.3 Computation of the local singularity exponent

Another point of our method that requires validation is the local estimate of the regularity. In particular, we have yet to justify how the scalar field $\tilde{h}$ defined in the previous part can be used as a pertinent measure of local regularity even if it is not the real Hölder exponent of the multifractal framework. For the purpose of this verification, we first compute it in the inertial range.

The computation follows the same steps as shown for the fractional Brownian motion in part 3.3. In this case, the scale ℓ is set at the value $\ell \approx 0.24$, well within the inertial range. The method involves computing box counting dimensions over isosurfaces of the velocity increments. As described in the previous chapter, this process consists in the counting of "boxes" of given size required to recover an entire isosurface. The process is repeated over all snapshots of velocity in the dataset. The total box counts in this case are reported in figure 4.4a for six different isovalues. We can verify that these counts follow convincing power laws as a function of the size of the boxes. The exponent of the power laws is the fractal dimension associated to the given isosurface.

The results of the box counting, shown figure 4.4b, can be interpreted in terms of distribution of the velocity increments within space. As such, extreme values of velocity increments, either low or high, are concentrated in smaller structures, leading to a fractal dimension lower than 3. Compared to the box counting results for a fBm from figure 3.5, we observe a range of velocity increments for which the corresponding box counting dimension exhibit a plateau close to 3. As observed in the box counts in figure 4.4a, the corresponding isosurfaces display very similar behavior, with close box counts. This can be interpreted as a approximate way to observe intermittency, with large change of the velocity increments over very short period. Such change would lead to the isosurfaces of increments being close to each other hence the similar box counts. It is however unclear how pertinent this metric alone can be for the study of intermittency.

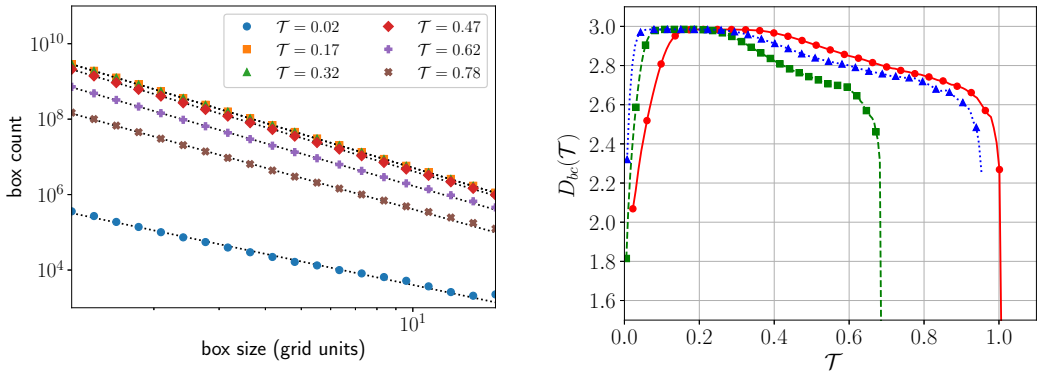

(a) (b)

Figure 4.4: **(a)** Box count of 6 isosurfaces of velocity increments as a function of the box size. The results are totaled over 10 snapshots of velocity. **(b)** Box counting dimension of the isosurfaces of the different components of the wavelet based velocity increments for $\ell \approx 0.24$ for the simulation in the inertial range. The color code for the different components is the same as for the previous figures.

The thresholds $\mathcal{T}_p(\ell)$ are computed over the same dataset. We verify in figure 4.5a that once renormalized by $\mathcal{T}_0(\ell)$, the results give a convincing power law over a wide range of scales, compatible with the prediction of equation (3.50). In order to compute the power law exponents, the fit are performed first over the renormalized thresholds, which yields a quantity $\gamma(p) = h(p) - h(0)$. The reference value $h(0)$ is then evaluated by fitting a power law over the thresholds $\mathcal{T}_0(\ell)$ in figure 4.5b over the inertial range. As a reminder, the thresholds and the corresponding power laws are only used to compute the coefficients c_p, which are not strictly required to recover the local Hölder exponents. We will however use these results to verify the invariance of c_p with respect to scale.

As the multifractal spectrum in this case is non degenerated, we can proceed differently from the fBm case. We use equation (3.45) to match the fractal dimensions from the WTMM method (figure 4.3) with the ones obtained by box counting (figure 4.4b). This gives us a direct relationship between the velocity increments and the local Hölder exponent $\tilde{h}$. In the process, the lower values of $\tilde{h}$ must be associated with the larger values of velocity increments, as it represents a more singular velocity field. The resulting matching function f_ℓ is represented figure 4.6. The perpendicular and longitudinal increments are no longer treated separately as we are interested in the regularity properties of the full velocity field.

This process allows us to produce maps of $\tilde{h}$ from the corresponding maps of velocity increments, with one pitfall: the range of velocity increment accessible

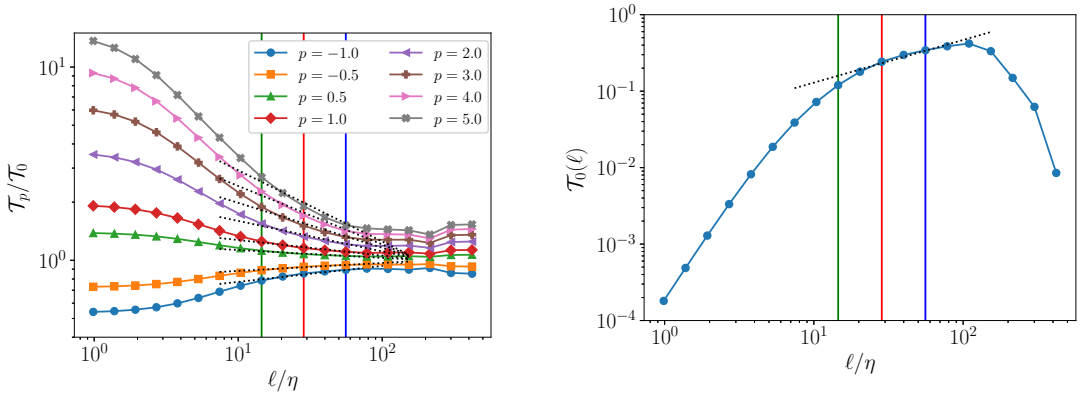

(a) (b)

Figure 4.5: **(a)** Values of the threshold $\mathcal{T}_p(\ell)$ for the global increments as a function of scale for several p computed over 10 snapshots of run I. The thresholds are renormalized by $\mathcal{T}_0(\ell)$. Fits corresponding to the scales delimited by the green and blue vertical lines are given in dotted lines. **(b)** Reference thresholds $\mathcal{T}_0(\ell)$. The fit used in the calibration of the method is materialized by a dotted line.

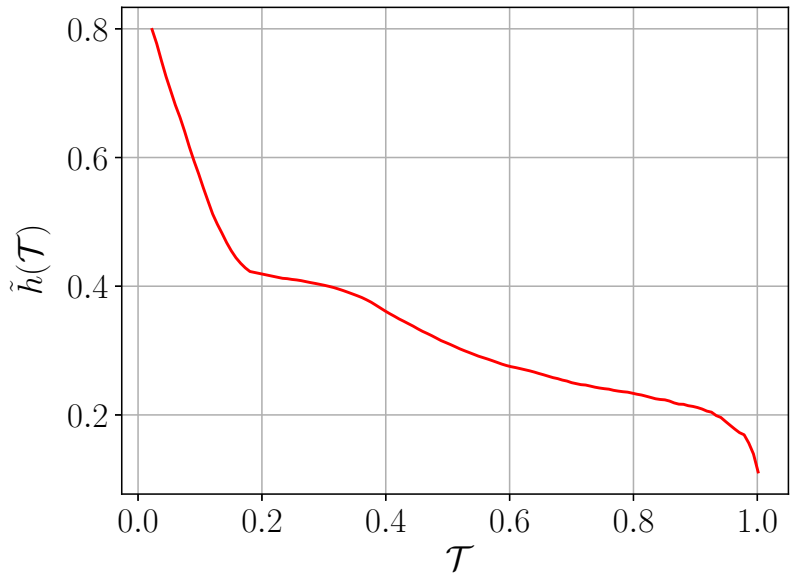

Figure 4.6: Mapping function of the coefficient $\tilde{h}$ from the global velocity increments at scale $\ell \approx 0.24$.

to this method is limited. In particular, for the boxcounting method to work for an isosurface at value $\mathcal{T}$, a minimum amount of data points with such value of velocity increment is required. Likewise, the WTMM method is also constrained by the amount of statistics available. A lower fractal dimension corresponds to rarer events, which makes the collect of sufficient statistics harder. As a result, no reliable fractal dimension has been computed for isosurfaces corresponding to a value $\mathcal{T} > 0.5$, which prevents us from measuring values of $\tilde{h} < 0.1$. In consequence, the maps of singularity exponent that we can compute have regions where we only know that $\tilde{h} < 0.1$ without being able to give any precise value.

4.1.4 Comparison with the local energy transfers

The production of these maps of $\tilde{h}$ is the opportunity to compare this measure of regularity to the local energy transfers. As mentioned in Chapter 2, the Duchon–Robert term D_I^ℓ of the energy budget is expected to be higher in the regions where the velocity field is singular. Confirming that this term is correlated to the field $\tilde{h}$ would validate the use of the latter as a criterion to detect pseudo singularities.

Computing maps of those two quantities in the snapshots from Run I shows that these two quantities are visually correlated, with structures of low regularity measured by $\tilde{h}$ being observed in the same location as structures of extreme energy transfer D_I^ℓ. This is illustrated in figure 4.7. In particular, regions with low $\tilde{h}$ appear to be surrounded by a pair of regions of high energy transfer. This also means that the extrema of those two quantities do not occur exactly in the same location.

Nevertheless, it is still relevant to compute the joint Probability Density Function (PDF) of these two terms in order to confirm their correlation. Such PDF, computed over 50 velocity fields extracted at regular interval over approximately 30 turnover times, is displayed in figure 4.8. With this dataset, small scales relevant to the computation of both the local Hölder exponent $\tilde{h}$ and the energy transfer D_I^ℓ should not be correlated between different snapshots. The conditional PDF is imperfectly converged for extreme values of $\tilde{h}$, as those correspond to rarer events. It is however enough to demonstrate a clear correlation between the two terms, with higher values of energy transfer being more predominant where the local Hölder exponent $\tilde{h}$ is lower. As such, the field $\tilde{h}$ compares favorably with the energy transfer to measure the regularity of the velocity field and can be used as a criterion for the detection of potential singularities and the quantification of their strength. Meanwhile, the complexity of the structures of energy transfer observed in figure 4.7 and the physical meaning of the term D_I^ℓ justifies its use alongside

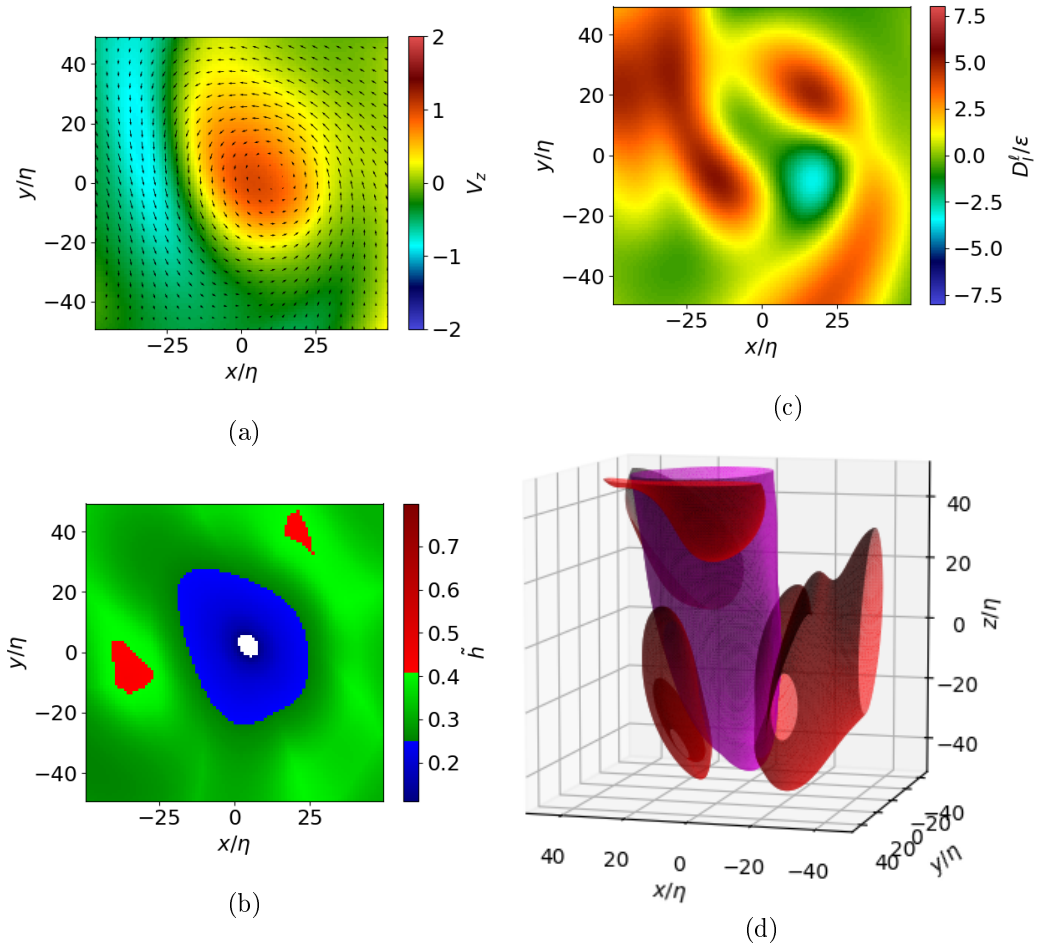

Figure 4.7: Region with strong irregularity extracted from one snapshot of Run I. **(a)** Velocity along a slice passing through the point of maximal velocity increment (corresponding to an undetermined minimal value of Hölder exponent). The arrows stand for the velocity in plane and the colormap for the third component of velocity. **(b)** Local energy transfers on the same slice. **(c)** Local Hölder exponents on the same slice. White area corresponds to velocity increments so strong we cannot associate a value of $\tilde{h}$ using the mapping function of figure 4.6. **(d)** 3D representation of the irregular region. The magenta isosurface corresponds to $\tilde{h} = 0.25$. The red isosurface corresponds to $D_I^\ell = 4\epsilon$.

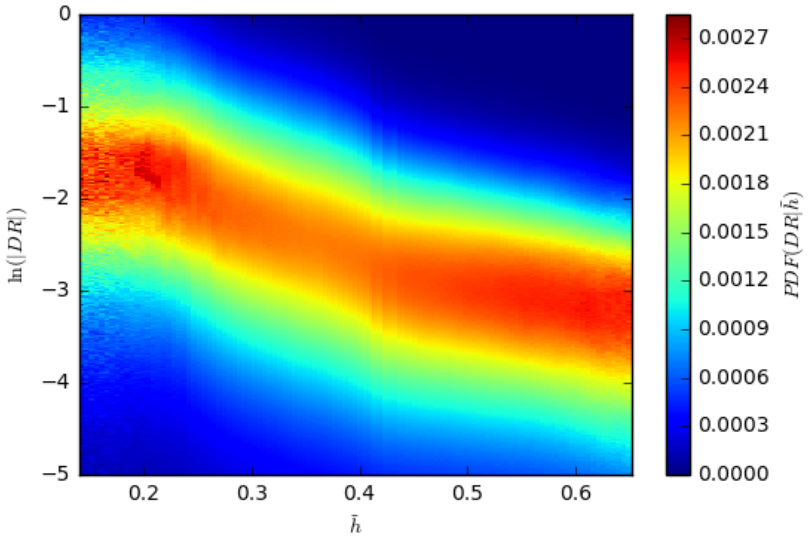

Figure 4.8: Joint PDF of $\tilde{h}$ and the Duchon–Robert energy transfer term D_ℓ^I over 50 fields regularly spaced over approximately 30 turnover times. In order to enlighten the correlation of those terms independently of the number of occurrence, the PDF is rescaled such that every vertical line is a conditional PDF of D_ℓ^I at given $\tilde{h}$.

the singularity exponent to characterize those singularities.

4.1.5 About the scale invariance of the c_p coefficients

At this point, we have yet to use the coefficients c_p defined in equation (3.40). As it has been discussed in section 3.2.4, those coefficients do not depend on the scale. This property makes it possible to compute the c_p at any one scale and recover the matching function from 4.6 at any other scale without having to perform the WTMM method or box counting algorithm again. We can use the data from the simulations to verify this property.

In order to do this, one must account for the errors generated by fitting power laws. Indeed, the computation of the multifractal spectrum using the WTMM requires to determine power laws according to equations (3.26) and (3.27). Likewise, the local method relies on the power law behaviour of the threshold as described in equation (3.39). While in theory, the equation (3.44) used to determinate the coefficients c_p involves quantities defined at a given scale, in practice the power law exponents have to be estimated over a range of scales ℓ. The accuracy of the power law fit and uncertainty of the corresponding scale limit the accuracy of the computation of the coefficients c_p.

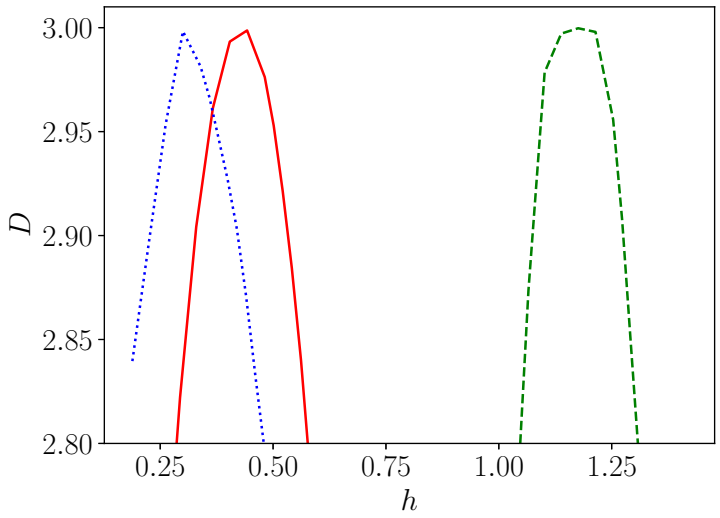

Figure 4.9: *Pseudo* spectra reconstituted using the coefficient c_p computed at scale $\ell \approx 0.24$ and the boxcounting dimensions of the velocity increments computed at scales $\ell \approx 0.12$ (green curve), $\ell \approx 0.24$ (red curve) and $\ell \approx 0.46$ (blue curve). The scale are also materialized by vertical lines of the same colour on the figure 4.5a.

The coefficients c_p do not have an obvious physical meaning, making it difficult to determine what range of error is acceptable. As a result, we use a similar method as for the fBm case to test their scale independence. This involves computing the c_p at a scale $\ell \approx 0.24$ and using the results to infer multifractal spectra of the velocity field at a different scale. Using the coefficients c_p and the box-counting dimensions of the isosurfaces of velocity increments computed at two different scales, we use the equation (3.42) to recover pseudo multifractal spectra at two different scales. The results are presented in figure 4.9 using the scales materialized in figure 4.5a. The blue curve shows that using a larger scale in the inertial range results in a similar multifractal spectrum. The shift towards Hölder exponents even lower than the value $h = 1/3$ can be attributed to the proximity to the injection scale. Conversely, the green curve demonstrate that using a scale at the lower bound of the inertial range shifts the spectrum, with much higher values of h. This is a result of the velocity field starting to regularize through the effects of viscosity.

Although a direct comparison with the output of the WTMM method would be ideal, too many statistics would be required in order to have accurate results with very small fitting range. Considering the qualitative aspect of the measure of local regularity through the singularity exponent $\tilde{h}$, we estimate that this analysis is enough to justify the scale independence of the coefficients c_p. The result of this analysis is that using coefficient c_p computed at a different scale will provide

qualitatively sound results. Since the complete method is dependent on fitting scaling exponents, it is reasonable to use the c_p for quantitative measurements.

4.1.6 VGT invariants

As we have analyzed the correlations between the Hölder exponents and the local energy transfers, it can be pertinent to reproduce the study by Paul Debue on the VGT invariants [15] as mentioned in Chapter 2. The objective is to verify that we obtain similar results for the location of high energy transfers on the QR-plane. Additionally, we can conduct a similar study focused on the local Hölder exponents.

Because most quantities computed in this thesis are filtered using a Fourier transform, we choose to do the same for the VGT invariants. As a result, instead of the standard velocity gradient, we use a mollified gradient defined similarly to equation (3.30):

$$Q = -\frac{1}{2}\operatorname{Tr}(A_\ell^2), \tag{4.1}$$

$$R = -\det(A_\ell) \tag{4.2}$$

where:

$$A_{\ell,ij} = -\int \nabla_j \Psi^\ell_{mex}(\boldsymbol{y}) u_i(\boldsymbol{x}+\boldsymbol{y}) \mathrm{d}\boldsymbol{y}. \tag{4.3}$$

with Ψ_{mex} the 3D Mexican wavelet at scale ℓ. The choice of a Mexican wavelet instead of a Gaussian wavelet is made in preparation for the study at the dissipative scale, for which the Gaussian wavelet is no longer adapted.

The results of the computations over 10 snapshots of velocity are shown in figure 4.10. The use of the mollified velocity gradient leads to smoother results compared to [15], but the qualitative observation are the same. We can verify that we obtain the same common droplet shape for the distribution of the invariants Q and R in figure 4.10a. We also recover similar results for the local energy transfer in figure 4.10b. Indeed, we have the same behavior with strong positive energy transfer along the Vieillefosse line in the lower right quadrant, corresponding to the limit between sheets and vortex compression, as well as in the vortex stretching region. Meanwhile, negative energy transfers are found for high values of Q, both in the vortex stretching and the vortex compressing regions.

The local Hölder exponents however do not follow the same distribution. Overall, we observe lower regularity whenever the invariants Q and R are far from the average, in particular but not only in the vortex region. This is not unexpected, as high values of the VGT invariants require strong velocity gradients, and hence a

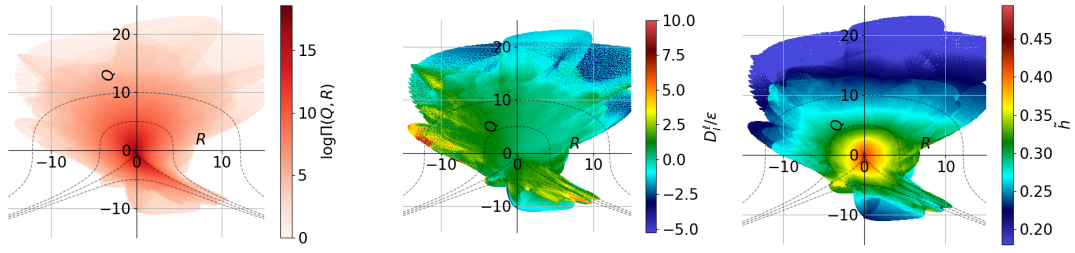

(a) (b) (c)

Figure 4.10: **(a)** Joint PDF of Q and R. **(b)** Conditional average of the local energy transfer D_I^ℓ at given Q and R. **(c)** Conditional average of the local Hölder exponents at given Q and R. For each figures, three Vieillefosse lines are drawn in dashed lines.

low regularity. It is however a confirmation that the structure of low local Hölder exponent are not limited to the same topologies as the local energy transfer. This corroborates the observations from figure 4.7.

4.2 Simulation in the dissipative range

The results in the inertial range serve as a second validation for our method to compute local Hölder exponents. This assurance acquired, our next objective is to apply the method in the dissipative range. By acquiring a concrete measurement of the local regularity of the velocity fields observed close to the Kolmogorov scale, we intend to localize regions of the flow with singular behavior. Used in addition to the local energy transfer, this would be an effective way to characterize extreme events.

The well resolved simulation (Run II) has been integrated over a total duration of 45s, or about 200 eddy turnover times t_η. The plot of the energy dissipation as a function of time is given in figure 4.11. As the objective of the study at the dissipative scale is the detection and characterization of quasi singular events, the simulation is split in two parts. During the first part, delimited by the two vertical lines in figure 4.11, velocity fields are saved every 600 time steps, with an interval of over 3 eddy turnover times between each snapshot. This gives us 40 velocity fields uncorrelated in time, which allows us to compute all statistical quantities. We also use this part of the dataset to extract singular events in order to identify the typical structures.

The second part of the simulation consists in saving a velocity field every 30 time steps, or $0.15t_\eta$. The purpose of this part is to analyze the time evolution of

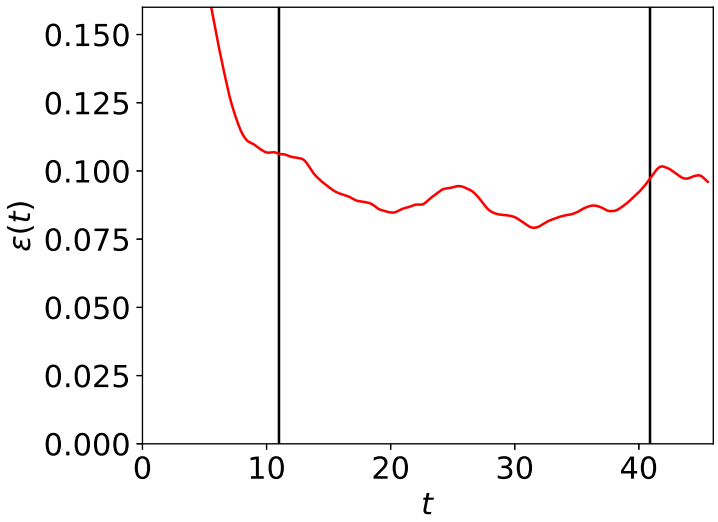

Figure 4.11: Time evolution of the energy dissipation rate as a function of time for the Run II. The first vertical bar materializes the time at which the first snapshot was extracted. The second vertical bar materializes the start of the time resolved dataset.

irregular events. This would be useful in order to identify the mechanism behind the formation of quasi singularities.

4.2.1 Multifractal spectrum in the dissipative range

One idea in order to accomplish this goal is to apply the method again for the new dataset. As such, we start by using the modified WTMM, while choosing the range of fitting for the power laws in the dissipative range. The range chosen is materialized in figure 4.2 and spans from around 3η to 9η. This range of scale is large for the purpose of measuring a trend particular to a single scale, as would be suitable in theory for the method. It is however a decent compromise between the localization of the scale and the accuracy of the power law fitted. As we do not expect consistent power law behavior of the velocity increments over this large range of scale in the dissipative range, the WTMM method might not work as well as in the dissipative case.

For similar statistics as for the inertial case, we use 10 snapshots from the Run II, decorrelated in time. With this amount of statistics, we are confident as before of the convergence of the results. The multifractal spectra obtained are displayed in figure 4.12. One first observation in comparison to the inertial case in figure 4.3 is that the spectra computed using the different components of the velocity gradient follow approximately the same curve. In other words, we have recovered

isotropy at the dissipative scale. This is an expected behavior, as the small scales structures should not be too heavily influenced by the large scale forcing. This nevertheless is an important property to note in order to generalize the small scale observations of this chapter.

One other striking observation is that the range of Hölder exponents observed at this small scale has much higher values than what was observed at large scale. Again, this is coherent with the expectations. As mentioned before, the effect of viscosity is to make the velocity field more regular. At this scale, the most frequent Hölder exponent observed is around $h_{max} = 2.7$. In effect, this means that most of the field appears to be twice differentiable at this scale. The spectrum is bounded on the right side by $h = 3$, which is the maximum value measurable using a Mexican wavelet, with three cancellations. In other words, if the actual Hölder exponent of the field was any higher, we would still only measure a value of $h = 3$.

On the other hand, the fractal dimension associated with a Hölder exponent of $h = 2$ is non zero. This means that there are locations in the velocity fields with a lower regularity at this scale.

One other observation about this spectrum is that the fractal dimension does not reach the dimension of the space. We can interpret it as the lines of maxima defined in the section 3.1.4 are not space filling at this scale. This means that the singular events followed across scales by the WTMM method are more sparse. This aspect is detrimental to our method as we need to match the dimension obtained from the box counting algorithm with the present spectra.

4.2.2 Calibration of the local Hölder for the dissipative range

The behavior of the multifractal spectrum at the dissipative scale makes it impossible to apply the method directly. In particular, the fractal dimension computed is much lower than 3, while we expect the box counting algorithm to give fractal dimensions close to 3 for the most common values of velocity increments. As a result, it is not suitable to use the full method described in part 3.2.

In order to overcome this difficulty, we use the property that the coefficients c_p are independent of the scale. The idea is thus to apply our method in the inertial range, where we know the method works properly. From the results we compute the coefficients c_p. Those coefficients can then be used to recover the matching function between the velocity increments at the dissipative scale and the Hölder exponents at the same scale using equation (3.44).

We thus compute the multifractal spectrum and the boxcounting dimensions at the scale $\ell \approx 1.4\lambda \approx 19\eta$. The results of these two operations, as well as the

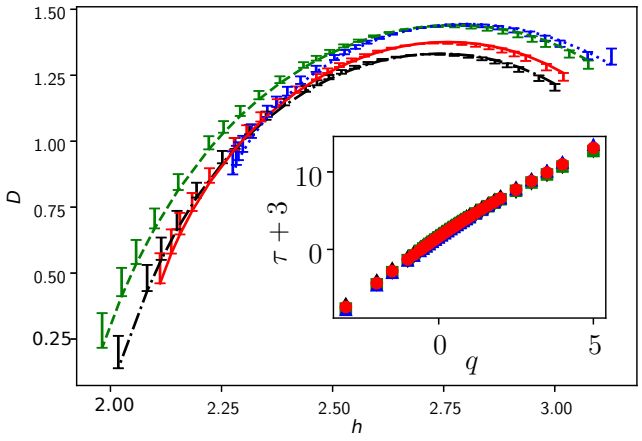

Figure 4.12: **Main figure:** Multifractal spectra for the velocity fields from simulation in the dissipative regime. The red (resp. green, blue) curve corresponds to the global (resp. longitudinal, perpendicular) increments. The black curve is the result using the velocity increments based on singular value decomposition. The error bars correspond to a shift of the fitting range by 10% for the power laws. **Inset:** Exponents τ as a function of q.

resulting matching function between the velocity increments and the local Hölder exponents, are shown figure 4.13. Because the inertial range is much shorter than for the previous simulation and the scale at which the computation is performed is much closer to the injection scale, we encounter difficulties for this step. In particular, it is difficult to get the WTMM method to converge, as there are much fewer lines of maxima compared to the previous case. In order to help with the convergence, we use all the 40 velocity fields uncorrelated in time from the first part of the simulation. We further verify that adding 60 more time resolved velocity fields from the second part of the simulation do not modify the results significantly. This does not prevent the effect of the proximity to the injection scale, which is made apparent by the fact the most probable Hölder coefficient in figure 4.13a drops to $h = 0.3$, compared to the results in the previous simulation. As such, we need to keep in mind for the future interpretation that there may be inaccuracies in the estimation of the local Hölder exponents.

From this matching function, the next step is to determine the coefficents c_p. In order to do this, we compute the thresholds $\mathcal{T}_p(\ell)$ for this dataset. Once again, the thresholds are renormalized by the reference value $\mathcal{T}_0(\ell)$. The results are show in figure 4.14. The statistics are computed using the same 40 uncorrelated velocity fields and 60 velocity fields from the time resolved period. From the results in 4.14a, we get two convincing fitting ranges, one for the inertial scales and one

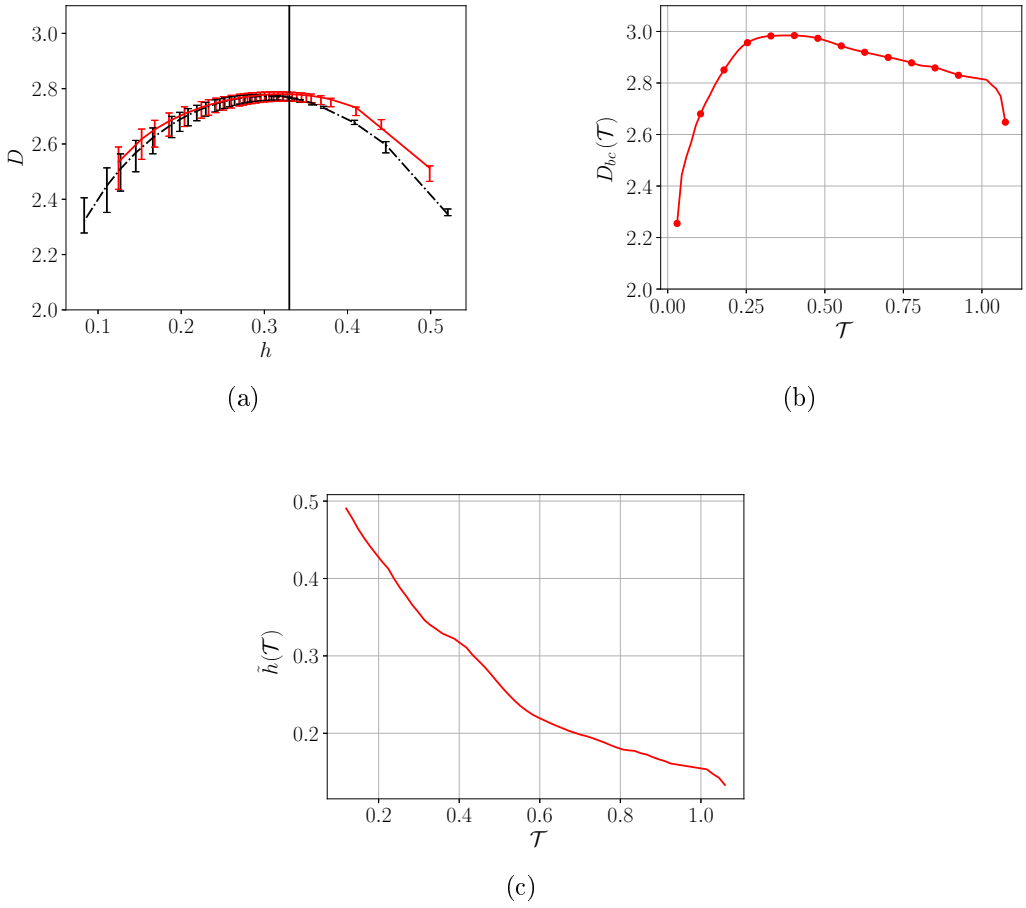

Figure 4.13: **(a)** Multifractal spectrum fitted around $\ell \approx 1.4\lambda$. The spectrum corresponding to the global increments is shown in red, while the spectrum obtained using the unmodified WTMM method is shown in black for comparison. The vertical line materializes $h = 1/3$. The error bars correspond to a shift of the fitting range by 5% for the power laws. **(b)** Box counting dimensions evaluated at the same scale. **(c)** Matching function resulting from the combination of **(a)** and **(b)**.

for the dissipative scale. While the inertial range is narrow, the power law over the dissipative range is sustained over about a decade. This justifies the use of multifractal based tools for the dissipative range.

Using the same method as for the inertial case, we can derive the values of $h(p)$ from the power laws fitted in 4.14 for both $\ell = 1.4\lambda$ in the inertial range and $\ell = 1.8\eta$ in the dissipative range. Using equation (3.44) for the first scale allows us to compute the coefficients c_p from the thresholds and the matching function of figure 4.13. We can then use the same equation at $\ell = 1.8\eta$ to recover the matching function in the dissipative range, shown in figure 4.15. The corresponding Hölder exponents are as expected much higher than those computed in the inertial range from figure 4.13c. This is the effect of viscosity regularizing the velocity fields at this scale. In terms of rarity of an event, one must understand a local Hölder exponent of 1.4 at this scale to be as exceptional as a Hölder exponent of 0.2 in the inertial range.

Note that the corresponding local Hölder exponents are lower than the one determined using WTMM in figure 4.12. We do not have a clear explanation for this discrepancy, as for both cases a Mexican wavelet is used, which is supposed to only cause problems when the regularity reaches $h = 3$. For the purpose of our analysis of the local regularity, we will trust the results from figure 4.15, at least for qualitative interpretations. Even taking into account the uncertainty on the exact values of Hölder exponent, it is clear that there are events with $h < 2$ at this scale, i.e. such that the velocity field does not appear to be twice differentiable.

In the following, we will try to probe for very irregular events at the dissipative scale. In order to give a value of Hölder exponent even if the velocity increment is greater than 0.2, we choose to extrapolate the matching function as shown in figure 4.15. Events with such low regularity are expected to be rare, and we expect the local Hölder exponent to reach such low value only in very localized regions, as it was the case for the maps shown in figure 4.7. As such, we deem that a simple linear extrapolation based on the last two datapoints should be enough for our purpose. In order to associate a local Hölder exponent to these quantities without the use of extrapolation, one would need to compute thresholds and multifractal spectrum for higher orders of p. However, the amount of statistics available to us is not enough to get converged results for $p > 5$.

Additionally, we are also unable to map a Hölder exponent to the very small values of velocity increments. This is because such values are also very rare, corresponding to the $p < 0$ branch of the multifractal spectrum. While this has no effect on our study of very singular events, one can expect the Hölder exponent to

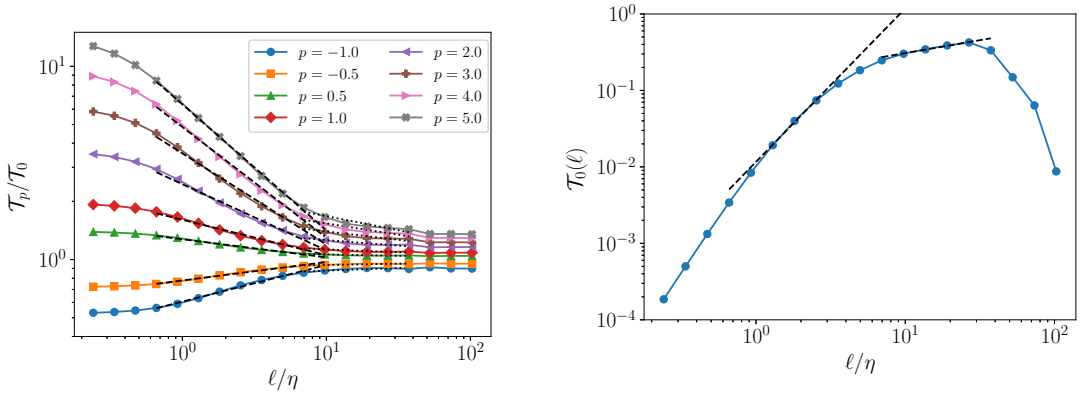

(a) (b)

Figure 4.14: **(a)** Values of the threshold $\mathcal{T}_p(\ell)$ for the global increments as a function of scale for several p computed over Run II. The thresholds are renormalized by $\mathcal{T}_0(\ell)$. **(b)** Reference thresholds $\mathcal{T}_0(\ell)$. Fits corresponding to the inertial range, associated to $\ell \approx 1.4\lambda$ are given in dotted lines while fit in the dissipative range associated to $\ell = 1.8\eta$ are given in dashed lines.

keep growing when the velocity increment goes to zero, corresponding to a velocity field almost constant.

4.2.3 Comparison to the local energy transfers in the dissipative range

Now that we have access to the local Hölder exponents at the dissipative scale, it is important to perform another comparison with the local energy transfer. Indeed, the purpose of the study performed in section 4.1.4 was to validate the use of the local Hölder exponents computed using this method as a criterion for the detection of quasi singularities. While a good correlation between these two scalars computed in the inertial range is a first step for validation, the detection of irregular event is to be performed at the dissipative scale.

As a result, we compute the joint PDF of these two terms computed at $\ell = 1.8\eta$. The statistics are aggregated over the same 100 velocity fields from Run II which have been used before. This ensures a good convergence, with the exception of the cases with extreme values of Hölder exponents. The results shown in figure 4.16 confirm the clear correlation between those two terms. This finally concludes the validation of the use of local Hölder exponents $\tilde{h}$ as a criterion for the detection of singularities.

The clear correlation exposed here might appear contradictory to the observation made in figure 4.7 that the mimima of $\tilde{h}$ exponents do not occur in the same

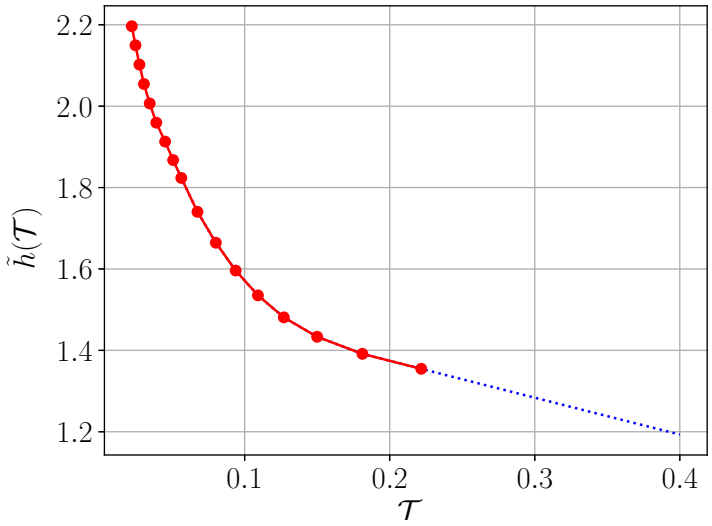

Figure 4.15: Matching function linking the velocity increment to a value of local Hölder exponent at the scale $\ell = 1.8\eta$. The red curve and dots corresponds to the result of the calibration. The dotted blue line is the extrapolation used in case the velocity increment is higher than the 0.2.

location as the maxima of D_I^ℓ. This contradiction is lifted by plotting the same PDF restricted to very low values of Hölder exponents. The results are shown in figure 4.17. We observe that for very small values of Hölder exponent, the correlation is reversed. This shows that, particularly at the dissipative scale, the structures of very low Hölder exponents and very large local energy transfer are not superposed. This observation will be further discussed in the following.

4.2.4 VGT invariant in the dissipative range

When analyzing extreme events at the dissipative scale, we will make use of the VGT invariants in order to get an idea of the topologies most representative of quasi singularities. For this purpose, we need to know the global, unconditioned PDF of the invariants Q and R as a reference. As for the Run I, we use VGT invariants computed over the mollified velocity gradient, as defined in equation (4.2). We compute as before the joint PDF of the invariants Q and R and the conditional average for both the local Hölder exponents $\tilde{h}$ and the local energy transfer D_I^ℓ. The results are shown in figure 4.18. The conclusions previously made in the inertial case are still applicable: We recover the common droplet shape for the joint PDF of Q and R in figure 4.18a. With the exception of a single excursion in the "vortex stretching" region, the strong positive Duchon Robert

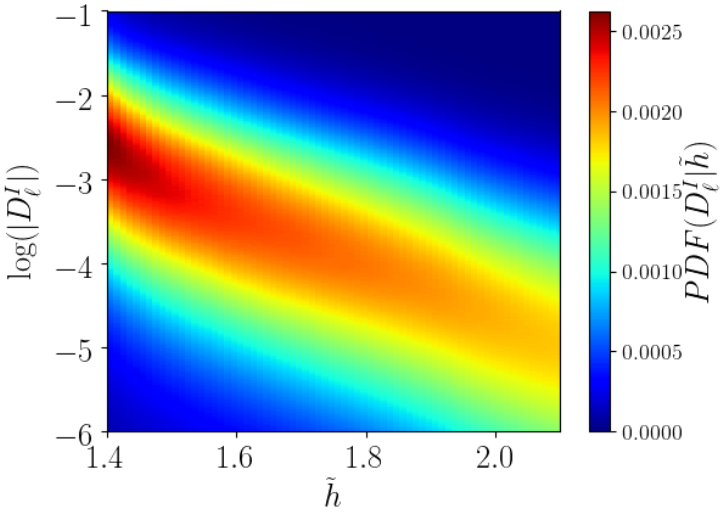

Figure 4.16: Joint PDF of $\tilde{h}$ and the Duchon–Robert energy transfer term D_ℓ^I over 100 fields from Run II. In order to enlighten the correlation of those terms independently of the number of occurrence, the PDF is rescaled such that every vertical line is a conditional PDF of D_ℓ^I at given $\tilde{h}$.

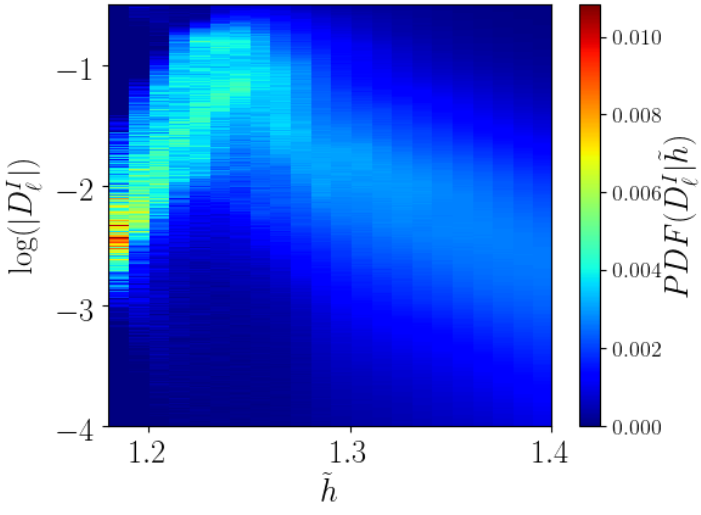

Figure 4.17: Detail of the joint PDF of $\tilde{h}$ and the Duchon–Robert energy transfer term D_ℓ^I over 100 fields from run II corresponding to very low Hölder exponents. The PDF is rescaled such that every vertical line is a conditional PDF of D_ℓ^I at given $\tilde{h}$.

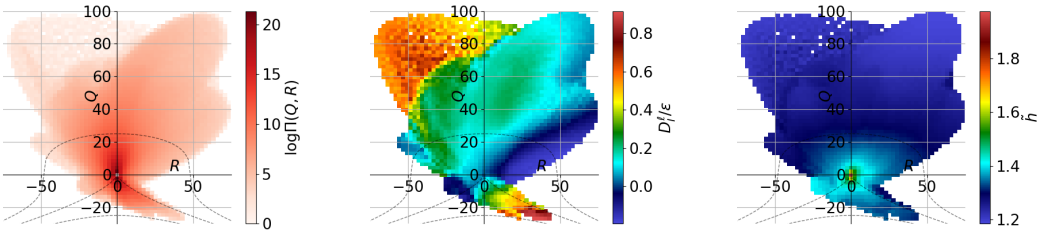

(a) (b) (c)

Figure 4.18: **(a)** Joint PDF of Q and R. **(b)** Conditional average of the local energy transfer D_I^ℓ at given Q and R. **(c)** Conditional average of the local Hölder exponents at given Q and R. For each figures, three Vieillefosse lines are drawn in dashed lines.

energy transfer term appear strongly segregated in the lower right quadrant of figure 4.18b, in the "sheet" region. This is even more salient than in the inertial case. Here again this is in agreement with the observations made by Paul Debue in experimental data [15]. Finally, we observe very low values of the local Hölder exponent wherever the VGT invariants are large.

4.3 Study of extreme singular events using uncorrelated data.

4.3.1 Extraction of the events and general statistics

Using the 40 velocity fields uncorrelated in time from run II, we can use the mapping function from figure 4.15 to compute the fields of Hölder exponents. From the results, we select all events where the minimum value of $\tilde{h}$ gets below 1.3. This value is chosen to strike a balance between the strength of the events and the number of events found. With such a low value of $\tilde{h}$ at the dissipative scale, only inferred through the matching function of figure 4.15 by using extrapolation, we target very irregular events. On the other hand, this threshold is high enough to allow us to extract 213 distinct events fulfilling this condition. This will be enough to perform statistics.

We can verify that the events detected are spread evenly among the snapshots of velocity fields, as shown in the histogram of figure 4.19. Likewise, we also verify that the events are not concentrated in a single region of the simulation domain. This guarantees that there is no bias caused by the forcing chosen.

Before analyzing the events in detail, we can use the VGT invariants to get a

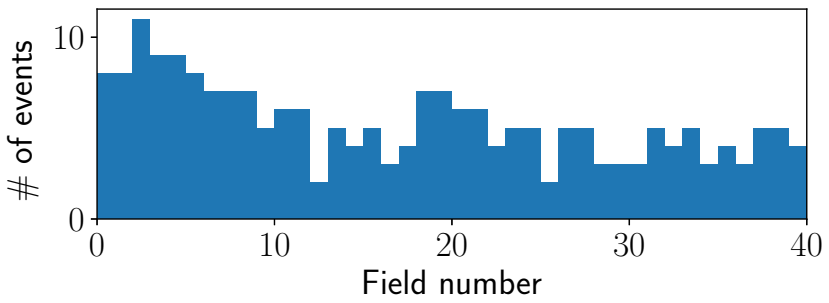

Figure 4.19: Histogram of the number of distinct events detected in the 40 velocity fields uncorrelated in time.

first grasp of the topology of the singular events. We define the location of the minimum of local Hölder exponent as the center of the event. The VGT invariants Q and R computed at the center of each using the mollified velocity gradient (see equation (4.2)) are represented in figure 4.20. The first observation is that, with only two exceptions, all events appear to be either in the "vortex compressing" or the "vortex stretching" regions of the QR-plane. Moreover, we observe a bias toward the later as more than 75% of the events detected verify $R < 0$. We confirm that this bias is stronger than what is observed in the whole domain in figure 4.18. This trend is in agreement with several studies relating singularities to vortex stretching (e.g. [33] in the case of Euler equations).

4.3.2 Visualization of singular events

The next step in the analysis is to observe the events directly. In order to reduce the influence of the large scale motion in the visualizations, we subtract the mean velocity over a cubic sub-domain of side 1.7λ centered on the point of minimal Hölder exponent.

For each events, we compute the vorticity, the inter scale energy transfer D_I^ℓ (from equation (2.8)), the viscous dissipation at this scale D_ν^ℓ (from equation (2.12)) and the mollified velocity gradient tensor invariants Q and R (from equation (4.2)).

A first overview of the events detected leads to two observations. First of all, we verify the conclusion obtained through the use of the VGT invariants in figure 4.20: the streamlines of velocity for most events are typical of vortices. Moreover, the isosurfaces of local Hölder exponents $\tilde{h}$ are oblong, seemingly oriented in the same direction as the lines of vorticity. The other principal observation is that

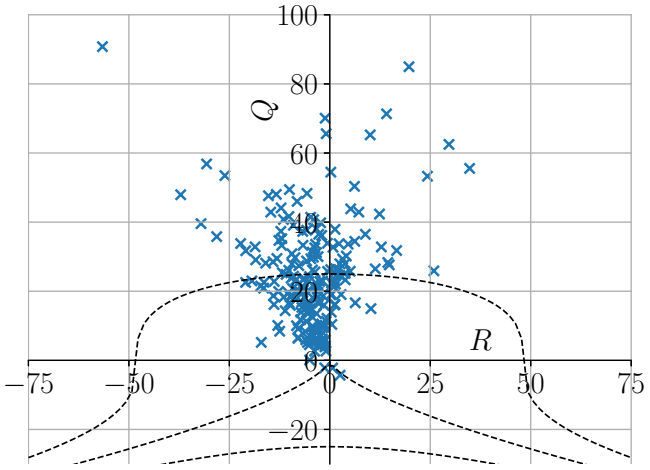

Figure 4.20: Scatterplot of the mollified velocity gradient tensor invariants Q and R at the location of minimal Hölder exponent for the 213 extreme events extracted at the dissipative scale. Three Vieillefossse lines at $27R^2 + 4Q^3 = -62500, 0$ and 62500 are drawn in dashed lines.

the structures of low local Hölder exponent appear to be sandwiched by a pair of structures of strong energy transfer D_I^ℓ, in a way similar to what was observed in figure 4.7.

In order to help with the analysis, it is preferable to have all of them oriented in the same way. The way the events are reoriented is as follow:

- As the local Hölder exponent $\tilde{h}$ is the most relevant scalar for our study, we define the direction of a first axis by using the first eigenvector $\boldsymbol{e}_1$ of the covariance matrix of $\tilde{h}$. Reorienting the events using this axis, the structures of Hölder exponent must be aligned along the x-axis.

- As singular events appear to be vortices, we want all vortices to face the same direction. We thus choose the direction of the first axis such that $\omega_x > 0$ at the center.

- We observed that the events are not axisymmetrical from the structures of D_I^ℓ and D_ν^ℓ. This justifies the definition of a second axis, orthogonal to the first one. Using the first eigenvector $\boldsymbol{e}_2$ of the covariance matrix of D_ν^ℓ, we reorient the events such that $\boldsymbol{e}_1 \times \boldsymbol{e}_2$ is along the z-axis.

Note that those choices do not impose a direction to the second axis, such that rotating the event by an angle π around $\boldsymbol{e}_1$ still fulfills the conditions. Three events

reoriented as explained are represented in figures 4.21 to 4.23. Additional events can be found in Appendix A.

Using the data collected, we can pick up the work of classification for the extreme events mentioned in Chapter 2. The thesis by Paul Debue [15] approaches the same problem using extreme events of D_I^ℓ. As was discussed before, those are closely related to the extreme events of Hölder exponents studied here. In that work, two types of vortices are distinguished based on the behavior of the helicity: the roll vortices and the screw vortices. The roll vortices corresponds to events where the helicity changes sign over the structures. On the other hand, the screw vortices are vortices without change of helicity in the structure. It is mentioned in this work that the difference between the two types of events might just be a simple Galilean transformation.

In our dataset, the predominant structure is the one corresponding to roll vortices. Such a structure is visible in the streamlines of figure 4.22. In some cases, the change of helicity occurs off centered, away from the location of minimum regularity. This can be attributed to a remnant contribution of the large scale velocity. Meanwhile, screw vortices rarely appear. One could interpret the aforementioned off centered roll vortices, like for example 4.23, as screw vortices. However, we observe no qualitative difference between those two types of vortices in any of the observable used here. The conclusion is that, as [15] supposed, those two structures are the same up to a Galilean transformation.

In the work of [15], a third type of structure is identified. The so called "U-turn" is characterized by a sharp change of direction of the velocity streamlines. We do not observe any "U-turns" in our dataset. The closest match are tight vortices, such that they could be seen as "U-turn" if observed at a lower resolution and with the addition of experimental noise. It is however possible that "U-turns" fit the criterion based on local energy transfer but not the one based on local Hölder exponents, hence they are not detected in our case. It is also possible that "U-turns" correspond to an earlier phase in the development of a quasi singularity, such that the local Hölder exponent is too high to be detected by our method. Finally, it could also be a different structure appearing at higher Reynolds number. If the last hypothesis is true, we would not be able to study this type of event through the simulations performed in this thesis.

Among the recurrent features of the events observed is an asymmetry of the vortices. This asymmetry is particularly manifest in figure 4.22, where the isosurfaces of vorticity are compressed in a pancake shape. This shape is shared by the isosurfaces of Hölder exponent, and the isosurfaces of D_I^ℓ and D_ν^ℓ appear as pairs of

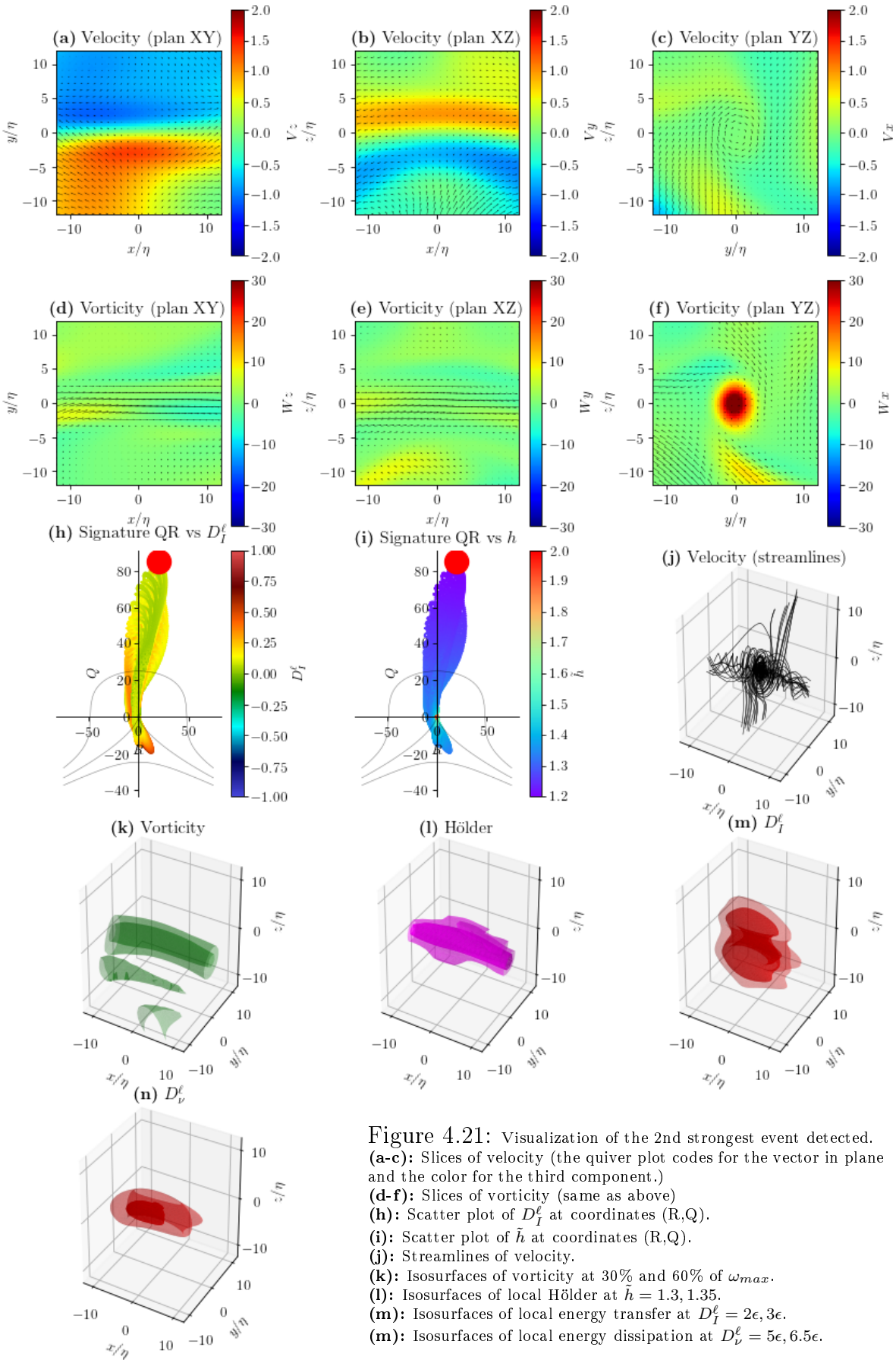

Figure 4.21: Visualization of the 2nd strongest event detected.
(a-c): Slices of velocity (the quiver plot codes for the vector in plane and the color for the third component.)
(d-f): Slices of vorticity (same as above)
(h): Scatter plot of D_I^ℓ at coordinates (R,Q).
(i): Scatter plot of $\tilde{h}$ at coordinates (R,Q).
(j): Streamlines of velocity.
(k): Isosurfaces of vorticity at 30% and 60% of ω_{max}.
(l): Isosurfaces of local Hölder at $\tilde{h} = 1.3, 1.35$.
(m): Isosurfaces of local energy transfer at $D_I^\ell = 2\epsilon, 3\epsilon$.
(m): Isosurfaces of local energy dissipation at $D_\nu^\ell = 5\epsilon, 6.5\epsilon$.

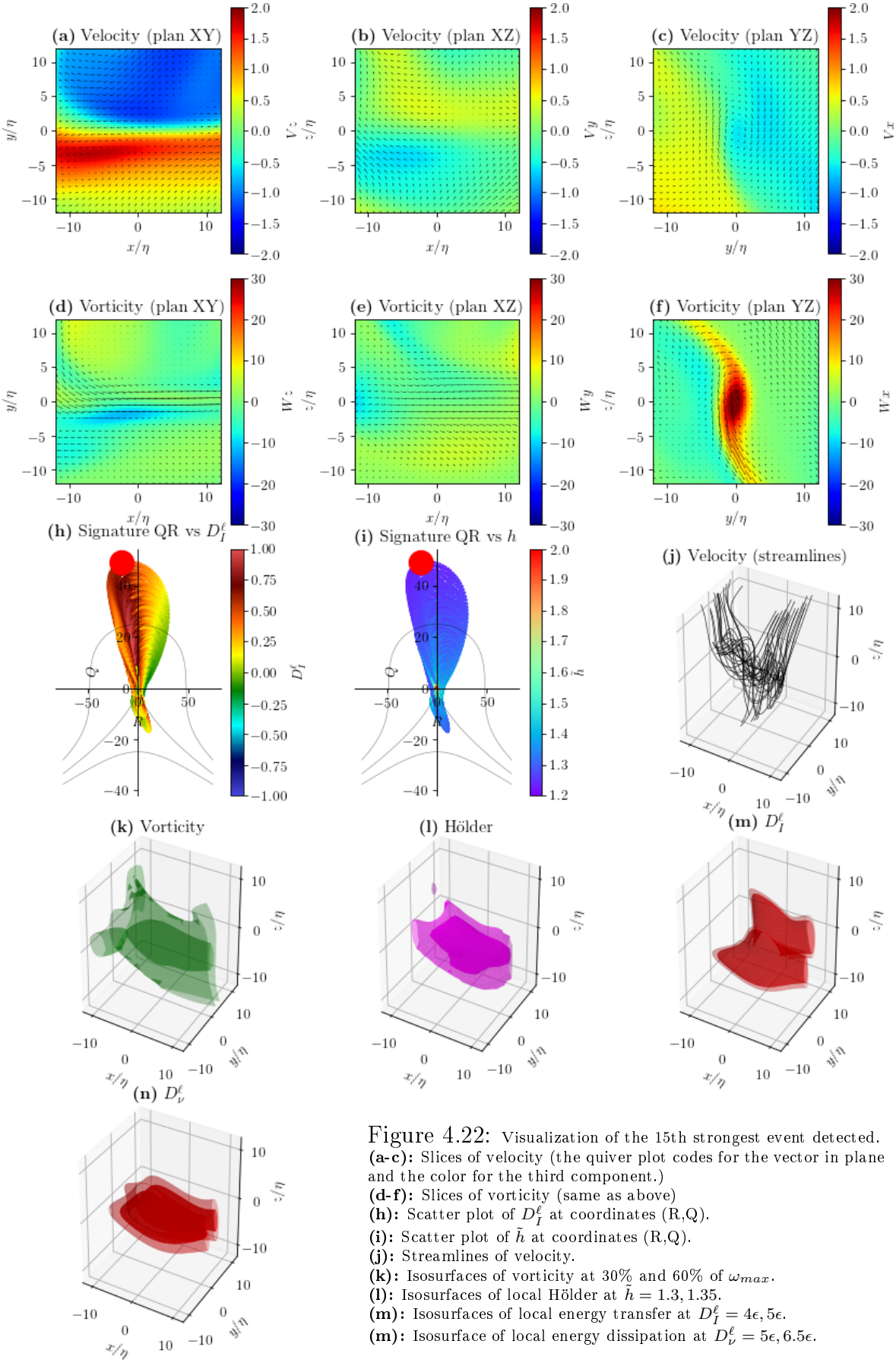

Figure 4.22: Visualization of the 15th strongest event detected.
(a-c): Slices of velocity (the quiver plot codes for the vector in plane and the color for the third component.)
(d-f): Slices of vorticity (same as above)
(h): Scatter plot of D_I^ℓ at coordinates (R,Q).
(i): Scatter plot of $\tilde{h}$ at coordinates (R,Q).
(j): Streamlines of velocity.
(k): Isosurfaces of vorticity at 30% and 60% of ω_{max}.
(l): Isosurfaces of local Hölder at $\tilde{h} = 1.3, 1.35$.
(m): Isosurfaces of local energy transfer at $D_I^\ell = 4\epsilon, 5\epsilon$.
(m): Isosurface of local energy dissipation at $D_\nu^\ell = 5\epsilon, 6.5\epsilon$.

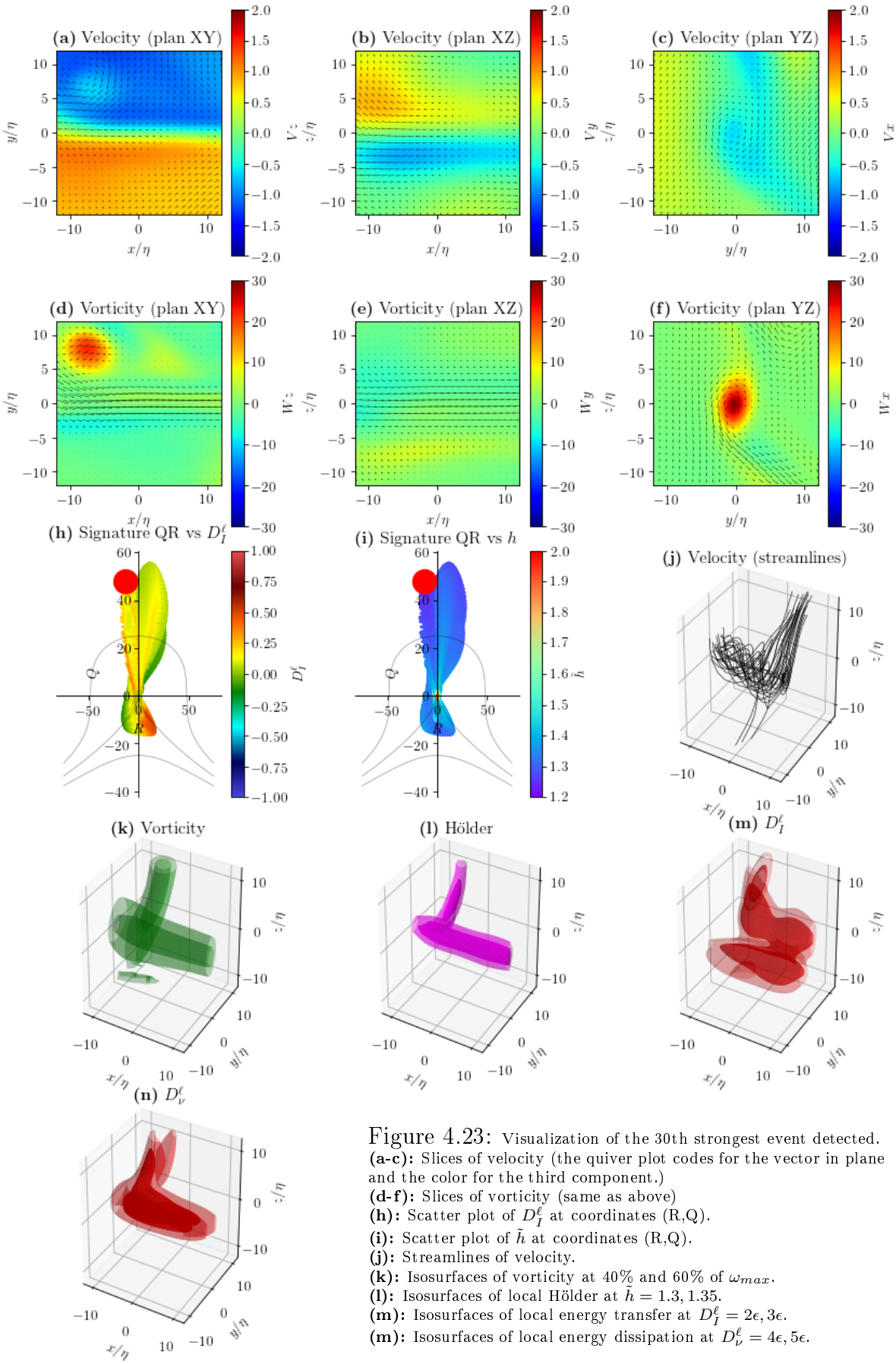

Figure 4.23: Visualization of the 30th strongest event detected.
(a-c): Slices of velocity (the quiver plot codes for the vector in plane and the color for the third component.)
(d-f): Slices of vorticity (same as above)
(h): Scatter plot of D_I^ℓ at coordinates (R,Q).
(i): Scatter plot of $\tilde{h}$ at coordinates (R,Q).
(j): Streamlines of velocity.
(k): Isosurfaces of vorticity at 40% and 60% of ω_{max}.
(l): Isosurfaces of local Hölder at $\tilde{h} = 1.3, 1.35$.
(m): Isosurfaces of local energy transfer at $D_I^\ell = 2\epsilon, 3\epsilon$.
(m): Isosurfaces of local energy dissipation at $D_\nu^\ell = 4\epsilon, 5\epsilon$.

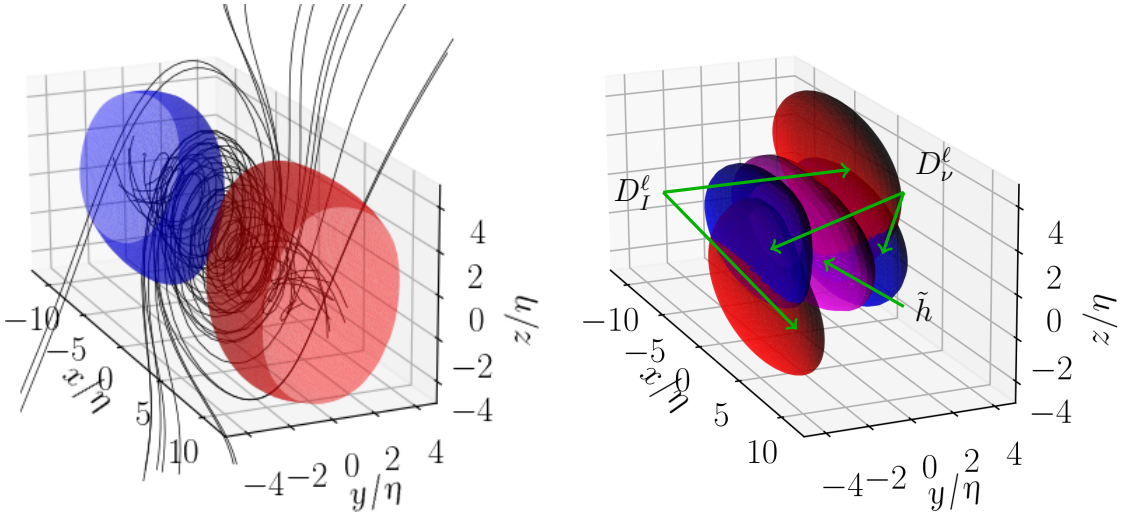

(a) (b)

Figure 4.24: (a): Streamlines of velocity. The axial velocity is oriented away from the $x = 0$ plane. The red (resp. blue) isosurface corresponds to an helicity of $H = 2.5$ (resp. $H = -2.5$). (b): The magenta isosurface corresponds to the local Hölder exponent $\tilde{h} = 1.35$. The red isosurface corresponds to $D_I^\ell = 2\epsilon$. The blue isosurface corresponds to $D_\nu^\ell = 4\epsilon$.

pancakes sandwiching the event. This reminds the behavior observed by Vincent and Meneguzzi [72]. In this study, the authors remark that regions of high vorticity are pancake like at their apparition, before bending and rolling up. A connection between this process and the energy cascade is also made. This could explain why the event in figure 4.22 features higher values of D_I^ℓ than the others. For this to occur at a scale of $\ell = 1.8\eta$ might be another hint of a structure carrying energy below the Kolmogorov scale.

4.3.3 Typical event

Having extracted a large amount of extreme irregular events, we can try to average them in order to obtain a "typical event". This is made possible by the fact all events have been reoriented along the same axis. This is also justified by the fact that most events detected share a similar structure of "roll vortex". Exceptions are composed of events happening close to each other, leading to complex streamlines pattern. However, in order to avoid introducing any bias in the average, we do not perform any filtering of the events. As the complex, non categorized events do not have clear common features, we expect them to not contribute too much in the average.

The average is taken over all 213 most singular events extracted. As a reminder,

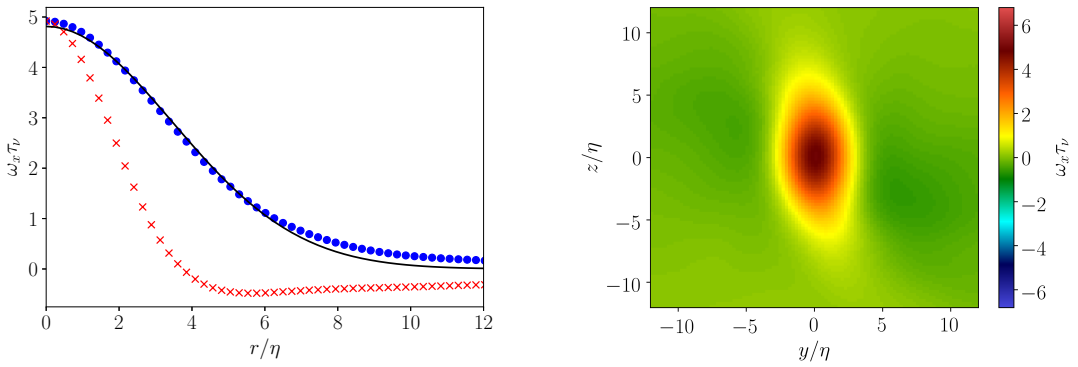

(a) (b)

Figure 4.25: (a) Fit of the component of the vorticity ω_x in the $x = 0$ plane for the averaged event. The vorticity along the z (resp. y) direction is represented with blue circles (resp. red crosses) while the Burgers fit is shown as a black continuous curve. (b) Colormap of the component of the vorticity ω_x in the $x = 0$ plane for the averaged event.

this corresponds to all events with a local Hölder exponent $\tilde{h} < 1.3$. Visualizations of the averaged event are provided in figure 4.24. Note that the quantities displayed are the averaged values of the exponent $\tilde{h}$, the energy transfer D_I^ℓ and the energy dissipation D_ν^ℓ. As those scalars are not linear functions of the velocity, they do not correspond to the quantities that would be computed from the averaged velocity field, materialized by the streamlines.

The pattern of streamlines for the averaged event corresponds to the roll vortices, which emphasizes the prevalent character of this type of structure among extremely singular events. As expected, averaging over many events completely removed the contribution of the large scale velocity, such that the helicity changes sign at the $x = 0$ plane corresponding to the minimum of Hölder exponent. From this structure one might recognize a Burgers vortex. This type of uniformly stretched vortex has been defined by [10] and it is characterized by its vorticity profile:

$$\omega_x(r) = \frac{\Gamma}{2\pi\nu} \exp\left(-\frac{\sigma r^2}{2\nu}\right). \tag{4.4}$$

This profile can be fitted over the vorticity of the averaged event in the plane $x = 0$. This yields $\Gamma = 5\tau_\nu$ and $\sigma = 0.36$. While the fit is accurate in the z direction, as shown in figure 4.25a, it fails in the y-direction. Because the x component of the vorticity actually changes sign, this fit cannot be fixed using the non axisymmetric Burger vortex profile. The figure 4.25b illustrates this asymmetry.

Likewise, the averaged D_I^ℓ and D_ν^ℓ show a very strong non axisymmetry. The invariance by a rotation of π around the x-axis can be explained by the way the events are averaged. However, the presence of two structures of D_I^ℓ and D_ν^ℓ on either side of the main axis is also observed in individual events (see figures 4.21 to 4.23). In order to interpret this asymmetry of the averaged event, we can emit the hypothesis that extreme events result of the interaction between several vortices. In the process of averaging, only the main, most singular vortex was conserved. This hypothesis is supported by the presence of nearby vortices in several of the extracted events as can be seen in the example of figure 4.23. Under this hypothesis, the structures of vorticity could be similar to what is observed in the bridge of a vortex reconnection [73, 74]. In order to refine this hypothesis, we can use time resolved data. Indeed, it is not clear whether the snapshots that have been extracted are captured before, during or after the peak of the event, defined as the time at which the local Hölder exponent reaches its minimum.

4.3.4 Link with the energy transfers

The local energy transfer D_I^ℓ stays positive in the averaged event, even though strong negative energy transfers are observed in individual events. This means that while there are large fluctuations, on average, extreme singular events transfer energy to the smaller scale. Furthermore, we observe that, at the scale $\ell = 1.8\eta$, the average of the dissipative term D_ν^ℓ in the typical event is slightly stronger than the average of the energy transfer term D_I^ℓ. Using the discussion from Chapter 2, this means that events used in this average are observed approximately at the scale at which they get regularized by viscosity. Note that as the study has been performed very close to the Kolmogorov scale, the Duchon Robert term D_I^ℓ is likely still comparable to the dissipative term D_ν^ℓ at $\ell = \eta$. This implies a contribution to the energy budget which would not have been captured if the cutoff scale for the simulation was the Kolmogorov scale.

Another observation that can be made on the averaged event is that the structures of D_I^ℓ and D_ν^ℓ are not on the same axis. From the point of view of the streamlines, the peak of energy transfer happens before the dissipation. This is not the effect of the averaging, as such structure is also observed in individual events (see figure 4.22).

4.4 Temporal evolution of an event.

The purpose of using a time resolved dataset is to try and uncover the generation mechanism for extreme events. In the time period covered by the time resolved part of the simulations, we found 11 events for which the minimum of local Hölder exponent is kept under the threshold of $\tilde{h} = 1.3$ for 10 snapshots or more. This corresponds to at least 3 eddy turnover times t_η. This very strict threshold keeps the number of events to analyze low. Indeed, analyzing time series of events is a lot more time consuming than what was done in the previous section.

The results support the hypothesis evoked previously: the extreme events of local Hölder exponent appear related to vortex interaction. Indeed, two or more vortices are observed for most of the events detected. One such event is illustrated at different times in figures 4.27 and 4.28. For this event, the structures of Hölder, energy transfer and energy dissipation start to appears in figure 4.27b, when the vortices are approaching each other. We recognize the structure of the typical event in figure 4.27d, as the vortex observed is deformed by another vortex coming from $z > 0$. This structure becomes more chaotic when the vortices further interact in figure 4.27e. For this particular event, the structure of strong energy dissipation D_ν^ℓ does not follow the structures of low Hölder exponents $\tilde{h}$ and high energy transfer D_I^ℓ in the second part of the interaction visualized in figure 4.28. The structures shown in figure 4.28 differ from the typical event obtained by averaging in figure 4.24. This might be the origin of the complex structures identified in the uncorrelated dataset. It is worth noting that the local Hölder exponents becomes greater than 1.3 before the reconnection is completed.

A timeline of the evolution of the scalars analyzed is given in figure 4.26. This event is particularly irregular, as the local Hölder exponent drops to almost $h = 1.2$. The rarity of the event can be visualized by how low this value is on figure 4.15.

From the time evolution of the event, the most singular moment happens during the interaction, as the vortices are close to each other, at the time corresponding to figure 4.27f. At this time, the vorticity and the energy dissipation reach their maximum, and the Hölder exponents reach their minimum. Interestingly, we observe that the energy transfer D_I^ℓ reaches its maximum slightly before the other scalars. This behavior is observed for multiple events. This coincides with the previous observation that regions of high energy transfer are located earlier on the streamlines of velocity. While this could be a hint toward the mechanism behind the formation of quasi singularities, we currently lack a physical explanation for

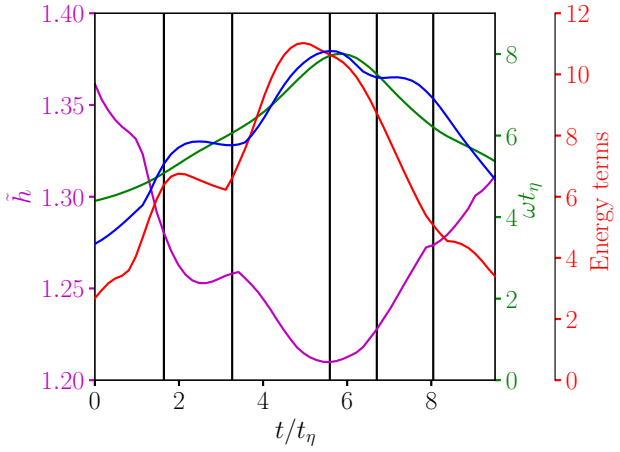

Figure 4.26: Time evolution of the local Hölder exponents (in magenta, left axis), the vorticity ωt_ν (in green, middle axis), the local energy transfer D_I^ℓ/ϵ (in red, rightmost axis) and the energy dissipation D_ν^ℓ/ϵ (in blue, rightmost axis). The vertical lines materializes the five snapshots represented in figures 4.27 and 4.28.

this behavior.

Finally, note that the local energy transfer reaches the same values as the dissipation term for this event. Again, according to the analysis from Chapter 2, this means that this event is susceptible to carry energy below the Kolmogorov scale.

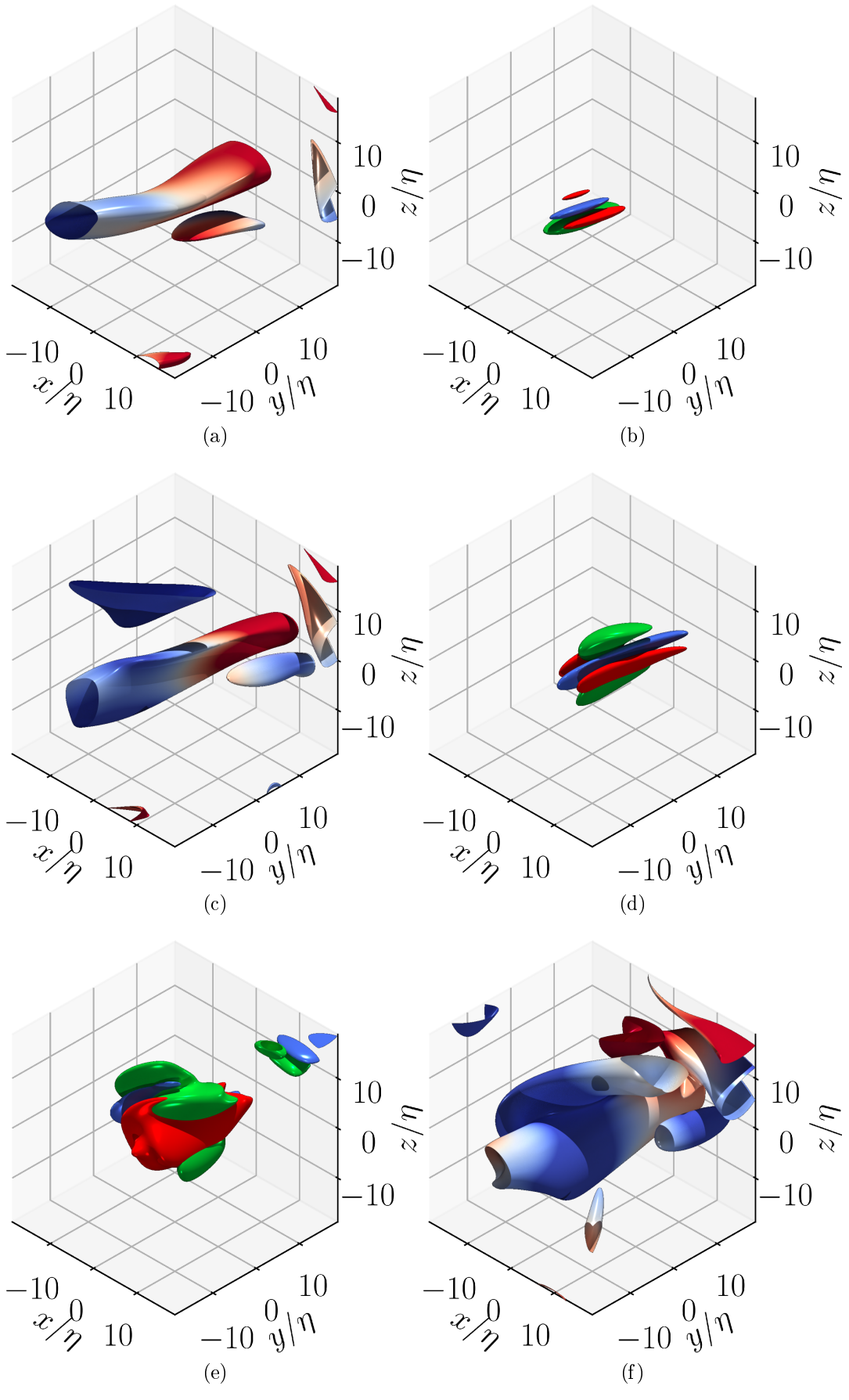

Figure 4.27: Snapshots of time resolved event: (a-b): Before the interaction. (c-d): Beginning of interaction. (e-f) Time of the minimum oh $\tilde{h}$. (a-c-e): Isosurfaces of vorticity $\omega t_\eta = 23$ colored in red and blue respectively for positive and negative helicity. (b-d-f) Isosurface $h = 1.3$ in blue, $D_I^\ell/\epsilon = 4$ in red, $D_\nu^\ell/\epsilon = 6$ in green.

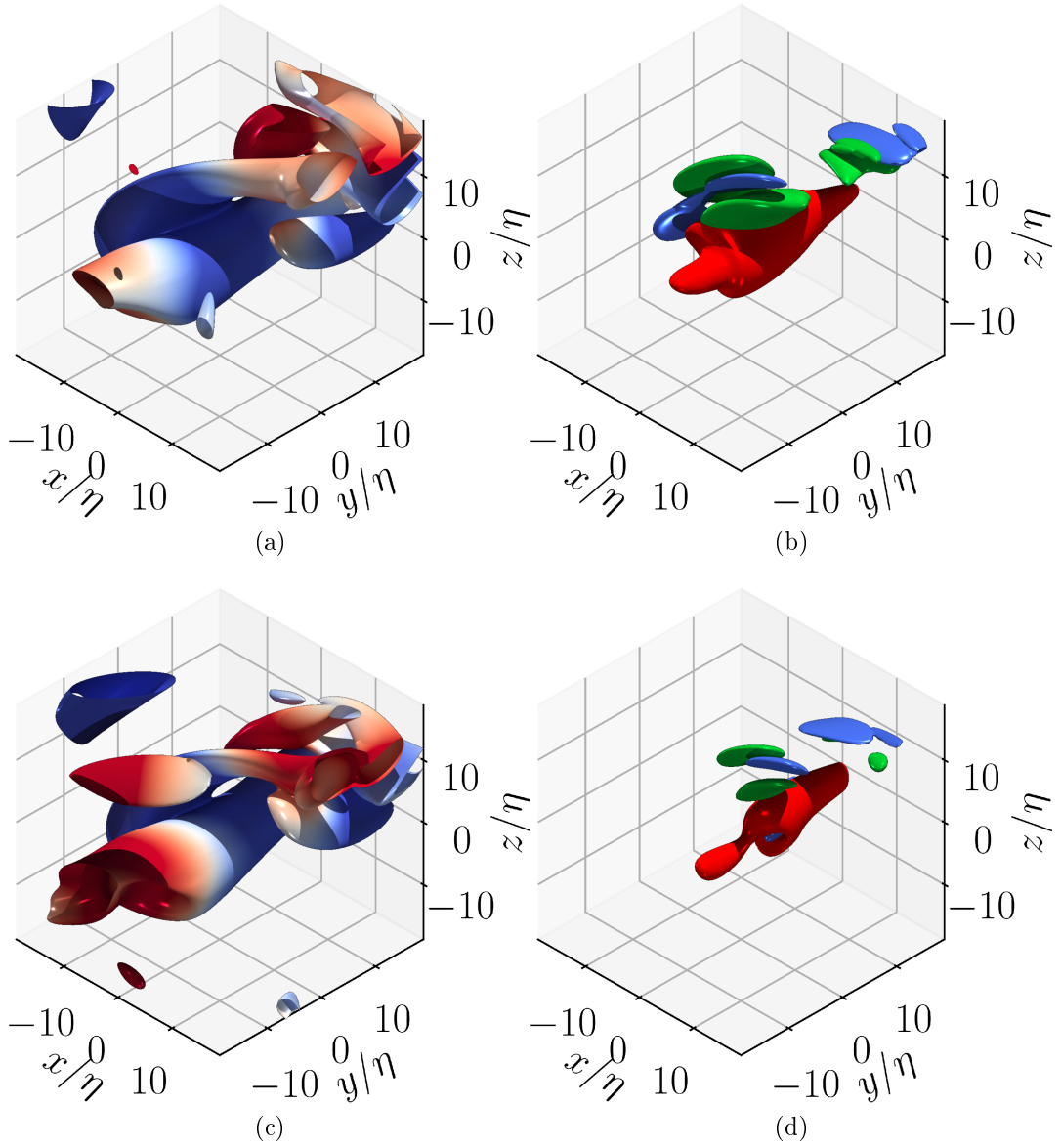

Figure 4.28: Snapshots of time resolved event: (a-b): Toward the end of interaction. (c-d): Slightly before the local Hölder exponent $\tilde{h}$ grows back above 1.3. (a-c): Isosurfaces of vorticity $\omega t_\eta = 23$ colored in red and blue respectively for positive and negative helicity. (b-d) Isosurface $h = 1.3$ in blue, $D_I^\ell/\epsilon = 4$ in red, $D_\nu^\ell/\epsilon = 6$ in green.

Chapter 5

A PIC simulation method using the Clebsch decomposition

The method exposed in the previous chapters allows us to localize potential singularities of Navier–Stokes in turbulent velocity fields. Because of the relatively low Reynolds number at which the method has been used, we are unable to follow those structures very far in scale. The objective of this chapter is to try and develop a new numerical method for Navier–Stokes simulations based on a Particles in Cells (PIC) method. This would allow us to use much smaller viscosity and potentially follow singular events much farther in scale. The general construction of this chapter is widely inspired from the thesis of Jean-Philippe Laval [44], who developed a PIC method for Navier–Stokes. The original method relies on particles of vorticity advected by the large scale velocity in order to model the small scales of the flow. In this chapter, we use the Clebsch decomposition of the velocity field to exhibit scalars field that can fulfill the same role as vorticity did. We then lay the basis for the simulation model using those scalars for the PIC method.

5.1 Motivations

In addition to the considerations for the simulations of singularities, the trigger for the work performed in this chapter comes from three publications, respectively by Yoshida and Morrison [76], Cartes et al. [12] and Ohkitani and Constantin [60]. Among those, the first one is dedicated to an analysis of the topology of the flow, while the two others develop simulation methods for Navier–Stokes. The common point of these papers is the usage of a *Clebsch parameterization* of the velocity field, also known as the *Weber-Clebsch representation*. This method decomposes

the initial vector field into several scalar fields, for which the evolution equations can be derived. Using the reasoning reproduced in section 5.4.1, these papers show that the evolution equations for these scalar fields are similar to the equation of diffusion of a passive scalar. This makes this scalar fields good candidate to the use of a PIC method: we expect to be able to model the small scales of the flow by particles carrying the information of the scalar fields passively advected by the large scale flow. This bears great similarity with the work performed by Laval[44]. In his thesis, Laval models 2D turbulence using a PIC method using the equation for vorticity. However, the approach used can not be generalized to the 3D equations of vorticity. The advantage of a method using the Clebsch parameterization over this previous work is that it would ba applicable to the 3D Navier–Stokes equation.

5.2 Decomposition between large scales and small scales

As a prerequisite to develop the new PIC method, we recall the Navier–Stokes equations in vector form:

$$\partial_t \boldsymbol{u} + (\boldsymbol{u} \cdot \nabla)\boldsymbol{u} = -\frac{1}{\rho}\nabla p + \nu \Delta \boldsymbol{u} + \boldsymbol{f} \tag{5.1}$$

$$\nabla \cdot \boldsymbol{u} = 0 \tag{5.2}$$

As expressed before, the general idea behind the PIC method is to decompose the velocity field into large scales and small scales. The large scales are to be simulated using a classical numerical method, while the small scales are to be approximated by particles advected by the large scales. Formally, the decomposition is as follow:

$$\boldsymbol{U}(\boldsymbol{x}) = \bar{\boldsymbol{u}}(\boldsymbol{x}) = \int G(\boldsymbol{x} - \boldsymbol{x}')\boldsymbol{u}(\boldsymbol{x}')\mathrm{d}\boldsymbol{x}', \tag{5.3}$$

$$\boldsymbol{u}'(\boldsymbol{x}) = \boldsymbol{u}(\boldsymbol{x}) - \boldsymbol{U}(\boldsymbol{x}). \tag{5.4}$$

Applying the filter on equation (5.1) yields:

$$\partial_t \boldsymbol{U} + \overline{(\boldsymbol{u} \cdot \nabla)\boldsymbol{u}} = -\frac{1}{\rho}\nabla P + \nu \Delta \boldsymbol{U} + \boldsymbol{F} \tag{5.5}$$

In a way not dissimilar to Large Eddy Simulations, this equation will be integrated while approximating the term $\overline{(\boldsymbol{u} \cdot \nabla)\boldsymbol{u}}$ thanks to the small scales. For this purpose, we get the small scale equation by subtracting equation (5.5) from

equation (5.1). This leads to:

$$\partial_t \boldsymbol{u}' + (\boldsymbol{u}\cdot\nabla)\boldsymbol{u} - \overline{(\boldsymbol{u}\cdot\nabla)\boldsymbol{u}} = -\frac{1}{\rho}\nabla p' + \nu\Delta\boldsymbol{u}' + \boldsymbol{f}' \tag{5.6}$$

At this point we need to make some hypothesis in order to simplify the equations. Those hypothesis are based on two little parameters. The first one is based on the ratio between the large scales L and the small turbulent structures l: $\epsilon = l/L$. The other one is based on the ratio between the characteristic time associated to the turbulent scales τ and the characteristic time associated to the large scales T (estimated as $T = 1/\nabla U$) : $\eta = \tau/T$. Using the results from Dubrulle Nazarenko [18], we take the hypothesis $\epsilon \lesssim 1/\eta \ll 1$.

Applying dimensional analysis to the non linear terms and taking $(\boldsymbol{U}\cdot\nabla)\boldsymbol{U}$ as a reference, we have in orders of magnitude:

$$\begin{aligned}
&(\boldsymbol{U}\cdot\nabla)\boldsymbol{u}' \sim 1/(\epsilon\eta) \quad && (\boldsymbol{U}\cdot\nabla)\boldsymbol{U}\\
&(\boldsymbol{u}'\cdot\nabla)\boldsymbol{U} \sim \epsilon/\eta && (\boldsymbol{U}\cdot\nabla)\boldsymbol{U}\\
&(\boldsymbol{u}'\cdot\nabla)\boldsymbol{u}' \sim 1/\eta^2 && (\boldsymbol{U}\cdot\nabla)\boldsymbol{U}
\end{aligned}$$

Keeping only the dominant terms, equations (5.5) and (5.6) reduce to:

$$\partial_t \boldsymbol{U} + \overline{(\boldsymbol{U}\cdot\nabla)\boldsymbol{U}} = -\frac{1}{\rho}\nabla P + \nu\Delta\boldsymbol{U} + \boldsymbol{F}_{forcing} + \boldsymbol{F}_{small\to large} \tag{5.7}$$

$$\partial_t \boldsymbol{u}' + (\boldsymbol{U}\cdot\nabla)\boldsymbol{u}' = -\frac{1}{\rho}\nabla p' + \nu\Delta\boldsymbol{u}' + \boldsymbol{F}_{large\to small} \tag{5.8}$$

with:

$$\boldsymbol{F}_{small\to large} = -\overline{(\boldsymbol{U}\cdot\nabla)\boldsymbol{u}'} \tag{5.9}$$

$$\boldsymbol{F}_{large\to small} = \overline{(\boldsymbol{U}\cdot\nabla)\boldsymbol{U}} - (\boldsymbol{U}\cdot\nabla)\boldsymbol{U} + \overline{(\boldsymbol{U}\cdot\nabla)\boldsymbol{u}'}. \tag{5.10}$$

The approximations realized here have already been verified in [44].

On the other hand, applying the decomposition between large and small scales to the incompressibility equation (5.2) yields:

$$\nabla\cdot\boldsymbol{U} = 0 \qquad \text{and} \tag{5.11}$$

$$\nabla\cdot\boldsymbol{u}' = 0. \tag{5.12}$$

5.3 Algorithm for the large scales

For this model, the large scales can be simulated using a conventional algorithm, similar to what is used for LES simulations. Our choice in this case is to use a spectral code, as it has the merit of simplicity.

In order to derive the equations for the spectral method, we take the Fourier transform and solenoidal projection of (5.7). Assuming the system is forced directly in the spectral space, this results in the following:

$$\partial_t \boldsymbol{U}(\boldsymbol{k},t) = -\nu \boldsymbol{k}^2 \boldsymbol{U}(\boldsymbol{k},t) + \boldsymbol{G}(\boldsymbol{k},t) + \boldsymbol{F}_{forcing}(\boldsymbol{k},t) \tag{5.13}$$

where $G(\boldsymbol{U})$ gathers the non linear terms:

$$\boldsymbol{G}(\boldsymbol{k},t) = FT(P_{sol}(-\overline{(\boldsymbol{U}\cdot\nabla)\boldsymbol{U}} + \boldsymbol{F}_{small\to large})) \tag{5.14}$$

where FT designate the Fourier transform and P_{sol} the solenoidal projection.

Putting the forcing aside and introducing $\widetilde{\boldsymbol{U}}(t) = e^{\nu k^2 t}\boldsymbol{U}(t)$, we get:

$$\partial_t \widetilde{\boldsymbol{U}}(\boldsymbol{k},t) = e^{\nu k^2 t} G(\boldsymbol{k},t). \tag{5.15}$$

This equation can be integrated numerically. One possible choice is to use a Runge-Kutta algorithm. For a time step of Δt, this would give:

$$\widetilde{\boldsymbol{U}}(\boldsymbol{k},t+\Delta t) - \widetilde{\boldsymbol{U}}(\boldsymbol{k},t) = \Delta t e^{\nu k^2 (t+\Delta t/2)} \boldsymbol{G}(\boldsymbol{k},t+\Delta t/2). \tag{5.16}$$

Going back to the original variables, the integration scheme is the following:

$$\boldsymbol{U}(\boldsymbol{k},t+\Delta t) = e^{-\nu k^2 \Delta t}\boldsymbol{U}(\boldsymbol{k},t) + \Delta t e^{-\nu k^2 \Delta t/2}\boldsymbol{G}(\boldsymbol{k},t+\Delta t/2) \tag{5.17}$$

where the computation of $G(\boldsymbol{k},t+\Delta/2)$ will require the use of:

$$\boldsymbol{U}(\boldsymbol{k},t+\Delta t/2) = e^{-\nu k^2 \Delta t/2}\Big(\boldsymbol{U}(\boldsymbol{k},t) + \frac{\Delta t}{2}\boldsymbol{G}(\boldsymbol{k},t)\Big). \tag{5.18}$$

As a result, the core of the model consists in evaluating the non linear term $\boldsymbol{G}$ with a good balance of accuracy and efficiency. This prominently factor the retro-action from the small scales to the large scales $\boldsymbol{F}_{small\to large}$.

The forcing can be added every time step simply as follow:

$$\boldsymbol{U}_{forced}(\boldsymbol{k},t+\Delta t) = \boldsymbol{U}(\boldsymbol{k},t+\Delta t) + \Delta t \boldsymbol{F}_{forcing}(\boldsymbol{k},t). \tag{5.19}$$

5.4 Equations for small scales

In this section, we derive the equations governing the small scales that will be implemented in a PIC model. This will eventually lead to the computation of the small scale contribution to the non linear term $\boldsymbol{G}$.

5.4.1 Clebsch decomposition

Deriving the equations with viscosity massively increases the complexity of the computation. This work has been done, in particular in [12], but the resulting equations are less suitable to a PIC method than in the inviscid case. For the time being, we consider the inviscid equation without the large scale contribution:

$$\partial_t \boldsymbol{u}' + (\boldsymbol{U} \cdot \nabla)\boldsymbol{u}' = -\frac{1}{\rho}\nabla p'. \tag{5.20}$$

Making the Particles of our Particles in Cells model not dissipative also participates in our overall objective of trying to observe singular behaviors. Indeed, this means that the small scales quantities will follow Euler's equations, and potentially transport energy to arbitrarily small scales.

The Clebsch decomposition is introduced by:

$$\boldsymbol{u}' = -\nabla\phi + \sum_{\alpha=1}^{p} \lambda_\alpha \nabla \mu_\alpha. \tag{5.21}$$

In this equation, ϕ is a scalar field working exactly as the potential in the Helmholtz decomposition. The specificity of the Clebsch decomposition comes from the scalar fields λ_α and μ_α for $\alpha = 1..p$. As we are working in 3 dimensions, a result by Yoshida [75] guarantees the existence of such scalar fields for $p \geqslant 2$. There is however no unicity of the decomposition.

Injecting the equation (5.21) into (5.20) gives:

$$\sum_{\alpha}^{p} \left(\frac{D\lambda_\alpha}{Dt}\nabla\mu_\alpha - \frac{D\mu_\alpha}{Dt}\nabla\lambda_\alpha \right) - \nabla\left(\frac{D\phi}{Dt} - \sum_{\alpha}^{p} \frac{D\mu_\alpha}{Dt}\lambda_\alpha \right) - \boldsymbol{u}' \cdot (\nabla \boldsymbol{U}) = -\frac{1}{\rho}\nabla p' \tag{5.22}$$

where we use the material derivative $\frac{D}{Dt} = \partial_t + (\boldsymbol{U} \cdot \nabla)$, computed using the large scale velocity. In this equation, the term colored in red is of the same order as $(\boldsymbol{u}' \cdot \nabla)\boldsymbol{U}$ which has already been neglected in the previous section, so we neglect it again.

For this equation to be satisfied, a sufficient but not necessary condition is:

$$\frac{D\lambda_\alpha}{Dt} = 0 \tag{5.23}$$

$$\frac{D\mu_\alpha}{Dt} = 0 \tag{5.24}$$

$$\frac{D\phi}{Dt} = \frac{p'}{\rho} \tag{5.25}$$

Combined with the non unicity of the scalar fields λ_α and μ_α in the Clebsch decomposition, we can afford to impose these conditions. The equations (5.23) and (5.24) are particularly interesting as it means the scalar fields can be portrayed as "passively" advected by the large scale velocity. This description is inaccurate as the model we develop here does include a retro-action on the large scale velocity, as described in the section 5.5.5. In this aspect, it is a situation strikingly similar to how the small scale vorticity is "passively" advected by the large scale in Laval's thesis [44]. This similarity is what lead us to try and develop a PIC based method, where the scalar fields λ_α and μ_α are decomposed into particles advected by the large scale velocity.

Supposing that the scalar fields λ_α and μ_α are known, we can recover the potential field ϕ using the incompressibility condition. Indeed, applying the Clebsch decomposition from equation (5.21) to the equation (5.12) yields:

$$\Delta\phi = \sum_\alpha^p \nabla \cdot (\lambda_\alpha \nabla \mu_\alpha). \tag{5.26}$$

This means we can avoid integrating the equation (5.25), and thus that we don't have to keep track of the small scale pressure.

5.4.2 Filter function and Gabor transform

In order to progress further, the filtering needs to be formalized. The filter is defined as:

$$\boldsymbol{U}(\boldsymbol{X}, t) = \bar{\boldsymbol{u}}(\boldsymbol{x}, t) = \int f^2\left(\epsilon^\star(\boldsymbol{x} - \boldsymbol{x}')\right) \boldsymbol{u}(\boldsymbol{x}')\mathrm{d}\boldsymbol{x}' \tag{5.27}$$

where $\epsilon^\star$ is a small parameter differentiating the "slow" spatial variable $\boldsymbol{X} = \boldsymbol{x}/\epsilon'$ and the "fast" variable $\boldsymbol{x}$. The small parameter $\epsilon^\star$ is such that $1 \gg \epsilon^\star \gg \epsilon$. The function f is an odd function with a fast decay toward infinity and a norm unity, i.e. $\int f^2(\boldsymbol{x})\mathrm{d}\boldsymbol{x} = 1$. This ensures an intuitive behavior of the filtering when applied to constant functions. The choice of a f^2 instead of f does not change the

properties of the problem and will simplify later computations.

Additionally, we introduce the **Gabor transform** using the same function f:

$$GT\{\boldsymbol{u'}\}(\boldsymbol{x},\boldsymbol{k},t) = \hat{\boldsymbol{u}}'(\boldsymbol{x},\boldsymbol{k},t) = \int f\left(\epsilon^\star(\boldsymbol{x}-\boldsymbol{x'})\right) e^{i\boldsymbol{k}(\boldsymbol{x}-\boldsymbol{x'})}\boldsymbol{u'}(\boldsymbol{x'},t)\mathrm{d}\boldsymbol{x'}. \tag{5.28}$$

This operation bears striking similarities with continuous wavelet transforms, as it conveys information about both space and frequency. It is the principal factor by which the small scale scalar fields will be modelled by particles evolving in the space-frequency domain.

Similarly to the continuous wavelet transforms, this transformation can be inverted as follow:

$$\boldsymbol{u'}(\boldsymbol{x},t) = \frac{1}{(2\pi)^3 f(0)} \int \hat{\boldsymbol{u}}'(\boldsymbol{x},\boldsymbol{k},t)d\boldsymbol{k}. \tag{5.29}$$

All fields in physical space are real valued, which leads to:

$$\begin{aligned} \hat{\boldsymbol{u}}'(\boldsymbol{x},-\boldsymbol{k},t) &= \hat{\boldsymbol{u}}'(\boldsymbol{x},\boldsymbol{k},t)^* \\ \hat{\lambda_\alpha}(\boldsymbol{x},-\boldsymbol{k},t) &= \hat{\lambda_\alpha}(\boldsymbol{x},\boldsymbol{k},t)^* \\ \hat{\mu_\alpha}(\boldsymbol{x},-\boldsymbol{k},t) &= \hat{\mu_\alpha}(\boldsymbol{x},\boldsymbol{k},t)^* \end{aligned} \tag{5.30}$$

where the star denotes the complex conjugate.

Several properties of the Gabor transform will be required for later computations. Those properties are also demonstrated in [44] and these demonstrations are reported here for the sake of convenience. By using integration by part, one can show that the Gabor transform and spatial derivatives commute:

$$TG\{\partial_i \boldsymbol{u'}\}(\boldsymbol{x},\boldsymbol{k},t) = \partial_i \hat{\boldsymbol{u'}}(\boldsymbol{x},\boldsymbol{k},t). \tag{5.31}$$

The same term can also be expanded using the small parameter $\epsilon^\star$. Indeed, we have:

$$\begin{aligned} \partial_i \hat{\boldsymbol{u'}}(\boldsymbol{x},\boldsymbol{k},t) &= \partial_i \int f\left(\epsilon^\star(\boldsymbol{x}-\boldsymbol{x'})\right) e^{i\boldsymbol{k}(\boldsymbol{x}-\boldsymbol{x'})}\boldsymbol{u'}(\boldsymbol{x'},t)\mathrm{d}\boldsymbol{x'} \\ &= ik_i \hat{\boldsymbol{u'}}(\boldsymbol{x},\boldsymbol{k},t) + \epsilon^\star \int f'\left(\epsilon^\star(\boldsymbol{x}-\boldsymbol{x'})\right) e^{i\boldsymbol{k}(\boldsymbol{x}-\boldsymbol{x'})}\boldsymbol{u'}(\boldsymbol{x'},t)\mathrm{d}\boldsymbol{x'} \\ &= ik_i \hat{\boldsymbol{u'}}(\boldsymbol{x},\boldsymbol{k},t) + O(\epsilon^\star) \end{aligned} \tag{5.32}$$

5.4.3 Main equations for the small scale velocity

The objective in this part is to derive the equations for the Gabor transformed scalar fields $\hat{\lambda_\alpha}$ and $\hat{\mu_\alpha}$ which would then be used as basis for the PIC model.

For this purpose, we apply the Gabor transform to equation (5.23). In the following Einstein summation convention for repeated indices is used:

$$\partial_t \hat{\lambda_\alpha} + GT\{U_j \partial_j \lambda_\alpha\} = 0. \tag{5.33}$$

We need to compute the Gabor transform of a product of a small scale quantity and a large scale quantity:

$$GT\{U_j \partial_j \lambda_\alpha\}(\boldsymbol{x}, t) = \int f\left(\epsilon^\star(\boldsymbol{x} - \boldsymbol{x'})\right) e^{i\boldsymbol{k}(\boldsymbol{x}-\boldsymbol{x'})} U_j(\boldsymbol{x'}, t) \partial_j \lambda_\alpha(\boldsymbol{x'}, t) \mathrm{d}\boldsymbol{x'}. \tag{5.34}$$

As the large scale quantity U is slowly varying compared to f, we perform a Taylor expansion of U around $\boldsymbol{x'}$:

$$U_j(\boldsymbol{x'}, t) = U_j(\boldsymbol{x}, t) + (\boldsymbol{x} - \boldsymbol{x'}) \cdot \nabla U_j(\boldsymbol{x}, t) + O((\boldsymbol{x'} - \boldsymbol{x})^2). \tag{5.35}$$

As such:

$$\begin{aligned}
&GT\{U_j \partial_j \lambda_\alpha\}(\boldsymbol{x}, t) \\
\approx &U_j(\boldsymbol{x}, t) GT\{\partial_j \lambda_\alpha\}(\boldsymbol{x}, t) \\
&+ \partial_l U_j(\boldsymbol{x}, t) \int f\left(\epsilon^\star(\boldsymbol{x} - \boldsymbol{x'})\right) e^{i\boldsymbol{k}(\boldsymbol{x}-\boldsymbol{x'})} (x_l - x'_l) \partial_j \lambda_\alpha(\boldsymbol{x'}, t) \mathrm{d}\boldsymbol{x'} \\
\approx &U_j(\boldsymbol{x}, t) GT\{\partial_j \lambda_\alpha\}(\boldsymbol{x}, t) + i \partial_l U_j(\boldsymbol{x}, t) \frac{\partial}{\partial k_l} GT\{\partial_j \lambda_\alpha\}.
\end{aligned} \tag{5.36}$$

Finally, using the propriety from equation (5.32), we have:

$$\begin{aligned}
0 = \partial_t \hat{\lambda_\alpha} + GT\{U_j \partial_j \lambda_\alpha\} &\approx \partial_t \hat{\lambda_\alpha} + U_j \partial_j \hat{\lambda_\alpha} + i \partial_l U_j \frac{\partial}{\partial k_l} (i k_j \hat{\lambda_\alpha}) \\
&\approx \partial_t \hat{\lambda_\alpha} + U_j \partial_j \hat{\lambda_\alpha} - \partial_l U_j k_j \frac{\partial}{\partial k_l} \hat{\lambda_\alpha} - \cancel{\hat{\lambda_\alpha} \partial_j U_j}
\end{aligned} \tag{5.37}$$

The term $\partial_j U_j$ is removed as a consequence of incompressibility from equation (5.11).

The exact same process can be applied to the equation (5.24). As a result, we

have the main equations for the Gabor transformed scalar fields $\hat{\lambda_\alpha}$ and $\hat{\mu_\alpha}$:

$$D_t\hat{\lambda_\alpha}(\boldsymbol{x},\boldsymbol{k},t) = 0, \tag{5.38}$$

$$D_t\hat{\mu_\alpha}(\boldsymbol{x},\boldsymbol{k},t) = 0, \tag{5.39}$$

with :

$$D_t = \partial_t + \dot{\boldsymbol{x}}\cdot\nabla + \dot{\boldsymbol{k}}\cdot\nabla_k, \tag{5.40}$$

$$\dot{\boldsymbol{x}} = \nabla_k\Phi, \tag{5.41}$$

$$\dot{\boldsymbol{k}} = -\nabla\Phi, \tag{5.42}$$

$$\Phi = \boldsymbol{U}\cdot\boldsymbol{k}. \tag{5.43}$$

5.5 Implementation of a PIC method

The differential operator D_t from equations (5.38) and (5.39) can be interpreted as a material derivative in the space-frequency domain with a well chosen "velocity" directly defined from the large scale velocity $\boldsymbol{U}$. This way, the Gabor transformed scalar fields $\hat{\lambda_\alpha}$ and $\hat{\mu_\alpha}$ are interpreted as scalar transported in the space-frequency domain. The idea of the PIC model is to decompose the small scale scalars into particles with given position and wave vector that are advected independently using equation (5.40). The retro-action of the small scale on the large scale motion would then be a combination of the action of all individual particles, with the estimation being more precise the more particles there are.

Such computing method have been first developed for computing the dynamic of charged particles within a plasma and has been used effectively ever since [8]. Its use has been expanded to less straightforward application with no actual particle involved, for example by Nazarenko, Zabusky and Sheidegger in order to simulate the interaction between wave packet of sound and vortices [58]. It has also been used by Laval to simulate the transport of vorticity [44].

The expected advantage of such method over a direct numerical simulation is that an individual particle might represent much smaller scale for a meager computation cost compared to a refinement of the resolution.

In order to implement the PIC model, we will first discuss the definition of the particles and how they are related to the scalar fields $\hat{\lambda_\alpha}$ and $\hat{\mu_\alpha}$. We will then proceed to detail how those particles implement the different contributions of small scales on the large scales of the flow. This means implementing the forcing $\boldsymbol{F}_{large\to small}$ from equation (5.10) that large scales exert on small scales in the form of **creation of new particles**. We will then discuss the implementation of a

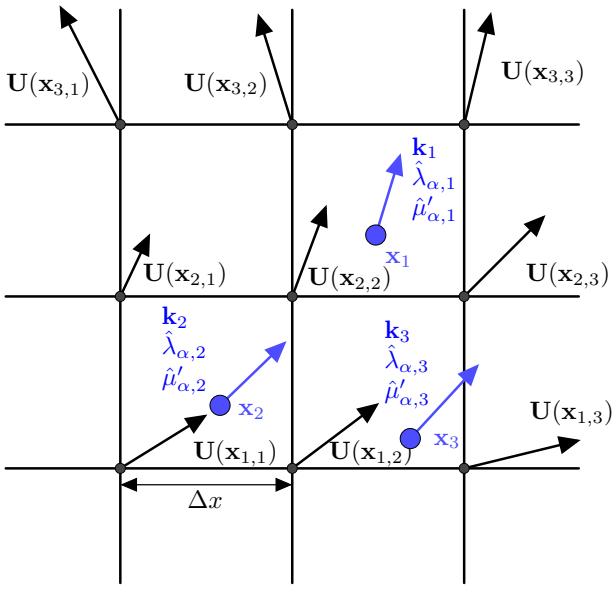

Figure 5.1: Schematic representation in 2D of the particles being advected by the large scale velocity.

numerical **dissipation** based on the removal of particles from the computations. The description of the implementation of the **advection** of particles will follow. Finally, we will explain how to derive the retro-action of the small scales on the large scales $\boldsymbol{F}_{small \to large}$ using the particles.

5.5.1 Definition of the particles

Let us suppose that the small scale scalar fields $\hat{\lambda_\alpha}$ et $\hat{\mu i_\alpha}$ are decomposed into N_p particles characterised by:

$$\begin{cases} \boldsymbol{x}_n & \text{the posistion of the particle,} \\ \boldsymbol{k}_n & \text{its corresponding wave vector (3D),} \\ \hat{\lambda}_{\alpha,n} & \text{the complex amplitudes for the } \lambda \text{ fields,} \\ \hat{\mu}_{\alpha,n} & \text{the complex amplitudes for the } \mu \text{ fields.} \end{cases}$$

The decomposition has to be such that the scalar fields can be reconstructed as follow:

$$\hat{\lambda_\alpha}(\boldsymbol{x}, \boldsymbol{k}, t) = \sum_{n=1}^{N_p} \hat{\lambda}_{\alpha,n} S_{\boldsymbol{x}}(\boldsymbol{x} - \boldsymbol{x}_n(t)) S_{\boldsymbol{k}}(\boldsymbol{k} - \boldsymbol{k}_n(t)). \tag{5.44}$$

where $S_{\boldsymbol{x}}$ et $S_{\boldsymbol{k}}$ are the interpolation functions for the PIC method.

By simplicity, we chose the interpolation function in the wave vector space

to be the Dirac function: $S_{\boldsymbol{k}}(\boldsymbol{k}) = \delta(\boldsymbol{k})$. This zero order function will spare us complications when dealing with particle interactions. For the interpolation function in space, we choose a simple first order interpolator:

$$S_{\boldsymbol{x}}(\boldsymbol{x}) = S_x(x) \times S_y(y) \times S_z(z), \tag{5.45}$$

where

$$S_x(x) = \begin{cases} dh - |x|/dh & \text{if } |x| < dh, \\ 0 & \text{otherwise.} \end{cases} \tag{5.46}$$

and likewise for S_y and S_x. We choose the parameter dh equal to the grid step for the large scales $dh = \Delta x$.

The figure 5.1 gives a representation of particles moving independently from the main simulation grid used for the large scales. In this representation, the field $\hat{\lambda}_\alpha$ at the point $\boldsymbol{x}_{2,2}$ can be reconstructed from the complex amplitudes carried by the particles numbered 1,2 and 3. With this choice of interpolation function $S_{\boldsymbol{x}}$, the reconstruction of a small scale field at a given node only depends on particles directly around the node. A higher order of interpolation might make the result more accurate, but the computational cost will be heavier.

One can observe that the equations (5.38) and (5.39) are symmetric under the transformation

$$\boldsymbol{k} \to -\boldsymbol{k}.$$

For our PIC model, it means that for every particle simulated, one can deduce the behaviour of a particle with the same position but opposite wave vector. In practice, it means we can simulate twice as many particles for the same cost. Let us assume we add N_p more particles to the system. We will distinguish pairs of particle with same position but opposite wave vector with a plus or minus index. The equation (5.44) then becomes:

$$\hat{\lambda_\alpha}(\boldsymbol{x}, \boldsymbol{k}, t) = \sum_{n=1}^{N_p} \big(\hat{\lambda}_{\alpha,n+}\delta(\boldsymbol{k}_n(t)) + \hat{\lambda}_{\alpha,n-}\delta(-\boldsymbol{k}_n(t))\big) S_{\boldsymbol{x}}(\boldsymbol{x} - \boldsymbol{x}_n(t)). \tag{5.47}$$

By taking the inverse Gabor transform of this equation using the formula (5.29), this results in:

$$\lambda_\alpha(\boldsymbol{x}, t) = \frac{1}{(2\pi)^3 f(0)} \sum_{n=1}^{N_p} \left(\hat{\lambda}_{\alpha,n+} + \hat{\lambda}_{\alpha,n-}\right) S_{\boldsymbol{x}}(\boldsymbol{x} - \boldsymbol{x}_n(t)). \tag{5.48}$$

Because the resulting scalar fields are real valued, this imposes $\hat{\lambda}_{n,\alpha+} = \hat{\lambda}^*_{n,\alpha-}$.In

the following, we drop the + index when there is no ambiguity. Adopting the notation $\Re[z]$ and $\Im[z]$ for respectively the real part and the imaginary part of a complex number z, the resulting equation is:

$$\lambda_\alpha(\boldsymbol{x},t) = \frac{2}{(2\pi)^3 f(0)} \sum_{n=1}^{N_p} \Re\left[\hat{\lambda}_{\alpha,n}\right] S_{\boldsymbol{x}}(\boldsymbol{x}-\boldsymbol{x}_n(t)). \tag{5.49}$$

Of course, the exact same reasonning can be applied for μ, leading to:

$$\mu_\alpha(\boldsymbol{x},t) = \frac{2}{(2\pi)^3 f(0)} \sum_{n=1}^{N_p} \Re\left[\hat{\mu}_{\alpha,n}\right] S_{\boldsymbol{x}}(\boldsymbol{x}-\boldsymbol{x}_n(t)) \tag{5.50}$$

When a spatial derivative is used, the property of the Gabor transform with respect to derivation (5.32) gives:

$$\partial_j \mu_\alpha(\boldsymbol{x},t) \approx \frac{-2}{(2\pi)^3 f(0)} \sum_{n=1}^{N_p} k_j \Im\left[\hat{\mu}_{\alpha,n}\right] S_{\boldsymbol{x}}(\boldsymbol{x}-\boldsymbol{x}_n(t)). \tag{5.51}$$

5.5.2 Forcing from the large scales: creation of particles

Similarly to the PIC method developed in the thesis of Laval, the effect of large scales on small scales is not modeled by interacting with the existing particles but by creating new particles. At this point, the equation for the small scales is as follows:

$$D_t \boldsymbol{u}' = -\frac{1}{\rho}\nabla p' + \boldsymbol{F}_{large\to small}. \tag{5.52}$$

The pressure term is already included in the dynamic of the particles. In order to model the contribution of the large scale to the small scales, we add at each time step particles corresponding to the velocity field $\boldsymbol{u}'_f = \Delta t \times \boldsymbol{F}_{large\to small}$, where Δt is the time step for the large scale simulation defined in section 5.4.

This is the opportunity to decide the number p of scalar fields used in the Clebsch decomposition, which has been left undetermined until now. We chose the value $p = 3$, which is also the value taken by Cartes et al. [12]. As this corresponds to the number of spatial dimensions, we adopt the same convention for the indices in the following.

This means that we can take the same choice as [12] for the Clebsch decomposition of $\boldsymbol{u}'_f$:

$$\lambda_i(\boldsymbol{x}) = u'_{fi}, \tag{5.53}$$

$$\mu_i(\boldsymbol{x}) = x_i. \tag{5.54}$$

This particular choice is inconvenient when using periodic boundary conditions. For this purpose, we set $\mu'_i(\boldsymbol{x}) = \mu_i(\boldsymbol{x}) - x_i$ and the complex amplitudes carried by the particle model will correspond to this new quantity μ'. Note that even if the μ_i are not periodic, their derivatives $\partial_j \mu_i$ are, so there is no problem for the decomposition of $\boldsymbol{u}'_f$ periodic.

From this change of variable, it entails that:

$$\hat{\mu'}_i(\boldsymbol{x}, \boldsymbol{k}) = \hat{\mu}_i(\boldsymbol{x}, \boldsymbol{k}) - \hat{x}_i(\boldsymbol{x}, \boldsymbol{k}). \tag{5.55}$$

This leads to:

$$\partial_j \hat{\mu'}_i(\boldsymbol{x}, \boldsymbol{k}) = \partial_j \hat{\mu}_i(\boldsymbol{x}, \boldsymbol{k}) - \delta_{ij} \hat{1}(\boldsymbol{x}, \boldsymbol{k}) \tag{5.56}$$

$$= \partial_j \hat{\mu}_i(\boldsymbol{x}, \boldsymbol{k}) - \delta_{ij} f(\boldsymbol{k}) \tag{5.57}$$

where $\hat{1}$ is the Gabor transform of the function unity, which is also the Fourier transform of the filter function $f(\boldsymbol{k})$.

The equation (5.39) becomes:

$$D_t \hat{\mu'_i}(\boldsymbol{x}, \boldsymbol{k}, t) = -U_i f(\boldsymbol{k}). \tag{5.58}$$

The fields λ and μ corresponding to this added velocity $\boldsymbol{u}'_f$ being determined, we needs to decompose these fields into particles to add to the system. A simple choice is to generate N^3 particles, indexed by n, with one particle at each node of the grid used for the simulation of the large scales. With the initial complex amplitude corresponding to the μ' fields being set at zero, we still need to determine the wave vectors $\boldsymbol{k}_n$ and the complex amplitudes $\hat{\lambda_{i,n}}$.

Applying equation (5.49) gives:

$$u'_{fi}(\boldsymbol{x}) = \frac{2}{(2\pi)^3 f(0)} \sum_{n=1}^{N^3} \Re\left[\hat{\lambda}_{\alpha,n}\right] S_{\boldsymbol{x}}(\boldsymbol{x} - \boldsymbol{x}_n). \tag{5.59}$$

By evaluating this formula at each grid point, the support of the interpolation function $S_{\boldsymbol{x}}$ is such that we have:

$$\Re\left[\hat{\lambda}_{i,n}\right] = \frac{(2\pi)^3 f(0)}{2} u'_{fi}(\boldsymbol{x}_n). \tag{5.60}$$

In order to obtain constraints on the wave vector $\boldsymbol{k}_n$ and the imaginary part of the complex amplitudes, one must use the derivatives of the velocity field $\boldsymbol{u}'_f$. Note that if we use a spectral method to simulate the large scales, those derivatives are exact quantities. By taking two components of the rotational $\boldsymbol{\omega}'_f = \nabla \times \boldsymbol{u}'_f$ as well

as the incompressibility condition, we obtain the following system:

$$\begin{pmatrix} 0 & \Im\left[\hat{\lambda}_{3,n}\right] & -\Im\left[\hat{\lambda}_{2,n}\right] \\ -\Im\left[\hat{\lambda}_{3,n}\right] & 0 & \Im\left[\hat{\lambda}_{1,n}\right] \\ \Im\left[\hat{\lambda}_{1,n}\right] & \Im\left[\hat{\lambda}_{2,n}\right] & \Im\left[\hat{\lambda}_{3,n}\right] \end{pmatrix} \begin{pmatrix} k1 \\ k2 \\ k3 \end{pmatrix} = \begin{pmatrix} -\frac{(2\pi)^3 f(0)}{2}\omega_1 \\ -\frac{(2\pi)^3 f(0)}{2}\omega_2 \\ 0 \end{pmatrix} \tag{5.61}$$

Further derivatives might give more constraints, at the cost of increased complexity. We follow the choice made by Laval in similar circumstances in the model described in [44], and impose:

$$\Im\left[\hat{\lambda}_{i,n}\right] = \Re\left[\hat{\lambda}_{i,n}\right](+\epsilon) \tag{5.62}$$

where the small quantity ϵ is added when necessary to prevent the matrix in (5.61) from being non inversible.

To summarize, the N^3 particles created at each time step at all node of the large scale grid have the following initial parameters:

$$\begin{cases} \boldsymbol{x}_n & \text{the position of the grid point,} \\ \boldsymbol{k}_n & \text{the wave vector solution of (5.61),} \\ \Re\left[\hat{\lambda}_{i,n}\right] = \frac{(2\pi)^3 f(0)}{2} u'_{fi} & \text{real part of the amplitude for } \lambda, \\ \Im\left[\hat{\lambda}_{i,n}\right] = \Re\left[\hat{\lambda}_{i,n}\right](+\epsilon) & \text{imaginary part of the amplitude for } \lambda, \\ \hat{\mu}'_{i,n} = 0 & \text{initial complex amplitude for } \mu' \text{ set to zero,} \end{cases} \tag{5.63}$$

The generation of new particles in this manner causes several complications for the model. The first one is caused by the properties of the Clebsch decomposition. Indeed, there is no unicity for the fields λ and μ. The concrete consequence is that the λ and μ fields decomposed at time T cannot be combined with the fields at time $T + \Delta T$. In other words, at each time step the Clebsch decomposition of the velocity field $\boldsymbol{u}'_f$ is performed using a different gauge condition.

This difficulty can be overcome by keeping track of the time at which the particles have been created. Assuming that the fields $\lambda_i^T(t)$ and $\mu_i^T(t)$ are recovered from the particles created at time T, the small scale velocity at time t is computed as such:

$$\boldsymbol{u}'(\boldsymbol{x}, t) = \sum_{T<t} \boldsymbol{u}'^T(\boldsymbol{x}, t) = \sum_{T<t} \left[-\nabla\phi^T(\boldsymbol{x}, t) + \lambda_\alpha^T(\boldsymbol{x}, t)\nabla\mu_\alpha^T(\boldsymbol{x}, t)\right]. \tag{5.64}$$

The computation is then developed as follow. First, the incompressibility con-

dition on the Clebsch decomposition from equation (5.26) is used to get rid of the potential fields. We then change from the μ fields to the modified μ':

$$\begin{aligned} u'_j(\boldsymbol{x},t) &= \left(\delta_{jl} - \partial_j \Delta^{-1} \partial_l\right) \sum_{T<t} \lambda_\alpha^T(\boldsymbol{x},t) \partial_l \mu_\alpha^T(\boldsymbol{x},t) \\ &= \left(\delta_{jl} - \partial_j \Delta^{-1} \partial_l\right) \sum_{T<t} \lambda_\alpha^T(\boldsymbol{x},t) \left(\partial_l {\mu'}_\alpha^T(\boldsymbol{x},t) + \delta_{\alpha l}\right) \end{aligned} \tag{5.65}$$

The final expression is obtained by injecting the equations (5.49) and (5.51):

$$\begin{aligned} u'_j(\boldsymbol{x},t) = \frac{4}{(2\pi)^6 f(0)^2} \left(\delta_{jl} - \partial_j \Delta^{-1} \partial_l\right) \Bigg[\sum_{T<t} \sum_{n=1}^{N_T} \Re\left[\hat{\lambda}_{\alpha,n}^T\right] S_{\boldsymbol{x}}(\boldsymbol{x} - \boldsymbol{x}_n(t)) \\ \left(\delta_{jl} - \sum_{m=1}^{N_T} k_l \Im\left[\hat{{\mu'}}_{\alpha,m}^T\right] S_{\boldsymbol{x}}(\boldsymbol{x} - \boldsymbol{x}_m(t))\right) \Bigg] \end{aligned} \tag{5.66}$$

where the sums over n and m are performed over the particles created at time T.

In this expression, the differential operator preceding the sum can be computed using a spectral method over the large scales. It is worth noting that this operation's computational complexity is quadratic in the number of particles created at time T, i.e. in N^3. While the small support of the interpolation function keeps the actual number of operation moderate, we will design the algorithm in a way that minimizes the use of this formula.

5.5.3 Dissipation

The other problem caused by the generation of particles is of practical order. Indeed, running such model would imply adding N^3 particles to the system at each time step. Following through this process would quickly increase the cost of computations, such that the computational advantage over a more classical method would be lost. We list here several ideas that could be used to keep the number of particles under control.

The first idea is to use the removal of particles to implement the numerical dissipation. The most natural approach would then be to use the equivalent of a spectral filter, removing all particles with a wave vector too large $\|\boldsymbol{k}\| > k_{max}$. This is coherent with the method used by Laval in his thesis [44].

Our situation present one major difference with the case discussed in [44]. This distinction is that we use the particle model to model the small scale *velocity* instead of the small scale *vorticity*. This remove the possibility to create particles only in the representative points, as there is no reason to not simulate particles

based on a threshold on velocity. We could use a threshold based on vorticity, at the cost of computing the rotational every time particles are created.

One option in common with [44] is the possibility to "recycle" the particles after a certain time. The idea is that once the number of particles has reached a certain threshold N_{max}, we can use equation (5.66) to reconstruct the small scale velocity $\boldsymbol{u}'$. This reconstructed velocity can then be transformed back into particles using the same process as described in part 5.5.2. In our case, this method can be applied to only "recycle" part of the particles by delimiting a range of time. In other words, we could choose to "recycle" only the particles from time T_1 to T_2. This would ensure that the number of particle do not fall so low that the PIC reconstruction loses in precision.

Recycling the particles also allows to limit the risk of a particle falling into a local reverse cascade, with the norm of the wave vector k reaching a value too low. This would cause the formalism to break as the small scale velocity would have a slowly varying component. While this event is unlikely in 3D turbulence, it is not forbidden locally.

All those methods require testing to verify the effect on the accuracy of the simulation and on the computational cost. As was discussed in the introduction to this chapter, the implementation of the algorithm has not been completed yet, hence nether are the tests.

5.5.4 Advection of particles

The dynamic of the particles is governed by equations (5.38) and (5.58). Expressed from the point of view of the particles parameters, these translate to:

$$\frac{\partial \boldsymbol{x}_n}{\partial t}(t) = \boldsymbol{U}(\boldsymbol{x}_n(t)), \tag{5.67}$$

$$\frac{\partial \boldsymbol{k}_n}{\partial t}(t) = -(\boldsymbol{k}_n(t) \cdot \nabla)\boldsymbol{U}(\boldsymbol{x}_n(t)), \tag{5.68}$$

$$\frac{\partial \hat{\mu}'_{i,n}}{\partial t}(t) = -U_i f(\boldsymbol{k}_n(t)). \tag{5.69}$$

Incidentally, the complex amplitude associated to the λ field is constant:

$$\hat{\lambda}_{i,n} = cst. \tag{5.70}$$

In order to implement these equations, we need to know the large scale velocity field $\boldsymbol{U}$ and its derivative at a point which is not on the grid. For this, we need to use the already defined interpolation function $S_{\boldsymbol{x}}$ from equation (5.45).

Formally, we consider the 8 closest nodes to the particle n, noted $\boldsymbol{x}_{n,\beta}$ for $\beta = 1 \,..\, 8$. Then the large scale velocity at the location $\boldsymbol{x}$ is obtained by:

$$\boldsymbol{U}(\boldsymbol{x},t) = \sum_{\beta=1}^{8} \boldsymbol{U}(\boldsymbol{x}_{n,\beta},t) S_{\boldsymbol{x}}(\boldsymbol{x}_{n,\beta} - \boldsymbol{x}_n). \tag{5.71}$$

Going back to the schematic representation of figure 5.1, one can visualize how the velocity at the position of a particle is computed as the weighted average of the velocity at the neighboring grid nodes. Like for the reconstruction, it is possible to choose a higher order for the interpolation function $S_{\boldsymbol{x}}$ in order to get more accurate results but this would be at higher computational cost.

The same can be done for the different spatial derivatives of $\boldsymbol{U}$, provided that these are computed exactly using the spectral method on the large scale grid.

The equations (5.67) to (5.69) can then be integrated using the second order stable Runge-Kutta method. In order to compute the new parameters of the particles at a time step $\Delta t/2$ required by the large scale scheme from equation (5.18) we need the intermediate variables:

$$\boldsymbol{x}_n^{\diamond} = \boldsymbol{x}_n(t) + \frac{\Delta t}{4} \boldsymbol{U}(\boldsymbol{x}_n(t)), \tag{5.72}$$

$$\boldsymbol{k}_n^{\diamond} = \boldsymbol{k}_n(t) - \frac{\Delta t}{4} (\boldsymbol{k}_n(t) \cdot \nabla) \boldsymbol{U}(\boldsymbol{x}_n(t)). \tag{5.73}$$

The time stepping over the duration $\Delta t/2$ is then given by:

$$\boldsymbol{x}_n\left(t + \frac{\Delta t}{2}\right) = \boldsymbol{x}_n(t) + \frac{\Delta t}{2} \boldsymbol{U}(\boldsymbol{x}_n^{\diamond}), \tag{5.74}$$

$$\boldsymbol{k}_n\left(t + \frac{\Delta t}{2}\right) = \boldsymbol{k}_n(t) - \frac{\Delta t}{2} (\boldsymbol{k}_n^{\diamond} \cdot \nabla) \boldsymbol{U}(\boldsymbol{x}_n^{\diamond}), \tag{5.75}$$

$$\hat{\mu}'_{i,n}\left(t + \frac{\Delta t}{2}\right) = \hat{\mu}'_{i,n}(t) - \frac{\Delta t}{2} U_i(\boldsymbol{x}_n^{\diamond}) f(\boldsymbol{k}_n^{\diamond}). \tag{5.76}$$

Note that the currently chosen numerical scheme means performing operations on the particles four times by time step in total.

5.5.5 Retro-action on large scales

Having determined the mechanic of creation/removal of particles and their dynamic, we can use them to determine the contribution of the small scale velocity to the large scales. The term involving the small scale velocity that need to be determined is $\overline{U_i \partial_i u'_j}$, which is present for both the forcing on small scales $\boldsymbol{F}_{large \to small}$

(equation (5.10)) and the retro-action on large scales $\boldsymbol{F}_{small\to large}$ (equation (5.9)). To simplify this expression, we use the Taylor development of the large scale velocity $\boldsymbol{U}$:

$$\begin{aligned}
\overline{U_i\partial_i u'_j}(\boldsymbol{x},t) &= \int f^2\left(\epsilon^\star(\boldsymbol{x}-\boldsymbol{x}')\right) U_i(\boldsymbol{x}',t)\partial_i u'_j(\boldsymbol{x}',t)\mathrm{d}\boldsymbol{x}' \\
&\approx \int f^2\left(\epsilon^\star(\boldsymbol{x}-\boldsymbol{x}')\right)\left[U_i(\boldsymbol{x},t)+(\boldsymbol{x}-\boldsymbol{x}')\cdot\nabla U_i(\boldsymbol{x}',t)\right]\partial_i u'_j(\boldsymbol{x}',t)\mathrm{d}\boldsymbol{x}' \\
&\approx U_i(\boldsymbol{x},t)\partial_i\overline{u'_j}(\boldsymbol{x},t) + \int f^2\left(\epsilon^\star(\boldsymbol{x}-\boldsymbol{x}')\right)(\boldsymbol{x}-\boldsymbol{x}')\cdot\nabla U_i(\boldsymbol{x}',t)\partial_i u'_j(\boldsymbol{x}',t)\mathrm{d}\boldsymbol{x}' \\
&= U_i(\boldsymbol{x},t)\partial_i\overline{u'_j}(\boldsymbol{x},t) + O(\epsilon^\star).
\end{aligned}$$

In this last development, only the first order is kept. This is because the next term is of comparable magnitude with terms already neglected when deriving the equations in section 5.2. As a result, we have:

$$\boldsymbol{F}_{small\to large} \approx -(\boldsymbol{U}\cdot\nabla)\overline{\boldsymbol{u}'}. \tag{5.77}$$

The final step consists in determining the filtered small scale velocity $\overline{\boldsymbol{u}'}(\boldsymbol{x},t)$ using the particle model. One possible option would be to compute the small scale velocity $\boldsymbol{u}'(\boldsymbol{x},t)$ using the formula from equation (5.66) then apply the filter. However, it has already been mentioned that this operation is computationally costly as it is quadratic with respect to the number of grid points N^3. A cheaper alternative is to use the following:

$$\begin{aligned}
\overline{u'}_j(\boldsymbol{x},t) &= \sum_{T<t}\overline{u'^T}_j(\boldsymbol{x},t) \\
&= \left(\delta_{jl}-\partial_j\Delta^{-1}\partial_l\right)\sum_{T<t}\overline{\lambda_\alpha^T\partial_l\mu_\alpha^T}(\boldsymbol{x},t).
\end{aligned} \tag{5.78}$$

In order to compute the filter of a product of two small scale quantities, we make the following remark:

$$
\begin{aligned}
&\int \Re\left[\hat{\lambda}_\alpha^T(\boldsymbol{x},\boldsymbol{k},t)\partial_l\hat{\mu}_\alpha^T(\boldsymbol{x},-\boldsymbol{k},t)\right]\mathrm{d}\boldsymbol{k}\\
=&\int \Re\left[\int f(\epsilon^\star(\boldsymbol{x}-\boldsymbol{x}'))e^{i\boldsymbol{k}(\boldsymbol{x}-\boldsymbol{x}')}\lambda_\alpha^T(\boldsymbol{x}',t)\mathrm{d}\boldsymbol{x}'\right.\\
&\qquad\left.\int f(\epsilon^\star(\boldsymbol{x}-\boldsymbol{x}''))e^{i\boldsymbol{k}(\boldsymbol{x}-\boldsymbol{x}'')}\partial_l\mu_\alpha^T(\boldsymbol{x}'',t)\mathrm{d}\boldsymbol{x}''\right]\mathrm{d}\boldsymbol{k}\\
=&\iint f(\epsilon^\star(\boldsymbol{x}-\boldsymbol{x}'))f(\epsilon^\star(\boldsymbol{x}-\boldsymbol{x}''))\lambda_\alpha^T(\boldsymbol{x}',t)\partial_l\mu_\alpha^T(\boldsymbol{x}'',t)\\
&\qquad\left(\int e^{i\boldsymbol{k}(\boldsymbol{x}''-\boldsymbol{x}')}\mathrm{d}\boldsymbol{k}\right)\mathrm{d}\boldsymbol{x}'\mathrm{d}\boldsymbol{x}''\\
=&(2\pi)^3\overline{\lambda_\alpha^T\partial_l\mu_\alpha^T}(\boldsymbol{x},t).
\end{aligned}
\tag{5.79}
$$

This leads to:

$$
\begin{aligned}
\overline{\lambda_\alpha^T\partial_l\mu_\alpha^T}(\boldsymbol{x},t)&=\frac{1}{(2\pi)^3}\int \Re\left[\hat{\lambda}_\alpha^T(\boldsymbol{x},\boldsymbol{k},t)\partial_l\hat{\mu}_\alpha^T(\boldsymbol{x},-\boldsymbol{k},t)\right]\mathrm{d}\boldsymbol{k}\\
&=\frac{1}{(2\pi)^3}\int \Re\left[\hat{\lambda}_\alpha^T(\boldsymbol{x},\boldsymbol{k},t)(\partial_l\hat{\mu}_\alpha'^T(\boldsymbol{x},-\boldsymbol{k},t)+\delta_{l\alpha}f(-\boldsymbol{k}))\right]\mathrm{d}\boldsymbol{k}\\
&\approx\frac{1}{(2\pi)^3}\int \Re\left[\hat{\lambda}_\alpha^T(\boldsymbol{x},\boldsymbol{k},t)(-ik_l\hat{\mu}_\alpha'^T(\boldsymbol{x},-\boldsymbol{k},t)+\delta_{l\alpha}f(-\boldsymbol{k}))\right]\mathrm{d}\boldsymbol{k}\\
&\approx\frac{1}{(2\pi)^3}\int \Re\left[\hat{\lambda}_l^T(\boldsymbol{x},\boldsymbol{k},t)f(-\boldsymbol{k})\right]\mathrm{d}\boldsymbol{k}\\
&\quad+\frac{1}{(2\pi)^3}\int k_l\Im\left[\hat{\lambda}_\alpha^T(\boldsymbol{x},\boldsymbol{k},t)\hat{\mu}_\alpha'^T(\boldsymbol{x},-\boldsymbol{k},t)\right]\mathrm{d}\boldsymbol{k}.
\end{aligned}
\tag{5.80}
$$

The first term can be computed directly by applying the relation (5.44). In the following computation, the first sum needs to include the particles with opposite wave vectors introduced in part 5.5.1. The filter f being real valued, we use the properties $f(\boldsymbol{k})=f(-\boldsymbol{k})^*$ and $\hat{\lambda}_{l,n-}^T=\hat{\lambda}_{l,n+}^{T*}$ to simplify the expression.

$$
\begin{aligned}
&\int \Re\left[\hat{\lambda}_l^T(\boldsymbol{x},\boldsymbol{k},t)f(-\boldsymbol{k})\right]\mathrm{d}\boldsymbol{k}\\
=&\int \Re\Big[\sum_{n=1}^{N_p^T}\left[\hat{\lambda}_{l,n+}^T\delta(\boldsymbol{k}-\boldsymbol{k}_n^T(t))+\hat{\lambda}_{l,n-}^T\delta(\boldsymbol{k}+\boldsymbol{k}_n^T(t))\right]\\
&\qquad f(-\boldsymbol{k})S_{\boldsymbol{x}}(\boldsymbol{x}-\boldsymbol{x}_n^T(t))\Big]\mathrm{d}\boldsymbol{k}\\
=&\,2\sum_{n=1}^{N_p^T}\Re\left[\hat{\lambda}_{l,n}^T f(-\boldsymbol{k}_n^T)\right]S_{\boldsymbol{x}}(\boldsymbol{x}-\boldsymbol{x}_n^T(t)).
\end{aligned}
\tag{5.81}
$$

The second term of equation (5.80) can be computed using the same method.

$$\begin{aligned}
&\int k_l \Im\left[\hat{\lambda}_\alpha^T(\boldsymbol{x},\boldsymbol{k},t)\hat{\mu}_\alpha'^T(\boldsymbol{x},-\boldsymbol{k},t)\right]\mathrm{d}\boldsymbol{k} \\
&= \int k_l \Im\left[\left(\sum_{n=1}^{N_p^T}\left[\hat{\lambda}_{l,n+}^T\delta(\boldsymbol{k}-\boldsymbol{k}_n^T(t))+\hat{\lambda}_{l,n-}^T\delta(\boldsymbol{k}+\boldsymbol{k}_n^T(t))\right]S_{\boldsymbol{x}}(\boldsymbol{x}-\boldsymbol{x}_n^T(t))\right)\right. \\
&\qquad\left.\left(\sum_{m=1}^{N_p^T}\left[\hat{\mu}_{l,m+}'^T\delta(-\boldsymbol{k}-\boldsymbol{k}_m^T(t))+\hat{\mu}_{l,m-}'^T\delta(-\boldsymbol{k}+\boldsymbol{k}_m^T(t))\right]S_{\boldsymbol{x}}(\boldsymbol{x}-\boldsymbol{x}_m^T(t))\right)\right]\mathrm{d}\boldsymbol{k}.
\end{aligned}$$

Using the fact that different particles are very unlikely to have the exact same wave vector, the choice of a Dirac for the interpolation function in the spectral space in part 5.5.1 allows us to simplify the computation:

$$\int k_l \Im\left[\hat{\lambda}_\alpha^T(\boldsymbol{x},\boldsymbol{k},t)\hat{\mu}_\alpha'^T(\boldsymbol{x},-\boldsymbol{k},t)\right]\mathrm{d}\boldsymbol{k} = 2\sum_{n=1}^{N_p^T} k_{l,n}^T \Im\left[\hat{\lambda}_{\alpha,n}^T\hat{\mu}_{\alpha,n}'^{T*}\right]S_{\boldsymbol{x}}(\boldsymbol{x}-\boldsymbol{x}_n^T(t))^2. \tag{5.82}$$

Finally, injecting the results of (5.81) and (5.82) in equation (5.80) and grouping the sums, the filtered small scale velocity is recovered as follow:

$$\begin{aligned}
\overline{u'}_j(\boldsymbol{x},t) = \frac{2}{(2\pi)^3}\left(\delta_{jl}-\partial_j\Delta^{-1}\partial_l\right)\sum_{n=1}^{N_p}\Bigg(&\Re\left[\hat{\lambda}_{l,n}f(-\boldsymbol{k}_n)\right]S_{\boldsymbol{x}}(\boldsymbol{x}-\boldsymbol{x}_n(t)) \\
&+k_{l,n}\Im\left[\hat{\lambda}_{\alpha,n}\hat{\mu}_{\alpha,n}'^{*}\right]S_{\boldsymbol{x}}(\boldsymbol{x}-\boldsymbol{x}_n(t))^2\Bigg).
\end{aligned} \tag{5.83}$$

The leading differential operator of this expression can be computed using a spectral method. Remarkably, the computation cost of this term is linear in the number of particles.

5.5.6 Constraints on the filter

The knowledge of the filter is required in order to complete the model. However, the choice of this filter is not left free. This constraint is apparent in the computation of the filter of a product of small scale variables. For the sake of argument, let us take the filtered product $\overline{\lambda_i^T\mu_i^T}$. A common rectangle integration over all the grid

points $\boldsymbol{x}_i$ would give:

$$\overline{\lambda_i^T \mu_i^T}(\boldsymbol{x}, t) = \sum_i \lambda_i^T(\boldsymbol{x}_i)\mu_i^T(\boldsymbol{x}_i) f^2(\boldsymbol{x} - \boldsymbol{x}_i)(\Delta x)^3. \tag{5.84}$$

Estimating the same quantity using the particle model yields:

$$\overline{\lambda_i^T \mu_i^T}(\boldsymbol{x}, t) = \frac{2}{(2\pi)^3} \sum_{n=1}^{N_p} \hat{\lambda}_{i,n}^T \hat{\mu}_{i,n}^T S_{\boldsymbol{x}}(\boldsymbol{x} - \boldsymbol{x}_n^T)^2. \tag{5.85}$$

As those two relations must be true for any two small scale fields, this imposed that f^2 and $S_{\boldsymbol{x}}^2$ are proportional to one another:

$$f^2 = C \times S_{\boldsymbol{x}}^2. \tag{5.86}$$

Additionally, the filter must be normalized such that $\int f^2(\boldsymbol{x}) d\boldsymbol{x} = 1$. As a result, we have:

$$f^2 = f^2(0) S_{\boldsymbol{x}}^2. \tag{5.87}$$

where

$$f(0) = \frac{1}{\sqrt{\int S_{\boldsymbol{x}}^2(\boldsymbol{x}) d\boldsymbol{x}}}. \tag{5.88}$$

For our choice of $S_{\boldsymbol{x}}$, this results in:

$$f(0) = \left(\frac{3}{2dh}\right)^{3/2}. \tag{5.89}$$

The Fourier transform of both the function and its square are required. Those are computed as follow:

$$f(\boldsymbol{k}) = f(0) dh^3 \mathrm{sinc}^2\left(\frac{k_x dh}{2}\right) \mathrm{sinc}^2\left(\frac{k_y dh}{2}\right) \mathrm{sinc}^2\left(\frac{k_z dh}{2}\right), \tag{5.90}$$

$$f^2(\boldsymbol{k}) = 6^3 \left(\frac{\mathrm{sinc}(k_x dh) - 1}{(k_x dh)^2}\right) \left(\frac{\mathrm{sinc}(k_y dh) - 1}{(k_y dh)^2}\right) \left(\frac{\mathrm{sinc}(k_z dh) - 1}{(k_z dh)^2}\right). \tag{5.91}$$

As a remark, we have:

$$\lim_{x \to 0} \frac{\mathrm{sinc}(x) - 1}{x^2} = -\frac{1}{6}. \tag{5.92}$$

so there is no divergence around the origin for f^2.

5.6 Accessing to small scale statistics: the energy spectrum

Assuming the algorithm described in this chapter is implemented, we would need to have some access to statistical values pertaining to the small scales. At the very least, this would be required in order to validate the model. At best, we could make use of these statistics to study some small scale behaviors with only a fraction of the computational cost of a large DNS.

The very first quantity that needs to be checked is the energy spectrum. Again, assuming the simulation runs smoothly and the energy spectrum of the large scale behave as expected, showing an inertial range, we would then focus our interest on the energy spectrum of the small scales. As the equations for the dynamic of the particles are inviscid, we would expect the inertial range to extend from the large scales to the cutoff k_{max} at which we remove the particles.

The similar work by Laval [45] used the energy carried by individual particles in order to reconstruct the complete energy spectra. This method is not strictly applicable the current model because of the non linearity of the Clebsch decomposition: the local energy is not a simple sum of the "energy" carried by neighboring particles. Nevertheless, we can still use this approach as an estimation. Starting from the expression of the velocity combined from the particles created at time T:

$$u'^T_i = (\delta_{ij} - \partial_i \Delta^{-1} \partial_j)(\lambda^T_j + \lambda^T_\alpha \partial_j \mu'^T_\alpha). \tag{5.93}$$

The λ and μ terms can be recovered using the particles by:

$$\lambda^T_i = \frac{2}{(2\pi)^3 f(0)} \sum_n \Re\left[\hat{\lambda}^T_{j,n}\right] S_{\boldsymbol{x}}(\boldsymbol{x} - \boldsymbol{x}^T_n), \tag{5.94}$$

$$\partial_j \mu'^T_\alpha \approx -\frac{2}{(2\pi)^3 f(0)} \sum_n k^T_{j,n} \Im\left[\hat{\mu'}^T_{\alpha,n}\right] S_{\boldsymbol{x}}(\boldsymbol{x} - \boldsymbol{x}^T_n). \tag{5.95}$$

If we ignore the contributions from the other particles, the velocity at point $\boldsymbol{x}_n$ associated to a single particle n is expressed as:

$$u'^T_{i,n} \approx \frac{2}{(2\pi)^3 f(0)} \Re\left[\hat{\lambda}^T_{i,n}\right] - \frac{4}{(2\pi)^6 f(0)^2} k^T_{i,n} \Re\left[\hat{\lambda}^T_{\alpha,n}\right] \Im\left[\hat{\mu'}^T_{\alpha,n}\right]. \tag{5.96}$$

As a result, the energy associated to this particle would be:

$$E^T_n = \frac{1}{2} \sum_i {u'^T_{i,n}}^2. \tag{5.97}$$

In order to recover the energy spectrum for the small particles, the idea would then be to sum the contributions of all particles with a wave vector of same length. More formally, the result would be:

$$E(k) = \frac{1}{dk} \sum_{T<t} \sum_{|\|\boldsymbol{k}_n^T\\|-k|<dk/2} E_n^T. \tag{5.98}$$

where the interval dk would be chosen large enough to have several particles per bin.

This method has the flaw of circumventing the base principle of the PIC model, by neglecting all the terms that result in the combination of several particles. It is however the best approach that we have developed at the time of the redaction of this manuscript.

5.7 Current state and discussion

The implementation of this PIC method is currently at the debugging phase. As the project has been stalled for some time, it is unlikely to be someday concluded. Should it continue, we would expect several roadblocks before completion.

From the point of view of the model, we expect that the process of creation of particles described in part 5.5.2 might require some revisions. The points with some degrees of freedom are the choice of the equations to constrain the wave vector $\boldsymbol{k}$ and the choice of imaginary part for the complex amplitudes $\hat{\lambda}_{\alpha,n}$. By analogy with the similar model developed in Laval thesis [44], we expect these choices to be valid. However, they need to be properly validated.

While the exact method of validation is yet undetermined, one potential approach would be to run an *a posteriori* validation test against a well resolved DNS. The principle of such validation would be to run the particle dynamic using the large scale velocity of the DNS as the large scales $\boldsymbol{U}$, and verify if the particle model reproduces the same small scale velocity. Another idea would be to compare the retroaction of the small scales on the large scales computed in section 5.5.5 to a common LES model, for example the Smagorinsky model [67].

At this point, it is difficult to evaluate how this model would perform, let alone if it could outperform existing models. It however shows potential with regards to our original motivation of investigating the simulation of quasi singularities. Indeed, the particle dynamics runs according to approximated Euler equations. This means that in absence of numerical cutoff, we would expect particles carrying energy to evolve such that their wave vector $\boldsymbol{k}$ would grow very large, corresponding

to very strong gradient, without viscous dampening. By following the track of a group of particles past the frequency cutoff, this could grant us access to quantities such as the rate of production of quasi singular events without having to use an expensive DNS followed by the complex computations presented in the first part of this thesis.

Chapter 6

Conclusions and perspectives

The starting point for this thesis was the question of the regularity of the solutions to the Navier–Stokes equations. Our approach to this question was to look for irregular events in turbulent velocity fields which could be interpreted as potential singularities.

In a first part, we developed a method based on multifractal analysis to estimate the local regularity of a turbulent velocity field through the Hölder coefficients. This method complements an existing criterion based on strong local energy transfers. That older method has already been used for the detection of potential singularities [41, 40]. Using this preexisting concept as a reference, we validated in the inertial range the value of the method based on local Hölder exponents as a new criterion for the detection of irregular events. We indeed showed that the lower values of Hölder exponents did correspond to strong energy transfers, and thus to more irregular events. However, we also show by comparison with the VGT invariants that the criterion based on the local Hölder exponents is not limited to the same structures as the local energy transfer. This is confirmed by visualization of maps of these two quantities at the inertial scale.

We then described a way to use this tool in the dissipative range using a calibration in the inertial range. The results obtained in the dissipative range are in agreement with the previous study performed using experimental data [15]. The use of numerical simulation allowed us to produce statistical results without the difficulties of experimental measurements. This comes with the drawback of a lower Reynolds number, which could potentially lead to less quasi singular events, or weaker events. Nevertheless, we obtained similar results for the topology of the streamlines of velocity around quasi singular events. Indeed, we observe the same shape of "roll vortices" previously identified by [15]. In addition, the amount of statistics available allowed us to define a "typical event", with the same topology,

by averaging many very singular events. This shows the existence of a structure of local Hölder exponents, energy transfer and dissipation that is common to most irregular events. Furthermore, we exhibit a relationship between the apparition of potential singularities and vortex interactions. This is apparent from isolated snapshots of irregular events figuring several vortices close to each other. This finding was confirmed by a detailed study of several events using a time resolved dataset. In particular, we found that the formation of a particular event coincides with an interaction between two vortices. Those findings might be a step toward explaining the physical mechanism behind the formation of quasi singularities. This in turn could potentially explain the phenomenon of anomalous dissipation.

In a second part, we tried to develop a new simulation scheme based on a PIC method. The principle of the method would be to model the small scale velocity as particles advected by the large scale. We show how this could be done using the Clebsch decomposition. We also derive a way to recover the effect of the small scale velocity on the large scales. The purpose of this new method of simulation in the context of this thesis would be to track potential singularities through the scales by the mean of the PIC model. The project is currently stalled before the new model could be validated.

6.1 Going forward

6.1.1 Universality of the local Hölder method

The method to compute local Hölder exponents developed in this thesis was meant to be later used on experimental data. This includes in particular the data from the study to which we compared our results in Chapter 4. However, we have shown that in order to apply the method to compute local Hölder exponents at the dissipative scale, one had to first perform a calibration in the inertial scale. This requirement to have a dataset with both an inertial range and a resolution close to the Kolmogorov scale is hard to fulfill with experimental data. The solution to this problem has been mentioned in Chapter 3 and comes from the universal nature of turbulence. As such, the idea would be to determine the coefficients c_p corresponding to a new dataset without having to do the calibration in the inertial range.

First of all, we can verify that this universality exists. The paper by Geneste et al. [25] shows that the structure functions verify an universal behavior. We can verify using our two simulations that this universal behavior is shared by

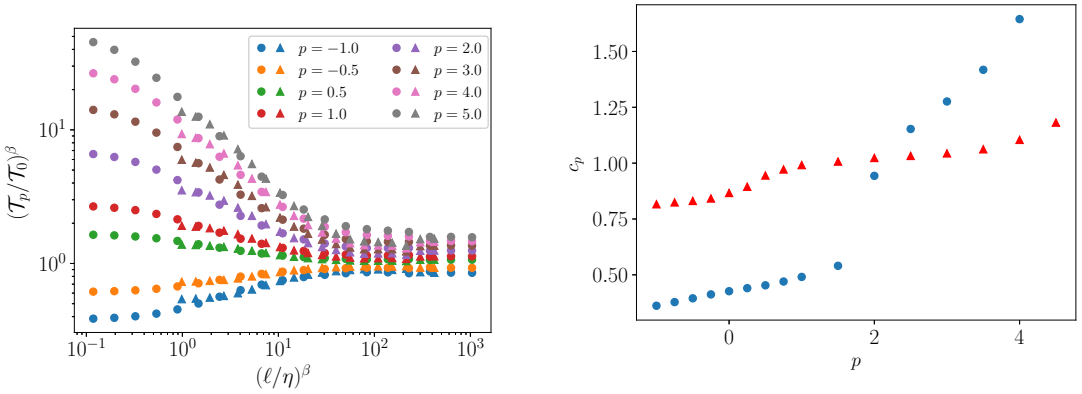

(a) (b)

Figure 6.1: **(a)** Test of universality of equation (3.49). The data points from run I are marked by triangles and the data points from run II are marked by circles. The orders of p are color coded. **(b)** Comparison of the coefficients c_p for the two runs. Blue circles correspond to Run I and red triangle to Run II.

the thresholds $\mathcal{T}_p$ used to compute the active volumes, as expressed in equation (3.49). The figure 6.1a shows a good collapse of the curves of thresholds. For this figure, we chose to use the thresholds from run I as a reference, such that the corresponding β is $\beta_1 = 1$. In order to obtain the collapse, the β for run II is set to $\beta_2 = 1.5$. Moreover we observe that the coefficients c_p computed for the two datasets follow similar trends, as is shown in figure 6.1b. The work from here would be to compute the coefficients c_p for some other datasets in order to find their dependency in Reynolds numbers. This would eventually allow us to apply the computation of local Hölder exponents to experimental data.

6.1.2 Improving the analysis

Obtaining the local Hölder exponents in experimental data, in particular with the dataset used by Debue [15] would be useful in determining whether the behaviors observed in Chapter 4 with simulations at relatively low Reynolds are robust. We would be particularly interested in verifying that the typical structure of low regularity is the same at higher Reynolds number. It would also be interesting to see whether events with lower singularity exponent can appear.

Similarly, this study would profit from using very large DNS, giving access to both higher resolutions and higher Reynolds numbers. In order to study such a DNS, it would be necessary to adapt the current post processing code to scale. Indeed, the resolution of 768^3 used in this thesis is close to the limit for a code parallelized in OpenMP.

6.1.3 Other applications of the Hölder exponent

Turbulence is not the only research field that can benefit from a tool for the detection of singularities. Indeed, such tools based on Hölder regularity have already been used in various domain. In the thesis by Kestener [36], the WTMM method is applied in the context of mammography. Other medical application include the study of human gait [65] or arrhythmia [31].

The method developed during this thesis relies on the multifractal framework and the active volumes, which makes it fine tuned for the case of turbulence. However, it could be adapted to other adjacent domains, with the example of Magneto Hydro Dynamics (MHD). As we have observed strong events of Hölder exponents at the location of vortex reconnections in Chapter 4, one might expect that a similar tool adapted to MHD would be able to detect events of magnetic reconnection.

Bibliography

[1] P. Abry, S. G. Roux, and S. Jaffard. Detecting oscillating singularities in multifractal analysis: Application to hydrodynamic turbulence. In 2011 IEEE International Conference on Acoustics, Speech and Signal Processing (ICASSP), pages 4328–4331. IEEE, 2011.

[2] A. Arneodo, B. Audit, P. Kestener, and S. Roux. Wavelet-based multifractal analysis. Scholarpedia, 3(3):4103, 2008. revision #121431.

[3] A. Arneodo, E. Bacry, and J. Muzy. The thermodynamics of fractals revisited with wavelets. Physica A: Statistical Mechanics and its Applications, 213(1-2):232–275, 1995.

[4] A. Arneodo, N. Decoster, and S. Roux. A wavelet-based method for multifractal image analysis. I. Methodology and test applications on isotropic and anisotropic random rough surfaces. The European Physical Journal B-Condensed Matter and Complex Systems, 15(3):567–600, 2000.

[5] A. Ayache. Multifractional Stochastic Fields. World Scientific, 2018.

[6] E. Bacry, J.-F. Muzy, and A. Arneodo. Singularity spectrum of fractal signals from wavelet analysis: Exact results. Journal of Statistical Physics, 70(3-4):635–674, 1993.

[7] J. T. Beale, T. Kato, and A. Majda. Remarks on the breakdown of smooth solutions for the 3-D Euler equations. Communications in Mathematical Physics, 94(1):61–66, 1984.

[8] C. K. Birdsall and A. B. Langdon. Plasma physics via computer simulation. CRC press, 2004.

[9] M. Brachet, M. Meneguzzi, H. Politano, and P. Sulem. The dynamics of freely decaying two-dimensional turbulence. Journal of Fluid Mechanics, 194:333–349, 1988.

[10] J. M. Burgers. A mathematical model illustrating the theory of turbulence. In Advances in Applied Mechanics, volume 1, pages 171–199. Elsevier, 1948.

[11] L. Caffarelli, R. Kohn, and L. Nirenberg. Partial regularity of suitable weak solutions of the Navier-Stokes equations. Communications on Pure and Applied Mathematics, 35(6):771–831, 1982.

[12] C. Cartes, M. D. Bustamante, and M. E. Brachet. Generalized Eulerian-Lagrangian description of Navier-Stokes dynamics. Physics of Fluids, 19(7):077101, 2007.

[13] M. S. Chong, A. E. Perry, and B. J. Cantwell. A general classification of three-dimensional flow fields. Physics of Fluids A: Fluid Dynamics, 2(5):765–777, 1990.

[14] P. Constantin et al. Euler and Navier-Stokes equations. Publicacions Matemàtiques, 52(2):235–265, 2008.

[15] P. Debue. Experimental approach to the problem of the Navier–Stokes singularities. PhD thesis, Université Paris-Saclay, 2019.

[16] N. Decoster. Analyse multifractale d'images de surfaces rugueuses à l'aide de la transformation en ondelettes. PhD thesis, Université Sciences et Technologies - Bordeaux I, 11 1999.

[17] B. Dubrulle. Beyond Kolmogorov cascades. Journal of Fluid Mechanics, 867:P1, 2019.

[18] B. Dubrulle and S. Nazarenko. Interaction of turbulence and large-scale vortices in incompressible 2d fluids. Physica D: Nonlinear Phenomena, 110(1-2):123–138, 1997.

[19] J. Duchon and R. Robert. Dissipation d'énergie pour des solutions faibles des équations d'Euler et Navier-Stokes incompressibles. Séminaire Équations aux dérivées partielles, 2000:1–10, 2000.

[20] G. L. Eyink. Turbulent cascade of circulations. Comptes Rendus Physique, 7(3):449–455, 2006.

[21] K. Falconer. Fractal geometry: mathematical foundations and applications. John Wiley & Sons, 2004.

[22] M. Frigo and S. G. Johnson. The design and implementation of FFTW3. Proceedings of the IEEE, 93(2):216–231, 2005. Special issue on "Program Generation, Optimization, and Platform Adaptation".

[23] U. Frisch. Turbulence: the legacy of AN Kolmogorov. Cambridge University Press, 1995.

[24] U. Frisch, T. Matsumoto, and J. Bec. Singularities of Euler flow? Not out of the blue! Journal of Statistical Physics, 113(5-6):761–781, 2003.

[25] D. Geneste, H. Faller, F. Nguyen, V. Shukla, J.-P. Laval, F. Daviaud, E.-W. Saw, and B. Dubrulle. About universality and thermodynamics of turbulence. Entropy, 21(3):326, 2019.

[26] T. Grafke, H. Homann, J. Dreher, and R. Grauer. Numerical simulations of possible finite time singularities in the incompressible Euler equations: comparison of numerical methods. Physica D: Nonlinear Phenomena, 237(14-17):1932–1936, 2008.

[27] R. Grauer and T. C. Sideris. Finite time singularities in ideal fluids with swirl. Physica D: Nonlinear Phenomena, 88(2):116–132, 1995.

[28] A. Grossmann and J. Morlet. Decomposition of functions into wavelets of constant shape, and related transforms. In Mathematics+ Physics: Lectures on Recent Results (Volume 1), pages 135–165. World Scientific, 1985.

[29] J. Hadamard. Sur les problèmes aux dérivées partielles et leur signification physique. Princeton university bulletin, pages 49–52, 1902.

[30] S. Jaffard and Y. Meyer. Wavelet methods for pointwise regularity and local oscillations of functions, volume 587. American Mathematical Soc., 1996.

[31] A. Joshi, S. Chandran, S. Phadke, V. Jayaraman, B. Kulkarni, et al. Arrhythmia classification using local hölder exponents and support vector machine. In International Conference on Pattern Recognition and Machine Intelligence, pages 242–247. Springer, 2005.

[32] R. Kerr. Vortex collapse and turbulence. Fluid Dynamics Research, 36(4-6):249, 2005.

[33] R. M. Kerr. Evidence for a singularity of the three-dimensional, incompressible euler equations. Physics of Fluids A: Fluid Dynamics, 5(7):1725–1746, 1993.

[34] R. M. Kerr. The role of singularities in turbulence. Unstable and Turbulent Motion of Fluid, page 102, 1993.

[35] R. M. Kerr. The role of singularities in Euler. In Small-Scale Structures in Three-Dimensional Hydrodynamic and Magnetohydrodynamic Turbulence, pages 17–23. Springer, 1995.

[36] P. Kestener. Analyse multifractale 2D et 3D à l'aide de la transformation en ondelettes : application en mammographie et en turbulence développée. PhD thesis, Université Sciences et Technologies - Bordeaux I, Nov. 2003.

[37] P. Kestener. xsmurf v1.0, June 2016.

[38] P. Kestener and A. Arneodo. Generalizing the wavelet-based multifractal formalism to random vector fields: application to three-dimensional turbulence velocity and vorticity data. Physical review letters, 93(4):044501, 2004.

[39] A. Kolmogorov. The local structure of turbulence in incompressible viscous fluid for very large Reynolds numbers. Dokl. Akad. Nauk SSSR, 30:9–13, 1941.

[40] D. Kuzzay. Investigations on the relevance of Onsager's conjecture in real incompressible turbulence. Theses, Université Paris-Saclay, Oct. 2016.

[41] D. Kuzzay, E.-W. Saw, F. Martins, D. Faranda, J.-M. Foucaut, F. Daviaud, and B. Dubrulle. New method for detecting singularities in experimental incompressible flows. Nonlinearity, 30(6):2381, 2017.

[42] M. Lachowicz. From kinetic to Navier-Stokes-type equations. Applied Mathematics Letters, 10(5):19 – 23, 1997.

[43] O. A. Ladyzhenskaya. The mathematical theory of viscous incompressible flow, volume 2. Gordon and Breach New York, 1969.

[44] J.-P. Laval. Développement d'un nouveau modèle dynamique pour la turbulence. PhD thesis, Université Paris 6, Oct. 1999.

[45] J.-P. Laval, B. Dubrulle, and S. Nazarenko. Dynamical modeling of sub-grid scales in 2d turbulence. Physica D: Nonlinear Phenomena, 142(3-4):231–253, 2000.

[46] J. Leray. Sur le mouvement d'un liquide visqueux emplissant l'espace. Acta Mathematica, 63(1):193–248, 1934.

[47] L. Li, Y. Li, and X. Yan. Homogeneous solutions of stationary Navier–Stokes equations with isolated singularities on the unit sphere. Archive for Rational Mechanics and Analysis, 227(3):1091–1163, 2018.

[48] G. Luo and T. Y. Hou. Potentially singular solutions of the 3D axisymmetric Euler equations. Proceedings of the National Academy of Sciences, 111(36):12968–12973, 2014.

[49] S. Mallat and W. L. Hwang. Singularity detection and processing with wavelets. IEEE Transactions on Information Theory, 38(2):617–643, 1992.

[50] S. Mallat, S. Zhong, et al. Characterization of signals from multiscale edges. IEEE Transactions on pattern analysis and machine intelligence, 14(7):710–732, 1992.

[51] B. Mandelbrot. Fractals: Form, Chance, and Dimension. Freeman New York, 1977.

[52] B. B. Mandelbrot. The fractal geometry of nature, volume 173. WH freeman New York, 1983.

[53] Y. Meyer. Ondelettes. Paris: Hermann, 1990.

[54] Y. Meyer. Wavelets and operators, volume 1. Cambridge University Press, 1992.

[55] A. Monin and A. Yaglom. Statistical fluid mechanics, vol. 2 cambridge. MA: MIT Press], 1975.

[56] J.-F. Muzy, E. Bacry, and A. Arneodo. Multifractal formalism for fractal signals: The structure-function approach versus the wavelet-transform modulus-maxima method. Physical review E, 47(2):875, 1993.

[57] J.-F. Muzy, E. Bacry, and A. Arneodo. The multifractal formalism revisited with wavelets. International Journal of Bifurcation and Chaos, 4(02):245–302, 1994.

[58] S. V. Nazarenko, N. J. Zabusky, and T. Scheidegger. Nonlinear sound–vortex interactions in an inviscid isentropic fluid: A two-fluid model. Physics of Fluids, 7(10):2407–2419, 1995.

[59] F. Nguyen, J.-P. Laval, P. Kestener, A. Cheskidov, R. Shvydkoy, and B. Dubrulle. Local estimates of Hölder exponents in turbulent vector fields. Physical Review E, 99(5):053114, 2019.

[60] K. Ohkitani and P. Constantin. Eulerian-lagrangian analysis of navier-stokes turbulence. In Mechanics of 21st Century - ICTAM04 Proceedings, 2004.

[61] L. Onsager. Statistical hydrodynamics. Il Nuovo Cimento (1943-1954), 6(2):279–287, 1949.

[62] G. Parisi and U. Frisch. On the singularity structure of fully developed turbulence. Turbulence and Predictability in Geophysical Fluid Dynamics and Climate Dynamics, 1985.

[63] B. Pearson, P.-Å. Krogstad, and W. Van De Water. Measurements of the turbulent energy dissipation rate. Physics of fluids, 14(3):1288–1290, 2002.

[64] A. Pumir and E. D. Siggia. Development of singular solutions to the axisymmetric euler equations. Physics of Fluids A: Fluid Dynamics, 4(7):1472–1491, 1992.

[65] N. Scafetta, L. Griffin, and B. J. West. Hölder exponent spectra for human gait. Physica A: Statistical Mechanics and its Applications, 328(3-4):561–583, 2003.

[66] A. Shnirelman. On the nonuniqueness of weak solution of the Euler equation. Communications on Pure and Applied Mathematics: A Journal Issued by the Courant Institute of Mathematical Sciences, 50(12):1261–1286, 1997.

[67] J. Smagorinsky. General circulation experiments with the primitive equations: I. the basic experiment. Monthly Weather Review, 91(3):99–164, 1963.

[68] Z. R. Struzik. Local effective Hölder exponent estimation on the wavelet transform maxima tree. In Fractals, pages 93–112. Springer, 1999.

[69] C. Uhlig and J. Eggers. Singularities in cascade models of the Euler equation. Zeitschrift für Physik B Condensed Matter, 103(1):69–78, 1997.

[70] J. Vassilicos and J. G. Brasseur. Self-similar spiral flow structure in low Reynolds number isotropic and decaying turbulence. Physical Review E, 54(1):467, 1996.

[71] P. Vieillefosse. Internal motion of a small element of fluid in an inviscid flow. Physica A: Statistical Mechanics and its Applications, 125(1):150–162, 1984.

[72] A. Vincent and M. Meneguzzi. The dynamics of vorticity tubes in homogeneous turbulence. Journal of Fluid Mechanics, 258:245–254, 1994.

[73] J. Yao and F. Hussain. On singularity formation via viscous vortex reconnection. Journal of Fluid Mechanics, 888:R2, 2020.

[74] J. Yao and F. Hussain. A physical model of turbulence cascade via vortex reconnection sequence and avalanche. Journal of Fluid Mechanics, 883:A51, 2020.

[75] Z. Yoshida. Clebsch parameterization: basic properties and remarks on its applications. Journal of Mathematical Physics, 50(11):113101, 2009.

[76] Z. Yoshida and P. Morrison. Epi-two-dimensional fluid flow: a new topological paradigm for dimensionality. Physical review letters, 119(24):244501, 2017.

[77] V. I. Yudovich. Non-stationary flows of an ideal incompressible fluid. Zhurnal Vychislitel'noi Matematiki i Matematicheskoi Fiziki, 3(6):1032–1066, 1963.

Appendix A

Visualization of events

This appendix is dedicated to the visualization of several more singular events extracted from Run II. The selection is made to cover a large range of events, not restriced to the few most singular ones.

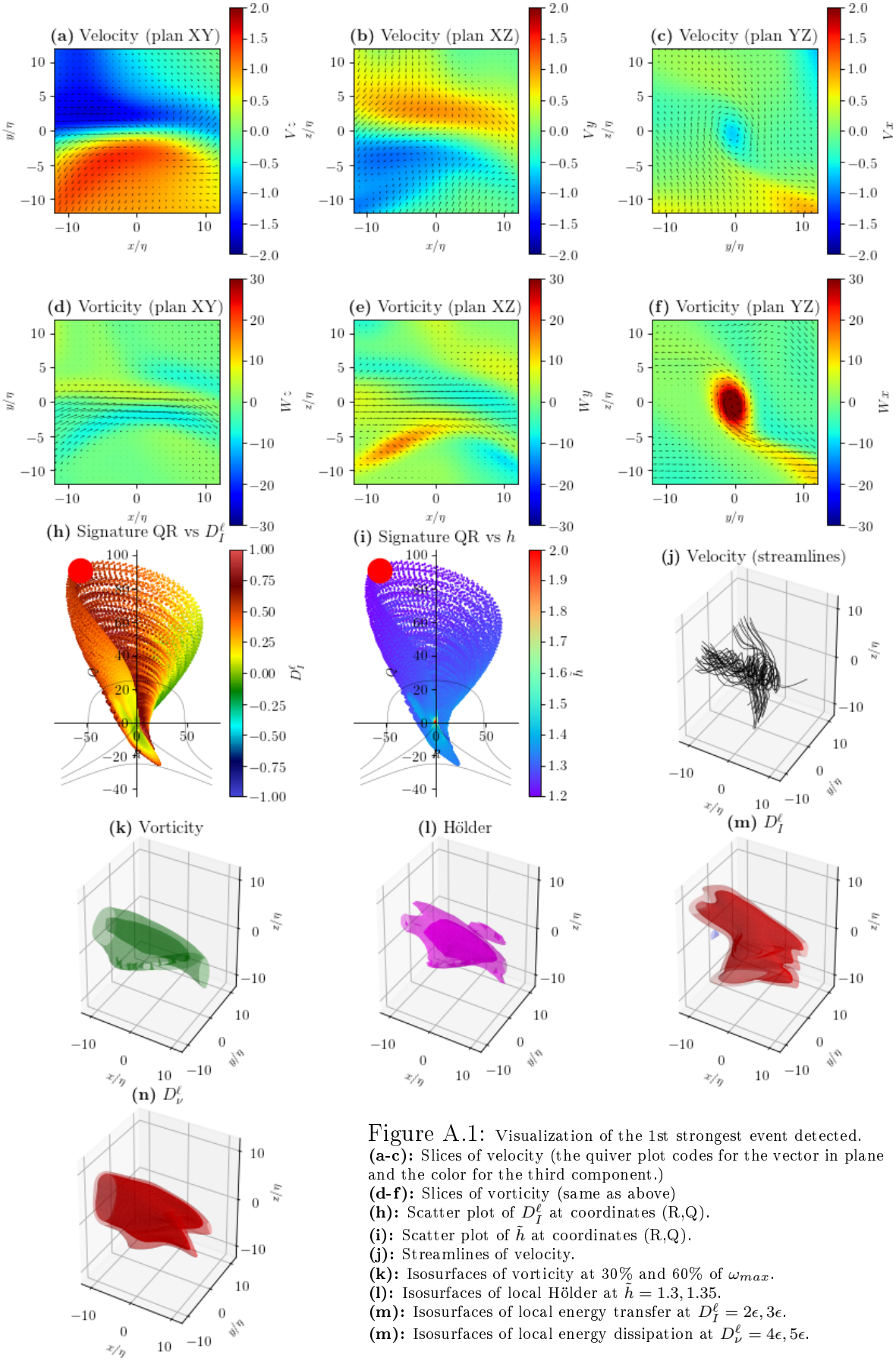

Figure A.1: Visualization of the 1st strongest event detected.
(a-c): Slices of velocity (the quiver plot codes for the vector in plane and the color for the third component.)
(d-f): Slices of vorticity (same as above)
(h): Scatter plot of D_I^ℓ at coordinates (R,Q).
(i): Scatter plot of $\tilde{h}$ at coordinates (R,Q).
(j): Streamlines of velocity.
(k): Isosurfaces of vorticity at 30% and 60% of ω_{max}.
(l): Isosurfaces of local Hölder at $\tilde{h} = 1.3, 1.35$.
(m): Isosurfaces of local energy transfer at $D_I^\ell = 2\epsilon, 3\epsilon$.
(m): Isosurfaces of local energy dissipation at $D_\nu^\ell = 4\epsilon, 5\epsilon$.

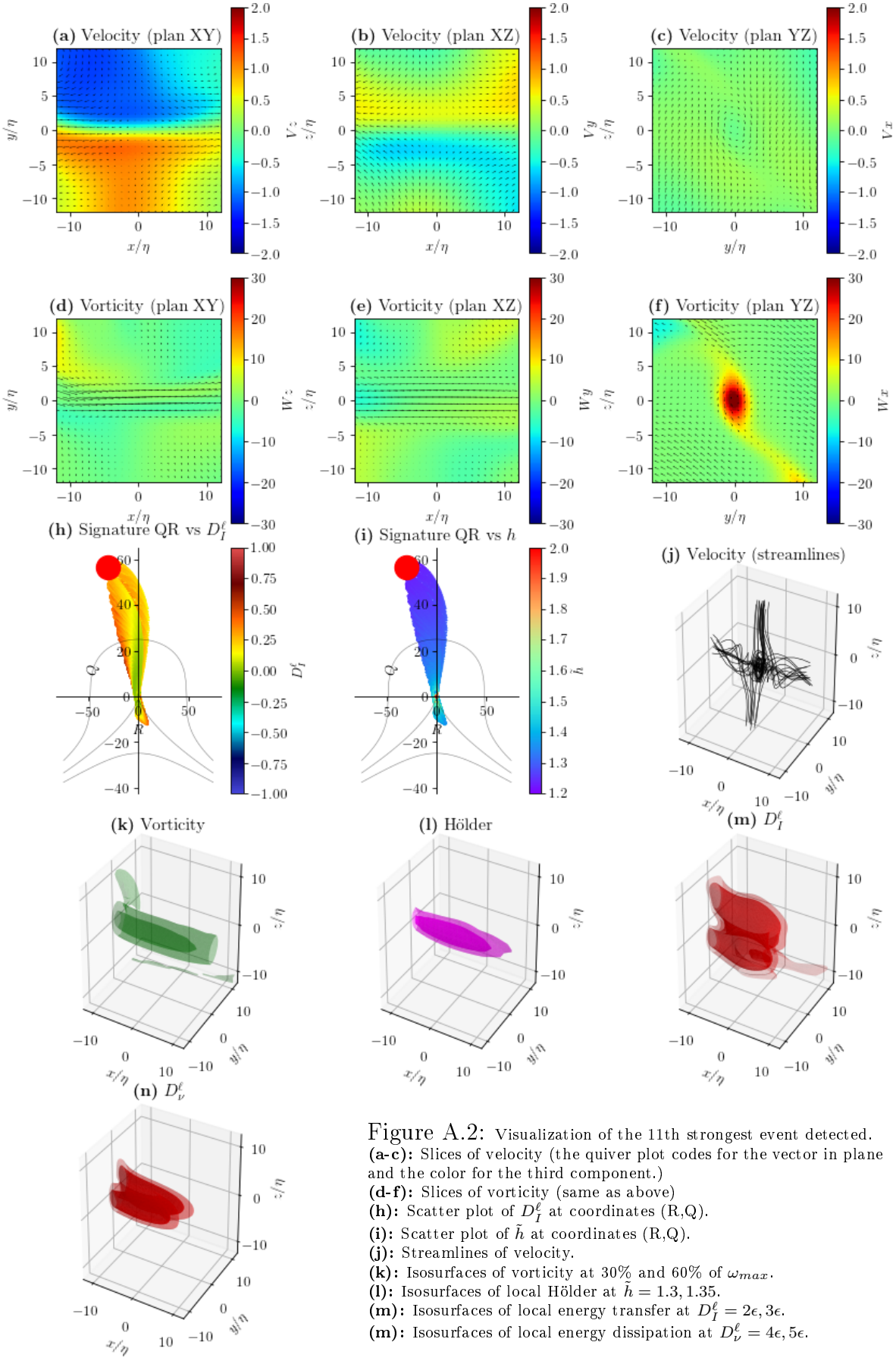

Figure A.2: Visualization of the 11th strongest event detected.
(a-c): Slices of velocity (the quiver plot codes for the vector in plane and the color for the third component.)
(d-f): Slices of vorticity (same as above)
(h): Scatter plot of D_I^ℓ at coordinates (R,Q).
(i): Scatter plot of $\tilde{h}$ at coordinates (R,Q).
(j): Streamlines of velocity.
(k): Isosurfaces of vorticity at 30% and 60% of ω_{max}.
(l): Isosurfaces of local Hölder at $\tilde{h} = 1.3, 1.35$.
(m): Isosurfaces of local energy transfer at $D_I^\ell = 2\epsilon, 3\epsilon$.
(m): Isosurfaces of local energy dissipation at $D_\nu^\ell = 4\epsilon, 5\epsilon$.

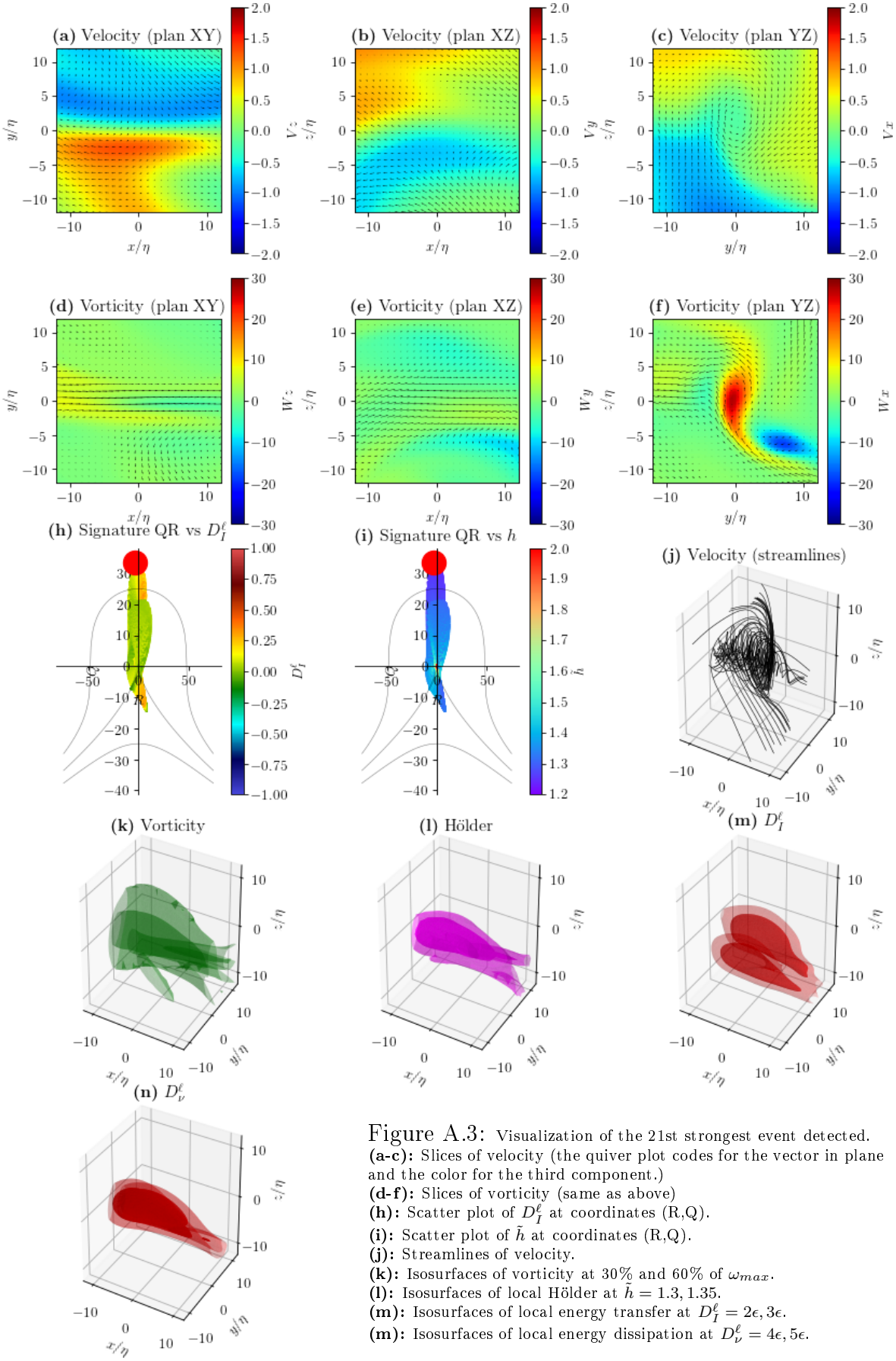

Figure A.3: Visualization of the 21st strongest event detected.
(a-c): Slices of velocity (the quiver plot codes for the vector in plane and the color for the third component.)
(d-f): Slices of vorticity (same as above)
(h): Scatter plot of D_I^ℓ at coordinates (R,Q).
(i): Scatter plot of $\tilde{h}$ at coordinates (R,Q).
(j): Streamlines of velocity.
(k): Isosurfaces of vorticity at 30% and 60% of ω_{max}.
(l): Isosurfaces of local Hölder at $\tilde{h} = 1.3, 1.35$.
(m): Isosurfaces of local energy transfer at $D_I^\ell = 2\epsilon, 3\epsilon$.
(m): Isosurfaces of local energy dissipation at $D_\nu^\ell = 4\epsilon, 5\epsilon$.

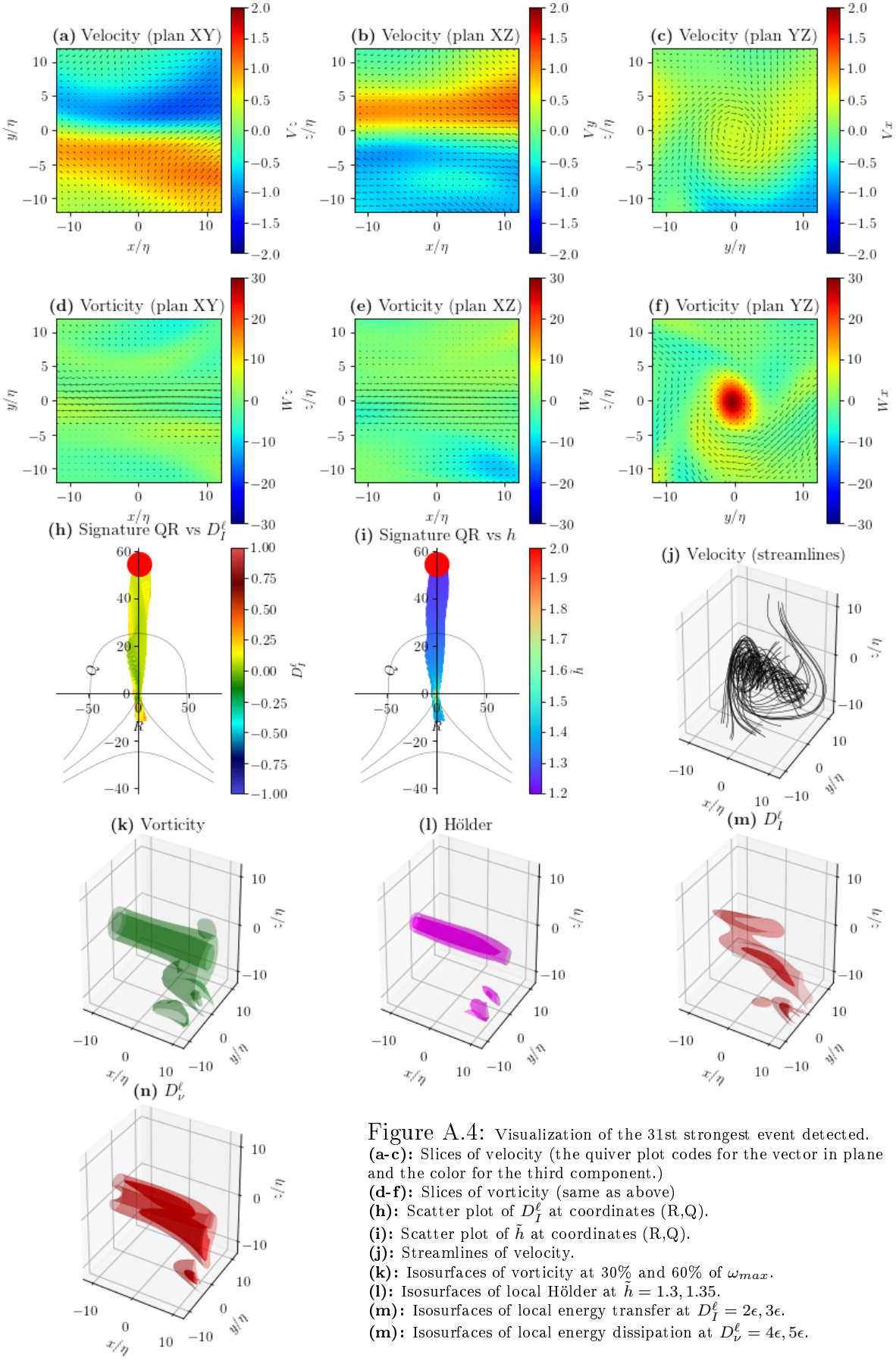

Figure A.4: Visualization of the 31st strongest event detected.
(a-c): Slices of velocity (the quiver plot codes for the vector in plane and the color for the third component.)
(d-f): Slices of vorticity (same as above)
(h): Scatter plot of D_I^ℓ at coordinates (R,Q).
(i): Scatter plot of $\tilde{h}$ at coordinates (R,Q).
(j): Streamlines of velocity.
(k): Isosurfaces of vorticity at 30% and 60% of ω_{max}.
(l): Isosurfaces of local Hölder at $\tilde{h} = 1.3, 1.35$.
(m): Isosurfaces of local energy transfer at $D_I^\ell = 2\epsilon, 3\epsilon$.
(m): Isosurfaces of local energy dissipation at $D_\nu^\ell = 4\epsilon, 5\epsilon$.

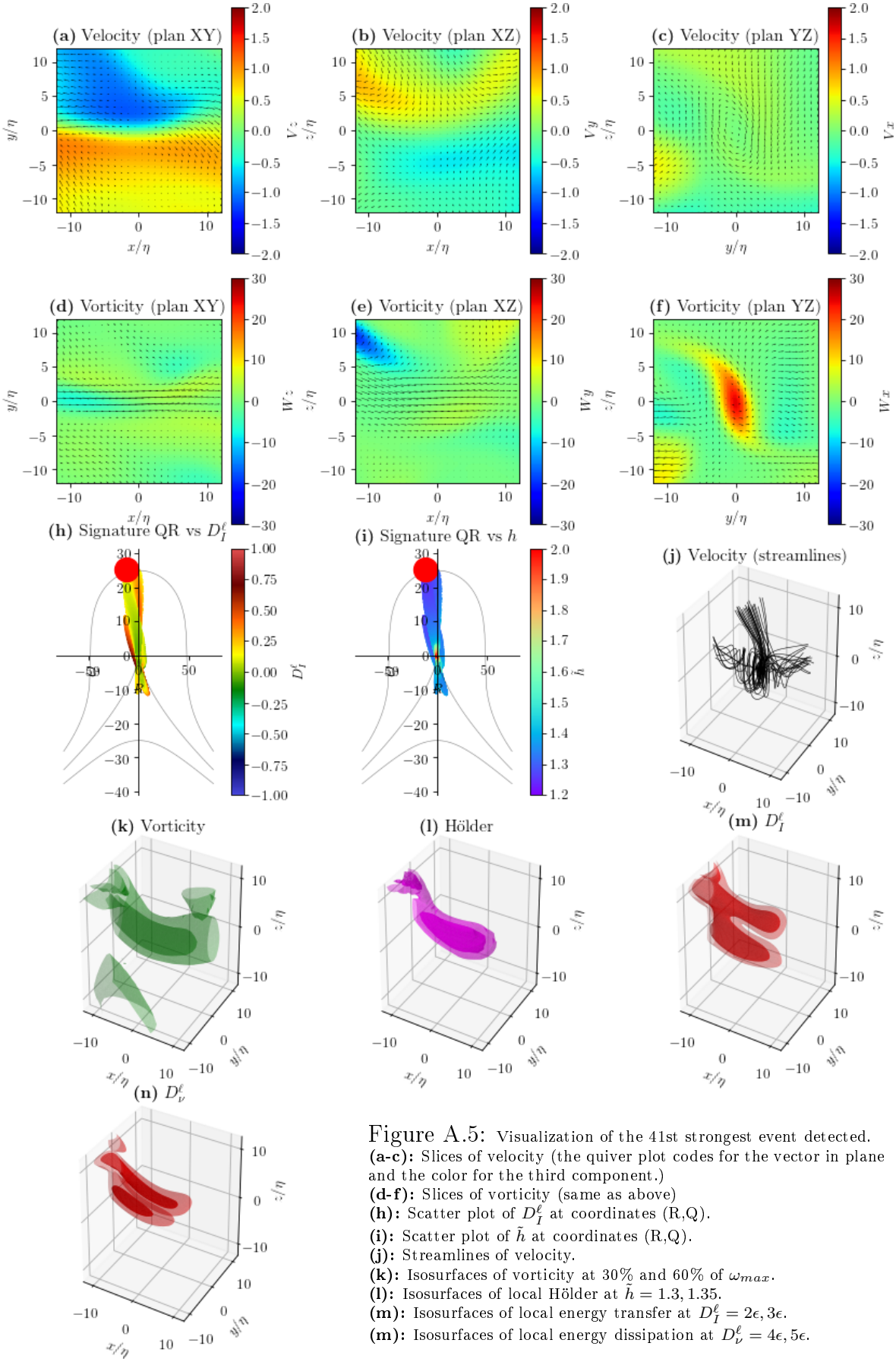

Figure A.5: Visualization of the 41st strongest event detected.
(a-c): Slices of velocity (the quiver plot codes for the vector in plane and the color for the third component.)
(d-f): Slices of vorticity (same as above)
(h): Scatter plot of D_I^ℓ at coordinates (R,Q).
(i): Scatter plot of $\tilde{h}$ at coordinates (R,Q).
(j): Streamlines of velocity.
(k): Isosurfaces of vorticity at 30% and 60% of ω_{max}.
(l): Isosurfaces of local Hölder at $\tilde{h} = 1.3, 1.35$.
(m): Isosurfaces of local energy transfer at $D_I^\ell = 2\epsilon, 3\epsilon$.
(m): Isosurfaces of local energy dissipation at $D_\nu^\ell = 4\epsilon, 5\epsilon$.

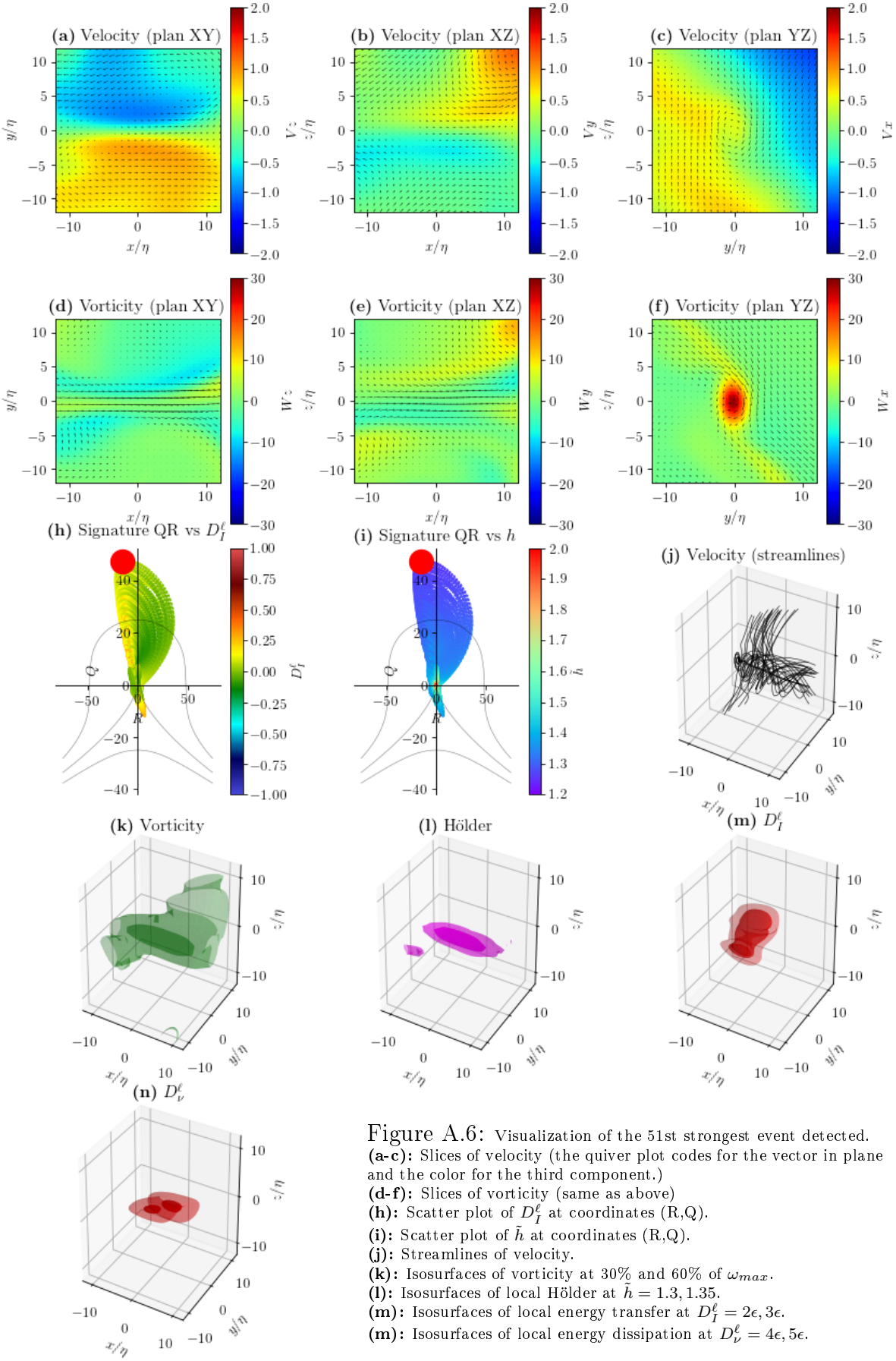

Figure A.6: Visualization of the 51st strongest event detected.
(a-c): Slices of velocity (the quiver plot codes for the vector in plane and the color for the third component.)
(d-f): Slices of vorticity (same as above)
(h): Scatter plot of D_I^ℓ at coordinates (R,Q).
(i): Scatter plot of $\tilde{h}$ at coordinates (R,Q).
(j): Streamlines of velocity.
(k): Isosurfaces of vorticity at 30% and 60% of ω_{max}.
(l): Isosurfaces of local Hölder at $\tilde{h} = 1.3, 1.35$.
(m): Isosurfaces of local energy transfer at $D_I^\ell = 2\epsilon, 3\epsilon$.
(m): Isosurfaces of local energy dissipation at $D_\nu^\ell = 4\epsilon, 5\epsilon$.

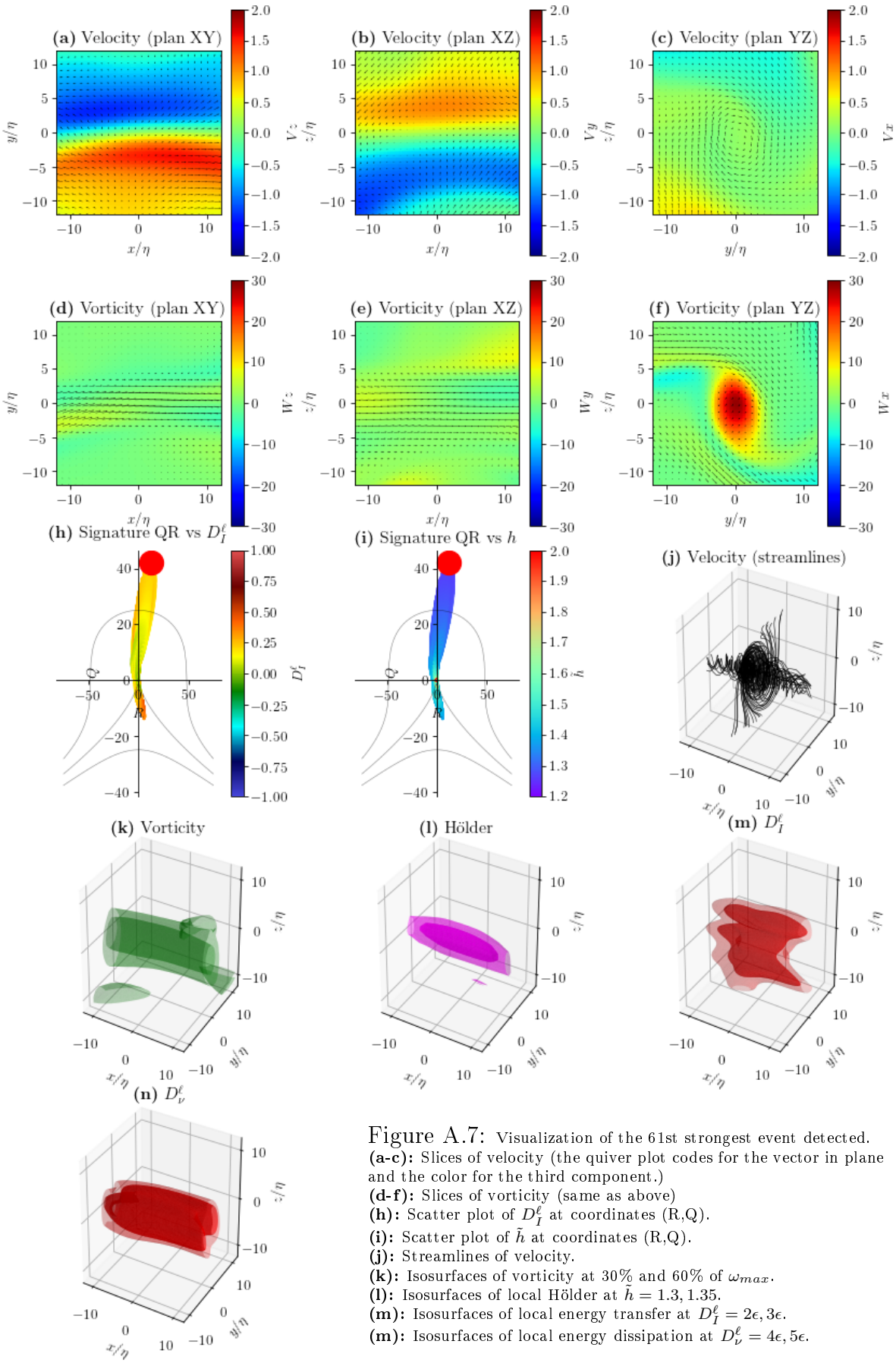

Figure A.7: Visualization of the 61st strongest event detected.
(a-c): Slices of velocity (the quiver plot codes for the vector in plane and the color for the third component.)
(d-f): Slices of vorticity (same as above)
(h): Scatter plot of D_I^ℓ at coordinates (R,Q).
(i): Scatter plot of $\tilde{h}$ at coordinates (R,Q).
(j): Streamlines of velocity.
(k): Isosurfaces of vorticity at 30% and 60% of ω_{max}.
(l): Isosurfaces of local Hölder at $\tilde{h} = 1.3, 1.35$.
(m): Isosurfaces of local energy transfer at $D_I^\ell = 2\epsilon, 3\epsilon$.
(m): Isosurfaces of local energy dissipation at $D_\nu^\ell = 4\epsilon, 5\epsilon$.

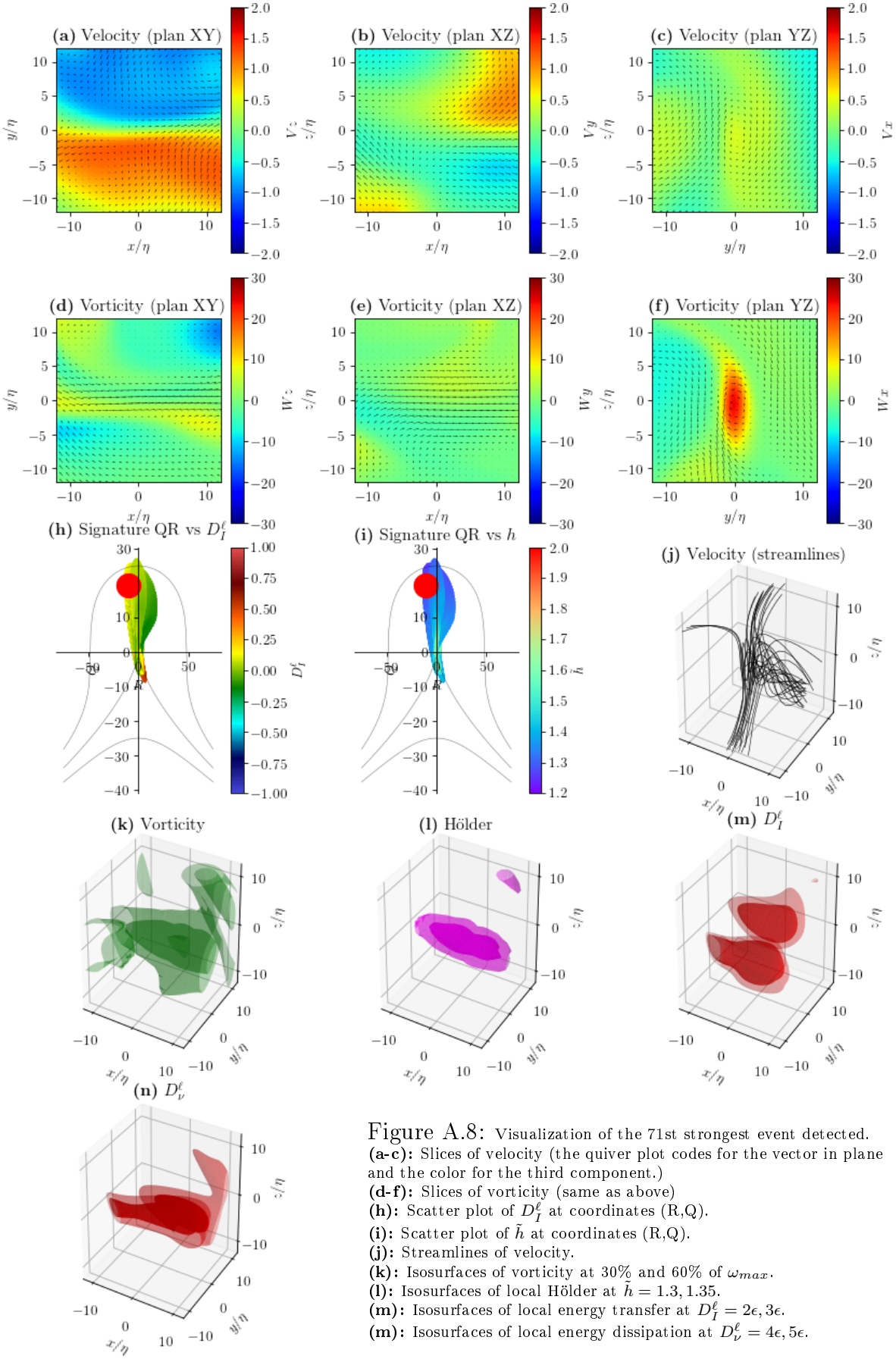

Figure A.8: Visualization of the 71st strongest event detected.
(a-c): Slices of velocity (the quiver plot codes for the vector in plane and the color for the third component.)
(d-f): Slices of vorticity (same as above)
(h): Scatter plot of D_I^ℓ at coordinates (R,Q).
(i): Scatter plot of $\tilde{h}$ at coordinates (R,Q).
(j): Streamlines of velocity.
(k): Isosurfaces of vorticity at 30% and 60% of ω_{max}.
(l): Isosurfaces of local Hölder at $\tilde{h} = 1.3, 1.35$.
(m): Isosurfaces of local energy transfer at $D_I^\ell = 2\epsilon, 3\epsilon$.
(m): Isosurfaces of local energy dissipation at $D_\nu^\ell = 4\epsilon, 5\epsilon$.

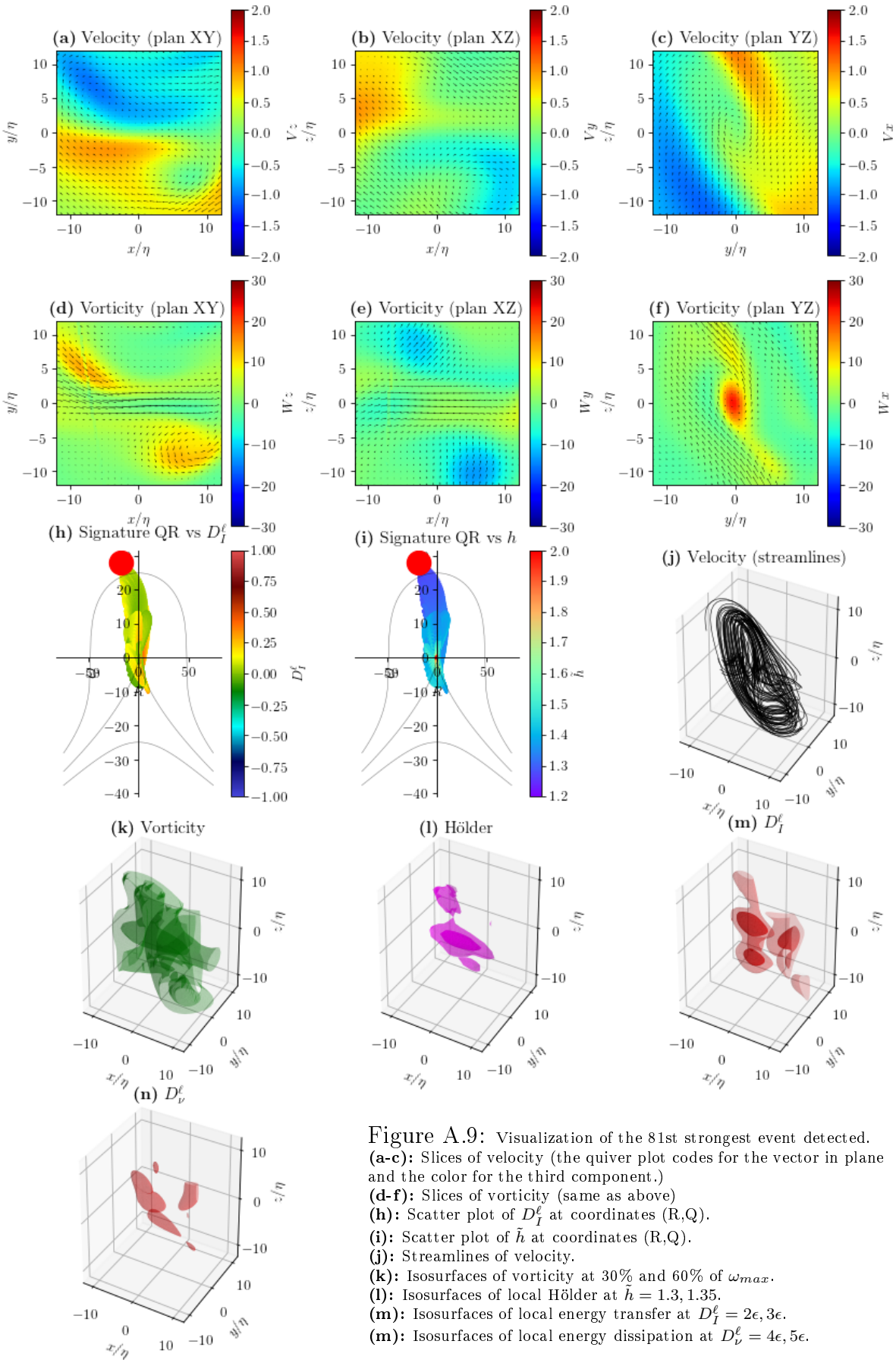

Figure A.9: Visualization of the 81st strongest event detected.
(a-c): Slices of velocity (the quiver plot codes for the vector in plane and the color for the third component.)
(d-f): Slices of vorticity (same as above)
(h): Scatter plot of D_I^ℓ at coordinates (R,Q).
(i): Scatter plot of $\tilde{h}$ at coordinates (R,Q).
(j): Streamlines of velocity.
(k): Isosurfaces of vorticity at 30% and 60% of ω_{max}.
(l): Isosurfaces of local Hölder at $\tilde{h} = 1.3, 1.35$.
(m): Isosurfaces of local energy transfer at $D_I^\ell = 2\epsilon, 3\epsilon$.
(m): Isosurfaces of local energy dissipation at $D_\nu^\ell = 4\epsilon, 5\epsilon$.

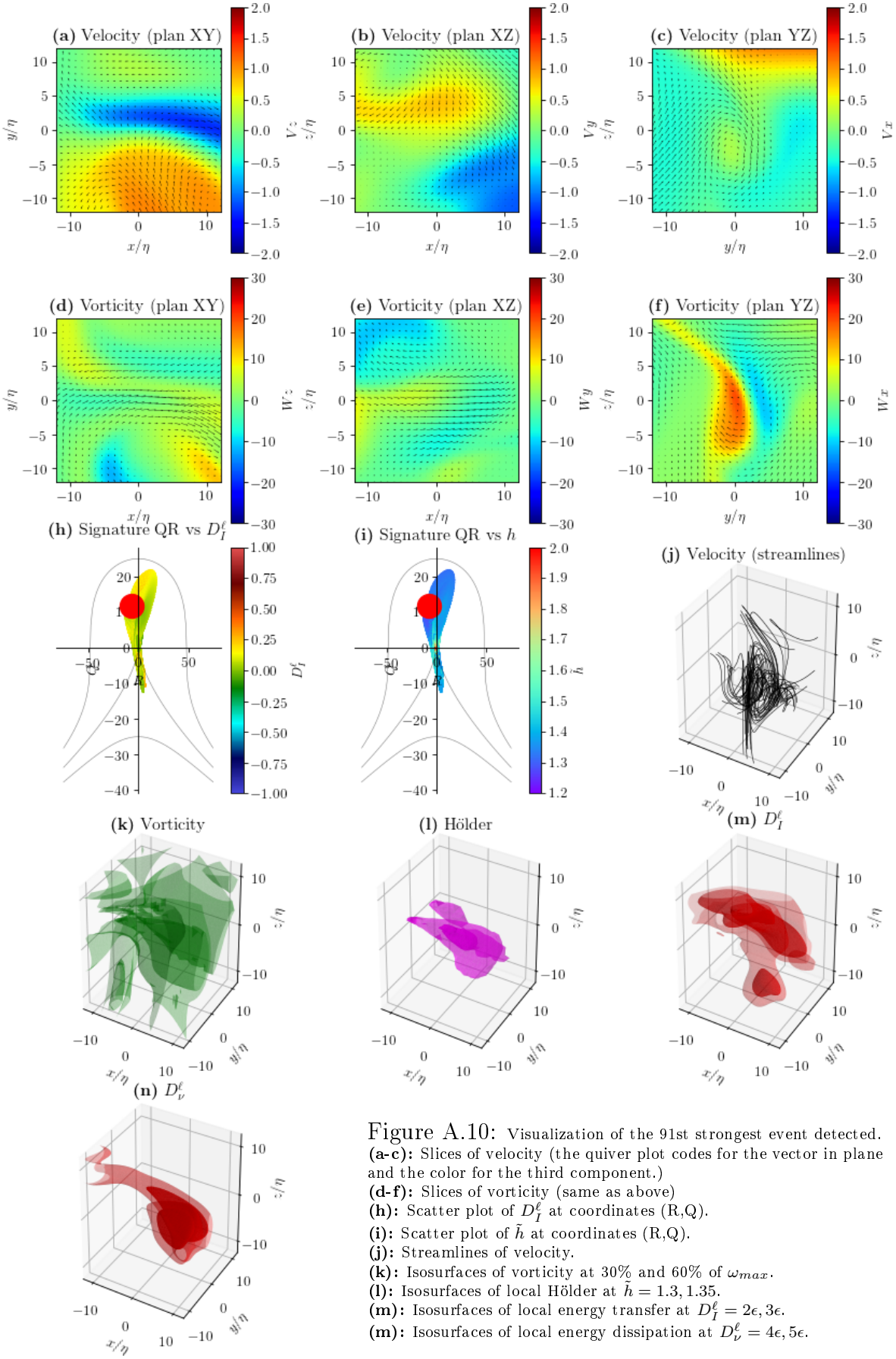

Figure A.10: Visualization of the 91st strongest event detected.
(a-c): Slices of velocity (the quiver plot codes for the vector in plane and the color for the third component.)
(d-f): Slices of vorticity (same as above)
(h): Scatter plot of D_I^ℓ at coordinates (R,Q).
(i): Scatter plot of $\tilde{h}$ at coordinates (R,Q).
(j): Streamlines of velocity.
(k): Isosurfaces of vorticity at 30% and 60% of ω_{max}.
(l): Isosurfaces of local Hölder at $\tilde{h} = 1.3, 1.35$.
(m): Isosurfaces of local energy transfer at $D_I^\ell = 2\epsilon, 3\epsilon$.
(m): Isosurfaces of local energy dissipation at $D_\nu^\ell = 4\epsilon, 5\epsilon$.

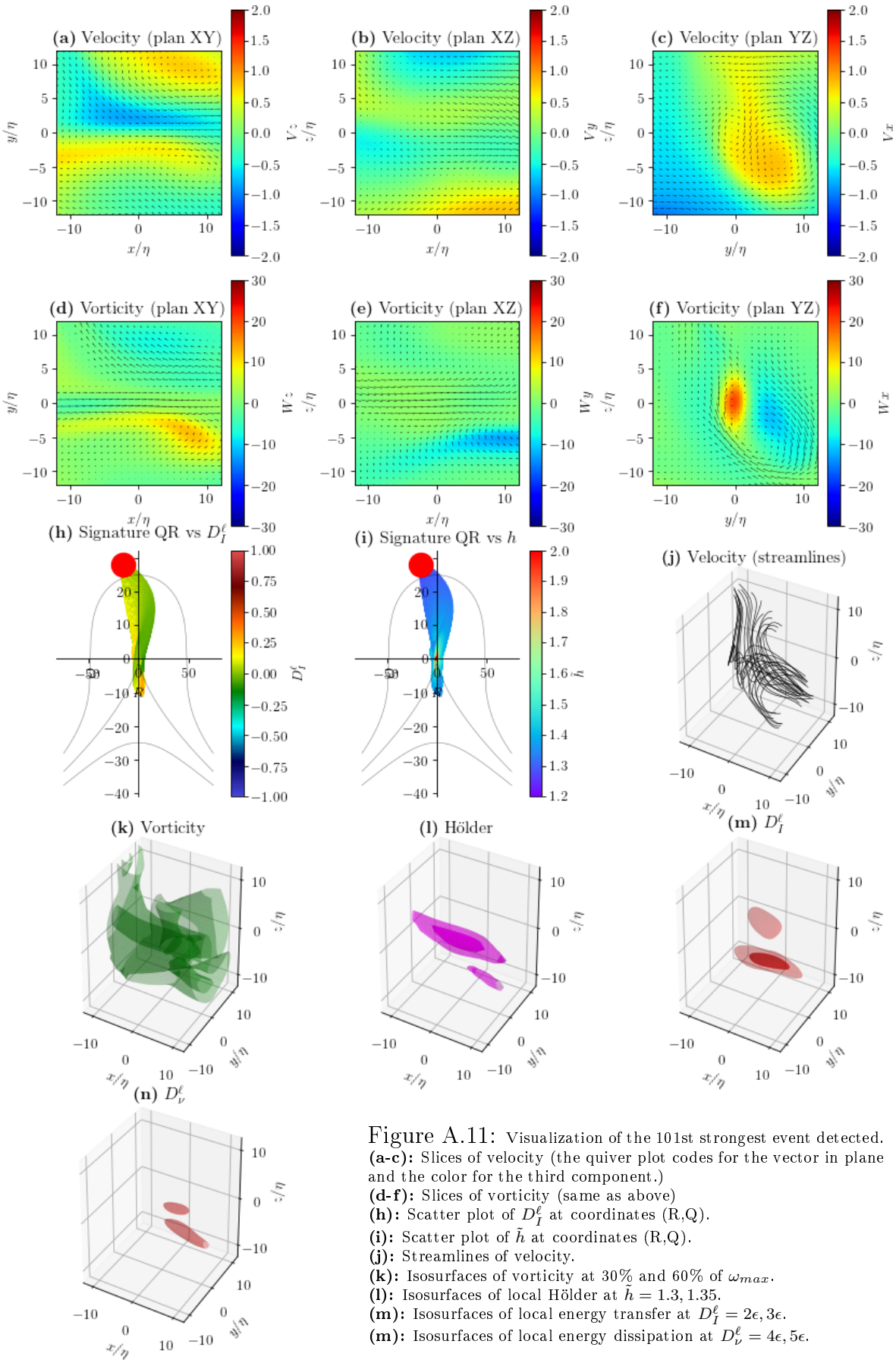

Figure A.11: Visualization of the 101st strongest event detected.
(a-c): Slices of velocity (the quiver plot codes for the vector in plane and the color for the third component.)
(d-f): Slices of vorticity (same as above)
(h): Scatter plot of D_I^ℓ at coordinates (R,Q).
(i): Scatter plot of $\tilde{h}$ at coordinates (R,Q).
(j): Streamlines of velocity.
(k): Isosurfaces of vorticity at 30% and 60% of ω_{max}.
(l): Isosurfaces of local Hölder at $\tilde{h} = 1.3, 1.35$.
(m): Isosurfaces of local energy transfer at $D_I^\ell = 2\epsilon, 3\epsilon$.
(m): Isosurfaces of local energy dissipation at $D_\nu^\ell = 4\epsilon, 5\epsilon$.

Appendix B

Local estimates of Hölder exponents in turbulent vector fields

Reproduction of an article in *Physical Review E* (2019).

Local estimates of Hölder exponents in turbulent vector fields

F. Nguyen, J-P. Laval
*Univ. Lille, CNRS, ONERA, Arts et Metiers ParisTech, Centrale Lille, FRE 2017-LMFL-Laboratoire de Mécanique des Fluides de Lille-Kampé de Fériet, F-59000, Lille, France**

P. Kestener
Maison de la Simulation CEA, CNRS, Université Paris-Saclay, CEA Saclay, 91190 Gif-sur-Yvette, France

A. Cheskidov and R. Shvydkoy
Department of Mathematics, Statistics, and Computer Science, M/C 249, University of Illinois, Chicago, IL 60607, USA†

B. Dubrulle
SPEC, CEA, CNRS, Université Paris-Saclay, CEA Saclay, 91190 Gif-sur-Yvette, France

It is still not known whether solutions to the Navier-Stokes equation can develop singularities from regular initial conditions. In particular, a classical and unsolved problem is to prove that the velocity field is Hölder continuous with some exponent $h < 1$ (i.e. not necessarily differentiable) at small scales. Different methods have already been proposed to explore the regularity properties of the velocity field, and the estimate of its Hölder exponent h. A first method is to detect of potential singularities via extrema of an "inertial" dissipation $D* = \lim_{\ell\to 0} D^I_\ell$ that is independent on viscosity [1]. Another possibility is to use the concept of multifractal analysis that provides fractal dimensions of the subspace of exponents h. However, the multifractal analysis is a *global statistical* method that only provides a *global* information about local Hölder exponents, via their probability of occurrence. In order to explore the local regularity properties of a velocity field, we have developed a *local statistical* analysis, that estimates locally the Hölder continuity. We have compared outcomes of our analysis, with results using the inertial energy dissipation D^I_ℓ. We observe that the dissipation term indeed gets bigger for velocity fields that are less regular according to our estimates. The exact spatial distribution of the local Hölder exponents however shows non trivial behavior and does not exactly match the distribution of the inertial dissipation.

I. INTRODUCTION.

Viscous incompressible fluids are described by the Incompressible Navier-Stokes equations (INSE) in space-time

$$\begin{aligned} \partial_t u_i + u_j \partial_j u_i &= -\frac{1}{\rho}\partial_i p + \nu \partial_j \partial_j u_i + f_i, \qquad (1)\\ \partial_j u_j &= 0, \end{aligned}$$

where Einstein summation convention over repeated indices is used and $u_i(x,y,z,t)$ is the velocity field, $p(x,y,z,t)$ the pressure field, ρ the (constant) mass density, $f_i(x,y,z,t)$ some forcing and ν the molecular viscosity. A natural control parameter for the INSE is the Reynolds number $Re = LU/\nu$, which is built using a characteristic length L and velocity U.

Mathematically, it is not known whether a solution of the INSE which is smooth at some initial time remains smooth at all later times. This problem was first addressed by Leray [2] who introduced the notion of weak solutions (i.e. in the sense of distribution). This notion has since remained a framework to explore regularity condition for both INSE and its inviscid limit, the Euler equation. It prompted people to consider weaker regularity conditions on $\boldsymbol{u}$. In particular, a classical and unsolved problem is to prove that the velocity field is Hölder continuous with some exponent $h < 1$ (i.e. not necessarily differentiable) at small scales, i.e. to find under which conditions the following holds:

$$|\boldsymbol{u}(\mathbf{x}+\boldsymbol{\ell}) - \boldsymbol{u}(\mathbf{x})| < C\ell^h. \qquad (2)$$

Let us note that Hölder continuity defined in equation (2) is a weaker regularity condition than differentiability and uses the velocity increment $\delta\mathbf{u}(\mathbf{x},\boldsymbol{\ell}) = \mathbf{u}(\mathbf{x}+\boldsymbol{\ell}) - \mathbf{u}(\mathbf{x})$ as a building block.

A perhaps more tractable problem is to consider local scaling (Hölder) exponents of the velocity fields. They are defined as:

$$h(\boldsymbol{x}) = \lim_{\ell\to 0} \frac{\ln\left(\max_{|\boldsymbol{\ell}|=\ell} |\delta\boldsymbol{u}(\boldsymbol{x},\boldsymbol{\ell})|\right)}{\ln(\ell/L)}, \qquad (3)$$

where L is a characteristic integral length of scale. Mathematically, these exponents are only defined under the assumption that the limit $\nu \to 0$ is taken, before the limit $\ell \to 0$. In the sequel, we consider extension of this definition by intermediate asymptotic in a range of scale

* florian.nguyen@univ-lille.fr
† shvydkoy@uic.edu; acheskid@uic.edu

$\eta_{h(x)} \ll \ell \ll L$, where $\eta_{h(x)} \sim LRe^{-1/(1+h(x))}$. It is however still difficult to estimate directly such local Hölder exponents via a simple fit on velocity increments based on equation (3). Indeed, since accessible resolutions numerically or experimentally do not allow to probe the velocity field at arbitrarily small scale, the range of scales over which the fit is performed is limited. This induces a lot of noise in the determination of $h(x)$, that makes it unreliable.

A *global* statistical method, was developed by Parisi and Frisch [3] to quantify the probability of observation of a singularity of scaling exponent h via a function $C(h)$. From $C(h)$ we may infer the multifractal spectrum as $D(h) = D - C(h)$, where D is the space dimension. The team of A. Arneodo developed a powerful method based on wavelet transform to measure such spectrum for 1D turbulent velocity fields. This method has been applied to experimental measurements of one velocity component at a single point at high Reynolds numbers in [4], where it was shown that the data are compatible with the multifractal picture, with a most probable h close to 1/3. Later Kestener and Arneodo [5] extended the method to 3D signals (3 components of the velocity field), and showed on a numerical simulation that the picture provided by the 1D measurements was still valid, with the most probable h shifting closer to 1/3.

Since the original MFR method is based on statistical properties, it is robust with respect to noise and limited statistics. However, it only provides a *global* information about local Hölder exponents, via their probability of occurrence. In order to explore the regularity properties of a velocity field, it would however be useful to devise a *local statistical* analysis, that keeps the robustness of the global MFR method and quantify *locally* the Hölder continuity, while avoiding pitfalls induced by a naive direct fit of equation (3). In the present paper, we extend recent mathematical results of [6] to multifractal settings to provide the best local estimate of Hölder regularity compatible with the global MFR analysis. Our method is in spirit similar to an inference algorithm based on information theory: the local estimate depends on non-dimensional constants that are are statistically fitted on the available data set. Therefore, the estimate depends on the data set, and can only provide information a posteriori. The larger the data set, the more information available, the better the estimate. In our case, the larger the data set, the lowest values of h can be explored.

The paper is organized as follows: in Section II, we describe the wavelet based velocity increments and our method for anisotropic multifactal analysis. In Section III, we generalize the notion of active volume introduced by [6] and show how it can be used to build a local estimate of the Hölder exponents . The method is tested using a fractional brownian motion in Section IV. It is further implemented on 3D turbulent velocity fields computed using DNS in Section V. Our results are discussed in Section VI.

II. VELOCITY INCREMENTS AND MULTIFRACTAL

Our method relies heavily on velocity increments and multifractal theory. We therefore provide some generalities about velocity increments in appendix A. We then proceed by defining our new approach using wavelet transforms.

A. Wavelet velocity increments

For an incompressible velocity field, both side of the first equation in (A6) are reduced to zero, so we cannot use it to get any information on ϕ, the potential part of the velocity field. The usual velocity increments defined in equation (A2) can be seen as the wavelet transform of the velocity with a Haar wavelet. This motivates us to define wavelet velocity increments $\delta W(\mathbf{u})$ through the smoothed velocity gradient G^ℓ_{ij} and its symmetric and antisymmetric parts defined as:

$$\begin{aligned} G^\ell_{ij} &= \ell \int \frac{d\mathbf{y}}{\ell^3} \nabla_j \Psi\left(\frac{\mathbf{y}}{\ell}\right) u_i(\mathbf{y}), \\ S^\ell_{ij} &= \frac{1}{2}\left(G^\ell_{ij} + G^\ell_{ji}\right), \\ A^\ell_{ij} &= \frac{1}{2}\left(G^\ell_{ij} - G^\ell_{ji}\right), \end{aligned} \tag{4}$$

where $\Psi(\mathbf{x}) = \exp(-x^2/2)/N$ is the Gaussian function. By construction, A^ℓ_{ij} is a function only of the rotational part $\mathbf{Q}$, and S^ℓ_{ii} is a function only of ϕ.

We then define normal, longitudinal and transverse wavelet velocity increments as:

$$\begin{aligned} \delta_L W_\ell(\mathbf{u}) &= \max_{ij} |S^\ell_{ij}|, \\ \delta_P W_\ell(\mathbf{u}) &= \max_{ij} |A^\ell_{ij}|, \\ \delta_G W_\ell(\mathbf{u}) &= \left(\delta_L W_\ell(\mathbf{u})^2 + \delta_P W_\ell(\mathbf{u}^2)\right)^{1/2}. \end{aligned} \tag{5}$$

By construction, $\delta_P W_\ell(\mathbf{u})$ provides information only on the rotational part of the velocity field, while all information regarding the potential part is stored in $\delta_L W_\ell(\mathbf{u})$. The component $\delta_G W_\ell(\mathbf{u})$ gives general scaling properties about the velocity field.

This definition bears some similarity with the definition by Kestener and Arneodo [5], that uses principal values of $|G^\ell_{ij}|$. Like theirs, our definition involves no derivative over velocity fields, so it does not introduce additional noise. However, our definition does not involve computation of singular values, that may generate some noise. So, our definition is the smoothest possible one can imagine that enables to quantify scaling properties of potential and rotational part of a given velocity field.

B. Multifractal theory

The multifractal (hereafter MFR) theory that assumes that the Hölder exponent at scale ℓ, defined as

$$h\left(\boldsymbol{x},\ell\right)=\frac{\ln\left(\max_{|\boldsymbol{\ell}|=\ell}\left|\delta\boldsymbol{u}\left(\boldsymbol{x},\boldsymbol{\ell}\right)\right|\right)}{\ln\left(\ell/L\right)}, \tag{6}$$

follows a large deviation property [3]

$$\mathrm{Prob}\left(h\left(\boldsymbol{x},\ell\right)=h\right)\sim\left(\frac{\ell}{L}\right)^{C(h)}. \tag{7}$$

Formally, $C(h)$ corresponds to the codimension of the set where the local Hölder exponent at scale ℓ is equal to h. From $C(h)$ we may infer the MFR spectrum as $D(h)=D-C(h)$, where D is the space dimension.

1. Computation of the multifractal spectrum

Parisi and Frisch devised in 1987 the first global determination of the multifractal spectrum through the structure functions [3]. The latter are defined from the velocity increments and are supposed to scale as:

$$\langle|\delta u|^p\rangle\propto\ell^{\zeta(p)}. \tag{8}$$

The set of scaling exponents $\zeta(p)$ is then connected to the multifractal spectrum through a Legendre transform:

$$\zeta(p)=min_h(ph+D-D(h)), \tag{9}$$

Assuming the spectrum $D(h)$ is strictly concave, we can apply a variational formula to recover:

$$h(p)=\frac{d\zeta(p)}{dp}. \tag{10}$$

Notice that for $p=0$, $h(0)$ represents the most probable scaling exponent (with $D(h)$ equals to the full space dimension). When $p\to-\infty$, the right part of the MFR spectrum (the more and more regular points) is explored; while when $p\to+\infty$, it is the left part of the MFR spectrum (the more and more singular points). This method is global in the sense that it uses global averages of velocity increments to get the multifractal spectrum, and the set of available Hölder exponents. It provides the probability to observe a given Hölder exponent, but provides no information about their exact location. Other methods have been designed based on structure functions. One notable example is the work of Jensen [7] which uses an inverted version of equation (8) to obtain potentially more accurate results for $p<0$. As we are more interested in probing the less regular region of the velocity field, corresponding to $p>0$, we will not use this method in the following.

2. WTMM method

In 1991, A. Arneodo and his group showed that a much more efficient algorithm of computation of the multifractal spectrum for scalar fields was possible, provided one uses structure functions based on wavelet increments instead of velocity increments. An extension of this method to 3D vector field was developed later by Kestener [5, 8] based on singular value decomposition of the wavelet transform of the velocity gradient $G_{ij}=\partial_j u_i$. Here, we apply their algorithm, using the smooth velocity increments equation (5). The algorithm follows the (*Wavelet Transform Modulus Maxima*) (WTMM) method. We first compute the wavelet transform skeleton, which provides us with a set of lines $\{\mathcal{L}_k\}$ where $\mathcal{L}_k(\ell)$ gives the position of the line indexed by k at scale ℓ. Then, one computes the partition functions for the different type of wavelet based increments as follow:

$$\mathcal{Z}_T(q,\ell)=\sum_{\mathcal{L}_k\in\mathcal{L}(\ell)}\Big(\delta_T W_\ell(\boldsymbol{u})(\mathcal{L}_k(\ell))\Big)^q \tag{11}$$

where T stands for G,L or P, $q\in\mathbb{R}$ and $\mathcal{L}(\ell)$ is the set of lines that exists at scale ℓ.

Those partitions functions behave as a power law of the scale:

$$\mathcal{Z}_T(q,\ell)\propto\ell^{\tau_T(q)}. \tag{12}$$

Then by Legendre transforming $\tau_T(q)$, we get the singularity spectrum $D_T(h)=\min_q(qh-\tau_T(q))$. Alternatively, we can bypass the Legendre transform by computing:

$$h_T(q,\ell)=\sum_{\mathcal{L}_k\in\mathcal{L}(\ell)}\ln|\delta_T W_\ell(\boldsymbol{u})(\mathcal{L}_k(\ell))|\mathcal{W}(q,\mathcal{L}_k,\ell), \tag{13}$$

$$D_T(q,\ell)=\sum_{\mathcal{L}_k\in\mathcal{L}(\ell)}\delta_T W_\ell(\boldsymbol{u})(\mathcal{L}_k(\ell))\ln\Big(\mathcal{W}(q,\mathcal{L}_k,\ell)\Big) \tag{14}$$

where $\mathcal{W}(q,\mathcal{L}_k,\ell)=\frac{1}{\mathcal{Z}_T(q,\ell)}\Big(\delta_T W(\boldsymbol{u},\ell)(\mathcal{L}_k(\ell))\Big)^q$ is a Boltzmann weight computed from the wavelet transform skeleton. These quantities behave as power laws as follows:

$$h_T(q,\ell)\propto\ell^{h_T(q)}, \tag{15}$$

$$D_T(q,\ell)\propto\ell^{D_T(q)} \tag{16}$$

and thus we can recover the singularity spectrum $D_T(h)$.

III. LOCAL CHARACTERIZATION OF MULTIFRACTAL VECTOR FIELDS

The previous section describes a procedure to compute globally a multifractal spectrum. We now describe a method that gives access to estimates of local scaling properties of the velocity field, using the notion of nested active volume described in appendix B.

A. Active volumes and multifractal

We first define $\mathcal{S}_{p,dp}$ as:

$$\mathcal{S}_{p,dp}(\ell) = \left(\frac{\langle (\delta W_\ell(\mathbf{u}))^{p+dp} \rangle}{\langle (\delta W_\ell(\mathbf{u}))^{p} \rangle}, \right)^{1/dp}. \tag{17}$$

The limit as $dp \to 0$ can be computed as:

$$\mathcal{S}_p(\ell) \equiv \mathcal{S}_{p,0}(\ell) = \exp\left(\frac{\langle \ln\left(\delta W_\ell(\mathbf{u})\right) \left(\delta W_\ell(\mathbf{u})\right)^p \rangle}{\langle \left(\delta W_\ell(\mathbf{u})\right)^p \rangle}, \right). \tag{18}$$

One can prove that if $\mathbf{u}$ is multifractal, then :

$$\ln \mathcal{S}_p(\ell) \approx h(p) \ln \ell, \tag{19}$$

which gives access to the value $h(p)$.

We can then define the active volume A_p by:

$$\mathbf{x} \in A_p \quad iff \quad \delta W_\ell(\mathbf{u})(\mathbf{x}) \geqslant c_p \mathcal{S}_p(\ell), \tag{20}$$

where c_p is a scale independent constant, to be fitted consistently later. The property verified by the points in the volume $F_{h(p)}$ is analogous to the property of equation (2). This analogy leads us to define a local singularity exponent $\tilde{h}$ such that all elements $\mathbf{x}$ in A_p verify $\tilde{h}(\mathbf{x}) \leqslant h(p)$. As a result, the frontier of this volume, i.e. the isosurface of the increment $\delta W_\ell(\mathbf{u})$ at value $c_p \mathcal{S}_{p,0}(\ell)$, is identified as the set of the points where the local singularity exponent is $\tilde{h}$.

While the local Hölder exponent h cannot be continuous in the multifractal formalism, the exponent $\tilde{h}$ is continuous by definition. As a result, it is not a real measure of the Hölder exponent. However, it will still be relevant as a measure of the local regularity of the field, hence the name "singularity exponent". This property will be shown by comparing it to other used criteria in the following part.

B. Statistical fitting of the constants

To completely define the field $\tilde{h}(\mathbf{x})$, we need to fix the scale independent constants c_p. These constants are the core of the method, as we can tune them such that the field of singularity exponents $\tilde{h}$ provide a meaningful estimation of the real Hölder exponent smoothed at the scale ℓ. In order to guarantee that the singularity exponent is physically consistent with the global multifractal properties, we set c_p such that the fractal dimensions of the isosurfaces of $\tilde{h}$ match with the multifractal spectrum. More formally:

$$\mathrm{Dim}\left(\left\{ \mathbf{x} | \tilde{h}(\mathbf{x}) = h \right\} \right) = D(h). \tag{21}$$

This leads directly to:

$$\mathrm{Dim}\left(\{ \mathbf{x} | \delta W_\ell(\mathbf{u})(\mathbf{x}) = c_p \mathcal{S}_p(\ell) \} \right) = D(h(p)). \tag{22}$$

In practice the dimension of the isosurfaces of $\tilde{h}$, which are also isosurfaces of the velocity increment, can be measured using a box-counting method. If we note $D^\ell_{bc}(\mathcal{T})$ the box-counting dimension of the isosurface of the velocity increment at scale ℓ of value $\mathcal{T}$, the problem reduces to the following equation:

$$D^\ell_{bc}(c_p \mathcal{S}_p(\ell)) = D(h(p)). \tag{23}$$

The multifractal spectrum are obtained by WTMM, the $\mathcal{S}_p(\ell)$ can be computed from the fields, as well as the function D^ℓ_{bc}. The quantity $h(p)$ can be accessed using the WTMM or power laws on the $S_p(\ell)$ as described in equation (19). As the two methods are expected to give similar results, we will choose in practice the method of fitting power laws over the functions $S_p(\ell)$ for simplicity. The functions involved are not monotonous so equation (23) could have multiple c_p solution. However, we can expect the function $D^\ell_{bc}(\mathcal{T})$ to be concave with a maximum at $\mathcal{T}_{max}$. If we impose $c_p \mathcal{S}_p(\ell) < \mathcal{T}_{max}$ for $p > 0$ and $\mathcal{T}_{max}$ and $c_p \mathcal{S}_p(\ell) > \mathcal{T}_{max}$ for $p < 0$, we get a unique definition of c_p.

Note that our method ensures that the field $\tilde{h}(\mathbf{x})$ can be recovered without computing explicitly the constant c_p. Indeed, we can derive a relationship $\tilde{h}(\mathcal{T})$ from the following equation:

$$D^\ell_{bc}(\mathcal{T}) = D(\tilde{h}), \tag{24}$$

which is derived from equation (21). We can ensure that this function is well defined by imposing $\tilde{h}(\mathcal{T}) < h(p = 0)$ for $\mathcal{T} > \mathcal{T}_{max}$ and reciprocally. While this is the method we will use preferentially to compute maps of $\tilde{h}$, the knowledge of c_p is still pertinent as it is scale independent. This property makes it possible to test the soundness of the method by checking that the procedure, repeated at a different scale, verify the equation (22) for the same value of c_p. Once a value of c_p is computed using one scale, one can then obtain maps of $\tilde{h}$ at any scale in the inertial range for a much lower computational cost. The accuracy of this statements will be discussed in the following.

IV. APPLICATION TO FRACTIONAL BROWNIAN MOTION (FBM)

A. Definition and implementation of fBm

In order to test our analysis, we used synthetic field with well determined fractal behavior. The simplest possible field in this case is the fractional Brownian motion (or fBm), which was already used in [5]. The fBm has properties of isotropy that can be characterized by a single Hölder exponent H for any point.

As a consequence, the multifractal spectrum of a fBm of exponent H in dimension d reduces to a single point:

$$\begin{aligned} D(h) &= d && if \quad h = H, \\ &= -\infty && otherwise. \end{aligned} \tag{25}$$

In this case, the exponent $\tau(q)$ of both the original WTMM method and our variation should have the following expression:

$$\tau(q) = qH - d. \tag{26}$$

The fBm used in the following are generated by filtering the Fourier transform of a white noise. This method gives a good approximation of the expected invariance properties. For all purposes requiring a range of Hölder exponents, it is assumed that this practical realization with a finite number of snapshots of finite size has a wider multifractal spectrum, centered around the theoretical value H. We chose the value of $H = 1/3$ for a 2 dimensions, 3 components (2D3C) fBm. The objective in the following is to recover this value H using both the original WTMM and our variation of it.

B. Test of the global MFR analysis

As a first test and benchmark of our methods, we generate a hundred 2D3C fBm ($H = 1/3$) in squares of size unity with a definition of 4096×4096. The Figure 1 shows the $\tau(q)$ corresponding to the different components, as well as the output of the original WTMM method.

The results of our new method are consistent with the theoretical predictions, although a little less accurate than the native method. The consequence of this lack of accuracy is an estimation of the Hölder exponent $h \approx 0.31$ using the global term, which is slightly inferior to the value of $h \approx 0.33$ evaluated by the original WTMM method. Furthermore, the computation of the perpendicular component suffers from the lack of the third dimension in the provided fields, hence a spectrum spreading over a much wider range of h than expected.

C. Test of the local estimate

In parallel, we can apply our second method to extract the local coefficients $\tilde{h}$ in one field of the same set of fBm. The computation requires to chose a value of ℓ. In the sequel, we fix the value $\ell = 2.8 \times 10^{-3}$ for any computation on the fBm at definite ℓ. This value, corresponding to 11.4 grid points at the resolution of the field, is small enough to probe the small structures and large enough so that wavelets are well resolved. The Figure 2 shows the function $D^{\ell}_{bc}(\mathcal{T})$ resulting from the boxcounting, while the Figure 3 illustrates the power law behavior of $\mathcal{S}_p(\ell)$. The values of h are convincingly independent with respect to p, with very little fluctuations. The value of h obtained is around $h \approx 0.34$, which is slightly higher than the expected value of $H = 1/3$ but still within acceptable range.

Applying the method described to compute fields of $\tilde{h}$ would normally require to match the box-counting dimensions from Figure 2 with the multifractal spectrum from Figure 1. Unfortunately, the degenerated spectrum makes it impractical. A solution is to use the fact that we are working with a monofractal and ensure that for all p, $c_p \mathcal{S}_p(\ell) = \mathcal{T}_{max}$. Considering the fact that it is very difficult to get measurements of box counting dimension that reach 2, the dimension of the space, we also take the liberty to renormalize $D^{\ell}_{bc}(\mathcal{T})$ such that $D^{\ell}_{bc}(\mathcal{T}_{max}) = 2$.

In this artificial case, analyzing maps of $\tilde{h}$ will not be very instructive, so we verify the validity of using the scale invariant coefficients c_p in order to compute fields

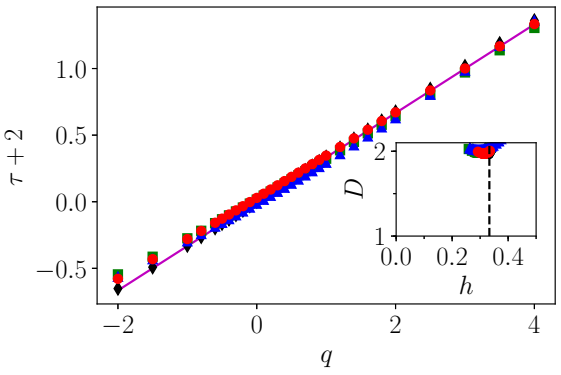

FIG. 1. **Main figure:** Exponent τ as a function of the parameter q for the global (red circles), longitudinal (green squares), perpendicular (blue triangles) components as well as for the native method (black diamonds) applied to 100 fields of fBm in 2 dimensions with 3 components of velocity at $H = 1/3$. The 3 components are generated independently before enforcing the divergence free condition. The theoretical curve from equation (26) is materialized by the solid magenta line. **Inset figure:** Corresponding parametric plot of $D(q)$ with respect to $h(q)$. The dashed line materializes the theoretical value of $H = 1/3$.

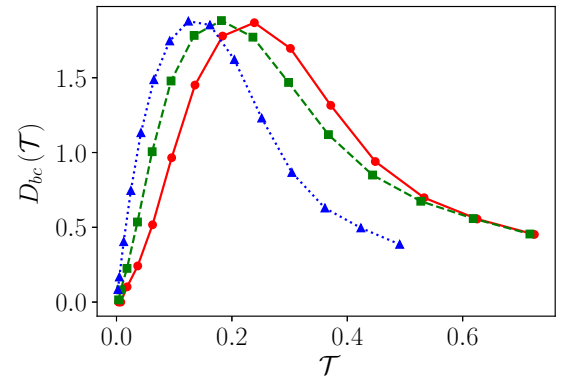

FIG. 2. Box counting dimension of the isocontours of the global (solid red), longitudinal (dashed green) and perpendicular (dotted blue) components of the wavelet based velocity increments for $\ell = 2.8 \times 10^{-3}$ for the fBm.

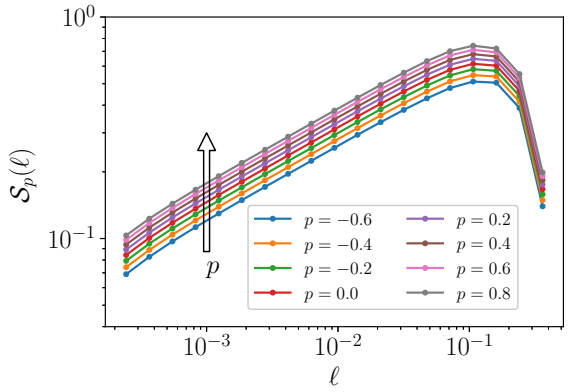

FIG. 3. Values of the threshold $\mathcal{S}_p(\ell)$ for the global increments as a function of scale for several p for the fBm. The values of p increase from bottom to top.

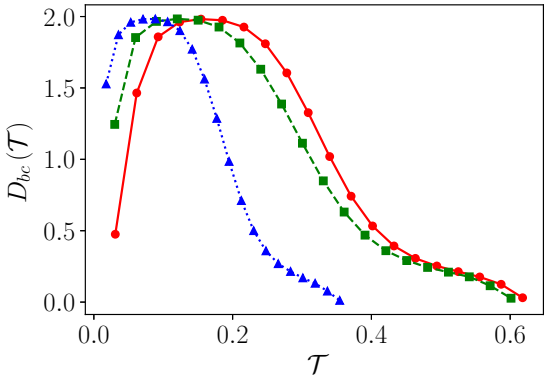

FIG. 4. Box counting dimension of the isocontours of the different components of the wavelet based velocity increments for $\ell = 8.2\times10^{-4}$ for the fBm. The color code for the different components is the same as for the previous figure.

of $\tilde{h}$ at a different scale. To such aim, we use instead the box-counting dimension at the lower scale $\ell_2 = 8.2\times10^{-4}$ corresponding to approximately 3.4 grid points. This allows to check that equation (23) is satisfied, thus proving the point in the case of fractional Brownian motion.

The Figure 4 shows the box-counting dimension of the isosurfaces of "velocity" increments computed at the scale ℓ_2. Although the quality of the measure is lower for less resolved wavelets, we can still verify that the pseudo multifractal spectra constructed using the scaling exponent from the $\mathcal{S}_p(\ell)$, the c_p obtained at higher scale and the box counting dimensions from Figure 4, is coherent with the theoretical spectrum, as illustrated in Figure 5.

Now that the methods have been tested in the case of fBms, we apply them in the more complex and realistic case of turbulence fields.

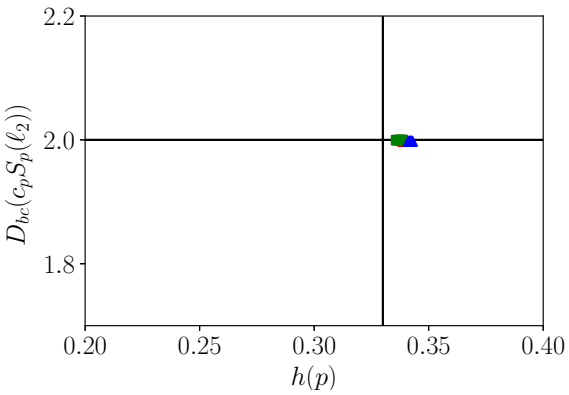

FIG. 5. Pseudo "multifractal spectrum" reconstructed from the boxcounting dimensions of isovalues of velocity increments at scale $\ell = 8.2\times10^{-4}$ and the scaling laws over the $S_p(\ell)$. The red circles (resp. green squares, blue triangles) correspond to the spectrum reconstructed using the global (resp. longitudinal, perpendicular) increments. The solid vertical line materializes the theoretical $h = 1/3$.

V. APPLICATION TO VELOCITY FIELDS IN NUMERICAL SIMULATION

A. Characteristics of the numerical simulation

We generate turbulent velocity fields via two simulations of turbulence in a box of size 2π. The corresponding parameters are presented in Table I. We use a pseudo spectral code [9] with a forcing term with the symmetries of the Taylor–Green vortex. The first simulation (Run I) provides velocity fields with an inertial range large enough to validate our method against known scaling laws. The second simulation (Run II) is very well resolved with an extensive dissipative range. It will allow us to probe the actual singular behavior of the flow at small scales of the order of the Kolmogorov scale. The energy spectra presented Figure 6 illustrate the difference of scale resolution between these two simulations.

B. MFR spectra

By applying the previously described variation of the WTMM method, we extract the global multifractal singularity spectra out of 10 snapshots of velocity fields for the two simulations, presented in Figure 7 and 8. As the velocity fields include 768^3 grid points and are decorrelated in time, this represents enough statistics to guarantee the convergence of the following results.

In the inertial regime, we recover spectra centered around $h = 0.40$ for all components but the perpendicular one, which is higher than the expected value of $h = 1/3$ according to the Kolmogorov 41 theory. The analysis by Arneodo [10] yielded a most probable Hölder

Run	N	ν	L	λ	η	$\langle u^2\rangle^{1/2}$	ϵ	ηk_{max}	Re	Re_λ
I	768^3	7.5×10^{-4}	0.79	0.19	0.0083	0.54	0.089	2.1	570	140
II	768^3	5×10^{-3}	0.94	0.48	0.034	0.55	0.097	8.5	104	53

TABLE I. Parameters used in the simulations. N is the linear grid resolution, ν the kinematic viscosity, L is the integral scale, λ is the Taylor scale, η is the Kolmogorov scale, $\langle u^2\rangle^{1/2}$ is the rms velocity, ϵ is the energy dissipation rate, ηk_{max} characterizes the resolution ($\eta k_{max} > \pi$ is well resolved), Re is the Reynolds number based on the integral scale, and Re_λ is the Taylor based Reynolds number.

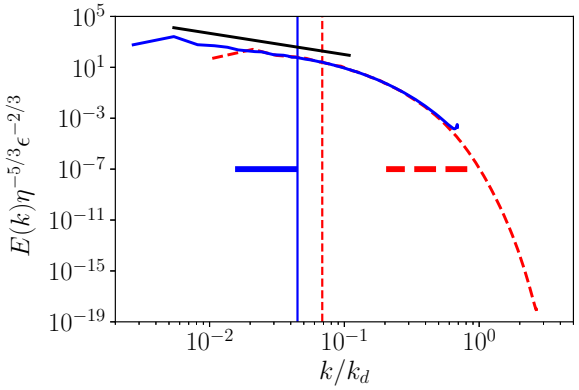

FIG. 6. Energy spectra for the two simulations. The solid blue (resp. dashed red) curve stands for the simulation in the inertial (resp. dissipative) range. The black line materializes the $k^{-5/3}$ slope for the inertial range. The horizontal lines of the same color as the curves materialize the corresponding fitting range used when computing power laws. The vertical lines materialize the k_λ corresponding to each simulation.

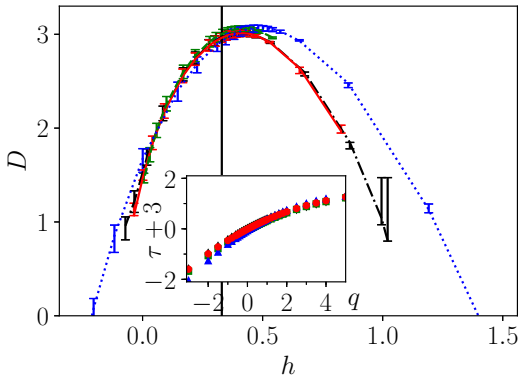

FIG. 7. **Main figure:** Multifractal spectra for the velocity fields from simulation in the inertial region. The solid red (resp. dashed green, dotted blue) curve corresponds to the global (resp. longitudinal, perpendicular) increments. The dash-dotted black curve corresponds to the native method. The vertical line materializes the expected exponent of $h = 1/3$ according to K41. The error bars correspond to a shift of the fitting range by 5% for the power laws. **Inset:** Exponents τ as a function of q for the global (red circles), longitudinal (green squares)and perpendicular (blue triangle) increments, as well as the native method (black diamonds).

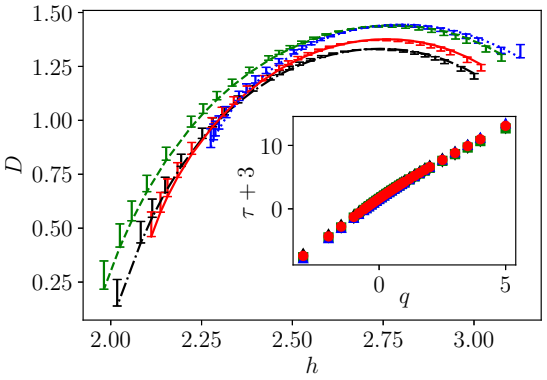

FIG. 8. **Main figure:** Multifractal spectra for the velocity fields from simulation in the dissipative regime. The solid red (resp. dashed green, dotted blue) curve corresponds to the global (resp. longitudinal, perpendicular) increments. The dash-dotted black curve corresponds to the native method. The error bars correspond to a shift of the fitting range by 10% for the power laws. **Inset:** Exponents τ as a function of q for the global (red circles), longitudinal (green squares)and perpendicular (blue triangle) increments, as well as the native method (black diamonds).

exponent of around $h = 0.34$, which was much closer to the Kolmogorov value. It is however not clear how universal this value should be, in particular as we use data from anisotropic turbulence where Arneodo used homogeneous turbulence. The fact that the perpendicular component does not follow exactly the same tendency is the manifestation of the anisotropy of the flow at this scale simulated with a Taylor–Green forcing. Additionally, one can also notice the remarkable agreement between the native method from Pierre Kestener and the modified method applied to global increments, which further validates the choice of the increments in equation (5).

The multifractal spectra for the simulation resolved under the Kolmogorov scale provide significantly different results, shown Figure 8. Indeed, the values of the singularity exponents are much higher since the velocity field is much more regular at this scale. As a reminder, a Hölder exponent $2 < h < 3$ means that the velocity field at this point is twice differentiable but not thrice. We also observe that the spectra reach a maximum $D \approx 1.4 < 3$. This can be interpreted as singularities appearing less

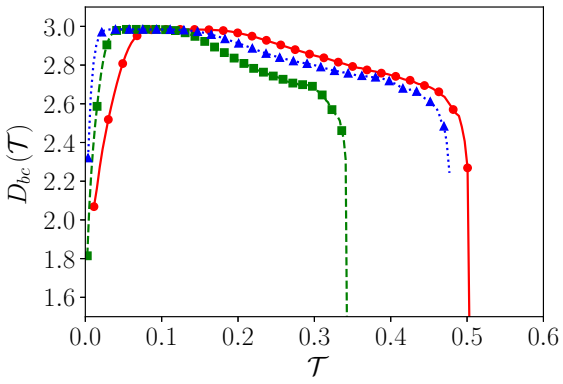

FIG. 9. Box counting dimension of the isosurfaces of the different components of the wavelet based velocity increments for $\ell \approx 0.24$ for the simulation in the inertial range. The color code for the different components is the same as for the previous figures.

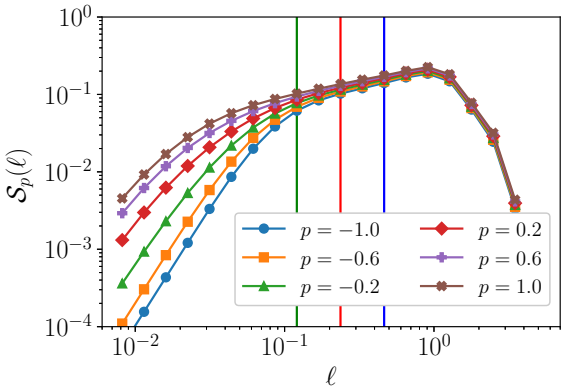

FIG. 10. Values of the threshold $\mathcal{S}_p(\ell)$ for the global increments as a function of scale for several p for the simulation in the inertial range.

likely once the behavior of the velocity fields at the dissipative scale is taken into account. Finally, the superposition of the spectra for the different components hint the recovery of isotropy at small scale.

C. Estimates of local singularity exponents

As already discussed, the multifractal spectra obtained here do not provide any local information. While the field $\tilde{h}$ defined with equation (21) is not equivalent to a measure of local Hölder exponents, we will show in the following that it is still relevant for the measure of local regularity.

To compute this field, we follow the same steps as for the fBms, and first compute boxcounting dimensions over isosurfaces of the increments (Figure 9), as well as the power law behavior of the coefficients $\mathcal{S}_p(\ell)$ (Figure 10). The computation of increments before applying the boxcounting algorithm implies to chose a value of ℓ. The value chosen in the following is $\ell \approx 0.24$, well within the inertial range.

The situation here slightly differs from the fBm case, since the multifractal spectrum is non degenerated. This allows us to match the dimensions from figures 9 and 7 using equation (24) to get a relationship directly connecting the velocity increments to the coefficient $\tilde{h}$. By taking care of associating the high velocity increments to low values of $\tilde{h}$ and reciprocally, we obtain the relationship represented Figure 11. At this point, we do not produce separate measurements for the perpendicular and longitudinal components anymore, as they only provide partial information about the velocity field.

Using this procedure, we are able to deduce maps of $\tilde{h}$ from the corresponding maps of velocity increments. One flaw of the process however is that the range of $\mathcal{T}$

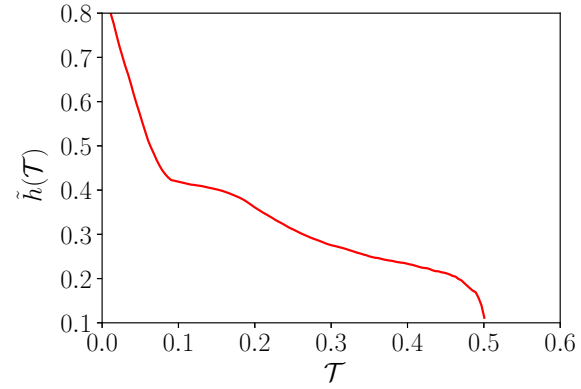

FIG. 11. Mapping function from the global velocity increments at scale $\ell \approx 0.24$ to the coefficients $\tilde{h}$.

shown in Figure 11 is smaller than the total range of velocity increments encountered in practice. The reason for this comes from the fact that both WTMM and the boxcounting of isosurfaces of the velocity increments are limited by the statistics available. The lower the fractal dimension, the harder it is to get enough statistics. With the amount of statistics available (10 fields of size 768^3), we cannot get reliable value of boxcounting dimension below approximately 2.4 as shown in Figure 9. As a result, we cannot get values of $\tilde{h}$ for velocity increments much higher than 0.5. This will eventually leads to the maps of singularity exponents having regions where we know that $\tilde{h} < 0.1$ but cannot give any precise value.

D. About the scale invariance of the c_p coefficients

We have stated in Section III that the coefficients c_p defined in equation (20) are scale independents. This property makes it possible to use the coefficient c_p mea-

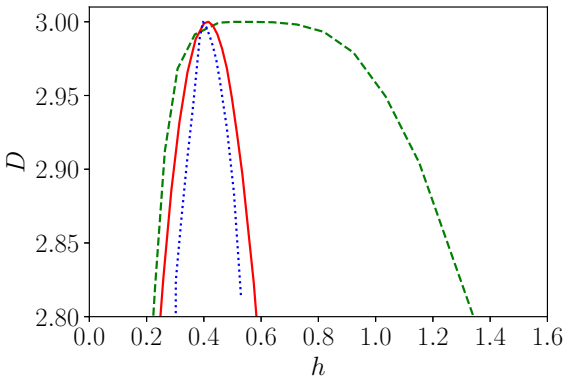

FIG. 12. *Pseudo* spectra reconstituted using the coefficient c_p computed at scale $\ell \approx 0.24$ and the boxcounting dimensions of the velocity increments computed at scales $\ell \approx 0.12$ (dashed green curve),$\ell \approx 0.24$ (solid red curve) and $\ell \approx 0.46$ (dotted blue curve). The scale are also materialized by vertical lines of the same color on the Figure 10.

sured at a given scale to extrapolate to all scales, thus saving computation time. Indeed, once these coefficients are known, the knowledge of the $S_p(\ell)$ is sufficient to recover the active volume at any scale without having to compute box-counting dimensions nor applying the WTMM method.

We use the present simulation data to test the validity of this property. The first hurdle here is that the coefficient $h(p)$ from equation (19) as well as the multifractal spectrum from the WTMM method are defined in sections II and III as dependent of the scale ℓ. However, both actually requires the estimation of the power law behavior with respects to ℓ, which are done in practice by fitting curves over a range of ℓ. The limited accuracy over the power law exponents, as well as the actual corresponding scale within the fitting range used, are expected to reduce the accuracy of the c_p computed.

As the c_p do not have an obvious physical meaning, it is difficult to estimate what range of error in the measures of c_p would be coherent with the property of scale independence. This leads us to use a slightly different method to test this property. Using the results computed at the scale of $\ell \approx 0.24$ used in the previous figures, we compute the coefficients c_p that we assume to be scale independent. Using these coefficients and the box-counting dimensions of the isosurfaces of velocity increments computed at two different scales, we recover *pseudo* multifractal spectra using equation (22). The results are presented in Figure 12. We observe that the spectra are qualitatively coherent. In particular, the green curve shows that when we reach the lower bound of the inertial range, the spectrum widen with much higher values of h. In other words, the velocity fields starts to get regularized by viscosity.

A direct comparison with the output of the WTMM method is unfortunately not possible, as the WTMM performs poorly with fitting ranges too short. More statistics would be required to perform the power law fit of equations (15) and (16) with a good accuracy on a very small fitting range. The result of this analysis is that using coefficient c_p computed at a different scale will provide qualitatively sound results. Since the complete method is dependent on fitting scaling exponents, it is reasonable to use the c_p for quantitative measurements.

E. Comparison with another indicator of regularity

By construction, our method guarantees that the local estimates of the Hölder exponent are statistically meaningful and respect the global MFR properties. To evaluate the physical soundness of our estimate (i.e. how good it is to detect area of lesser regularity), we may compare our maps of $\tilde{h}(\mathbf{x})$ with maps of local energy transfer [1], hereafter referred to as Duchon-Robert term. Indeed, this quantity has been used in [11] to build a new criterion to detect areas with Hölder exponent $h < 1/3$, by looking at local maxima of such quantities. The Duchon–Robert term is expressed as:

$$D^I_\ell(\boldsymbol{x}) = \frac{1}{4}\int \mathrm{d}\boldsymbol{y}\boldsymbol{\nabla}\Psi^\ell(\boldsymbol{y})\cdot\delta\boldsymbol{u}(\boldsymbol{x},\boldsymbol{y})||\delta\boldsymbol{u}(\boldsymbol{x},\boldsymbol{y})||^2 \quad (27)$$

where $\Psi^\ell(\boldsymbol{x}) = \Psi(\boldsymbol{x}/\ell)/\ell^3$ and $\delta\boldsymbol{u}(\boldsymbol{x},\boldsymbol{y})$ is the conventional velocity increment as defined in equation A2. When ℓ goes to 0, the term $D^I_\ell(\boldsymbol{x})$ scales as ℓ^{3h-1}, hence it diverges for an Hölder exponent $h < 1/3$. In practice, at any given scale ℓ, the higher the term $D^I_\ell(\boldsymbol{x})$ the less regular the velocity field is in $\boldsymbol{x}$. So if our new index $\tilde{h}$ is meaningful, its areas of lower values should correlated with areas of higher value for the Duchon–Robert term.

We computed maps of both the singularity exponent $\tilde{h}$ and the Duchon–Robert term $D^I_\ell(\boldsymbol{x})$. The Figure 13 illustrates one of the strong events that can be found in our velocity fields. It appears in this case that the two quantities are correlated, meaning that regions of lower $\tilde{h}$ visually corresponds to regions of high $|D^I_\ell(\boldsymbol{x})|$ in absolute value. However, looking in more detail, the region of low $\tilde{h}$ seems to be enclosed between two regions of high $|D^I_\ell(\boldsymbol{x})|$.

While it appears that the minima of $\tilde{h}$ are not located at the same location as the extrema of $|D^I_\ell(\boldsymbol{x})|$, it is still relevant to observe the joint PDF of those two terms in order to confirm this observation. The results of statistics aggregated over 50 fields extracted at regular interval over approximatively 30 turnover times are reported in Figure 14. We estimate that the small scales of two different fields are not correlated. While the conditional PDF is not perfectly converged for the extreme values of h, it is enough to do qualitative observations. We observe a very clear correlation between the two quantities. In particular, lower values of $\tilde{h}$ correspond to higher values of $|D^I_\ell(\boldsymbol{x})|$ in absolute value, which can be associated to

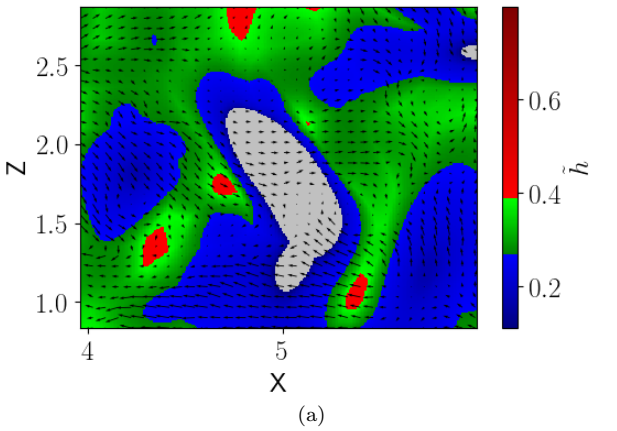

(a)

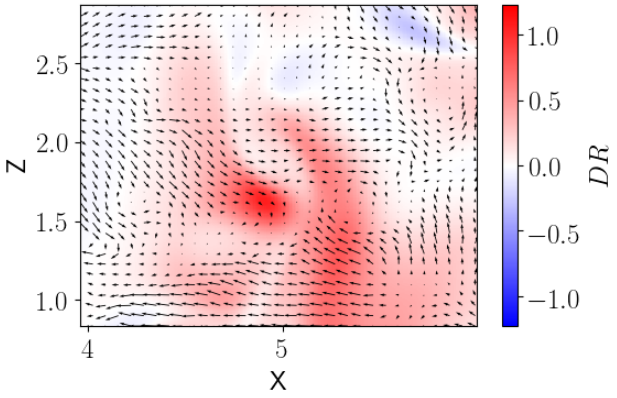

(b)

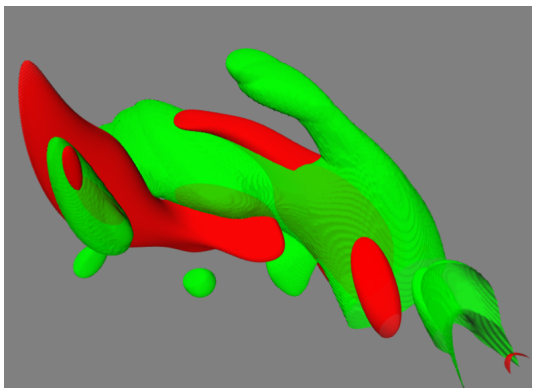

(c)

FIG. 13. (a): Arrows stand for in plane velocity; color plot for the singularity exponent $\tilde{h}(\boldsymbol{x})$. The gray areas corresponds to increments outside of the domain of the mapping function. (b): Arrows stand for in plane velocity; color plot for the Duchon–Robert term $D^I_\ell(\boldsymbol{x})$. (c): 3D representation of the same event. The green surface is an isosurface of $\tilde{h}(\boldsymbol{x})$ at value $\tilde{h} = 0.14$, the red surface is an isosurface of $D^I_\ell(\boldsymbol{x})$ at value $D^I_\ell = 0.5$. All computations are done for a value of $\ell \approx 0.24$.

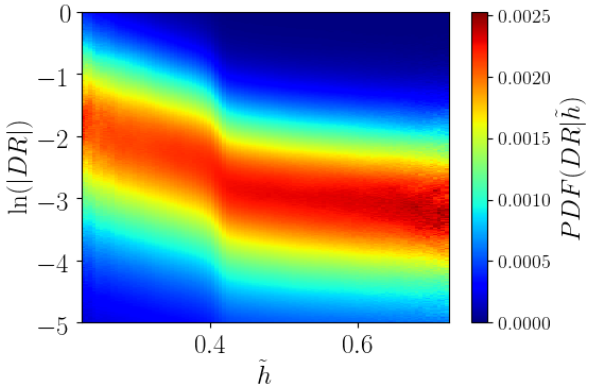

FIG. 14. Joint PDF of $\tilde{h}$ and the Duchon–Robert energy transfer term D^I_ℓ over 50 fields regularly spaced over approximatively 30 turnover times . For the sake of better displaying the correlation of those terms, the PDF is rescaled such that every vertical line is a conditional PDF of D^I_ℓ at given $\tilde{h}$.

a more singular velocity field. This observation comforts us in the idea that the field of singularity exponents $\tilde{h}$ can be used as a measure of the local regularity.

VI. DISCUSSION

In this paper, we have introduced a tool to estimate the regularity of velocity fields. It is derived using the *Wavelet Transform Modulus Maxima* method and associates the multifractal spectra and the isosurfaces of velocity increments to compute a field $\tilde{h}(\boldsymbol{x})$ which has similar properties than the Hölder exponents. We have checked the physical soundness of our estimate by comparing it with the energy transfer term $|D^I_\ell(\boldsymbol{x})|$ [1], that can be used as a marker of regions of lesser regularity [11]. We have found that our $\tilde{h}(\boldsymbol{x})$ and $|D^I_\ell(\boldsymbol{x})|$ are globally statistically correlated, but that local maxima of $|D^I_\ell(\boldsymbol{x})|$ do not coincide exactly with local minima of $\tilde{h}(\boldsymbol{x})$. On the practical side, we found that, once the relation between the wavelet based velocity increments and the coefficients $\tilde{h}$ shown Figure 11 is established, computing $\tilde{h}(\boldsymbol{x})$ from a new velocity field is approximately three times faster than computing the field of $D^I_\ell(\boldsymbol{x})$. As a result, our method can be used to process velocity fields for candidates of singularities faster than through the energy transfer term.

The study of particular events like the one presented in Figure 13 shows a non trivial correlation of the low $\tilde{h}$ regions with respect to the extreme D^I_ℓ regions. This encourages further studies using both scalars to characterize the velocity structures and the regularity properties of turbulent flows. Finally, this study has been focused on turbulence driven by a Taylor-Green forcing. It could be interesting to study other types of flows like turbulence induced by Rayleigh-Taylor and Richtmyer-Meshkov in-

stabilities [12, 13].

Acknowledgments. FN has been funded by École Normale Supérieure and was granted access to the HPC resources of IDRIS under the allocation 2A10096 made by GENCI (Grand Équipement National de Calcul Intensif). This work was funded by the ANR EXPLOIT, grant agreement no. ANR-16-CE06-0006-01. Research was supported in part by NSF grant DMS 1515705, Simons Foundation, and the College of LAS at UIC.

Appendix A: General considerations about velocity increments

Consider a 3D velocity field $\mathbf{u}$. Without loss of generality, it can be decomposed using Helmoltz decomposition as:

$$\begin{aligned} \mathbf{u} &= \nabla\phi + \nabla\times\mathbf{Q}, \\ \nabla\cdot\mathbf{Q} &= 0. \end{aligned} \tag{A1}$$

By construction, $\nabla\times\mathbf{u} = -\Delta\mathbf{Q}$ and $\nabla\cdot\mathbf{u} = \Delta\phi$. So, if the fluid is incompressible (which we do not assume for the present time), $\Delta\phi = 0$. We can further define velocity increments of such field over a scale ℓ as:

$$\delta\mathbf{u}(\mathbf{x},\boldsymbol{\ell}) = \mathbf{u}(\mathbf{x}+\boldsymbol{\ell}) - \mathbf{u}(\mathbf{x}), \tag{A2}$$

that can be further decomposed into longitudinal $\delta_L\mathbf{u}(\ell)$ and perpendicular $\delta_P\mathbf{u}(\ell)$ velocity increments as:

$$\begin{aligned} \delta_L\mathbf{u}(\boldsymbol{\ell}) &= \delta\mathbf{u}\cdot\frac{\boldsymbol{\ell}}{\|\boldsymbol{\ell}\|}, \\ \delta_P\mathbf{u}(\boldsymbol{\ell}) &= \delta\mathbf{u}\times\frac{\boldsymbol{\ell}}{\|\boldsymbol{\ell}\|}. \end{aligned} \tag{A3}$$

With this definition, $\delta_L\mathbf{u}(\boldsymbol{r})$ is a scalar and $\delta_P\mathbf{u}(\boldsymbol{r})$ is a vector orthogonal to both $\delta\mathbf{u}$ and $\boldsymbol{r}$. The definition of the perpendicular velocity increment is similar to the more commonly used transverse increment, as they have the same norm but different orientation.

We consider now the angle average of $\|\boldsymbol{r}\|\delta_L\mathbf{u}(\boldsymbol{r})$ and $\|\boldsymbol{r}\|\delta_P\mathbf{u}(\boldsymbol{r})$ over a sphere of radius ℓ, defined through convolution with a Gaussian function $\Psi(\mathbf{x}) = \exp(-x^2/2)/N$, where N is chosen so that the Gaussian is of norm unity:

$$\begin{aligned} \langle\|\boldsymbol{r}\|\delta_L\mathbf{u}(\mathbf{x},\boldsymbol{r})\rangle_{ang,\ell} &= \int\frac{d\mathbf{y}}{\ell^3}\Psi\left(\frac{\mathbf{y}}{\ell}\right)\|\mathbf{y}\|\delta_L\mathbf{u}(\mathbf{x},\mathbf{y}), \\ \langle\|\boldsymbol{r}\|\delta_P\mathbf{u}(\mathbf{x},\boldsymbol{r})\rangle_{ang,\ell} &= \int\frac{d\mathbf{y}}{\ell^3}\Psi\left(\frac{\mathbf{y}}{\ell}\right)\|\mathbf{y}\|\delta_P\mathbf{u}(\mathbf{x},\mathbf{y}) \end{aligned} \tag{A4}$$

Using properties of the Gaussian, it can be easily checked that:

$$\Psi\left(\frac{\mathbf{y}}{\ell}\right)\mathbf{y} = -\ell^2\nabla\Psi\left(\frac{\mathbf{y}}{R}\right). \tag{A5}$$

Using this property and the Helmoltz decomposition, we then see that after an integration by part that:

$$\begin{aligned} \langle\delta_L\mathbf{u}(\boldsymbol{r})\|\boldsymbol{r}\|\rangle_{ang,\ell} &= \ell^2\int\frac{d\mathbf{y}}{\ell^3}\Psi\left(\frac{\mathbf{y}}{\ell}\right)\Delta\phi(\mathbf{x}+\mathbf{y}), \\ \langle\delta_P\mathbf{u}(\boldsymbol{r})\|\boldsymbol{r}\|\rangle_{ang,\ell} &= -\ell^2\int\frac{d\mathbf{y}}{\ell^3}\Psi\left(\frac{\mathbf{y}}{\ell}\right)\Delta\mathbf{Q}(\mathbf{x}+\mathbf{y}) \end{aligned} \tag{A6}$$

Rephrasing this, we see that the angle averaged longitudinal velocity increment is connected with the potential part of the Helmoltz decomposition (or the divergence of the velocity field), while the angle averaged transverse velocity increment is connected with the rotational part of the Helmoltz decomposition (or the vorticity). The connection is through a wavelet transform, using a Gaussian wavelet. That way, studying the scaling properties of either $\langle\delta_L\mathbf{u}(\boldsymbol{r})\|\boldsymbol{r}\|\rangle_{ang,\ell}$ or $\langle\delta_P\mathbf{u}(\boldsymbol{r})\|\boldsymbol{r}\|\rangle_{ang,\ell}$ provides information about the scaling of the potential or rotational part of the velocity. Such decomposition has already been used by [14] and [15] to study structure functions in experimental turbulence.

Appendix B: Volumetric concentration and amplitude factors

In this section we introduce several scalar factors associate to a general vector or scalar field f, which capture a measure of concentration and size of f.

We use the following definition of the space-time average

$$\langle f\rangle = \frac{1}{|\Omega_T|}\int_{\Omega_T} f(x,t)\,\mathrm{d}\mathbf{x}\,\mathrm{d}t, \tag{B1}$$

where $\Omega_T = \Omega\times[0,T]$, and Ω denotes a fluid domain. We also denote $\mathrm{d}\mu = \frac{1}{|\Omega_T|}\,\mathrm{d}\mathbf{x}\,\mathrm{d}t$, the averaging measure.

1. Concentration factors

We now present formalities of the active volume/region theory. Let $f\in L^\infty(\Omega_T)$ be an arbitrary field. Let $1\leqslant p,r\leqslant\infty$, $r\neq p$. We define the (r,p)-*concentration factor* of f as follows

$$V_{r,p} = \frac{\langle|f|^r\rangle^{\frac{p}{p-r}}}{\langle|f|^p\rangle^{\frac{r}{p-r}}}. \tag{B2}$$

Let us list a few elementary properties: $V_{r,p}$ is adimensional, $V_{r,p} = V_{p,r}$, and by Hölder, $V_{r,p}\leqslant 1$. For any triple $p_1<p_2<p_3$ we have by interpolation,

$$V_{r,p_2}\leqslant (V_{r,p_1})^{\frac{r-p_1}{r-p_2}\frac{p_3-p_2}{p_3-p_1}}(V_{r,p_3})^{\frac{r-p_3}{r-p_2}\frac{p_2-p_1}{p_3-p_1}}$$

The idea is that $V_{r,p}$ measures a proportion of the volume of Ω_T where much of the L^p-weight of f concentrates provided $p>r$. More precisely, we have the following lemma.

Lemma B.1. *There exists a set $A \subset \Omega_T$ with $|A| = V_{r,p}|\Omega_T|$ such that*

$$(1 - c_{r,p}) \int_{\Omega_T} |f|^p \, d\mu \leqslant \int_A |f|^p \, d\mu, \tag{B3}$$

where $c_{r,p} = \left(\frac{p-r}{p}\right)^{\frac{p-r}{p}} \left(\frac{r}{p}\right)^{\frac{r}{p}}$.

Proof. We can assume that $|\Omega_T| = 1$. If $V_{r,p} = 1$, the statement is trivial. Suppose $V_{r,p} < 1$. Note that the function $\mu(\{|f| \geqslant \alpha\})$ is continuous from the left, and at a point of a jump the size of the jump is exactly $\mu(\{|f| = \alpha\})$. Hence, there exists an $\alpha \geqslant 0$ and a set $B \subset \{|f| = \alpha\}$ such that $A = \{|f| > \alpha\} \cup B$ has measure exactly $V_{r,p}$. By Chebyshev,

$$V_{r,p} \leqslant \frac{1}{\alpha^r} \int_A |f|^r d\mu.$$

Using this and that on $\Omega_T \backslash A$, $|f| \leqslant \alpha$ we obtain

$$\begin{aligned}
\langle |f|^p \chi_{\Omega_T \backslash A} \rangle &\leqslant \alpha^{p-r} \langle |f|^r \chi_{\Omega_T \backslash A} \rangle \\
&\leqslant \frac{1}{V_{r,p}^{\frac{p-r}{r}}} \langle |f|^r \chi_A \rangle^{\frac{p-r}{r}} \langle |f|^r \chi_{\Omega_T \backslash A} \rangle \\
&\leqslant \langle |f|^p \rangle \frac{\langle |f|^r \chi_{\Omega_T \backslash A} \rangle^{\frac{r}{p}} \langle |f|^r \chi_A \rangle^{\frac{p-r}{r}}}{\langle |f|^r \rangle}
\end{aligned}$$

Note that the latter fraction is of the form $\theta^{\frac{r}{p}}(1-\theta)^{\frac{p-r}{r}}$, $\theta \in [0,1]$, which attains its maximum exactly at the value $c_{r,p}$. This proves the lemma. □

Note that as $r \to p$, $c_{r,p} \to 1$, and as a result the information about concentration of f gets lost. However, the corresponding concentration factors converge to something non-trivial, namely,

$$V_p = \lim_{r \to p} V_{r,p} = \langle |f|^p \rangle \exp\left\{ -\frac{\langle |f|^p \ln |f|^p \rangle}{\langle |f|^p \rangle} \right\}. \tag{B4}$$

Let us call it *p-concentration factor*. The factor have some natural monotonicity properties, which will be addressed in the next section.

2. Amplitude

Although Lemma B.1 explains why the measure of concentration of f can be defined by $V_{r,p}$, the method of proof provides little constructive information about the threshold amplitude α. Such amplitude can be defined quite explicitly, if one is ready to sacrifice precise measure of the set A. Namely, let us denote

$$s_{r,p} = \frac{\langle |f|^p \rangle^{\frac{1}{p-r}}}{\langle |f|^r \rangle^{\frac{1}{p-r}}}. \tag{B5}$$

We will call it (r,p)-*amplitude*. Note that the physical units of $s_{r,p}$ and f coincide.

Let us further expand our dictionary by calling a point $(\mathbf{x}, t) \in \Omega_T$ (r,p)-*active* if the amplitude of f passes the $s_{r,p}$ threshold:

$$|f(\mathbf{x}, t)| > c_{r,p} s_{r,p},$$

where $0 < c_{r,p} < 1$ are empirical adimensional factors. Collectively the set of all (r,p)-active points form a (r,p)-*active domain*:

$$A_{r,p} = \{|f| \geqslant c_{r,p} s_{r,p}\}. \tag{B6}$$

Directly by Chebyshev, we readily obtain the bound

$$|A_{r,p}| \leqslant \frac{1}{c_{r,p}^p s_{r,p}^p} \langle |f|^p \rangle |\Omega_T| = \frac{1}{c_{r,p}^p} V_{r,p} |\Omega_T|,$$

and

$$\langle |f|^p \chi_{\Omega_T \backslash A_{r,p}} \rangle \leqslant c_{r,p}^{p-r} \frac{\langle |f|^p \rangle}{\langle |f|^r \rangle} \langle |f|^r \chi_{\Omega_T \backslash A_{r,p}} \rangle \leqslant c_{r,p}^{p-r} \langle |f|^p \rangle,$$

which implies

$$(1 - c_{r,p}^{p-r}) \langle |f|^p \rangle \leqslant \langle |f|^p \chi_{A_{r,p}} \rangle. \tag{B7}$$

Note again that as $r \to p$, the information about concentration of f gets lost. However, the corresponding threshold amplitudes converge to a non-trivial value, namely,

$$\lim_{r \to p} s_{r,p} = s_p = \exp\left\{ \frac{\langle |f|^p \ln |f| \rangle}{\langle |f|^p \rangle} \right\}. \tag{B8}$$

Let us call it p-amplitude. One can easily restore $s_{r,p}$ from s_τ by the formula

$$s_{r,p} = \exp\left\{ \frac{1}{p-r} \int_r^p \ln s_\tau \, d\tau \right\}. \tag{B9}$$

The amplitudes have several monotonicity properties. First, applying Jensen's inequality,

$$\begin{aligned}
s_r^{p-r} &= \exp\left\{ \frac{\langle |f|^r \ln |f|^{p-r} \rangle}{\langle |f|^r \rangle} \right\} \\
&\leqslant \frac{\langle |f|^r \exp(\ln |f|^{p-r}) \rangle}{\langle |f|^r \rangle} = s_{r,p}^{p-r}.
\end{aligned}$$

Thus, $s_r \leqslant s_{r,p}$, for all $r < p$. Second, one versifies again by Jensen, that $\partial_r s_{r,p}, \partial_p s_{r,p} \geqslant 0$. By taking the limit as $r \to p$, $s_{r,p} \leqslant s_p$. This in turn implies that

$$s_r \leqslant s_{r,p} \leqslant s_p, \text{ for all } r < p.$$

From (B9) we see that $\ln s_{r,p}$ is precisely the mean value of $\ln s_\tau$ on $[r,p]$. In view of the identities

$$s_{r,p}^p V_{r,p} = \langle |f|^p \rangle, \quad s_{r,p}^r V_{r,p} = \langle |f|^r \rangle$$

we deduce the opposite monotonicity properties of the concentration factors: $\partial_r V_{r,p}, \partial_p V_{r,p} \leqslant 0$, and thus

$$V_r \geqslant V_{r,p} \geqslant V_p, \text{ for all } r < p.$$

3. p-active regions

Let U_0 be a characteristic size of f, and let us assume that the units of f is velocity as well. It is then more natural to rewrite the formula for s_p as follows:

$$s_p = U_0 \exp\left\{ \frac{\left\langle |f|^p \ln \frac{|f|}{U_0} \right\rangle}{\langle |f|^p \rangle} \right\}. \tag{B10}$$

(note that this holds for any $U_0 > 0$). This way of expressing s_p makes the main exponent adimensional. We can view the ratio s_p/U_0 as an adimensional threshold value for an active size. Next, we show the active region defined in (26) with $0 < c_p < 1$ and s_p as above captures an appreciable concentration of the renormalized probability density $F_p = \frac{|f|^p}{\langle |f|^p \rangle}$, provided U_0 as chosen appropriately. So, let us define as before

$$A_p = \{ |f| \geqslant c_p s_p \}. \tag{B11}$$

Let us consider the entropy concentration on the complement of A_p:

$$\left\langle |f|^p \ln \frac{|f|}{U_0} \chi_{\Omega_T \setminus A_p} \right\rangle \leqslant \ln c_p \left\langle |f|^p \chi_{\Omega_T \setminus A_p} \right\rangle + \frac{\left\langle |f|^p \ln \frac{|f|}{U_0} \right\rangle}{\langle |f|^p \rangle} \left\langle |f|^p \chi_{\Omega_T \setminus A_p} \right\rangle \tag{B12}$$

Let us choose $U_0 = \langle |f|^p \rangle^{1/p}$, and denote $I = \left\langle |f|^p \ln \frac{|f|}{U_0} \right\rangle$. Then

$$\frac{p}{\langle |f|^p \rangle} I = \langle F_p \ln F_p \rangle ,$$

which by the classical Csiszar-Kullback bounded from below by $\|F_p - 1\|_1^2$, i.e. non-negative. This allows to continue the line of (B12):

$$\left\langle |f|^p \ln \frac{|f|}{U_0} \chi_{\Omega_T \setminus A_p} \right\rangle \leqslant \ln c_p \left\langle |f|^p \chi_{\Omega_T \setminus A_p} \right\rangle + \left\langle |f|^p \ln \frac{|f|}{U_0} \right\rangle . \tag{B13}$$

Multiplying the above by the factor of $\frac{p}{\langle |f|^p \rangle}$ and rewriting in terms of F_p we obtain

$$\left\langle F_p \ln F_p \chi_{A_p} \right\rangle \geqslant \left\langle F_p \chi_{\Omega_T \setminus A_p} \right\rangle \ln \frac{1}{c_p^p}. \tag{B14}$$

Note that $\ln \frac{1}{c_p^p} > 0$. Thus, (B14) expresses quantitatively a concentration proportion of the entropy relative to the complementary probability of the event A_p.

[1] J. Duchon and R. Robert, Séminaire Équations aux dérivées partielles **1999-2000**, 1 (1999-2000).
[2] J. Leray, Acta mathematica **63**, 193 (1934).
[3] U. FRISCH, Turbulence and Predictability in Geophysical Fluid Dynamics and Climate Dynamics (1985).
[4] J.-F. Muzy, E. Bacry, and A. Arneodo, Physical review letters **67**, 3515 (1991).
[5] P. Kestener and A. Arneodo, Physical review letters **93**, 044501 (2004).
[6] A. Cheskidov, S. Friedlander, and R. Shvydkoy, in *Advances in mathematical fluid mechanics* (Springer, 2010) pp. 171–175.
[7] M. H. Jensen, Physical review letters **83**, 76 (1999).
[8] P. Kestener, "xsmurf v1.0," (2016).
[9] M. Brachet, M. Meneguzzi, H. Politano, and P. Sulem, Journal of Fluid Mechanics **194**, 333 (1988).
[10] A. Arneodo, B. Audit, P. Kestener, and S. Roux, Scholarpedia **3**, 4103 (2008), revision #121431.
[11] D. Kuzzay, E.-W. Saw, F. J. W. A. Martins, D. Faranda, J.-M. Foucaut, F. Daviaud, and B. Dubrulle, Nonlinearity **30**, 2381 (2017).
[12] Y. Zhou, Physics Reports **723-725**, 1 (2017).
[13] Y. Zhou, Physics Reports **720-722**, 1 (2017).
[14] K. Sreenivasan, S. Vainshtein, R. Bhiladvala, I. San Gil, S. Chen, and N. Cao, Physical review letters **77**, 1488 (1996).
[15] S. Chen, K. R. Sreenivasan, M. Nelkin, and N. Cao, Physical review letters **79**, 2253 (1997).

Appendix C

About Universality and Thermodynamics of Turbulence

Reproduction of an article in *Entropy* (2019).

Universality and Thermodynamics of Turbulence

Damien Geneste[1], Hugues Faller[1]*, Florian Nguyen[2], Vishwanath Shukla[3], Jean-Philippe Laval[2], Francois Daviaud[1], Ewe-Wei Saw[1] and Bérengère Dubrulle [1]

[1] *SPEC, CEA, CNRS, Universit Paris-Saclay, CEA Saclay, Gif-sur-Yvette, France*

[2] *Laboratoire de Mcanique des Fluides de Lille,*

CNRS, ONERA, Centrale Lille, Univ. Lille,

Arts et Metiers ParisTech, Kamp de Friet, F-59000, Lille, France

[3] *Université Côte d'Azur, Institut de Physique de Nice, CNRS, Nice, France and*

Correspondence: hugues.faller@normalesup.org; Tel.: +33-16908 3015

(Dated: Friday, March 1 2019)

We investigate universality of the Eulerian velocity structure functions using velocity fields obtained from the stereoscopic particle image velocimetry (SPIV) technique in experiments and the direct numerical simulations (DNS) of the Navier-Stokes equations. We show that the numerical and experimental velocity structure functions up to order 9 follow a log-universality[1]; we find that they collapse on a universal curve, if we use units that include logarithmic dependence on the Reynolds number. We then investigate the meaning and consequences of such log-universality, and show that it is connected with the properties of a "multifractal free energy", based on an analogy between multifractal and themodynamics. We show that in such a framework, the existence of a fluctuating dissipation scale is associated with a phase transition describing the relaminarisation of rough velocity fields with different Hölder exponents. Such a phase transition has been already observed using the Lagrangian velocity structure functions, but was so far believed to be out of reach for the Eulerian data.

I. INTRODUCTION

A well-known feature of any turbulent flow is the Kolmogorov-Richardson cascade by which energy is transferred from large to small length scales until the Kolmogorov length scales below which it is removed by viscous dissipation. This energy cascade is a non-linear and an out-of-equilibrium universal process. Moreover, the corresponding non-dimensional energy spectrum $E(k)/\epsilon^{2/3}\eta^{5/3}$ is an universal function of $k\eta$, where $\eta = (\nu^3/\epsilon)^{1/4}$ is the Kolmogorov length scale, ϵ the mean energy dissipation rate per unit mass, and ν the kinematic viscosity. However, there seem to be little dependences on the Reynolds number, boundary, isotropy or homogeneity conditions[2]. In facts, the energy spectrum is based upon a quantity, the velocity correlation, that is quadratic in velocity. Nevertheless, it is now well admitted that the universality does not carry over for statistical quantities that involve higher order moments. For example, the velocity structure functions of order p, given by $S_p(\ell) = \langle \|u(\mathbf{x}+\mathbf{r}) - u(\mathbf{x})\|^p \rangle_{\mathbf{x},\|\mathbf{r}\|=\ell}$ are not universal, at least when expressed in units of the Komogorov scale η and velocity $u_{\mathrm{K}} = (\nu\epsilon)^{1/4}$(see below, section III B for an illustration).

The mechanism behind this universality breaking was identified by, wherein a generalization of the Kolmogorov theory introduced, based on the hypothesis that a turbulent flow is multifractal. In this model, the velocity field is characterized locally by an exponent h, such that $|\delta_\ell u(\mathbf{x})| \equiv \langle \|\mathbf{u}(\mathbf{x}+\mathbf{r}) - \mathbf{u}(\mathbf{x})\| \rangle_{\|\mathbf{r}\|=\ell} \sim \ell^{h(\mathbf{x})}$; here h is a stochastic function that follows a large deviation property[3] $\mathbb{P}\left(\log(|\delta_\ell u|/u_0) = h \log\left(\ell/L_0\right)\right) \sim \left(\ell/L_0\right)^{C(h)}$, where u_0 (resp. L_0) is the caracteristic integral velocity (resp. length), and $C(h)$ is the multifractal spectrum. Velocity fields with $h < 1$ are rough in the limit $\ell \to 0$. In real flows, any rough field with $h > -1$ can be regularized at sufficiently small scale (the "viscous scale") by viscosity. The first computation of such dissipative scale was performed by Paladin and Vulpiani, who showed that it scales with viscosity like $\eta_h \sim \nu^{1/(1+h)}$, thereby generalizing the Kolmogorov scale, which corresponds to $h = 1/3$. Such a dissipative scale fluctuates in space and time (along with h), resulting in non-universality for high order moments, at least when expressed in units of η and u_{K}.

A few years later, Frisch and Vergassola[4] claimed that the universality of the energy spectrum can be recovered, if the fluctuations of the dissipative length scale are taken into account by introducing a new non-dimensionalisation procedure. The new prediction is that $\log\left(E(k)\epsilon^{-\frac{2}{3}}\eta^{-\frac{5}{3}}\right)/\log(\mathrm{Re})$ should be a universal function of $\log(k\eta)/\log(\mathrm{Re})$, where Re is the Reynolds number. This claim was examined by Gagne et al., later using data from the Modane wind tunnel experiments[1]. They further suggested that the prediction can be extended to the velocity structure functions, so that, at any given p $\log(S_p(\ell)/u_{\mathrm{K}}^p)/\log(\mathrm{Re})$ should be a universal function of $\log(\ell/\eta)/\log(\mathrm{Re})$; they

found good agreement for p up to 6. The velocity measurements, in the above experiments, were performed using hot wire anemometry, which provide access to only one component of velocity. To our knowledge, no further attempts have been made to check the claim with more realistic measurements.

The purpose of the present paper is to reexamine this claim; however, now using the velocity fields obtained from the Stereoscopic Particule Image Velocimetry (SPIV) in experiments and the direct numerical simulations (DNS) of the Navier-Stokes equations (NSE). We show that the numerical and experimental velocity structure functions up to order 9 follow a log-universality[1]; they indeed collapse on a universal curve, if we use units that include log(Re) dependence. We then investigate the meaning and consequences of such a log-universality, and show that it is connected with the properties of a "multifractal free energy", based on an analogy between multifractal and thermodynamics (see for summary). We show that in such a framework, the existence of a fluctuating dissipation length scale is associated with a phase transition describing the relaminarisation of rough velocity fields with different Hölder exponents.

II. EXPERIMENTAL AND NUMERICAL SETUP

A. Experimental facilities and parameters

We use experimental velocity field described in[5]. The radial, axial and azimuthal velocity are measured in a von Krmn flow, using Stereoscopic Particule Image Velocimetry technique at different resolutions Δx. The von Krmn flow is generated in a cylindrical tank of radius $R = 10\,\mathrm{cm}$ through counter-rotation of two independent impellers with curved blades. The flow was maintained in a turbulent state at high Reynolds number by two independent impellers, rotating at frequency F. Figure 1 shows the sketch of the experimental setup. The five experiments were performed in conditions so that the non-dimensional mean energy dissipation per unit mass is constant. The viscosity was monitored using mixture of water and glycerol, so as to vary the Kolmogorov length η. Table I summarizes the different parameters; $R_\lambda = \lambda u^{\mathrm{rms}}/\nu$ is the Reynolds number based on the Taylor length scale $\lambda = \sqrt{\frac{\langle \mathbf{u}^2 \rangle}{\langle \nabla \mathbf{u}^2 \rangle}}$, the mean squared velocity u^{rms} and the viscosity ν.

All velocity measurements are performed in a vertical plane that contains the rotation axis. The case A corresponds to measurements over the whole plane contained in between the two impellers, and extending from one side to the other side of the cylinder. Its resolution is 5 to 10 times coarser than similar measurements performed by zooming on a region centered around the symmetry

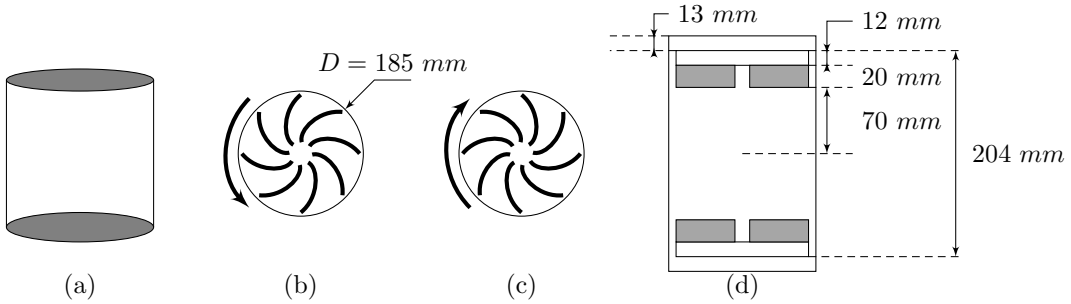

FIG. 1: Von Krmn swirling flow generator. (a) normal view, bottom (b) and top (c) impellers rotating -both seen from the center of the cylinder, and (d) sketch with the relevant measures. A device not shown here maintains the temperature constant during the experiment. Both impellers are counter-rotating.

Case	F (Hz)	Glycerol part	Re	R_λ	η (mm)	Δx	Frames	Symbol
A	5	0%	3×10^5	$1,9 \times 10^3$	0.02	2.4	3×10^4	$\circ$
B	5	0%	3×10^5	$2,7 \times 10^3$	0.02	0.48	3×10^4	$\square$
C	5	0%	3×10^5	$2,5 \times 10^3$	0.02	0.24	2×10^4	$\Diamond$
D	1	0%	4×10^4	$9,2 \times 10^2$	0.08	0.48	1×10^4	$\triangle$
E	1.2	59%	6×10^3	$2,1 \times 10^2$	0.37	0.24	3×10^4	$\star$

TABLE I: Parameters for the 5 experiments realized ($\mathbf{A}, \mathbf{B}, \mathbf{C}, \mathbf{D}$ *and* $\mathbf{E}$). F is the rotation frequency of the discs, Re refers to the Reynolds number based on the diameter of the tank, R_λ is the Reynolds based on the Taylor micro-scale. η gives the estimated Kolmogorov length according to the experiment and Δx refers to the spatial resolution of SPIV measurements. The last columns gives the number of frames used and the number of points over which are calculated the statistics. Except for ($\mathbf{E}$), the Reynolds are much larger than those available with DNS. Table taken from[5]

point of the experiment (on the rotation axis, half way in between the two impellers), over a square window of size 2 cm × 2 cm.

B. Direct Numerical Simulation

The direct numerical simulations (DNS), based on pseudo-spectral method, were performed in order to compare with our experimental data. The DNS runs with $R_\lambda = 25$, $R_\lambda = 80$, $R_\lambda = 90$ and $R_\lambda = 138$ were performed using the NSE solver VIKSHOBHA[6], whereas the run with $R_\lambda = 56$

R_λ	η	$k_{\max}\eta$	$N_x \times N_y \times N_z$	$\ell_{\min}/\eta$	$\widetilde{k_f}$	Samples	Symbol
25	0.079	3.35	128^3	0.635	1	5000	$\star$
56	0.034	6.42	256^3	0.31	1	105 000	$\triangle$
80	0.020	1.68	256^3	1.22	1	270 000	$\square$
90	0.017	5.70	1024^3	0.36	1	10 000	$\Diamond$
138	0.009	1.55	512^3	1.37	1	12 000	$\circ$

TABLE II: Parameters for the DNS. R_λ is the Reynolds based on the Taylor micro-scale. η is the Kolmogorov length. The third column gives resolution of the simulation through $k_{\max}\eta$,where $k_{\max} = N/3$ is the maximum wavenumber. The fourth column gives the grid size; notice that the length of the box is 2π. Here, $\ell_{\min}$ is the smallest scale available for the calculations of the wavelets. $\tilde{k}_f$ is the forcing scale. The Sample columns gives the number of points (frames $\times$ gridsize) over which are calculated the statistics.

was carried out using another independent pseudo-spectral method based NSE solver. The velocity field $\boldsymbol{u}$ was computed on a 2π triply-periodic box.

Turbulent flow in a statistically steady state was obtained by using the Taylor-Green type external forcing in the NSE at wavenumber $k_f = 1$ and amplitude $f_0 = 0.12$, the value of viscosity was varied in order to obtain different values of R_λ (see Ref.[6] for more details).

III. THEORETICAL BACKGROUND

A. Velocity increments vs Wavelet Transform (WT) of velocity gradients

The classical theories of Kolmogorov[7?] are based on the scaling properties of the velocity increment, defined as $\delta_\ell \mathbf{u} = \mathbf{u}(\mathbf{x}+\mathbf{r}) - \mathbf{u}(\mathbf{x})$, where $\ell = |\mathbf{r}|$ is the distance over which the increment is taken. As pointed out by, a more natural tool to characterize the local scaling properties of the velocity field is the wavelet transform of the tensor $\partial_j u_i$, defined as:

$$G_{ij}(\mathbf{x},\ell) = \int \mathrm{d}\mathbf{r} \nabla_j \Phi_\ell(\mathbf{r})\, u_i(\mathbf{x}+\mathbf{r}), \tag{1}$$

where $\Phi_\ell(\mathbf{x}) = \ell^{-3}\Phi(\mathbf{x}/\ell)$ is a smooth function, non-negative with unit integral. In what follows, we choose a Gaussian function $\Phi(\mathbf{x}) = \exp(-\|\mathbf{x}\|^2/2)/(2\pi)^{\frac{3}{2}}$ such that $\int \Phi(\mathbf{r})\mathrm{d}\mathbf{r} = 1$. We then compute the wavelet velocity increments as

$$\delta W(\mathbf{u})(\mathbf{x},\ell) = \ell \max_{ij} |G_{ij}(\mathbf{x},\ell)|. \tag{2}$$

This formulation is especially well suited for the analysis of the experimental velocity field, as it naturally allows to average out the noise. It has been verified that the wavelet based approach yields the same values for the scaling exponents as those computed from the velocity increments[6].

B. K41 and K62 universality

In the first theory of Kolmogorov[7], the turbulence properties depend only on two parameters: the mean energy dissipation per unit mass ϵ and the viscosity ν . The only velocity and length unit that one can build using these quantities are the Kolmogorov length $\eta = (\nu^3/\epsilon)^{1/4}$ and velocity $u_{\rm K} = (\epsilon\nu)^{1/4}$. The structure functions are then self-similar in the inertial range $\eta \ll \ell \ll L_0$, where L_0 is the integral scale, and follow the universal scalings:

$$S_p(\ell) \equiv \langle |\delta_\ell u|^p \rangle \sim u_{\rm K}^p \left(\frac{\ell}{\eta}\right)^{p/3}, \tag{3}$$

which can also be recast into:

$$\tilde{S}_p \equiv \frac{S_p}{S_3^{p/3}} = C_p, \tag{4}$$

where C_p is a (non universal) constant.

This scaling is typical of a global scale symmetry solutions, and was criticized by Landau, who considered it incompatible with observed large fluctuations of the local energy dissipation. Kolmogorov then built a second theory (K62), in which fluctuations of energy dissipation were assumed to follow a log-normal statistics, and taken into account via an intermittency exponent μ and a new length scale L, thereby breaking the global scale invariance. The resulting velocity structure functions then follow the new scaling:

$$S_p(\ell) \sim (\epsilon\ell)^{p/3} \left(\frac{\ell}{L}\right)^{\mu p(3-p)}, \tag{5}$$

which implies a new kind of universality involving the relative structure functions $\tilde{S}_p$ as:

$$\tilde{S}_p \equiv \frac{S_p}{S_3^{p/3}} \sim A_p \left(\frac{\ell}{L}\right)^{\tau(p)}, \tag{6}$$

where $\tau(p) = \mu p(3-p)$ and A_p is a constant. Such a formulation already predicts an interesting universality, if $L = L_0$, as we should have:

$$\left(\frac{L_0}{\eta}\right)^{\tau(p)} \tilde{S}_p \sim A_p \left(\frac{\ell}{\eta}\right)^{\tau(p)}. \tag{7}$$

Therefore, we should be able to collapse all structure functions, at different Reynolds number by plotting $(\frac{L_0}{\eta})^{\tau(p)}\tilde{S}_p$ as a function of $\frac{\ell}{\eta}$, given that $L_0/\eta \sim \mathrm{Re}^{3/4}$. There is however no clear prediction about the value of L and we show in the data analysis section that L differs from L_0.
The relation (7) shows that $\log\left(\left(\frac{L_0}{\eta}\right)^{\tau(p)}\tilde{S}_p\right)$ is a linear function of $\log(\frac{\ell}{\eta})$. In principle, such universal scaling is not valid outside the inertial range, i.e. for example when $\ell < \eta$. To be more general than previously thought, it can however be shown using the multifractal formalism as first shown by[4].

C. Multifractal and fluctuating dissipation length

For the multifractal (MFR) model, it is assumed that the turbulence is locally self-similar, so that there exists a scalar field $h(\mathbf{x}, \ell, t)$, such that

$$h\left(\mathbf{x}, t, \ell\right) = \frac{\log\left(|\delta_\ell \mathbf{u}(\mathbf{x}, t)|/u_0\right)}{\log(\ell/L)}, \tag{8}$$

for a range of scales in a suitable "inertial range" $\eta_h \ll \ell \ll L$, where L is a characteristic integral-length-scale, η_h a cut-off length scale, and u_0 a characteristic large-scale velocity. This scale is a generalization of the Kolmogorov scale, and is defined as the scale where the local Reynolds number $\ell|\delta_\ell \boldsymbol{u}|/\nu$ is equal to 1. Writing $\delta_\ell u = |\delta_\ell \mathbf{u}| = u_0(\ell/L)^h$ leads to the expression of η_h as a function of the global Reynolds number $\mathrm{Re} = u_0 L/\nu$ as $\eta_h \sim L\mathrm{Re}^{-1/(1+h)}$. This scale thus appears as a fluctuating cut-off which depends on the scaling exponent and therefore on $\boldsymbol{x}$. This is the generalization of the Kolmogorov scale $\eta \sim \nu^{3/4} \equiv \eta_{\frac{1}{3}}$, and was first proposed in. Below η_h, the velocity field becomes laminar, and $|\delta_\ell \mathbf{u}| \propto \ell$. When the velocity field is turbulent, $h \equiv \log(|\delta_\ell \mathbf{u}|/u_0)/\log(\ell/L)$ varies stochastically as a function of space and time. Also, if the turbulence is statistically homogeneous, stationary and isotropic, h only depends on ℓ, the scale magnitude. Therefore, formally, h can be regarded as a continuous stochastic process labeled by $\log(\ell/L)$. By Kramer's theorem[8], one sees that as in the limit $\ell \to 0$, $\log(L/\ell) \to \infty$, we have

$$\mathbb{P}\left[\log(\delta_\ell u/u_0) = h\log(\ell/L)\right] \sim e^{\log(\ell/L)C(h)} = \left(\frac{\ell}{L}\right)^{C(h)}, \tag{9}$$

where $C(h)$ is the rate function of h, also called multifractal spectrum. Formally, $C(h)$ can be interpreted as the co-dimension of the set where the local Hölder exponent at scale ℓ is equal to h. Using Gärtner-Elis theorem[8], one can connect C and the velocity structure functions as:

$$S_p(\ell) = \langle(\delta_\ell u)^p\rangle = \int_{h_{\min}}^{h_{\max}} u_0^p \left(\frac{\ell}{L}\right)^{ph+C(h)} \mathrm{d}h. \tag{10}$$

To proceed further and make connection with previous section, we set $\epsilon = u_0^3/L$ so that $S_p(\ell)$ can now be written:

$$S_p(\ell) = (\epsilon\ell)^{p/3} \int_{h_{\min}}^{h_{\max}} \Big(\frac{\ell}{L}\Big)^{p(h-1/3)+C(h)} \mathrm{d}h \sim (\epsilon\ell)^{p/3} \Big(\frac{\ell}{L}\Big)^{\tau(p)}. \tag{11}$$

This shows that $\tau(p)$ is the Legendre transform of the rate function $C(h+1/3)$, i.e. $\tau(p) = \min_h(p(h-1/3)+C(h))$, and equivalently, that $C(h)$ is the Legendre transform of $\tau(p)$. Because of this, it is necessarily convex. The set of points where it satisfies $C(h) \leq d$, represents the set of admissible or observable h, is therefore necessarily an interval, bounded by $-1 \leq h_{\min}$ and $h_{\max} \leq 1$.

As noted by[4], the scaling exponent $\zeta(p) = p/3 + \tau(p)$ defined via Equation (11) is only constant in a range of scale where $\ell > \eta_h$ for any $h \in [h_{\min}, h_{\max}]$. For small enough ℓ, this condition is not met anymore, since as soon as $\ell < \eta_h$, all velocity fields corresponding to h are "regularized", and do not contribute anymore to intermittency since they scale like ℓ. This results in a slow dependence of $\zeta(p)$ with respect to the scale, which is obtained via the corrected formula:

$$S_p = (\epsilon\ell)^{p/3} \int_{\eta_h \leq \ell} \Big(\frac{\ell}{L}\Big)^{p(h-1/3)+C(h)} \mathrm{d}h \sim (\epsilon\ell)^{p/3} \Big(\frac{\ell}{L}\Big)^{\tau(p,\ell)}. \tag{12}$$

To understand the nature of the correction, we can compute the value of h such that $\ell = \eta(h)$. It is simply: $h(\ell) = -1 + \log(\mathrm{Re})/\log(L/\eta)$. We note $\theta = \log(L/\ell)/\log(\mathrm{Re})$. We can now rewrite equation (12) as:

$$\tilde{S}_p \equiv \frac{S_p}{S_3^{p/3}} = \int_{-1+1/\theta}^{h_{\max}} \Big(\frac{\ell}{L}\Big)^{p(h-1/3)+C(h)} \mathrm{d}h \sim \exp\left(-\theta\tau(p,\theta)\log(\mathrm{Re})\right), \tag{13}$$

where $\tau(p,\theta) = \tau_p$ when $\theta \leq 1/(1+h_{\max})$ and $\tau(p,\theta) = p(\theta-1/3)+C(-1+1/\theta)$ when $1/(1+h_{\max}) \leq \theta \leq 1/(1+h_{\min})$. As discussed by[4], this implies a new form of universality that extends beyond the inertial range, into the so-called extended dissipative range, as;

$$\frac{\log(\tilde{S}_p)}{\log(\mathrm{Re})} = -\tau(p,\theta)\theta, \quad \theta = \log(L/\ell)/\log(\mathrm{Re}). \tag{14}$$

If the scale L is constant and equal to L_0, the integral scale, then we have $\mathrm{Re} = (L_0/\eta)^{4/3}$ and the multifractal universality implies that $\log(\tilde{S}_p)/\log(L_0/\eta)$ is a function of $\log(\ell/\eta)/\log(L_0/\eta)$. When the function is linear, we thus recover the K62 universality. The multifractal universaility is thus a *generalization* of the K62 universality.

This form of universality is however not easy to test, as the scale L is not known a priori, and may still depend on Re. In what follows, we demonstrate a new form of universality, that allows more freedom upon L and encompass both K62 and multifractal universality.

D. General universality

Using the hypothesis that turbulence maximizes some energy transfer in the scale space, Castaing[9] suggested a new form of universality for the structure functions, that reads:

$$\gamma(\mathrm{Re}) \log\left(\frac{S_p}{A_p u_{\mathrm{K}}^p}\right) = G\left(p, \gamma(\mathrm{Re}) \log(\ell K_0/\eta)\right), \tag{15}$$

where A_p and K_0 are universal constant and β and G are general functions, F being linear in the inertial range, $G(p,x) \sim \tau(p)x$. The validity of this universal scaling was checked by Gagne and Castaing[1] on data obtained from the velocity fields measured in a jet using hot wire anenometry. They found good collapse of the structure functions at different Taylor Reynolds R_λ, provided $\gamma(\mathrm{Re})$ is constant at low Reynolds numbers and follows a law of the type: $\gamma(\mathrm{Re}) \sim \gamma_0/\log(R_\lambda/R_*)$, where R_* is a constant, whenever $R_\lambda > 400$. Since we have $R_\lambda \sim \mathrm{Re}^{1/2}$ and $(L_0/\eta) \sim \mathrm{Re}^{3/4}$, we can rewrite equation (15) as:

$$\beta(\mathrm{Re}) \left(\frac{\log(\tilde{S}_p/S_{0p})}{\log(L_0/\eta)}\right) = G\left(p, \beta(\mathrm{Re}) \frac{\log(\ell/\eta)}{\log(L_0/\eta)}\right), \tag{16}$$

where S_{0p} are some constants and β and F are general functions. Comparing with the K62 or MFR universality formulae (7) or (14), we see that formula (16) is a generalization of these two universality with $L = L_0$. It allows however more flexibility than K62 or MFR universality through the function $\beta(\mathrm{Re})$, that is a new fitting function. We test these predictions in Section IV and provide a physical interpretation of (16) in Section V.

IV. CHECK OF UNIVERSALITY USING DATA ANALYSIS

The various universality are tested using the velocity structure functions based on the wavelet velocity increments Eq. (2), in order to minimize the noise in the experimental data. We define:

$$S_p = \langle |\delta W(\mathbf{u})(\mathbf{x}, \ell)|^p \rangle. \tag{17}$$

We then apply this formula to both experimental data (Table I) and numerical data (Table II), to get wavelet velocity structure functions at various scales and Reynolds numbers.

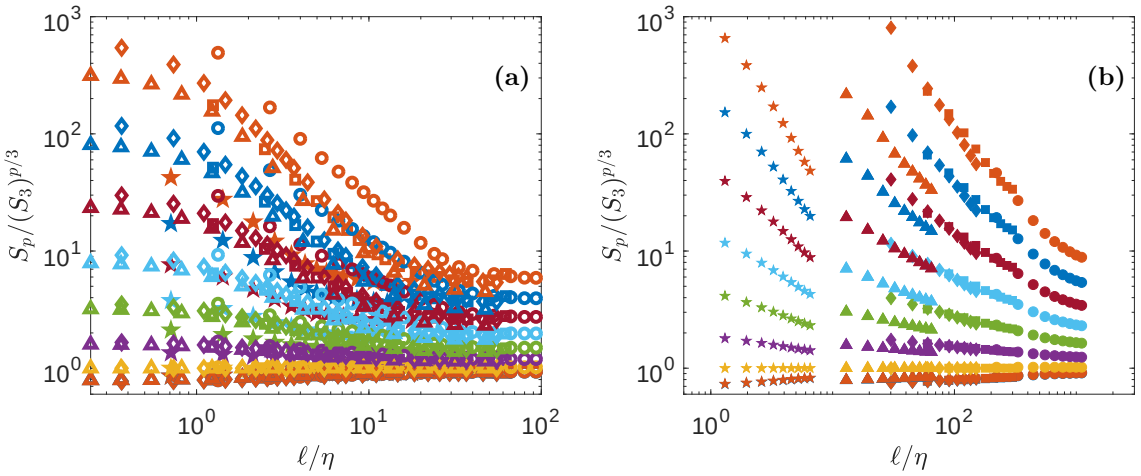

FIG. 2: Test of K41 universality Eq. (4). a) Numerical data b) Experimental data. The structure functions have been shifted by arbitrary factors for clarity and are coded by color: $p = 1$: blue symbols; $p = 2$: orange symbols; $p = 3$: yellow symbols; $p = 4$: magenta symbols; $p = 5$: green symbols; $p = 6$: light blue symbols; $p = 7$: red symbols; $p = 8$: blue symbols; $p = 9$: orange symbols. For K41 universality to hold, all the function should be constant, for a given p.

A. Check of K41 universality

The K41 universality (3) can be checked by plotting:

$$\log\left(\frac{S_p}{u_{\mathrm{K}}^p}\right) = F\left(\log\left(\frac{\ell}{\eta}\right)\right). \tag{18}$$

This is shown in figure 2 for both experimental and numerical data. Obviously, the data do not collapse on a universal curve, meaning that K41 universality does not hold. This is well known, and is connected to intermittency effects[10].

B. Check of K62 universality

The K62 universality (7) can be checked by plotting:

$$\log\left[\left(\frac{L_0}{\eta}\right)^{\tau(p)}\tilde{S}_p\right] = F\left(\log\left(\frac{\ell}{\eta}\right)\right). \tag{19}$$

The collapse depends directly on $\tau(p)$, the intermittency exponents. Obtaining the best collapse of all curves is in fact a way to fit the best scaling exponents $\tau(p)$. We thus implemented a minimization algorithm that provides the values of $\tau(p)$ that minimized the distance between the

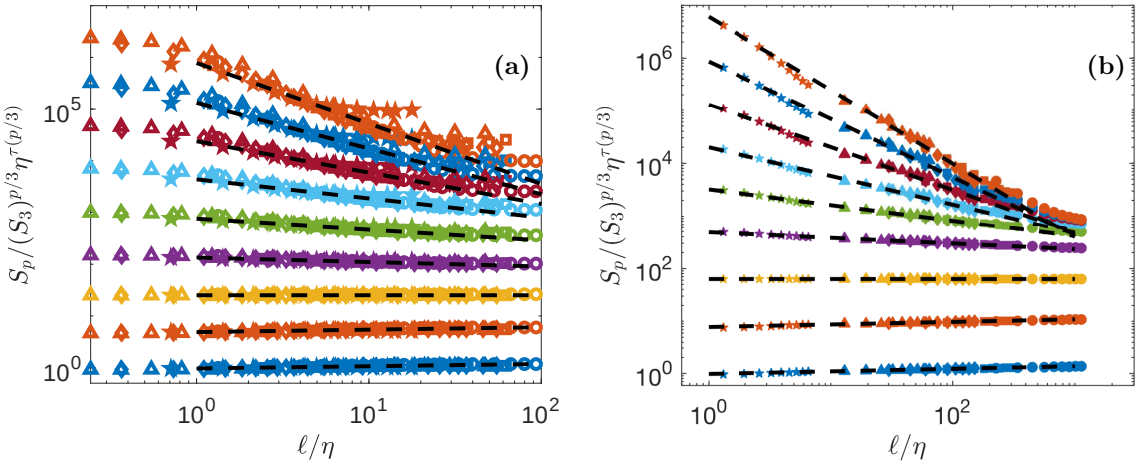

FIG. 3: Test of K62 universality Eq. (7). a) Numerical data b) Experimental data. The structure functions have been shifted by arbitrary factors for clarity and are coded by color: $p = 1$: blue symbols; $p = 2$: orange symbols; $p = 3$: yellow symbols; $p = 4$: magenta symbols; $p = 5$: green symbols; $p = 6$: light blue symbols; $p = 7$: red symbols; $p = 8$: blue symbols; $p = 9$: orange symbols. The dashed lines are power laws with exponents $\tau(p) = \zeta(p) - \zeta(3)p/3$, with $\zeta(p)$ shown in figure 4-a.

curve and the line of slope $\tau(p)$. The values of $\tau(p)$ are reported in Table III. The best collapse is shown on Figure 3-a for the DNS, and Figure 3-b for the experiment. The collapse is better for experiments than for the DNS. However, in both cases, there are significant differences in between points at different R_λ, at larger scales, showing that universality is not yet reached.

C. Check of General Universality

We can now check the most general universality, by plotting:

$$\beta(\mathrm{Re})\left(\frac{\log(\tilde{S}_p/S_{0p})}{\log(L_0/\eta)}\right) = F\left(p, \beta(\mathrm{Re})\frac{\log(\ell/\eta)}{\log(L_0/\eta)}\right), \tag{20}$$

In this case, best collapse is obtained by fitting two families of parameters: S_{0p}, $\beta(\mathrm{Re})$ that were obtained through a procedure of minimization. We take the DNS at $R_\lambda = 138$ as the reference case, and find for both DNS and experiments, the values of $\beta(\mathrm{Re})$ and S_{0p} that best collapse the curves. The corresponding collapses are provided in figure 5. The collapse is good for any value of Re, except for the DNS at the lowest Reynolds number, which does not collapse in the far dissipative range.

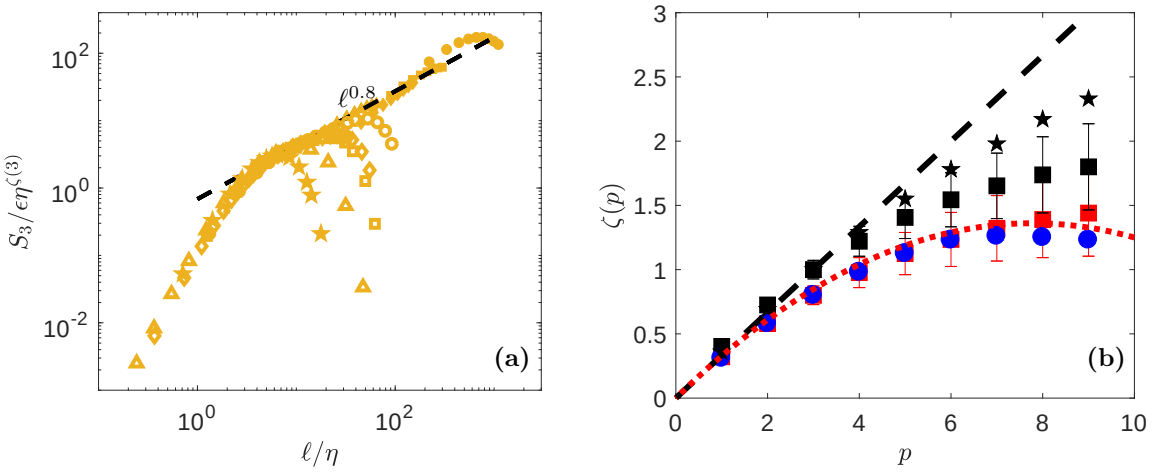

FIG. 4: . a) Determination of $\zeta(3)$ by best collapse using both DNS (open symbols) and experiments (filled symbols). The black dashed line is $\ell^{0.8}$. b) Scaling exponents $\zeta(p)$ of the wavelet structure functions of δW as a function of the order, from Table III, for DNS (blue circle) and experiments (red square) . The red dotted line is the function $\min_h(hp + C(h))$ with $C(h)$ given by $C(h) = (h-a)^2/2b$, with $a = 0.35$ and $b = 0.045$. The black stars correspond to $\zeta_{\rm SAW}(p)/\zeta_{\rm SAW}(3)$ (see Table III), while the black triangle correspond to $\zeta_{\rm EXP}(p)/\zeta_{\rm EXP}(3)$.

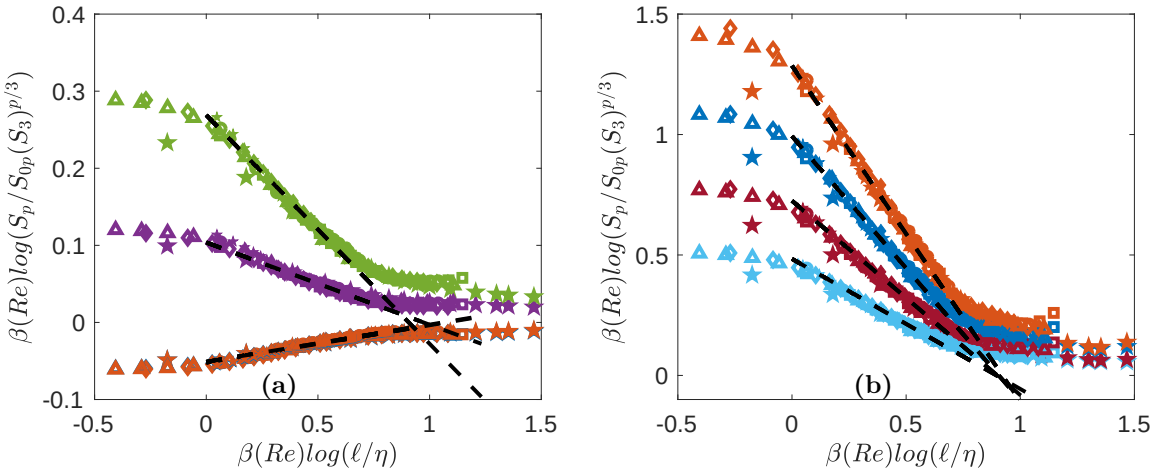

FIG. 5: Test of general universality equation (20) using both DNS (open symbols) and experiments (filled symbols). The functions are coded by color. a) $p = 1$: blue symbols; $p = 2$: orange symbols; $p = 4$: magenta symbols; $p = 5$: green symbols; b) $p = 6$: light blue symbols; $p = 7$: red symbols; $p = 8$: blue symbols; $p = 9$: orange symbols. The functions have been shifted by arbitrary factors for clarity. The dashed lines are power laws with exponents $\tau(p) = \zeta(p) - \zeta(3)p/3$, with $\zeta(p)$ shown in figure 4-a.

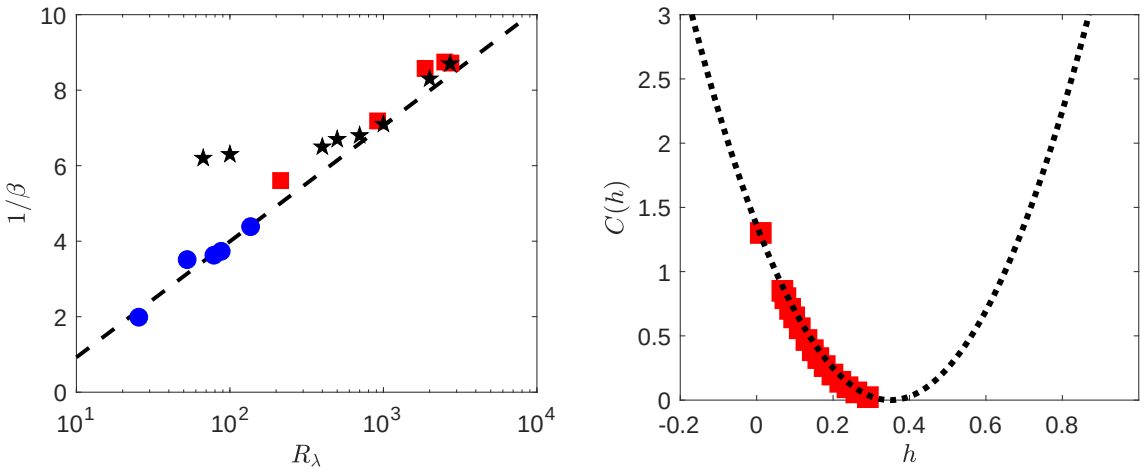

FIG. 6: a) Variation of $1/\beta(\mathrm{Re})$ versus $\log(R_\lambda)$ in experiments (red square) and DNS (blue circle) when using the DNS at $R_\lambda = 138$ as the reference case. We plotted in black the values found by Gagne and Castaing in[1] shifted by an arbitrary factor to coincide the values at large Reynolds. The black dashed line is $(4/3)\log(R_\lambda/5)$. b) Multifractal spectrum $C(h)$ for the experiments. The spectrum has been obtained by taking inverse Legendre transform of the scaling exponents $\zeta(p)$ shown in figure 4-b. The dotted line is a parabolic fit $C(h) = (h-a)^2/2b$ with $a = 0.35$ and $b = 0.045$.

D. Function β(Re)

Motivated by earlier findings by[1], we plot in figure 6 the value $1/\beta$ as a function of R_λ.
Our results are compatible with $1/\beta \sim \beta_0/\log(R_\lambda)$, with $\beta_0 \sim 4/3$ over the whole range of Reynolds number. For comparison, we provide also on figure 6 the values found by Gagne and Castaing[1] in jet of liquid Helium, shifted by an arbitrary factor to make our values coincide with them at large Reynolds number. This shift is motivated by the fact that $\beta(\mathrm{Re})$ is determined up to a constant, depending upon the amplitude of the structure functions used as reference. At large Reynolds, our values are compatible with theirs. At low Reynolds, however, we do not observe the saturation of $1/\beta$ that is observed in the jet experiment of[1]. An interpretation of the meaning of $\beta(\mathrm{Re})$ will be provided in Section V.

E. Scaling exponents

Our Collapse method enables us to obtain the scaling exponents of the structure functions $\zeta(p)$ by the following two methods:

i) Using the K62 universality, we get $\tau(p)$, and then $\zeta(p) = \zeta(3)p/3 + \tau(p)$. These estimates still depend on the value of $\zeta(3)$, which is not provided by the K62 universality plot. To obtain it, we use a minimization procedure on both experimental $\log(S_3/u_{\rm K}^3)$ from the one hand, and the numerical $\log(S_3/u_{\rm K}^3)$ on the other hand (see figure 4-a), to compute $\zeta(3)$ as the value that minimizes the distance between the curve and a straight line of slope $\zeta(3)$. The values so obtained are reported in Table III, and have been used to compute $\zeta(p)$ from $\tau(p)$.

ii) Using the general universality, we may also get $\tau_{p,\rm univ}$ by a linear regression on the collapse curve. Note that since the data are collapsed, this provides a very good estimates of this quantity, with the lowest possible noise. In practice, we observe no significant differences with the two estimates; therefore, we only report the values obtained by following the first method.

The corresponding values are plotted in figure 4 and summarized in Table III. Note that for both DNS and experiments, the value of $\zeta(3)$ is different from 1, which is apparently incompatible with the famous Kolmogorov 4/5th law, that predicts $\zeta(3) = 1$. This is because we use *absolute* values of wavelet increments, while the Kolmogorov 4/5th law uses signed values. We have checked that using unsigned values, we obtain a scaling that is closer to 1, but with larger noise. Note also that when we consider the relative value $\zeta(p)/\zeta(3)$, we obtain values that are close to the values obtained[5] on the same set of experimental data, using velocity increments and Extended Self-Similarity technique[11].

F. Multifractal spectrum

From the values of $\zeta(p)$, one can get the multifractal spectrum $C(h)$ by performing the inverse Legendre transform:

$$C(h) = \min_p [ph + \zeta(p))]. \tag{21}$$

Practically, this amount to use the following formula:

$$C\Big(\frac{\mathrm{d}\,\zeta(p)}{\mathrm{d}\,p}\Big|_{p^*}\Big) = \zeta(p^*) - p^* \frac{\mathrm{d}\,\zeta(p)}{\mathrm{d}\,p}\Big|_{p^*}. \tag{22}$$

To estimate C, we thus first perform a polynomial interpolation of order 4 on $\zeta(p)$, then derivate the polynom to estimate $\frac{\mathrm{d}\,\zeta(p)}{\mathrm{d}\,p}$, thus get C through equation (22). The result is provided in figure

exponent \ order	$p=1$	$p=2$	$p=3$	$p=4$	$p=5$	$p=6$	$p=7$	$p=8$	$p=9$
$\zeta_{\rm SAW}/\zeta_{\rm SAW}(3)$	0.36	0.69	1	1.29	1.55	1.78	1.98	2.17	2.33
$\zeta_{\rm DNS}$	0.31	0.58	0.80	0.98	1.12	1.23	1.26	1.25	1.23
$\zeta_{\rm EXP}$	0.32	0.58	0.80	0.98	1.12	1.23	1.32	1.39	1.44
$\tau_{\rm DNS}$	0.04	0.05	0	-0.09	-0.21	-0.37	-0.61	-0.88	-1.17
$\tau_{\rm EXP}$	0.05	0.05	0	-0.09	-0.21	-0.36	-0.54	-0.74	-0.96

TABLE III: Scaling exponents $\tau(p)$ and $\zeta(p)$ found by the collapse method based on K62 universality for experimental data (subscript EXP) or numerical data (subscript DNS). The subscript SAW refers to the values obtained by[5] on the same set of experimental data, using velocity increments and Extended Self-Similarity technique[11]. The exponents $\tau_{\rm EXP}(p)$(red square) and $\tau_{\rm DNS}$ (blue circle) have been computed through a least square algorithm upon $\tau(p)$, minimizing the scatter of the rescaled structure functions $\log\left[\left(\frac{L_0}{\eta}\right)^{\tau(p)}\tilde{S}_p)\right]$ with respect to the line $(\ell/\eta)^{\tau(p)}$. The corresponding $\zeta(p)$ were inferred using the formula $\zeta(p)=\tau(p)+\zeta(3)p/3$, where $\zeta(3)$ is computed in figure 4-a.

6-b for both the DNS and the experiment.

The curve look like the portion of a parabola, corresponding to a log-normal statistics for the wavelet velocity increments. Specifically, fitting by the shape:

$$C(h)=\frac{(h-a)^2}{2b}, \tag{23}$$

we get $a=0.35$ and $b=0.045$. This parabolic fit also provides a good fit of the scaling exponents, as shown in figure 4 by performing Legendre transform of $C(h)$ given by equation (23).

V. THERMODYNAMICS AND TURBULENCE

A. Thermodynamical analogy

Multifractals obey a well-known thermodynamical analogy[12?,13] that will be useful to interpret and extend the general universality unraveled in the previous section. Indeed, consider the quantity:

$$\mu_\ell=\frac{|\delta W_\ell|^3}{\langle|\delta W_\ell|^3\rangle}. \tag{24}$$

By definition μ_ℓ is positive definite and $\langle \mu_\ell \rangle = 1$ for any ℓ. It is therefore the meaning of a scale dependent measure. It then also follows a large-deviation property as:

$$\mathbb{P}\left[\log(\mu_\ell) = E\log(\ell/\eta)\right] \sim e^{\log(\ell/\eta)S(E)}, \tag{25}$$

where $S(E)$ is the large deviation function of $\log(\mu_\ell)$ and has the meaning of an energy while $\log(\ell/\eta)$ has the meaning of a volume, and $\log(\mu_\ell)/\log(\ell/\eta)$ is an energy density. Because of the definition of μ_ℓ, it is easy to see that S is connected to C, the large deviation function of $|\delta W_\ell$. In fact, since in the inertial range where $\langle |\delta W_\ell|^3 \rangle \sim \ell^{\zeta(3)}$, we have $S(E) = C(3h - \zeta(3))$. By definition, we also have:

$$\tilde{S}_{3p} = \frac{S_{3p}}{S_3^p} = \langle e^{p\log(\mu_\ell)} \rangle, \tag{26}$$

so that $Z = \tilde{S}_{3p}$ is the partition function associated to the variable $\log(\mu_\ell)$, at the pseudo-inverse temperature $p = 1/kT$. Taking the logarithm of Z, we then get the free energy F as:

$$\log(\tilde{S}_{3p}) = F. \tag{27}$$

By the Gärtner-Elis theorem, F is the Legendre transform of the energy S: $F = \min_E(pE - S(E))$. The free energy a priori depends on the temperature; i.e. on $T = 1/kp$, on the volume $V = \log(\ell/\eta)$ and on the number of degrees of freedom system N. If we identify $N = (1/\beta(\mathrm{Re}))\log(L_0/\eta)$, we see that the general universality means:

$$F(T, V, N) = NF(T, \frac{V}{N}, 1), \tag{28}$$

i.e. can be interpreted as *extensivity* of the free energy.

	Thermodynamics	Turbulence
Temperature	$k_B T$	$1/p$
Energy	E	$\log(\mu_\ell)$
Number of d.f.	N	$\log(\mathrm{Re}) \equiv \log(L_0/\eta)/\beta_0$
Volume	V	$\log(\ell/\eta)$
Pressure	P	$\tau(p, \ell)$
Free energy	F	$\log(\tilde{S}_{3p})$

TABLE IV: Summary of the analogy between the multifractal formalism of turbulence and thermodynamics.

The thermodynamic analogy is thus meaningful and is summarized in Table IV. It can be used to derive interesting prospects.

B. Multifractal pressure and phase transition

Given our free energy, $F = \log(\tilde{S}_{3p})$, we can also compute the quantity conjugate to the volume, i.e. the multifractal pressure as: $P = \partial F/\partial V$. In the inertial range, where $\tilde{S}_p \sim \ell^{\tau(p)}$, we thus get $P = \tau(p)$, which only depends on the temperature. Outside the inertial range, P has the meaning of a local scaling exponents also depends upon the scale, i.e., on the volume V and on N (Reynolds number). Using our universal functions derived in figure 5, we can then compute empirically the multifractal pressure P and see how it varies as a function of T, V and N. It is provided in figure 7 for $R_\lambda = 25$ and $R_\lambda = 56$, and in figure 8 for $R_\lambda = 90$ and $R_\lambda = 138$. We see that at low Reynolds number, the pressure decreases monotonically from the dissipative range, reaches a lowest points and then increases towards the largest scale. There is no clear flat plateau that would correspond to an "inertial" range. In contrast, at higher Reynolds number, a plateau appears for $p = 1$ to $p = 4$ when going towards the largest scale, the value of the plateau corresponding to $\tau_{\rm DNS}$. The plateau transforms into an inflection point for $p \geq 5$ making the derivative $\partial P/\partial V$ change sign. This is reminiscent of a phase transition occurring in the inertial range, with coexistence of two phases: one "laminar" and one "turbulent". We interpret such a phase transition as the result of the coexistence of region of flows with different Hölder exponents, with areas where the flow has been relaminarized due to the action of viscosity, because of the random character of the dissipative scale (see below).

VI. CONCLUSION

We have shown that a deep analogy exists between multifractal and classical thermodynamics. In this framework, one can derive from the usual velocity structure function an effective free energy that respects the classical extensivity properties, provided one uses a number of degrees of freedom (given by $N = 1/\beta(\mathrm{Re})$) that scales like $\log(R_\lambda)$. This number is much smaller than the classical $N \sim \mathrm{Re}^{9/4}$ that is associated with the number of nodes needed to discretize the Navier-Stokes equation down to the Kolmogorov scale. It would be interesting to see whether this number is also associated with the dimension of a suitable "attractor of turbulence". Using the analogy, we also found the "multifractal" equation of state of turbulence, by computing the multifractal pressure $P = \partial F/\partial V$. We found that for large enough R_λ and p (the temperature), the system obeys a phase transition, with coexistence of phase like in the vapor-liquid transition. We interpret this phase transition as the result of the coexistence of region of flows with different Hölder exponents,

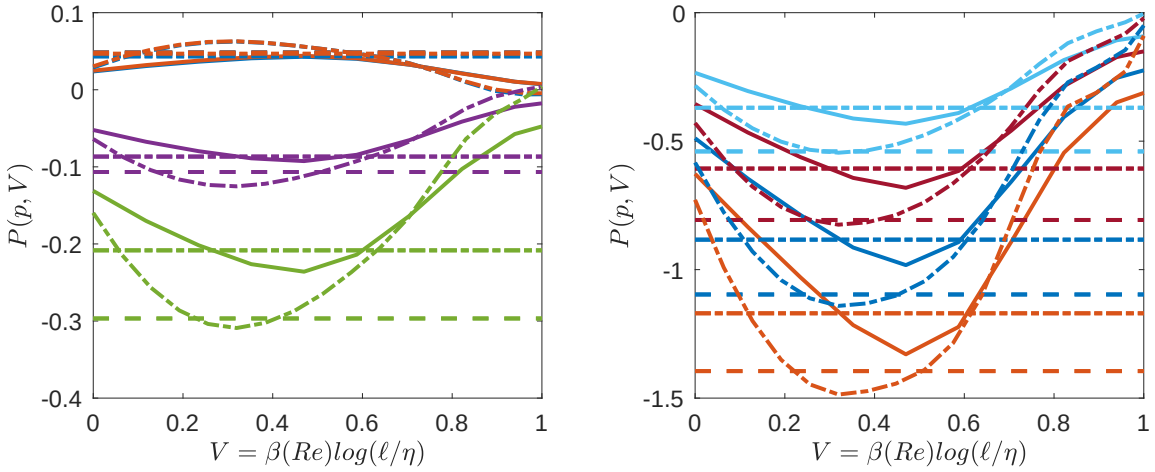

FIG. 7: Multifractal equation of state of turbulence. Multifractal pressure as a function of the volume for $R_\lambda = 25$ (line) , $R_\lambda = 56$ (dashed-dotted line). The functions are coded by color. a) $p = 1$: blue symbols; $p = 2$: orange symbols; $p = 4$: magenta symbols; $p = 5$: green symbols; b) $p = 6$: light blue symbols; $p = 7$: red symbols; $p = 8$: blue symbols; $p = 9$: orange symbols. The colored dotted line (resp. dashed dotted line) are values corresponding to $P(p, V) = \tau_{\rm EXP}(p)$ (resp. $\tau_{\rm DNS}(p)$, that are reported in Table III.

with areas where the flow has been relaminarized due to the action of viscosity, because of the random character of the dissipative scale. We note that this kind of phenomenon has already been observed in the context of Lagrangian velocity increments, using the local scaling exponent $\zeta(p, \tau) = {\rm d}(\log(S_p(\tau)))/{\rm d}(\log(\tau))$[14]. The phase transition is then associated with the existence of a fluctuating dissipative time scale. It has further been shown that in a multifractal without fluctuating dissipative time scale, the local exponent decreases monotically from dissipative scale to large scale, implying a disappearance of the phase transition[15].

[1] B. Castaing, Y. Gagne, and M. Marchand, Physica D: Nonlinear Phenomena **68**, 387 (1993).

[2] B. Dubrulle, Journal of Fluid Mechanics Perspectives , xx (2019).

[3] G. L. Eyink, "Turbulence Theory," http://www.ams.jhu.edu/ eyink/Turbulence/notes/ (2007-2008), course notes, The Johns Hopkins University,.

[4] U. Frisch and M. Vergassola, Europhysics Letters (EPL) **14**, 439 (1991).

[5] E.-W. Saw, P. Debue, D. Kuzzay, F. Daviaud, and B. Dubrulle, Journal of Fluid Mechanics **837**, 657669 (2018).

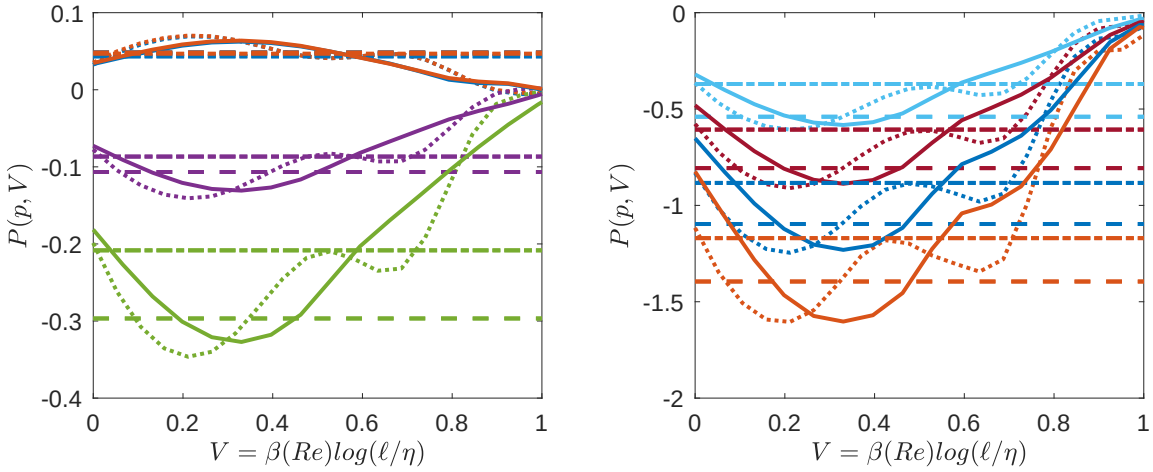

FIG. 8: Same as figure 7 for $R_\lambda = 90$ (line), $R_\lambda = 138$ (dotted line). Note the inflexion point appearing in the curves.

[6] P. Debue, V. Shukla, D. Kuzzay, D. Faranda, E.-W. Saw, F. Daviaud, and B. Dubrulle, Phys. Rev. E **97**, 053101 (2018).

[7] A. N. Kolmogorov, Dokl. Akad. Nauk SSSR [Sov. Phys.-Dokl.] **30**, 913 (1941).

[8] H. Touchette, Physics Reports **478**, 1 (2009).

[9] Castaing, B., J. Phys. France **50**, 147 (1989).

[10] U. Frisch, in Turbulence, the legacy of A. N. Kolmogorov (Cambridge University Press, 1996).

[11] R. Benzi, S. Ciliberto, R. Tripiccione, C. Baudet, F. Massaioli, and S. Succi, Phys. Rev. E **48**, R29 (1993).

[12] T. Bohr and D. Rand, Physica D: Nonlinear Phenomena **25**, 387 (1987).

[13] A. Rinaldo, A. Maritan, F. Colaiori, A. Flammini, R. Rigon, I. Rodriguez-Iturbe, and J. R. Banavar, Physical review letters **76**, 3364 (1996).

[14] A. Arneodo, R. Benzi, J. Berg, L. Biferale, E. Bodenschatz, A. Busse, E. Calzavarini, B. Castaing, M. Cencini, L. Chevillard, R. T. Fisher, R. Grauer, H. Homann, D. Lamb, A. S. Lanotte, E. Lévèque, B. Lüthi, J. Mann, N. Mordant, W.-C. Müller, S. Ott, N. T. Ouellette, J.-F. Pinton, S. B. Pope, S. G. Roux, F. Toschi, H. Xu, and P. K. Yeung (International Collaboration for Turbulence Research), Phys. Rev. Lett. **100**, 254504 (2008).

[15] L. Biferale, G. Boffetta, A. Celani, B. J. Devenish, A. Lanotte, and F. Toschi, Phys. Rev. Lett. **93**, 064502 (2004).

Detection and characterization of quasi singularities in turbulence

Abstract

It is still not known whether the equations of Navier–Stokes are well posed, i.e. whether their solutions can develop singularities from regular initial conditions. This unsolved problem might be the key to explain anomalous dissipation. As such, a method based on local energy transfers has been developed as a mean to identify potentially singular events in turbulence data. In this thesis, a local statistical method derived from multifractal analysis is developed in order to measure local Hölder coefficients. This method provides an estimate of the local regularity of turbulent velocity fields. Combined with local energy transfers, this allows us to locate and characterize quasi singular events. The method is applied in simulation to extract rare irregular structures at the dissipative scale. From the data aggregated, we derive a "typical singular event" bearing similarities with a Burgers vortex. Extending the analysis to time resolved data shows that irregular events are connected with vortex interactions. In parallel, we developed a new simulation scheme for Navier–Stokes based on a particles-in-cell model and using the Clebsch decomposition. Its purpose is to track potential singularities in scale for a comparatively low computational cost.

Keywords: Navier–Stokes, Singularities, Turbulence, Multifractal, Simulations, PIC method

---

Détection et caractérisation des singularités en turbulence

Résumé

Il n'est pas encore démontré que les équations de Navier–Stokes sont bien posées, c'est à dire que leur solutions ne développent pas de singularités à partir de condition initiales régulières. Résoudre ce problème pourrait conduire à expliquer l'anomalie dissipative. Ainsi, une méthode fondée sur les transferts d'énergie locaux a été développée comme un critère de détection de singularités potentielles. Dans cette thèse, nous développons une méthode à la fois locale et statistique, dérivée de l'analyse multifractale, afin de mesurer des coefficients de Hölder locaux. Cette méthode nous permet d'estimer la régularité locale de champs de vitesse turbulents. Combiné au critère fondé sur les transferts d'énergie, ceci nous permet de localiser et quantifier des événements quasi singuliers. La méthode a été appliquée sur des données de simulation afin d'extraire des structures irrégulières à l'échelle dissipative. A partir des données ainsi obtenues, nous reconstituons un "événement singulier typique" qui présente des similarités avec le vortex de Burgers. L'analyse sur des données résolues en temps montre une connexion avec les interactions entre tourbillons. En parallèle, nous avons construit un nouveau schéma de simulation pour Navier–Stokes fondé sur un modèle particulaire et la décomposition de Clebsch. L'objectif affiché est de suivre à moindre coût les singularités potentielles en échelle.

Mots clés : Navier–Stokes, Singularités, Turbulence, Multifractal, Simulations, Méthode PIC

Laboratoire de Mécanique des Fluides de Lille-Kampé de Fériet
Boulevard Paul Langevin, 59655 Villeneuve d'Ascq